

**Development of Experimental and Numerical Methods
for Flaw Interaction Assessment in a Strain-Based Context**

**Ontwikkeling van experimentele en numerieke technieken
voor de beoordeling van foutinteractie in een rekgebaseerde context**

Kaveh Samadian

Promotoren: prof. dr. ir. W. De Waele, prof. dr. ir. S. Hertelé
Proefschrift ingediend tot het behalen van de graad van
Doctor in de ingenieurswetenschappen: werktuigkunde-elektrotechniek



**UNIVERSITEIT
GENT**

Vakgroep Elektrische Energie, Metalen, Mechanische Constructies en Systemen
Voorzitter: prof. dr. ir. L. Dupré
Faculteit Ingenieurswetenschappen en Architectuur
Academiejaar 2018 - 2019

ISBN 978-94-6355-274-5

NUR 978, 950

Wettelijk depot: D/2019/10.500/82

Examination board:

- Prof. Dr. Ir. Patrick De Baets– Chairman
Department of Electrical Energy, Metals, Mechanical Construction & Systems
(EEMMeCS)
Faculty of Engineering and Architecture
Ghent University
- Prof. Dr. Ir. Wim De Waele– Supervisor
Department of Electrical Energy, Metals, Mechanical Construction & Systems
(EEMMeCS)
Faculty of Engineering and Architecture
Ghent University
- Prof. Dr. Ir. Stijn Hertelé- Co-supervisor
Department of Electrical Energy, Metals, Mechanical Construction & Systems
(EEMMeCS)
Faculty of Engineering and Architecture
Ghent University
- Prof. Dr. Ir. Patricia Verleysen
Department of Electrical Energy, Metals, Mechanical Construction & Systems
(EEMMeCS)
Faculty of Engineering and Architecture
Ghent University
- Dr. Ir. Koen Van Minnebruggen – Secretary
Department of Electrical Energy, Metals, Mechanical Construction & Systems
(EEMMeCS)
Faculty of Engineering and Architecture
Ghent University
- Dr. Ir. Phuc Phung Van
Department of Electrical Energy, Metals, Mechanical Construction & Systems
(EEMMeCS)
Faculty of Engineering and Architecture
Ghent University
- Dr. Ir. Valéry Lacroix
TRACTEBEL - ENGIE Group
- Dr. Harry Coules
Solid Mechanics Research Group
Faculty of Engineering
Bristol University

Ghent University
Faculty of Engineering and Architecture
Department of Electrical Energy, Metals, Mechanical Construction & Systems - EA08
Soete Laboratory
Technologiepark 46, 9052 Zwijnaarde, Belgium

Tel: +32 9 331 04 84
Fax: +32 9 331 04 82
Email: Kaveh.samadian@ugent.be

Acknowledgment

The dissertation in front of you represents over four years of thought, trial-and-error, trial-and-success, antisocial time spent in front of a computer screen, social time spent getting to chat with colleagues and many boring as well as exciting experiments. In the life of an adult human, four (make that five) years is a quite long time. Although I was not in my homeland in these years, I consider myself extremely lucky to be surrounded by friends, who became as close as family members, and colleagues that have my back, both when I am on top of the world and when everything comes crashing down.

I am deeply indebted to many people who have greatly inspired and supported me throughout my PhD. First and foremost, I thank my promoter prof. Wim De Waele for giving me the chance to start this entire venture in the first place, for bearing with me, for giving me the necessary space and for his guidance during my research. Wim's efforts to keep me on track were supplemented by my co-promoter prof. Stijn Hertelé. I would like to express my profound gratitude to him for being my mentor and source of inspiration. I am fortunate that I have worked under his guidance and could not expect a better and friendlier supervisor. This work was made possible by the financial support of Ghent University through grant no. BOF13/24J/122, for which I would like to express my gratitude.

I would like to thank prof. Patrick De Baets for accepting my request to chair my PhD examination board and for his support during the examination process. I take this opportunity to thank jury members prof. Patricia Verleysen, Dr. Valéry Lacroix, Dr. Harry Coules, Dr. Phuc Phung Van and Dr. Koen Van Minnebruggen for being a part of my PhD jury and for providing valuable feedback to improve quality of my PhD thesis.

I would like to acknowledge Dr. Kunio Hasegawa, Dr. Rudi Denys, Dr. Erling Østby and Tore Andre Kristensen for providing me valuable information, fruitful suggestions and illuminating hints.

I am thankful to the technical and administrative staff of Labo Soete, Hans Van Severen for his supports and sense of humor, Johan Van Den Bossche for machining the specimens, Wouter Ost for knowing everything, Jonathan Vancoillie for IT and other supports, and a special thank goes to Georgette D'hondt for being so supportive and for her never-ending smile.

I'd like to thank all of my colleagues for lightening up the times of hard work and for the entertaining and interesting discussions we had; Sameera Naib, Vitor Adriano, Rahul Iyer, Kannaki Pondicherry, Ádam Kálácska, Levente Tóth, Saosometh Chhith, Jules Bossert, Kris Hectors, Jie Zhang, Saeedeh Bakhtiari, Mojtaba Khayatadzad, Ni Junyan, Diego Belato Rosado, Timothy Galle, Nahuel Micone and Jacob Sukumaran. Thanks also go to all other colleagues for nice chats, good discussions and many laughs.

I was blessed to have very good friends in Belgium; it is never easy to stay far away from home and family for me, but the overwhelming support and friendship I received from my friends is priceless and always made me feel like a family here. Farzaneh, Behrooz, Azadeh, Hadi, Sahel, Kavooos, Navid and Jessica thanks for all those parties, drinks, journeys and memorable days and nights.

This was not possible without her; special thanks to my girlfriend Mahtab for her unconditional supports, for motivating me, for listening to my complaints, for nodding to my repetitive explanations about the difference between fracture and fatigue and for waking me up in the mornings.

Finally, the highest gratitude goes to my parents and my sister Azadeh. This dream would never have been fulfilled without the efforts and supports of my family. No words can describe the energy and love I received from them during my entire life.

مامان، بابا و آرزو عزیزم
برای خیلی چیزها از شما ممنونم، برای همه چیزهایی که دارم
ممنونم که همیشه به من سرهاور داشتید

Thank you all!

Kaveh Samadian

September 2019- Ghent

Contents

- 1. INTRODUCTION.....1
 - 1.1. RESEARCH TOPIC.....2
 - 1.2. BACKGROUND2
 - 1.3. STRAIN BASED DESIGN OF PIPELINES.....4
 - 1.4. MOTIVATION6
 - 1.5. RESEARCH OBJECTIVES7
 - 1.6. THESIS ORGANIZATION8
- 2. AN INTRODUCTION TO ANALYTICAL FLAW ASSESSMENT PROCEDURES AND TOOLS.....11
 - 2.1. INTRODUCTION.....12
 - 2.2. BASIC CONCEPTS OF ANALYTICAL FLAW ASSESSMENT14
 - 2.2.1. Stress intensity factor (SIF).....14
 - 2.2.2. J-integral16
 - 2.2.2.1. Crack tip opening displacement (CTOD).....16
 - 2.2.2.2. Plastic collapse and limit load.....20
 - 2.2.3. Failure Assessment Diagram (FAD).....23
 - 2.2.4. Tearing resistance curve (R-curve).....24
 - 2.3. CONCLUSION25
- 3. FLAW INTERACTION29
 - 3.1. INTRODUCTION.....30
 - 3.2. (COMPARISON OF) INTERACTION RULES IN ECA GUIDELINES.....32
 - 3.2.1. Alignment rules for non-coplanar surface flaws33
 - 3.2.2. Coplanar surface breaking flaws.....34
 - 3.2.3. Coplanar surface and embedded flaws.....39
 - 3.3. HIGHLIGHTED RESEARCHES ON FLAW INTERACTION42
 - 3.3.1. Non-coplanar adjacent flaws42
 - 3.3.2. Coplanar adjacent flaws46
 - 3.4. STRAIN-BASED FLAW INTERACTION47
 - 3.5. CONCLUSION49
- 4. FINITE ELEMENT MODEL DEVELOPMENT53
 - 4.1. INTRODUCTION.....54
 - 4.2. GENERAL REQUIREMENTS54
 - 4.3. SMALL-SCALE MODEL.....56
 - 4.4. MEDIUM SCALE MODEL.....58
 - 4.3.1. Modelling strategy.....58
 - 4.3.2. Nodal coordinate transformation functions61

4.5.	PIPE MODEL (ELEMENT DELETION APPROACH).....	66
4.6.	CONCLUSION	70
5.	EXPERIMENTAL PROCEDURES AND FE MODEL VALIDATIONS.....	73
5.1.	INTRODUCTION.....	74
5.2.	TEST INSTRUMENTATION	74
5.2.1.	<i>(Double) Clip gauge measurements</i>	<i>74</i>
5.2.2.	<i>Digital Image Correlation (DIC).....</i>	<i>75</i>
5.2.3.	<i>Crack replication procedure (replica casting).....</i>	<i>77</i>
5.2.4.	<i>CTOD measurement by profilometry using DIC</i>	<i>80</i>
5.3.	SMALL-SCALE MODEL VALIDATION	89
5.3.1.	<i>Specimens and testing procedure</i>	<i>89</i>
5.3.2.	<i>DIC validation.....</i>	<i>91</i>
5.3.3.	<i>FE model validation.....</i>	<i>93</i>
5.3.4.	<i>FE model validation by experimental results</i>	<i>98</i>
5.3.5.	<i>Validation with the analytical solution</i>	<i>101</i>
5.4.	MEDIUM SCALE (WIDE PLATE) MODEL VALIDATION BY DOUBLE NOTCHED SPECIMEN ..	102
5.4.1.	<i>Non-coplanar notches.....</i>	<i>103</i>
5.4.2.	<i>Coplanar notches</i>	<i>105</i>
5.5.	CONCLUSION	107
6.	FLAW INTERACTION EVALUATION BASED ON CRACK DRIVING FORCE	111
6.1.	INTRODUCTION.....	112
6.2.	INTERACTION OF TWO SURFACE BREAKING FLAWS.....	112
6.2.1.	<i>Effect of flaw shape idealization</i>	<i>112</i>
6.2.2.	<i>Elastic-plastic interaction between adjacent surface flaws</i>	<i>128</i>
6.3.	EVALUATION OF THE INTERACTION BETWEEN SURFACE-BREAKING AND EMBEDDED FLAWS USING THE ELEMENT DELETION METHOD.....	136
6.3.1.	<i>Parametric Study.....</i>	<i>138</i>
6.3.2.	<i>General observation.....</i>	<i>140</i>
6.3.3.	<i>Effect of through-thickness spacing between flaws on their interaction.....</i>	<i>140</i>
6.3.4.	<i>Effect of transverse offset between flaws on their interaction</i>	<i>142</i>
6.3.5.	<i>Effect of load level on flaw interaction</i>	<i>143</i>
6.3.6.	<i>Effect of internal pressure on flaw interaction.....</i>	<i>144</i>
6.4.	CONCLUSION	145
7.	FLAW INTERACTION BASED ON ALTERNATIVE CRITERIA	149
7.1.	INTRODUCTION.....	150
7.2.	EVALUATION OF INTERACTION OF TWO NON-COPLANAR FLAWS BASED ON STRAIN CONCENTRATION BANDS (SCB).....	150
7.2.1.	<i>Evaluation of defect interaction based on strain trajectory</i>	<i>151</i>
7.2.2.	<i>Strain patterns morphology.....</i>	<i>154</i>

7.2.3.	<i>Analysis of SCB regression line angle</i>	<i>156</i>
7.2.4.	<i>Discussion on application of SCB in flaw interaction analysis.....</i>	<i>159</i>
7.3.	INTERACTION OF SEMI-ELLIPTICAL SURFACE NOTCHES	161
7.3.1.	<i>Experimental results for semi-elliptical notches in a wide plate specimen</i>	<i>161</i>
7.3.2.	<i>Ductile crack growth evaluation</i>	<i>169</i>
7.3.3.	<i>Numerical results for semi-elliptical surface notches in a wide plate specimen</i>	<i>176</i>
7.4.	CONCLUSION	190
8.	CONCLUSIONS AND RECOMMENDATIONS FOR FUTURE RESEARCH	193
8.1.	BACKGROUND AND METHODOLOGY	194
8.2.	RESULTS.....	195
8.2.1.	<i>Flaw idealization effect on the interaction</i>	<i>195</i>
8.2.2.	<i>Linear-elastic and elastic-plastic interaction of coplanar surface breaking flaws.....</i>	<i>196</i>
8.2.3.	<i>Linear-elastic and elastic-plastic interaction of coplanar (circumferential) surface braking flaw and an embedded flaw</i>	<i>197</i>
8.2.4.	<i>Effect of interaction on the strain trajectory.....</i>	<i>197</i>
8.2.5.	<i>Strain-based flaw interaction criteria</i>	<i>198</i>
8.3.	OUTLOOK FOR FUTURE RESEARCH	200
8.3.1.	<i>Extensions in FE simulations</i>	<i>200</i>
8.3.2.	<i>Effect of stress triaxiality (constraint).....</i>	<i>201</i>
8.3.3.	<i>Interaction of arbitrarily shaped flaws and coupled NDT-FE</i>	<i>201</i>
8.3.4.	<i>Developing experimental techniques for measuring crack extension in specimens with multiple notches</i>	<i>202</i>
	PUBLICATIONS.....	203

Symbols and acronyms

Symbols

a	flaw or notch depth	mm
a_0	initial flaw or notch depth at the deepest point	mm
a_x	initial flaw or notch depth at an arbitrary location	mm
A_m	equivalent area of a cross section contains multiple notches	mm ²
A_s	area of a cross section contains a single notch	mm ²
c	half flaw or notch length	mm
D	average pipe diameter	mm
D_i	inner pipe diameter	mm
D_o	outer pipe diameter	mm
E	elastic (Young's) modulus	MPa
E'	corrected elastic modulus for plane strain condition	MPa
F_P	yield load	N
G	shear modulus	MPa
H	vertical spacing distance between non-coplanar flaws	mm
J	J-integral (non-linear energy release rate)	N/mm
J_{el}	elastic contribution of J-integral	N/mm
J_p	plastic contribution of J-integral	N/mm
K_I	mode I stress intensity factor	N.mm ^{1/2}
K_{II}	mode II stress intensity factor	N.mm ^{1/2}
L	length of prismatic section of specimen	mm
n	strain hardening exponent (Ramberg-Osgood model)	-
m	m-factor	-
p	internal pipe pressure	MPa
r_p	plastic rotation factor	-
R_i	non-deformed crack width	mm
R_m	ultimate tensile strength	MPa
$R_{p0.2}$	0.2 % proof stress (measure of yield strength)	MPa

S	horizontal spacing distance flaws	mm
t	wall thickness	mm
U	distance between the opposite crack flanks at the replica's cross section	mm
W	width of specimen	mm
Y/T	yield-to-tensile ratio	-
α	crack aspect ratio (a/c)	-
α	angle of the SCB regression line	°
β	normalized global strain	-
γ	elastic interaction factor	-
γ_{Cr}	critical elastic interaction factor	-
δ	CTOD of specimen with multiple notch	mm
δ_0	CTOD of specimen with single notch	mm
δ_{DIC}	CTOD measured by DIC	mm
δ_{Rep}	CTOD measured at casted silicone replicas of the crack	mm
δ_θ	CTOD measured by FE method using rotation angle	mm
δ_{90}	CTOD measured by FE based on 90-degree intercept definition	mm
Δa	Ductile crack growth	mm
ε	engineering strain	%
ε_G	global strain	%
ε_L	local strain	%
ε_R	remote strain	%
η	elastic-plastic interaction factor	-
η_{Cr}	critical elastic-plastic interaction factor	-
θ	angle between the two non-coplanar flaw tips	°
θ_1	the rotation angle measured at the surface plane	°
θ_2	the rotation angle measured at the crack tip	°
κ	factor reflecting out-of-plane boundary conditions	-
λ	crack depth normalized by the plate thickness	-
σ	stress at the cross section	MPa

σ_m	remote membrane stress	MPa
σ_y	yield strength	MPa
ν	Poisson's ratio	-
φ	angle indicating position along semi-elliptical crack front	°
ω	strain-based interaction factor	-

Acronyms

API	American Petroleum Institute
ASME	American Society of Mechanical Engineers
ASTM	American Society of Testing and Materials
BS	British Standard
CDF	crack driving force
CMOD	crack mouth opening displacement
CSA	Canadian Standards Association
CTOA	crack tip opening angle
CTOD	crack tip opening displacement
CWP	curved wide plate
DIC	digital image correlation
DNV	Det Norske Veritas
ECA	engineering critical assessment
EPFM	elastic plastic fracture mechanics
EPRG	European Pipeline Research Group
EXP	experimental results
FAD	failure assessment diagram
FEM	finite element method
FFS	Fitness for service
FITNET	European fitness-for-service network
GMAW	gas metal arc welding
GSC	gross section collapse
HAZ	heat-affected zone
HSLA	high strength low alloy
LEFM	linear elastic fracture mechanics
NDT	non-destructive testing
NSC	net section collapse
R	resistance (in CTOD-R, J-R)
Rep	replica cast from silicone
RO	Ramberg-Osgood
SBD	strain based design
SENB	single edge notched bend
SENT	single edge notched tension
SMAW	shielded metal arc welding
SMYS	specified minimum yield strength
SCB	strain concertation band
X-FEM	extended finite element modelling

Summary

The increasing demand for energy requires exploiting fossil fuels from more hostile and remote regions. Pipelines are the most economically efficient and the most environmentally sound means of transporting hydrocarbons from their place of exploitation to the points of storage, treatment, processing, loading or consumption. However, their design requirements in hostile environments are quite challenging since these environments can be prone to landslides, discontinuous permafrost, ground settlement, seismic, and other phenomena. Due to these extreme loading conditions, in addition to the pipe hoop strength and toughness requirements, the axial strain capacity becomes critical. Ensuring safe service in such extreme loading conditions, including above-mentioned hostile environments and offshore pipe laying, imposes a tailored design framework known as “strain based design”. In this approach, the allowable strain in the structure (instead of allowable stress in conventional “stress based design”) is estimated and compared with strain capacity, which by itself depends on various factors including material properties (e.g. tearing resistance, weld strength mismatch, yield to tensile ratio), geometrical factors (e.g. high-low weld misalignment, weld thickness), internal pressure and the possible presence of flaws. Strain capacity estimation is far more challenging compared to stress capacity not only because of the many variable factors involved, but also because of the complex nature of the interaction between these factors. A critical point in this design is the assessment of the girth welds that connect pipe sections, given the fact that welds are prone to have flaws which can detrimentally affect the structural integrity.

Flaws are often detected in close proximity of each other. When this is the case, they may interact with each other, which may promote failure (compared to the case when only one flaw is present). Therefore, an adequate assessment procedure not only addresses the effect of each of detected flaws separately, but also provides guidelines to address their possible interaction. In contrast with the availability of various interaction assessment rules in stress based Engineering Critical Assessment (ECA) procedures, there are no fully satisfactory methods which can assess the interaction between the flaws in strain based design. Present interaction rules are basically developed based on Linear Elastic Fracture Mechanics (LEFM), for the sake of simplicity and conservativeness. Already for stress based flaw interaction, there is a lack of consensus regarding the most suitable flaw interaction rule for a given scenario. Strain based design adds even more complexity since inherently significant plastic deformation is expected and post-yield material properties come into play. Moreover, due to the employing of sufficiently tough material, the failure mode is unstable ductile tearing and plastic collapse rather than brittle fracture. Thus, due to lack sufficient justifying evidences, applying the present interaction rules to strain based designed components might lead to either under-estimation or over-estimation of the interaction severity.

This work aims to provide an illuminating insight into the interaction behavior between adjacent flaws in high strain regimes. Focus goes to longitudinally tensioned samples containing surface breaking flaws extracted from such pipe steel grades that have sufficient toughness to avoid brittle fracture. The main research goal is to investigate different factors which can influence the interaction, given unstable ductile

tearing and plastic collapse are the governing failure modes. In addition, through an in-depth review over the existing interaction assessment procedures available in various codes, standards, guidelines and research works, their suitability for strain based design framework is evaluated, and an alternative procedure is developed to overcome the shortcomings of the current rules. With a more accurate flaw interaction procedure in hand, flaw tolerability can be defined more robustly, and consequently the structural integrity of strain based design components can be ensured more effectively.

To systematically investigate the flaw interaction phenomenon in a strain based design framework, numerous cases with different flaw sizes, spacing distances and material properties are required. Such large parametric studies are not practically possible without numerical models that can be automatically generated and post-processed. Thus, a series of object-oriented 3D numerical (finite element) simulation tools have been developed to evaluate the interaction in high strain regimes. These developments resulted in the following models: small-scale model double edge notched tensile test specimen, a medium scale flat/curved wide plate containing semi-elliptical surface notches, and a full scale (pressurized) pipe section contains surface breaking and embedded flaws. In the latter model, a novel approach based on element deletion has been adopted to model arbitrarily shaped flaws. Numerical procedures are subjected to of tailored experimental validation using 3D Digital Image Correlation (DIC) for full-field deformation measurement and silicone replica casting to measure Crack Tip Opening Displacement (CTOD) and ductile tearing. Due to specific requirements of this study to measure the CTOD and strains around the notches, a novel mythology to measure CTOD along the finite length notches using 3D-DIC has been developed and validated during this study as well. With these tools following changes are addressed:

First, in a fracture mechanics framework, the interaction between adjacent flaws is assumed to be significant when the Crack Driving Force (CDF) has been affected substantially. This is the most acknowledged approach to investigate multiple flaws and is used in most ECA guidelines because of its simplicity and conservativeness. Since strain based design inherently requires considering the effect of material plasticity, though CDF-based approaches are normally confined to Linear Elastic Fracture Mechanics (LEFM) assumptions (e.g. KI stress intensity factor), the interaction should be investigated using Elastic Plastic Fracture Mechanics (EPFM) to quantify the affecting parameters. Unlike the assumption of the current ECA interaction rules that assess the interaction independent from the load level and material properties, results showed that the severity of interaction is increased when load level is increased, and strain hardening can affect the outcome. Even though these effects are seemingly neglected in ECA procedures, still their final assessments are proved to be conservative for higher load levels. Note that this conclusion is confined only to the studied cases and cannot be generalized. However, potential non-conservativeness in interaction assessment is observed from the flaw idealization process, which basically takes place in the course of the flaw characterization before the interaction assessment.

The second challenge was to develop a method which can describe the interaction for failure modes relevant to strain based design (e.g. plastic collapse). CDF-based interaction solely cannot be applied for strain based design on the grounds that the

failure mode is not be governed by fracture only. Therefore, an alternative concept is introduced based on deformation patterns and strain fields around the flaws. This new concept, named Strain Concentration band (SCB), is basically showing the trajectory of maximum equivalent strains, developed based on the slip-line concept. Combining SCB patterns analysis with CDF parameters like CTOD provides a methodology to study the interaction which comprises the coupled effects of CDF with global deformation patterns.

Thirdly, to evaluate the effect of interaction on strain based design components, the strain capacity of the component with multiple flaws should be estimated. It is crucial to note that the effect of flaw interaction on the plastic collapse load (maximum load) can be distinctly different with that on the maximum strain (strain capacity). However, accurate estimation of the strain capacity apart from the post-yielding material behavior, depends on ductile tearing as well, and this has not been implemented in FE models. Experimental investigations are employed to determine the effect of interaction on ductile tearing for various configurations. Strain capacity, as mentioned earlier, can be influenced by multiple parameters; in this study, based on the experimental observations, it is assumed that unstable ductile tearing and plastic collapse happen simultaneously and therefore the amount of global strain at plastic collapse can adequately estimate the component's strain capacity. Since ductile tearing is not directly implemented in FE models, a mapping technique is employed to determine single-notched specimen's Crack Mouth Opening Displacement (CMOD) at unstable ductile tearing. Then, the plastic collapse of the specimen with two equal notches is estimated given that it is assumed plastic collapse happens when CMOD any of them reaches to the above determined critical CMOD.

The experimental and numerical developments and results are finally combined to evaluate the current ECA rules' capabilities in assessing the interaction in a strain based design framework. Based on the obtained results, a new criterion for alignment of non-coplanar surface flaws is suggested. This criterion, which is based on effective cross sections, is proved to be more accurate than current procedures in estimating the effect of interaction on strain capacity. In addition, unlike the current rules which may underestimate the interaction in small diameter tubes, this new criterion can effectively distinguish the critical configurations.

Future research opportunities are identified in the experimental and numerical investigation of broader range of parameters for a confirmation of the obtained results, and in the extension of the work towards welded connections (where differences between mechanical properties of weld metal, base metal and heat-affected zones will play a role). Additional attention should be directed to the effect of stress triaxiality and interaction between the arbitrarily shaped flaws. In the course of this study the lack of experimental methods suitable for multi notched specimens has been observed, which requires further development.

Samenvatting

(Dutch summary)

Pijpleidingen zijn het meest efficiënte en ecologisch verantwoorde middel voor het transport van fossiele brandstoffen van hun ontginningsplek tot hun verwerkingssite en, uiteindelijk, de eindgebruiker. De stijgende vraag naar energie vereist de ontginning van fossiele brandstoffen in steeds uitdagender omgevingen (onderhevig aan grondzetting, discontinue permafrost, seismische activiteit, ...). Ontwerpsvereisten in deze omstandigheden zijn uitdagend. Bovenop de belasting ten gevolge van inwendige druk (en de daarbijhorende vereisten naar taaiheid en materiaalsterkte) wordt potentieel een axiale vervorming opgedrongen die het faalgedrag kan domineren. De voorspelling van dit faalgedrag vereist een zogenaamd ‘rekgebaseerd ontwerp’ waarbij de toelaatbare rek (eerder dan spanning) in de structuur geschat wordt. Deze zogenaamde rekapaciteit hangt van vele factoren af, waaronder materiaaleigenschappen (e.g. weerstand tegen scheurgroei, rekverstevigingsgedrag, sterkte van de las relatief t.o.v. het basismateriaal), geometrische karakteristieken (e.g. uitlijningsfout van een las, dikte van het buismateriaal), inwendige druk en de potentiële aanwezigheid van fouten in de structuur. Het inschatten van rekapaciteit is veel uitdagender dan traditionele spanningsgebaseerde voorspellingen, gezien het grote aantal invloedsfactoren en de complexe interacties tussen deze factoren. Een kritiek aspect van rekgebaseerd ontwerp is de foutbeoordeling van omtrekklassen die buissecties verbinden, aangezien (a) lasfouten quasi onvermijdelijk zijn en (b) deze lasfouten loodrecht georiënteerd zijn t.o.v. de axiale rekriching.

Meerdere fouten treden vaak op in elkaars nabijheid. Wanneer dit het geval is, kan foutinteractie optreden, waarbij de fouten zwaarder belast worden dan het geval zou zijn als ze geïsoleerd waren. Een adequate foutbeoordelingsprocedure dient richtlijnen te geven over hoe om te gaan met potentiële foutinteractie. De meest courante foutbeoordelingsprocedures bevatten dergelijke richtlijnen voor spanningsgebaseerd ontwerp, maar niet voor rekgebaseerd ontwerp. Deze richtlijnen werden ontwikkeld met behulp van linear-elastische breukmechanica, met het oog op conservatisme en eenvoud. Deze aannames zijn twijfelachtig voor rekgebaseerd ontwerp, waarbij rekening gehouden wordt met een doorgedreven ontwikkeling van plasticiteit. Bovendien zijn er fundamentele verschillen tussen verschillende foutinteractiecriteriën, en is er geen consensus over welk criterium het meeste geschikt is voor een bepaald scenario. De complexiteit van rekgebaseerd ontwerp is nog hoger omwille van de grote invloed van het rekverstevigingsgedrag van het materiaal, en het in rekening brengen van ductiele scheurgroei voorafgaand aan onstabiel falen. Samenvattend kan gesteld worden dat het simpelweg overnemen van spanningsgebaseerde foutinteractieregels in rekgebaseerd ontwerp kan leiden tot zowel onveilige als veilige inschattingen van het faalgedrag.

Dit werk doelt om meer inzicht te verschaffen in het interactiegedrag van fouten in aanwezigheid van plastische vervorming. Er wordt nader gekeken naar trekproeven op gekerfde proefstukken uit pijpleidingstaal met voldoende taaiheid om bros falen te vermijden. Het hoofddoel van dit werk is het onderzoeken van de verschillende

invloedsfactoren die bijdragen aan foutinteractie met inbegrip van stabiele ductiele scheurgroei en plastisch bezwijken. Het werk start met een doorgedreven literatuuronderzoek van bestaande procedures voor beoordeling van foutinteractie uit standaarden, richtlijnen en onderzoeksliteratuur. Hun geschiktheid voor rekgebaseerd onderzoek wordt geëvalueerd en een alternatieve procedure wordt voorgesteld om de tekortkomingen van de huidige procedures teniet te doen. Hierdoor kan foutaanvaardbaarheid nauwkeuriger beoordeeld worden, wat kan leiden tot een betere inschatting van de structurele draagkracht van componenten onderhevig aan (plastische) vervormingen.

De onderzoeksaanpak bestaat uit het systematisch onderzoeken van foutinteractie op een groot aantal configuraties met verschillende foutgroottes, afstanden tussen fouten en materiaaleigenschappen. Het uitvoeren van deze onderzoeker vereiste de ontwikkeling van numerieke (eindige-elementen) modellen die automatisch gegenereerd, uitgerekend en geanalyseerd kunnen worden a.h.v. een objectgeoriënteerde programma-architectuur. De volgende modellen werden ontwikkeld: een kleinschalig dubbelzijdig gekerfd trekproefstuk, een middenschallig plaatmodel met semi-elliptische oppervlaktekerven onder trekbelasting, en een volschalig buismodel met oppervlakte- en ingebedde fouten, onderhevig aan inwendige druk en een axiale trekbelasting. De creatie van fouten in het laatste model werd verwezenlijkt a.h.v. een innovatieve aanpak, gebaseerd op het verwijderen van elementen. Deze aanpak laat toe om arbitraire foutgeometrieën te introduceren. De numeriek modellen worden experimenteel gevalideerd a.h.v. daartoe ontworpen proeven. Hierbij werd gebruik gemaakt van geavanceerde meettechnieken, waaronder 3D digitale beeldcorrelatie (DIC) voor metingen van vervormingen in het volledige oppervlak, het gieten van silicone replicas van kerven voor meting van scheurtipopening (CTOD) en ductiele scheurgroei tijdens de proef. DIC werd onder anderen aangewend om CTOD te begroten over de hele lengte van oppervlaktekerven d.m.v. driedimensionale profielmetingen aan de kerfmond.

De hierboven beschreven onderzoeksmethodiek leidde tot veelbelovende resultaten, die hieronder onder vier noemers samengevat worden.

Een eerste studie behelst invloeden van foutinteractie op scheurdrijvende kracht in een breukmechanisch kader. De meeste huidige interactieregels zijn gebaseerd op linear-elastische breukmechanicatheorie (LEFM). De doorgedreven aanwezigheid van plasticiteit in rekgebaseerd ontwerp ontkracht echter de geldigheid van deze theorie, en vereist een studie van het probleem in een elastisch-plastisch breukmechanisch (EPFM) kader. In dit kader gaan additionele factoren een rol spelen, zoals het belastingsniveau en het rekverstevigingsgedrag van het materiaal. Hoewel bestaande procedures deze invloeden negeren, blijken hun voorspellingen toch conservatief te blijven onder de onderzochte voorwaarden. Potentiële onveiligheid wordt echter geïntroduceerd in de idealisatie van de foutgeometrie, die typisch plaatsvindt voorafgaand aan de interactieprocedure.

Een tweede uitdaging behelst de studie van foutinteractie voor faalmechanismen gerelateerd aan uitputting van plasticiteit (plastisch bezwijken). Dit mechanisme kan niet beschreven worden a.h.v. de breukmechanische grootheden die voor de eerste studie werden aangewend. Een alternatieve onderzoeksmethode werd ontwikkeld, en is gebaseerd op de lokale vervormingspatronen rond de fouten. Het concept

‘rekconcentratieband’ wordt gedefinieerd als het traject van maximum equivalente rek tussen fouttippen, of tussen fouttip en proefstukrand. Het verloop van deze banden verschaft inzicht in de plastische interactie tussen nabijgelegen fouten. De combinatie van deze nieuwe techniek met een breukmechanische analyse gebaseerd op CTOD laat toe de gekoppelde effecten op breukgedrag en plastisch bezwijken te begrijpen.

Een derde onderzoek omvatte de rekapaciteit van componenten met meerdere fouten. Een cruciale vaststelling is dat de invloed van foutinteractie op bezwijkspanning substantieel verschillend kan zijn van haar invloed op bezwijkrek. Een belangrijke invloedsfactor is ductiele scheurgroei. In deze studie wordt aangenomen dat ductiele scheurinitiatie en plastisch bezwijken op een gelijkaardig moment starten, en dat de rek bij plastisch bezwijken dus representatief is voor de rekapaciteit van de component. Ductiele scheurgroei is niet direct geïmplementeerd in de eindige-elementenmodellen, maar werd in rekening gebracht door verschillende simulaties met stijgende foutgrootte afzonderlijk te modelleren, en te koppelen ten opzichte van de weerstandscurve van het materiaal. Vervolgens wordt aangenomen dat plastisch bezwijken optreedt zodra de scheurmondopening (CMOD) gelijk wordt aan de kritische CMOD-waarde voor configuraties met één kerf.

Tot slot worden de experimentele en numerieke ontwikkelingen gekoppeld om de huidige foutinteractiecriteria te evalueren in het kader van rekgebaseerd ontwerp. De bekomen resultaten leiden tot een nieuw criterium voor “foutalignering”, d.i. een procedure waarbij fouten die zich in verschillende vlakken bevinden, naar hetzelfde vlak geprojecteerd worden voor verdere analyse. Het criterium is gebaseerd op een definitie van “effectieve dwarsdoorsnede”, en blijkt nauwkeurige voorspellingen van foutinteractie op te leveren voor de onderzochte configuraties.

Toekomstige onderzoeksideeën spitsen zich toe op de experimentele en numerieke evaluatie van bijkomende parameters, met bijzondere aandacht voor laseigenschappen (bijvoorbeeld de mismatch tussen eigenschappen van las en basismetaal). Ook is het interessant de lokale spanningstoestand (triaxialiteit) nabij de fout in detail te bestuderen, zodoende effecten van foutinteractie op taaiheid en scheurgroeiweerstand te trachten te begroten. Daarnaast kan aandacht geschonken worden aan de verbetering van instrumentatietechnieken voor proefstukken met meerdere kerven.

“We live on an island surrounded by a sea of ignorance. As our island of knowledge grows, so does the shore of our ignorance.”

John Archibald Wheeler

Chapter 1

Introduction

1.1. Research topic

Multiple adjacent flaws may occur in structures due to welding defects, corrosion, fatigue and overloading. The first of these reasons is particularly relevant for large transmission pipelines made out of steel, since the majority of the welding required for their installation is conducted in the field. The challenging conditions for welding results in a large likelihood of weld imperfections. The present work is carried out to study the interaction effect of multiple adjacent flaws when pronounced plastic deformation can be expected in structures, as is for instance the case during installation of offshore pipelines, for onshore pipelines located in discontinuous permafrost regions. However, application of the outcomes is not limited to pipelines, since then majority of the results can be employed in other applications where plastic collapse is the failure mode and ductile crack growth is included in the analysis.

1.2. Background

In a report of DNV-GL, it has been predicted that gas followed by oil will be worldwide the two largest energy sources until the end of the forecast period (2050) [1] and gas will meet 25% of world energy demand by the mid-century [2]. DNV-GL predicted that offshore gas production volumes will increase by approximately 20% by 2030. However, offshore gas producers face a substantial challenge as some of the world's largest natural gas resources are being found at great distance from the biggest gas markets and without access to export infrastructure means [1]. Besides, the majority of world gas reservoirs belongs to a limited number of countries. The three largest reserve holders, Russia, Iran and Qatar together hold about 57% of global gas reserves, and therefore vast quantities of gas should be transferred from the origin to refinery plants and eventually the consumer. Pipelines and Liquefied Natural Gas (LNG) ships are two main means of natural gas transportation.

Geopolitics, national economic and social development agendas affect the direction of the future development in fossil fuel supply and transportation. For example, beyond the current construction of new cross-border and national pipelines, the European Union (EU) supports the development and expansion of Liquefied Natural Gas (LNG) import facilities in addition to related downstream onshore gas infrastructure throughout Eastern Europe, which would otherwise rely on pipelines from sole suppliers such as Russia. The EU also supports pipelines from new sources of supply such as the Mediterranean and Caspian regions as indigenous production in historical demand centers such as North West Europe declines. These ambitions require new investments in infrastructures to transport the gas across longer distances in high-pressure, large-diameter pipelines [2].

More than 4 million kilometers of transmission or distribution gas pipelines exist all over the world, the majority of them being built more than 30 years ago. Given the global increasing energy demand, it seems inevitable that there will be further replacement and refurbishment of older pipeline systems in regions such as Europe, Middle East and North Africa, North East Eurasia and North America. Therefore, a continued and likely increasing effort in asset lifetime extension for existing pipelines is expected [2].

Apart from conventional fossil fuels, pipelines can be employed for transport of less conventional energy sources as well. For instance, huge amounts of methane hydrate trapped in ice crystals have been found beneath Arctic permafrost, beneath Antarctic ice and in sedimentary deposits along continental margins worldwide. The current challenge is to inventory these resources and to find safe and economical ways to develop these. One alternative is to inject CO_2 into the hydrate formation to warm it and release the methane, thereby producing a valuable resource whilst trapping an environmentally damaging one [1]. This application requires massive investments in pipelines at harsh environments like offshore and Arctic regions.

Pipeline application is not limited to fossil fuels. A highly promising application of pipelines is to store, and transfer hydrogen or methane produced by Power to Gas (PtG) techniques. PtG in its simplest form is the conversion of the surplus power into a grid compatible gas that can be later distributed on an as-needed basis. The process normally contains two steps: H_2 production by water electrolysis and H_2 conversion with an external CO or CO_2 source to CH_4 via methanation. An alternative would be the direct injection of H_2 into the gas grid [3].

CO_2 transportation is another application of pipelines. This has been taking place since the 1980s in West Texas for Enhanced Oil Recovery (EOR). EOR, also called tertiary recovery, is a term used for a wide variety of technologies used to boost the amount of crude oil that can be extracted from an oil field. Carbon dioxide injection, besides other methods, has been found to be commercially successful to improve oil production. The deployment of captured, anthropogenic carbon dioxide, derived from industrial or mineral sources to support EOR provides a multifaceted solution to energy, environmental, and economic challenges [4].

Pipelines can also be employed to transfer CO_2 for greenhouse gas reduction projects. The European Union has committed to achieve an economy-wide domestic target of at least 40% greenhouse gas (GHG) emission reductions for 2030 and at least 80% GHG reductions by 2050. This should allow the EU to contribute to keep global warming well below 2°C as agreed in the 2015 Paris climate agreement [5]. Achieving these goals requires the deployment of novel and efficient methods including Carbon Capture and Storage (CCS) and Carbon Capture and Utilization (CCU). CCS is the process of capturing waste carbon dioxide (CO_2) from large sources, such as fossil fuel power plants, and transporting it to a storage site, followed by long-term isolation from the atmosphere in an underground geological formation. CCU stands for the capture of anthropogenic CO_2 and its consecutive use in a synthesis process (normally biologically), transforming CO_2 into commercially valuable products (i.e. ethanol). CCS and CCU can be employed as complementary processes.

For these applications, particularly CCS, either new pipelines are required to be constructed or existing pipelines, particularly in case of offshore reservoir injection, can be re-purposed [6]. As an example, various feasibility study programs are supported by the Norwegian government for three CCS concepts in the ammonia, cement, and waste processing industries as part of their policy to reduce greenhouse gas emissions. These projects contain an onshore CO_2 storage which captures the gas from industrial plants through a pipeline or ship, and then at these plants CO_2 will be exported via an offshore pipeline and injected for permanent storage down to 1000-2000 meters below the sea bed [2,7].

1.3. Strain based design of pipelines

The increasing demand of energy promotes the economic feasibility to acquire fossil fuels from remotely located reservoirs in deep water offshore and harsh onshore environments. Constructing pipelines in such an environment stipulates more restrictive requirements in design procedures and material properties, compared to less challenging environments. Very often, besides internal pressure, pipelines should be designed to withstand external events that generate substantial additional load such as earthquakes, landslides, and other types of large differential ground movement events. For instance, in 1964 a massive earthquake in Anchorage, Alaska, caused a shift in the ground surface of up to 20 m. In another more recent event, the Denali Fault¹ in Alaska in 2002 generated a 7.9 Richter magnitude scale earthquake with horizontal offsets around 9 m. Seismic events of such a high magnitude at locations with saturated, low density, or uncompacted sandy soils can result in soil liquefaction, a phenomenon whereby a saturated or partially saturated soil loses strength and stiffness and behaves rather like a liquid. Consequently, pipelines in these regions can experience large longitudinal plastic strains as well as plastic circumferential deformation as the pipeline experiences alignment changes [5].

Offshore pipelines can experience even higher longitudinal strain during their installation or service. Offshore pipelaying technology historically stood on the shoulders of the undersea telegraph cable laying procedures developed in the 1840s. Modern offshore pipe laying techniques can be categorized into three main categories: S-lay, J-lay and reeling (or reel-lay). Common to all procedures for offshore pipe laying is that pipelines experience deformation beyond material yielding. Significant plastic deformation can be imposed on the pipeline, the exact amount of this deformation being expressed as a ‘strain demand’. This is the global strain caused by plastic deformation imposed by installation procedures or hostile environment events. Strain demand varies from around 1% in events like landslides to 2-2.5% in offshore pipe installation and can reach to 3% in seismic events [8].

It should be mentioned that the strain demand estimation is a highly cumbersome aspect in pipeline projects within hostile environments. It often requires statistical estimation of the frequency of geological phenomena with a certain severity and soil characterization with extensive computational models of pipe-soil interaction. Nevertheless, reported cases of imposed strains are limited to values of 3 % and below [8]. For these cases, since loading scenarios tend to impose a certain deformation rather than a given force to the pipe, design methodologies based on strain should supplement conventional stress-based designs. Strain based design (SBD) in the pipeline industry started in early 1980s with the use of high-strength materials (API 5L [9] X70 and higher grades) for pipeline construction in harsh environments [10]. Hereby, the number following “X” in the API 5L steel grade reflects the specified minimum yield strength of the pipe steel in ksi (1 ksi = 6.89 MPa).

Strain based design refers to design procedures which have a specific goal of maintaining pipeline service and integrity under imposed longitudinal strains

¹ The Denali Fault is a major intracontinental dextral (right lateral) strike-slip fault in western North America, extending from northwestern British Columbia, Canada to the central region of the U.S. state of Alaska [65].

(exceeding 0.5%, which is typically considered as the strain at which plastic deformation starts). Conventional pipeline design (stress-based design) limits the circumferential stresses often to a percentage of the allowable design strength.

The differences between stress-based and strain-based analyses only appear above yield and are more significant for high strain hardening materials (i.e., showing a larger Y/T or yield-to-tensile ratio). When reaching the ultimate tensile strength (UTS), an increase in load is impossible because it will lead to collapse, while an increase in the imposed deformation may lead to further stable plastic straining (Figure 1-1). Below yield, strain-based and stress-based analysis return the same answers. Above yield, strain-based analysis is appropriate when the loading is largely displacement controlled [11].

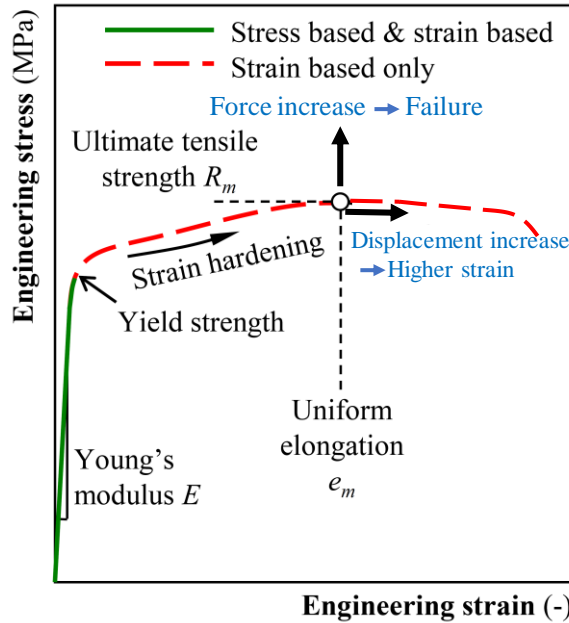


Figure 1-1: Stress-strain curve, illustrating the difference between strain-based and stress-based design [8].

To assess the structural integrity of a pipeline subjected to large strains, it is necessary to know the magnitude of strain demand and strain capacity (strain limit). Two ultimate limit states are normally associated with SBD, i.e. tensile rupture and compressive buckling. The limiting failure mode for a pipeline subjected to axial tension is fracture or plastic collapse, while for a pipeline subjected to axial compression the limiting failure mode is buckling. In cases where a pipeline is subjected to global bending, fracture or collapse can occur on the tensile side of the pipe and buckling can occur on the compression side of the pipe; both phenomena can interact. Nonetheless, compressive strains are normally associated with a limit state that does not involve catastrophic failure or loss of pressure containment as does the tensile limit. This work is further focused towards the tensile limit state of pipelines.

As a chain is only as strong as its weakest link, the tensile strain capacity of a pipeline is at most equal to the tensile strain capacity of its circumferential welds (also named girth welds). The girth welds here refer to the entire weld region, including the weld metal, fusion boundary, and the heat-affected zone (HAZ). Although most of the SBD oriented weld procedures stipulate that the weld metal should be at least evenmatching in strength [12], girth welds are likely a weakest link. This is associated to the possible existence of weld imperfections and often deteriorative metallurgical and/or mechanical property changes from welding thermal cycles. Consequently, the Tensile Strain Capacity (TSC) of pipelines is directly related to the girth welding procedure and flaw acceptance criteria [13].

Welds produced in the field will almost unavoidably contain imperfections, out of which cracks can initiate and grow until failure of the joint (leak or total rupture) occurs. Flaw acceptance criteria are driven from a fracture resistance calculation which is typically performed based on the limiting of allowable stresses below yield strength and/or marginal yielding at the flaw tip. This approach is mostly focused towards brittle fracture dominated failures. However, the failure mode of modern high strength steel grades – used in pipelines, storage tanks and pressure vessels – is often dominated by plastic collapse (extensive yielding). Contemporary steel grades and weld metals are indeed mainly selected based on a minimum level of toughness (or tearing resistance) such that small (‘workmanship’) weld flaws can safely be tolerated. Conventional design approaches based on allowable stresses would lead to overconservative evaluations of flaw tolerance in constructions which have to withstand large plastic strains.

1.4. Motivation

A pre-existing defect in a component can cause failure in the loading range from brittle fracture to plastic collapse. ECA guidelines should ensure that the calculated defect size is acceptable in unstable (brittle) as well as stable (plastic collapse) failure scenarios. When multiple flaws are found, and their dimensions are determined (flaw characterization), the possible interaction between them should be addressed. If multiple flaws are not interacting, then the largest among them is treated as single isolated flaw. If they are interacting, then treated as a single encompassing flaw (flaw re-characterization). This procedure is summarized in Figure 1-2 for the case of interacting adjacent surface breaking flaws (see chapter 3 for more details). Flaw interaction rules compare the spacing distance between flaws with a representative flaw dimension (length or height). If the spacing distance is too small, interaction is deemed to occur, and the flaws have to be combined into a single equivalent flaw for the purpose of the flaw assessments. If the spacing distance is too large for interaction, the flaws can be treated separately and only the worst case flaw needs to be considered.

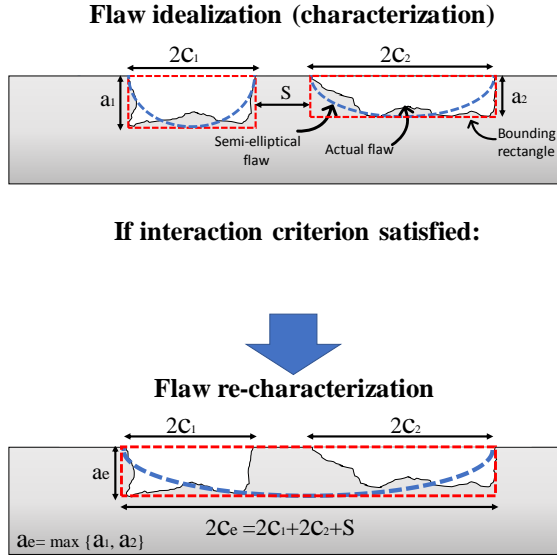


Figure 1-2- Schematic summary of flaw characterization and re-characterization procedure

Flaw interaction rules are applied to various loading conditions and failure mechanisms. Although there are only limited references available for the technical background of many of these criteria, they have typically been based on Linear Elastic Fracture Mechanics (LEFM) for the sake of simplicity and intuitively aiming for conservativeness. However, due to the fundamentally different failure mechanisms that take place when comparing LEFM with plastic collapse, the LEFM based rules may either be conservative or non-conservative for plastic collapse. Thus, the application of these procedures might be questioned when applied to failure modes other than brittle fracture. Large scale tension tests have indicated that available flaw interaction rules are inconsistent and can lead to both conservative and un-conservative predictions for plastic collapse conditions.

1.5. Research objectives

This research project will contribute to the extension of fundamental knowledge with respect to the deformation capacity of structures with embedded and/or multiple flaws. Experimental and numerical research is needed to quantify the (un-) conservativeness of current interaction rules and to develop more accurate flaw acceptance criteria for structures under plastic collapse. The main objectives of this study, going beyond the current state of the art, can be summarized as:

- to understand the behavior of adjacent flaws when large plastic deformation is imposed to the component
- to study the fracture resistance of multiple flaws under plastic collapse conditions.

- to examine the present interaction rules for failure modes other than brittle fracture and to develop improved procedures, if required.

1.6. Thesis organization

The remaining chapters in this thesis are organized as follows:

Chapter 2 provides a basic overview on flaw assessment methods, analytical tools, parameters and main theoretical concepts required for design against fracture and plastic collapse.

Chapter 3 reviews the flaw interaction rules in existing ECA procedures and state of the art in literatures.

Chapter 4 elaborates the development of finite element based methods for analysis of flaw interaction. This chapter includes all relevant model details including simplifying assumptions, boundary conditions, model geometries, material property definitions, and mesh design. In this chapter an alternative procedure is also introduced to model embedded realistic flaws.

Chapter 5 deals with an experimental evaluation of the accuracy of the FE models. The details about the material, equipment and experimental testing procedures are first presented in this chapter. Then, the experimental results are compared to their simulated equivalents.

Chapter 6 studies flaw interaction on the basis of crack driving force. Either by Linear Elastic Fracture mechanics (LEFM) or Elastic Plastic Fracture Mechanics (EPFM) assumptions, crack driving force defines the proximity of the component to fracture.

Chapter 7 studies flaw interaction from an additional point of view, namely plastic collapse. In this chapter strain-based studies in conjunction with plastic collapse assessment are employed to study the flaw interaction behavior.

Chapter 8 concludes and provides recommendations for further work.

References

- [1] DNV GL Energy. Oil and gas forecast to 2050, energy transition outlook 2017. 2017.
- [2] DNV GL Energy. Oil and gas forecast to 2050, energy transition outlook 2018. 2018.
- [3] Götz M, Lefebvre J, Mörs F, McDaniel Koch A, Graf F, Bajohr S, et al. Renewable Power-to-Gas: A technological and economic review. *Renew Energy* 2016;85:1371–90. doi:10.1016/J.RENENE.2015.07.066.
- [4] Essandoh-Yeddu J, Gülen G. Economic modeling of carbon dioxide integrated pipeline network for enhanced oil recovery and geologic sequestration in the Texas Gulf Coast region. *Energy Procedia* 2009;1:1603–

- 10.
- [5] EU. Novel carbon capture and utilization. Brussel: 2018. doi:10.2777/824461.
- [6] Noothout P, Wiersma F, Hurtado O, Macdonald D, Kemper J, van Alphen K. CO2 Pipeline Infrastructure – Lessons Learnt 2014. doi:10.1016/j.egypro.2014.11.271.
- [7] Jakobsen J, Roussanaly S, Anantharaman R. A techno-economic case study of CO2 capture, transport and storage chain from a cement plant in Norway. J Clean Prod 2017;144:523–39. doi:10.1016/J.JCLEPRO.2016.12.120.
- [8] Hertelé S. Coupled Experimental-Numerical Framework for the Assessment of Strain Capacity of Flawed Girth Welds in Pipelines. PhD dissertation. Ghent University; 2012.
- [9] API Specification 5L, specification for Line Pipe. American Petroleum Institute; 2004.
- [10] Gao H, Yu Z, Zhang Z, Shi H. The Concepts For Pipeline Strain-Based Design. Twent. Int. Offshore Polar Eng. Conf., Beijing, China: International Society of Offshore and Polar Engineers; 2010, p. 7.
- [11] Law M. Review of Strain Based Analysis for Pipelines Review of Strain Based Analysis for Pipelines. Menai, NSW: 2007.
- [12] Offshore standard DNV-OS-F101. DET NORSKE VERITAS AS; 2010.
- [13] Wang YY, Liu M, Song Y, Stephens M, Petersen R, Gordon R. Second generation models for strain-based design. 2011.
- [14] Edwards BR, Russell JK. Distribution, nature, and origin of Neogene–Quaternary magmatism in the northern Cordilleran volcanic province, Canada. n.d.

An introduction to analytical flaw assessment procedures and tools

2.1. Introduction

Due to limitations in the transportation of long pipes, pipes are manufactured in transportable length and welded together during the installation of the pipeline. The majority of these welds are performed in the field and are therefore prone to flaws. The presence of flaws might adversely affect the structural integrity and if this effect is deemed to be significant, the weld should be repaired. The process of flaw detection and assessment of its severity contains several consecutive steps that are normally elaborated in related standards and guidelines.

A fundamental reason why flaws can adversely affect pipeline integrity is that these imperfections act as a stress raiser. Stress concentration is partly related to the local reduction in wall thickness, but the sharpness of the flaw magnifies the effect significantly. For instance, a notch like flaw such as lack of fusion, has a higher stress concentration factor than a porosity, and a crack-like flaw has a higher stress concentration than both of them. The high local stress at the flaw tip can reduce the burst pressure. In addition, crack-like flaws can grow over time, which gradually reduces burst pressure until it reaches the local operating pressure. A similar statement can be made regarding the axial strain capacity, which may reduce down to the level of the strain demand imposed by the environment [14].

EN 12732:2013, for instance, dictates that the entire weld length should be inspected for possible presence of weld flaws in case of pipelines installed in built-up areas [15]. To this end, non-destructive inspection (NDI) is performed by means of ultrasonic and/or radiographic techniques. These techniques provide an approximate insight in defect features such as shape, length or height. Based on these dimensions, a defect assessment procedure can be performed to evaluate whether the detected flaws are tolerable. This procedure can have a substantial impact on structure integrity and the project final costs. On the one hand, if a marginal flaw is classified as non-acceptable, unnecessary repair costs and delays are imposed to the project. On the other hand, if a critical flaw is mistakenly classified as an acceptable flaw, the structure integrity might be in question.

The presence of flaws and their adverse effect is neither limited to welds, nor limited to pipes. For example, a corrosive environment accompanied by tensile stress can cause Stress Corrosion Cracking (SCC). Fatigue is another cause of cracks, for instance in power plants where fatigue crack initiation and propagation may occur at multiple sites of piping due to flow-induced vibration, thermal stratification or hot/cold water mixing. Numerous other examples exist.

To acknowledge the difference in terminology as notch, flaw, defect and crack found in literature, in the FE models and experimental specimens used in this work the discontinuity will be referred to as a notch, relating to the fact that it is achieved by machining. A flaw, to be consistent with ASME B&PV Code sec. XI [16], is an imperfection or unintentional discontinuity that is detectable by NDE. In the present study “notch” and “flaw” are used as synonyms, whereby a flaw is always assumed to have a blunt tip. A defect is a flaw of such size, shape, orientation, location and/or properties that it is unacceptable for continued service according to the assessment

procedure. A crack is essentially a defect having an infinitely sharp tip and is not studied in the present project. The effect of infinite sharpness is neglected, because in tough materials a crack tip blunts out from the first stages of the loading. However, the terms “crack front” and “crack driving force” will be used for cracks, defects and flaws similarly, as these terms are commonly adopted in fracture mechanics theory.

In stress-based design procedures, the stress applied to the component is compared with a limit stress such as (a fraction of) yield strength. As long as the former does not exceed the latter, the component is considered as safe. This approach assumes that the component is defect free, however in real components defects might be found either in the construction phase or during service. Existence of a crack can reduce the load bearing capacity of the structure and fracture mechanics and plasticity based calculations should be employed to estimate this capacity. Since these calculations can be very challenging, more simple engineering guidelines are often employed.

In general, defect assessment procedures comprise multiple tiers of complexity, where a higher complexity results in a higher defect acceptance, nonetheless lower complexity tiers comparatively are faster and far simpler to conduct and require less detailed input. A first level is typically based on comparing flaw dimensions against “workmanship criteria” described in pipeline design and construction codes such as API 1104 [17] and DNV OS F101[12]. Such criteria inherently are very simple and require limited input such as e.g. defect length. Normally, the allowed limit is a fixed value, regardless of material properties and loading conditions. Using workmanship-based flaw assessment, however, can result in a high rate of repair and increased costs, mainly arising from the delay to installation, but without any significant benefit to the integrity of the girth welds. Weld repair may even deteriorate the integrity of the structure due to the introduction of new defects and/or deterioration of material properties. Indeed, there have been instances where an unnecessary and improperly executed repair has initiated failure [18]. Although this method takes advantage of its simplicity, it can lead to (over-)conservative assessments. Considering that the cost of a weld repair can be estimated as high as ten times the cost of the original weld [19], it becomes clear why the pipeline industry aims at minimizing repair welding, of course without sacrificing safety. Accordingly, a higher-level assessment based on fracture mechanics approaches, often referred to as engineering critical assessment (ECA), is employed to achieve a more accurate estimation. Guidelines and standards like BS7910 [20], ASME Sec. XI [16], DNVGL-RP-F108 [21] and API 579 [22] provide a quantitative means for deciding which weld flaws, identified by non-destructive testing (NDT), potentially compromise weld integrity with respect to defined failure criteria and therefore require repair. For performing an ECA, more detailed information is required, and this implies extra costs for material testing, more accurate non-destructive testing and sophisticated analysis. However, this is far outweighed by the benefits in reducing repair costs and delays during pipe-lay operations.

Strain-based fracture mechanics assessment procedures are more complex than their stress-based counterparts. They need more input data in terms of material properties and loading conditions. Although 3-D elastic-plastic finite element analysis is sometimes employed for critical projects, there is always the question of validation and whether acceptable flaw sizes determined from such analyses are fully supported

by full-scale tests. Since one needs to assess many pipe dimensions, considering material variation and several flaw cases, closed form solutions are still desirable in preference to running finite element analyses. The derivation of such closed form solutions is not straightforward owing to the large number of variables that need to be considered when plasticity takes place [18].

2.2. Basic concepts of analytical flaw assessment

2.2.1. Stress intensity factor (SIF)

Fracture mechanics describes the structural response of a cracked structure, thereby focusing on unstable fracture and stable crack growth. Historically, fracture mechanics originates from Griffith's research in the early 20th century [23]. He found that for a marginal crack growth to occur, the resulting release of potential energy should at least be equal to the dissipated energy. Griffith's original experiment, known as surface energy approach, was with very brittle materials, specifically glass rods. When the material exhibits more ductile behavior, using the surface energy approach alone fails to provide an accurate model for fracture. This issue was later addressed independently by Irwin [24] and Orowan [25], at least in part. According to their model, the vast majority of the released strain energy was absorbed not by creating new surfaces as Griffith suggested, but by energy dissipation due to plastic flow in the material near the crack tip. They suggested that unstable fracture occurs when the strain energy is released at a sufficient rate to satisfy these energy needs. This energy, named 'critical strain energy' (G_c), is defined by equation 2-1:

$$\sigma_f = \sqrt{\frac{EG_c}{\pi a}} \quad 2-1$$

This equation shows the relation between the three main aspects of a fracture process: the material represented by its critical strain energy (G_c); the stress level at fracture (σ_f); and the size of the crack (a). One could determine a value of the crack size based on the smallest flaw that can be detected by NDI. Then, for a known material, the safe level of stress can be determined. Vice versa, when material and stress level are known a critical flaw size can be calculated. The critical flaw size is an absolute number and does not depend on the size of the structure containing it.

While the energy balance approach is reflecting a general understanding of the fracture process, an alternative method developed based on the direct estimation of the stress state near an infinitely sharp crack tip has proven to be more applicable in engineering applications. As shown in Figure 2-1 three modes of loading a crack can be assumed, namely mode I, II, and III. Mode I is the normal opening mode, when tensile stress is acting normal to the plane of the crack. Mode II is the in-plane sliding mode, when a shear stress acts parallel to the plane of the crack perpendicular to the crack front. Mode III is the out-of-plane tearing mode, when a shear stress acts parallel to the crack front. Focusing on Mode I, and assuming linear elastic material, the so-called stress intensity factor (SIF) K_I is described by equation 2-2:

$$\lim_{r \rightarrow 0} \sigma_{ij} = \frac{K_I}{\sqrt{2\pi r}} f_{ij}^{(I)}(\theta) \quad 2-2$$

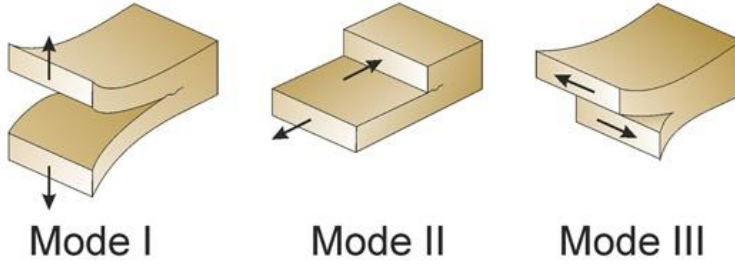


Figure 2-1- Fracture modes.

In equation 2-2, r and θ are coordinates in a polar coordinate system (with $r=0$ at the crack tip and $\theta=0$ the direction of the crack front), and $f_{ij}^{(I)}$ a tensor of known functions. Considering the linear elastic assumption, K_I is proportional to the remotely applied stress σ and generally expressed as:

$$K_I = Y\sigma\sqrt{\pi a} \quad 2-3$$

Where Y is a non-dimensional correction factor that depends on geometry, σ is the remotely applied stress level, and a is the crack size. Theoretically, if K_I reaches a critical value, namely K_{Ic} , fracture occurs. K_{Ic} is a measure of the fracture toughness of the material in linear-elastic conditions.

The stress intensity factor and energy release concepts have been linked by Irwin [26]:

$$\sigma = \sqrt{\frac{E'G_c}{\pi a}} = \frac{K_{Ic}}{\sqrt{\pi a}} \rightarrow K_{Ic}^2 = E'G_c \quad 2-4$$

Where E' is Young's modulus E or $E/(1-\nu^2)$ for plane stress and plane strain configurations respectively (ν is Poisson coefficient).

Linear Elastic Fracture Mechanics (LEFM) can be applied to brittle materials as well as plastically deforming materials provided that the region of plastic deformation is relatively small compared to the other dimensions of the structural problem. This condition is referred to as 'small scale yielding'. In many situations, however, the influence of crack tip plasticity of fracture behaviour becomes significant and LEFM loses its validity. There are two main issues:

1. To obtain K_{Ic} in a laboratory test, small specimens are preferred (for cost and convenience). However, in order to achieve a valid K_{Ic} for materials with high toughness or low yield strength a very large test specimen may be required.
2. In real components there may be significant amounts of plasticity, in which case LEFM is neither valid nor applicable. For these reasons one needs to examine non-linear fracture mechanics where the inelastic near tip response is accounted for.

Therefore, the application of LEFM is mostly limited to brittle materials, fatigue problems and assessments intended to be straightforward and conservative. For the investigation of problems involving significant plasticity, near the crack tip or global, Elastic Plastic Fracture Mechanics (EPFM) is required. In this framework, two main parameters have been introduced, namely J -integral and Crack Tip Opening Displacement (CTOD).

2.2.2. J -integral

The J -integral concept is an approach to calculate strain energy release rate or work per unit of fracture surface in a material. The J -integral method as a line integral (path-independent) around the crack tip initially has been suggested by Jim Rice in 1968 [27]. Rice's approach was developed based on the works of Eshelby [28] and Cherepanov [29].

J -integral represents the net potential energy's changing rate with respect to the crack growth in a non-linear elastic material. J -integral can be interpreted both as stress measure and energy, just like K .

For the particular case of a linear elastic material:

$$J_e = G = \frac{K^2}{E'} \quad 2-5$$

For plastically deforming material, Kumar, German and Shih developed the so-called h -factor approach towards J estimation in the EPRI handbook (1981) [30]. This approach is represented by equation 2-6 (alternative equations can be found in [31,32]):

$$J_p = \alpha \varepsilon_0 \sigma_0 a h_1 \left(\frac{P}{P_0} \right)^{n+1} \quad 2-6$$

Where P_0 is a normalization load, J_p is proportional to a dimensionless factor h_1 , which depends on the choice of P_0 , the geometry of the structure, the crack size, the strain hardening exponent n and the position of the crack front. P is the applied load and α and n are defined by assuming power law material response (equation 2-7) considering that n is equal to unity for elastic material and equal to infinity for perfectly plastic response. σ_0 is reference yield stress and ε_0 is reference yield strain ($\varepsilon_0 = \sigma_0 / E$):

$$\frac{\varepsilon}{\varepsilon_0} = \frac{\sigma}{\sigma_0} + \alpha \left(\frac{\sigma}{\sigma_0} \right)^n \quad 2-7$$

2.2.1. Crack tip opening displacement (CTOD)

The CTOD (δ) parameter was first proposed by Wells in 1963 [33]. It was defined with primary focus on mode-I loading as the opening of the crack at its original tip and has validity in both LEFM and EPFM.

Following Wells' introduction of CTOD, alternative definitions have been proposed. Most acknowledged is Rice's 90-degree intercept definition of CTOD [27,34], where CTOD is equal to the displacement between two points at the intersection of the crack flanks and lines originating from the crack tip at angles of 45° with respect to the crack direction. In practice it can be hard to exactly locate the crack tip (e.g., when the crack grows) and the 90° intercept lines are often inferred from the original crack tip. In finite element (FE) analysis and cast replica measurements the displacement at the original crack tip is also commonly used [27]; this definition is in line with the original definition introduced by Wells. It is easily shown that the abovementioned definitions are equivalent if the crack tip blunts into a semicircle. Different definitions for stationary and growing cracks are shown in Figure 2-2. Depending on the material response, the variation in CTOD is depicted in Figure 2-3.

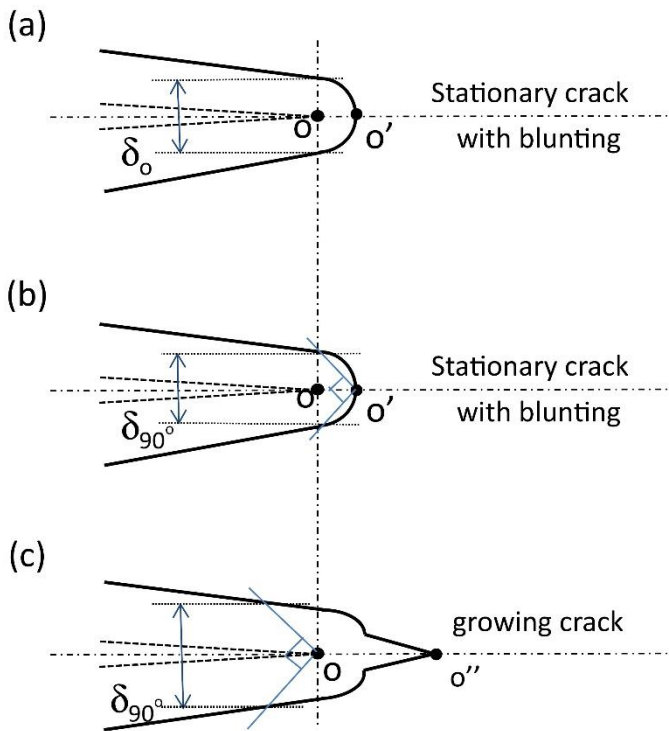


Figure 2-2: Three typical CTOD definitions: (a) CTOD defined at the original crack tip, (b) CTOD defined by the 90° intercept approach at the blunted crack tip and (c) CTOD defined by the 90° intercept approach at the original crack tip [35]

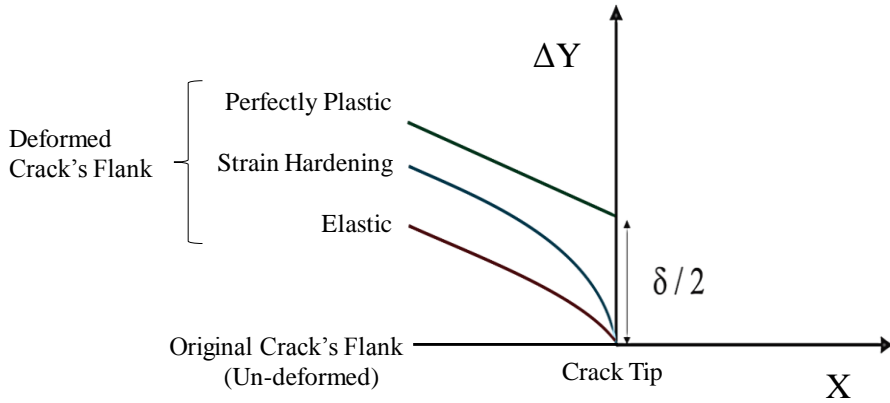


Figure 2-3: Variation of CTOD for different material responses, plotted for half of the crack.

The subsurface nature of CTOD makes its direct measurement very difficult. Early CTOD measurements were made using injection, removal and dimensional measurement of dental implant compound [36]. Since this is a highly cumbersome procedure, alternative measurement methods were sought. Contemporary methods typically estimate the CTOD through geometrical models that extrapolate remote displacements (e.g. at the crack mouth) down to the crack tip. Hereby, CTOD is often defined as a sum of two contributions: elastic and plastic components [37]. The elastic component is normally calculated based on applied force and a function of initial crack depth to specimen width ratio (a_0/W) and the specimen dimensions. The plastic component is derived from the plastic component of the crack mouth opening displacement (CMOD) using a model which assumes that two rigid parts of the specimen rotate around a plastic hinge point in the uncracked ligament. The plastic hinge model was adopted first in 'Draft for Development' (DD19) published for CTOD testing by British Standards Institute (BSI) in 1972 [38], and later this became the first CTOD test standard BS 5762, published in 1979 [39]. Following BS 5762, various standards and procedures including BS7448–1991 [40], ISO 12135-2002 [41], AS2205.7.3-2003 [42] and GB2358-80 [43] used this model for CTOD measurement.

ASTM E-1290 [44] and E-1820 [45], however, have a different approach in comparison to the abovementioned standards. Although in their early revisions they had also used the plastic hinge model, since 2002 E-1290 and from 2005 E-1820 discarded the plastic hinge model. In their recent versions, CTOD is converted from J -integral considering that this approach is insensitive to strain hardening differences in materials. Although the source of J -integral calculation is not described in the ASTM standards, J -integral is obtained using the plastic area under a load versus crack mouth opening displacement (CMOD) curve [46]. J is the sum of J_e (elastic contribution) and J_p (plastic contribution). The elastic component of J is calculated based on the stress-intensity factor, and J_p is proportional to the plastic area under the load versus load point displacement curve. Tagawa et al. [46] recently showed that although ASTM does not refer to the plastic hinge model, still its plastic contribution calculation plastic

hinge is involved in plastic load point displacement curve. They also pointed out that ASTM 1290 tends to result in a smaller value of CTOD than BS 7448.

GKSS² also suggested its own definition for CTOD, known as δ_5 . Based on the δ_5 approach, CTOD is equal to the displacement of two nodes placed 2.5 mm apart and symmetrically with respect to the original crack tip. This measurement can be performed either through a clip gauge or by full field optical measurements [47]. The former method requires a special device to make spot contact between the gauge and the specimen, which is not always possible. The latter technique requires less preparation and restrictions and can be performed without contact with the specimen. This can be a practical merit for measuring CTOD in comparison to the 90-degrees intercept approach which is normally measured by a cumbersome double clip gauge method [48,49]. The possibility of direct measurement of CTOD, without knowing the material's mechanical parameters (Young's modulus, yield strength, Poisson's ratio) is a significant advantage for δ_5 .

The most basic plastic hinge model relates CTOD to CMOD and assumes a fixed position of the plastic hinge described by a dimensionless plastic rotation factor r_p . As an advantage, it only requires one clip gauge measurement at the crack mouth. As a disadvantage, its accuracy relies on a sound estimation of the plastic hinge position. Therefore, CTOD estimations by the abovementioned procedures differ marginally due to (subtle) differences in r_p [50].

The actual position of the plastic hinge depends on crack depth, strain hardening behavior and in addition, since the rotational center can change during initial crack opening [51], it may be subject to change during the test. To avoid using a presumed rotation factor, Deng et al. [52] and Willoughby & Garwood [53] developed the double clip gauge technique to directly measure CTOD for Single Edge Notch Bending (SENB) specimens. Hereby, the extrapolation of two clip gauge measurements at different heights above (or at) the crack mouth allows to directly measure the position of the plastic hinge. In 2012, DNV-OS-F101[12] accepted the double clip gauge technique to measure CTOD for SENB and Single Edge Notch Tension (SENT) specimens, and recently BS 8571 [54] adopted the double clip gauge method to measure the plastic contribution of CTOD.

CTOD is a standard parameter used to determine the fracture toughness of thin walled structures under low constraint conditions [55]. CTOD has also been used in Fitness-For-Service (FFS) procedures; initially through alternative flaw acceptance criteria in API1104 published in 1973 [56], and within the failure analysis diagram in BS7910 (prior to 2013 version) [20] which also allowed employing CTOD to determine maximum allowable weld flaw sizes [57]. Though, still there is a discussion on whether J or CTOD is the most appropriate fracture parameter in FFS assessment of plastic and high strain regimes. Pipeline defect assessment research and development continues towards strain-based designs and the CTOD is considered as an appropriate parameter for this particular application, either as a toughness parameter or to describe the crack driving force. For instance, the strain-based

² German Society for utilization of atomic energy in shipbuilding and shipping; in German: Gesellschaft für Kernenergieverwertung in Schiffbau und Schifffahrt

assessment procedure for offshore pipelines developed by ExxonMobil uses CTOD [49].

For small scale yielding conditions, J -integral and CTOD can be linked through equation 2-8:

$$J = m\sigma_0\delta \quad 2-8$$

Where m is the plastic constraint factor depending on the configuration and material properties (varies between 1.15 and 2.95) [58].

K , CTOD and J -integral are known as crack driving force (CDF) parameters and assessments based on them basically consist of calculation of these parameters and comparing the calculated value with their critical value, which is a material property.

2.2.2. Plastic collapse and limit load

Besides fracture, plastic collapse is another main mechanism of failure in flawed structures. Plastic collapse may be defined as the event where accumulation of localized deformation exhausts the ductility of the material (similar to localized necking in a tensile test) [8]. Two collapse types can be distinguished. First, Net Section Collapse (NSC) corresponds to the collapse of the flawed section. This type of failure is common for homogeneous material (e.g. a plate with a crack in absence of a weld). Second, in presence of an overmatched weld, the collapse may occur in a section remote from the flaw. This failure mode is called Gross Section Collapse (GSC).

Net Section Collapse can be further categorized into Local Collapse and Global Collapse. The former involves crack ligament collapse and the latter involves collapse of the entire flawed section. From another perspective, global collapse is related to the load at which the load-displacement becomes unbounded and is relevant to the whole structure failure. While local collapse corresponds to the loading level at which plastic strains at the ligament become sufficiently large and may be relevant to ligament fracture. The local collapse can occur long before global collapse and therefore assessments based on local collapse reveal more conservative results for flawed structures.

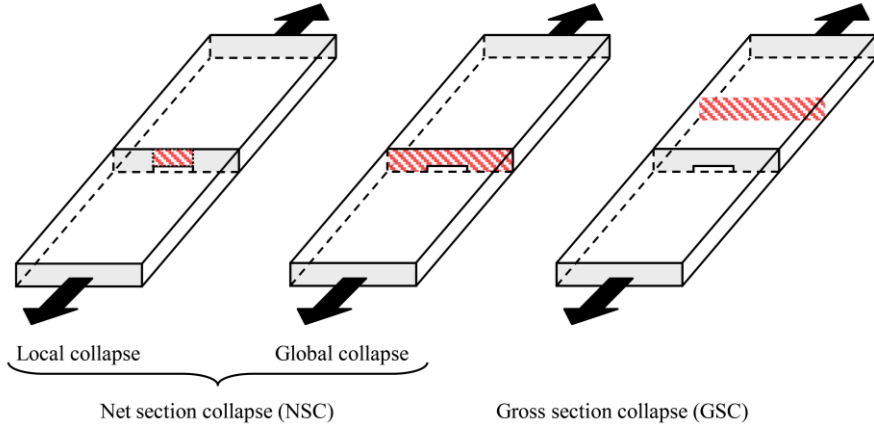


Figure 2-4- Definition of different plastic collapse types [8].

To quantify the plastic collapse load, mechanical behavior is typically simplified to elastic-perfectly plastic. Thus, in the case of elastic-perfectly plastic assumption strain hardening is fully neglected, which adds conservativeness to the calculation. With these assumptions, plastic collapse load is referred to as ‘limit load’. (Limit load can also consider strain hardening by using flow stress concept)

It should be noted that the limit load corresponds to the yield strength of the flawed section. However, due to the strain hardening, in reality this does not correspond to immediate failure of the whole structure. Such failure may not happen until the ‘plastic collapse load’ is reached. The distinction between limit load and plastic collapse load is crucial for fracture mechanics based higher-level assessments. However, in common solid mechanics this distinction is not usually made due to the assumption of elastic-perfectly plastic material behavior [59]. These two different approaches are depicted in Figure 2-5, and elaborated in the following paragraphs.

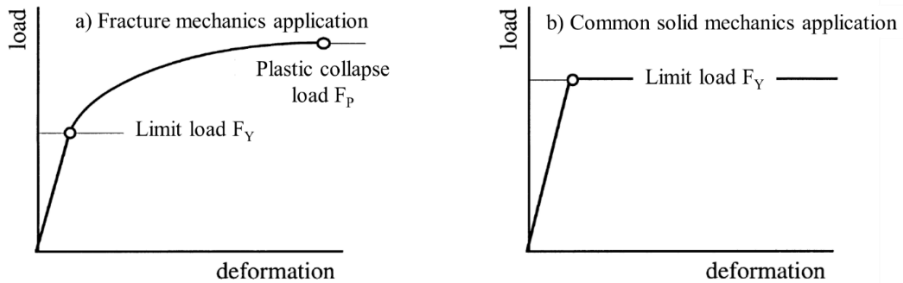


Figure 2-5- Schematics of limit and plastic collapse load: a) in fracture mechanics application, b) in common solid mechanics application [59].

The limit load concept is used in several design codes and guidelines. For instance, ASME B&PV Code sec. VIII Division 2 Appendix 4 provides guidelines for Design by Analysis (DBA) based on elastic and elastic-plastic stress analysis. For elastic analysis, gross plastic deformation is prevented by limiting the primary stress

in the vessel to a threshold depending on material yield stress. For elastic-plastic (often referred to as inelastic), gross plastic deformation is averted by restricting the allowable stress to either limit load or plastic load. According to ASME B&PV Code (sec. III and sec. VIII), the limit load is the maximum load satisfying equilibrium between the external and internal forces, provided that perfectly plastic material and small deformation theory are assumed.

The plastic collapse load is more complex and should include the effect of strain hardening and large deformations (stress redistribution occurring in the structure). ASME B&PV Code sec. III (NB-3213.25) [60] defines the plastic load by the so-called Twice Elastic Slope (TES) numerical criterion. As shown in Figure 2-6 in the TES method, a load–deflection or load–strain curve is plotted with load as the ordinate and deflection or strain as the abscissa. The angle between the linear part of the load–deflection or load–strain curve and the ordinate axis is called ϕ_1 . A second straight line, hereafter called the collapse limit line, is drawn through the origin so that it makes an angle $\phi_2 = \tan^{-1} (2 \tan \phi_1)$ with the ordinate. The collapse load is the load at the intersection of the load–deflection or load–strain curve and the collapse limit line. In other words, the material response is characterized by plotting force against displacement. A straight limit load line is then drawn from the origin of the force-displacement curve with a slope equal to twice that of the elastic response (with respect to the vertical load axis). The plastic collapse load is then obtained as the intersection between the TES line and the force-displacement curve. If, for a given load, any system of stresses can be found which everywhere satisfies equilibrium, and nowhere exceeds the material yield strength, the load is at or below the structure collapse load. Therefore, this is the lower bound theorem of limit analysis which permits calculations of a lower bound to the (plastic) collapse load by calculation of the limit load. Further descriptions about plastic collapse calculation can be found in ASME B&PV code, Section VIII, Division 2, Paragraph 5.2.4 (perfectly plastic material) or Division 3, Paragraph KD-230 (true stress–strain material model).

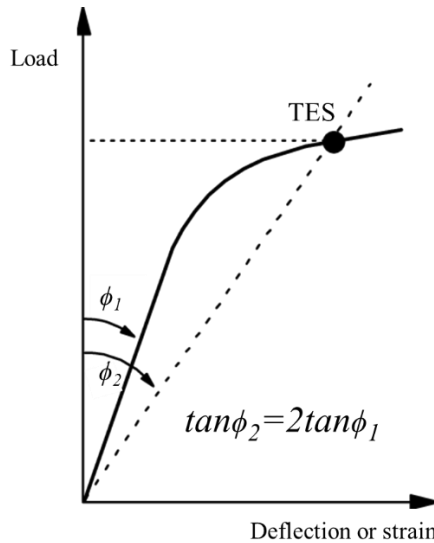


Figure 2-6: Twice Elastic Slope (TES) definition.

2.2.3. Failure Assessment Diagram (FAD)

The failure assessment diagram (FAD) is a graphical assessment approach, which combines the fracture proximity with the proximity to plastic collapse. In other words, failure is assumed either when the stress intensity factor in the component exceeds the fracture toughness or when the applied load exceeds the plastic collapse load of the net section of the component. The FAD approach is considered as an alternative to CDF approaches, like the EPRI approach [61], in flaw assessment procedures [59]. In a FAD diagram, a roughly geometry-independent failure line is generated by normalizing the crack tip loading by material's fracture resistance. Then the component is assessed based on the geometry dependent location of the assessment point (depends on material, geometry, flaw and loading) with respect to the above-mentioned failure line. The component is regarded as safe as long as its assessment point remains below the failure line. By increasing the load or flaw size, the assessment point moves towards the failure line. If an assessment point is located above the limit curve, it is regarded as potentially unsafe (See Figure 2-7).

FAD is standardized in various guidelines including R6:2015, BS7910:2013 and API579:2009. The definition of the failure line and the background of the stress intensity factor and plastic collapse load in these guidelines slightly differ.

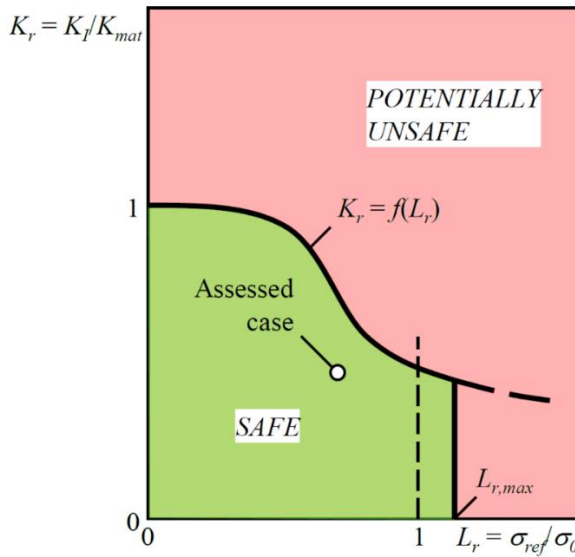


Figure 2-7: Failure assessment diagram according to R6 definition [8].

In the SIF approach, in contrast to FAD, the applied load and the material resistance are strictly separated. In other words, the calculation of the crack driving force, and its comparison with the fracture resistance (toughness) are conducted in two separate steps. Like FAD, for CDF approach a geometry-independent failure line can be constructed by suitable normalization against the load. In principle, the two concepts can be made fully compatible.

2.2.4. Tearing resistance curve (R-curve)

The FAD based assessments are developed based on the concept that, once the crack driving force reaches to a failure state defined by the toughness threshold (K_{mat} , J_{mat} , $CTOD_{mat}$), which includes any amount of crack extension. However, tough material can tear in a stable manner before final fracture, particularly in cases of low stress triaxiality at the crack tip (low “crack tip constraint”). Thus, in low constraint configurations combined with tough material properties (like contemporary pipeline girth welds [62]) there is no single value for the toughness and instead the concept of tearing resistance curve (R-curve) should be employed.

A tearing resistance curve represents the required crack driving force for a certain amount of progressive ductile crack growth; which implies that the material fracture toughness changes with crack extension. The R-curve is a plot of fracture toughness against crack growth (e.g. J -integral vs Δa or $CTOD$ vs Δa , where Δa is crack growth). Depending on the parameter adopted for crack driving force, the tearing resistance curve is referred to as J-R curve or $CTOD$ -R curve.

Ductile crack growth basically occurs by the process of micro void coalescence. When the material ahead of the crack tip deforms plastically, micro voids are generated in the plastic zone, and by increasing the load these voids are growing and linking together. Considering that many ductile materials exhibit work hardening in their post yielding response, as the crack grows the plastic zone at the crack tip increases. Thus, to further increase of the plastic zone size, each unit of crack extension requires more energy than the preceding unit (known as ‘rising R-curve’). Of course, this trend stops when the material reaches the unstable fracture onset. The experimental procedure to develop tearing resistance curves is standardized in BS 7448-Part 4 [63] and ASTM E1820 [58].

To estimate the stable ductile tearing, the intersection of the R-curve and crack driving force curve as function of crack size at constant loading level, is employed in flaw assessment procedures. Moreover, the onset of unstable fracture can be determined as the situation where two curves touch each other tangentially. This approach is known as ‘tangency approach’ and depicted in Figure 2-8.

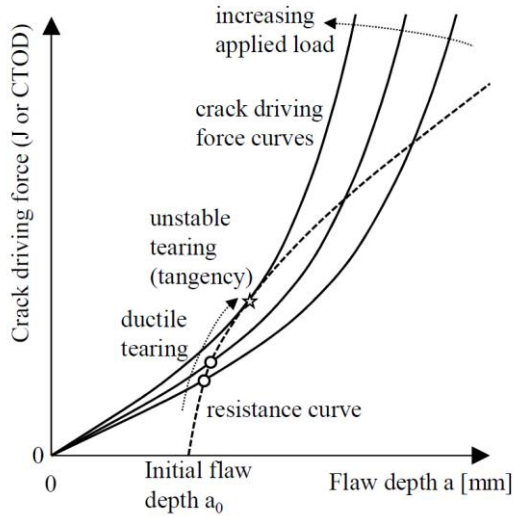


Figure 2-8: The R-curve and tangency approach [64].

2.3. Conclusion

Failure in components may occur due to various causes, including inadequacies in design, uncertainties in the loading or environment, defects in the materials and deficiencies in construction or maintenance. Among them, design against fracture, when the presence of a crack or flaw is assumed, has a technology of its own. The goal of this assessment is to find quantitative relations between the flaw size, the material's resistance to crack growth, and the stress at which the crack propagates unstably to cause structural failure.

To address this challenge, various analytical tools have been developed in the past years. This chapter reviewed the most important procedures used to assess cracked structures from different perspectives. These procedures are typically based on K (linear elastic), J or CTOD (elastic plastic), all of which are measures of crack driving force. While the measurement techniques of K and J -integral are fairly mature, measurement procedures for CTOD are subject to debate and developments are ongoing. While some Fitness-For-Service guidelines in the past years replaced CTOD with J -integral due to uncertainty in CTOD measurement, CTOD to date remains the main assessment parameter in pipeline industry.

Unlike stress-based design procedures, strain-based design procedures normally permit a certain amount of stable ductile crack growth. Therefore, strain capacity is determined by the onset of unstable crack growth (rather than crack initiation). The corresponding assessment requires knowledge of the crack growth resistance curve (also known as R-curve).

All of the listed methods in this chapter are basically developed for the case of single isolated cracks. ECA guidelines tend to assess multiple flaws as an equivalent single flaw after an additional procedure known as “flaw interaction”, which will be introduced in the next chapter.

References

- [1] DNV GL Energy. Oil and gas forecast to 2050, energy transition outlook 2017. 2017.
- [2] DNV GL Energy. Oil and gas forecast to 2050, energy transition outlook 2018. 2018.
- [3] Götz M, Lefebvre J, Mörs F, McDaniel Koch A, Graf F, Bajohr S, et al. Renewable Power-to-Gas: A technological and economic review. *Renew Energy* 2016;85:1371–90. doi:10.1016/J.RENENE.2015.07.066.
- [4] Essandoh-Yeddu J, Gülen G. Economic modeling of carbon dioxide integrated pipeline network for enhanced oil recovery and geologic sequestration in the Texas Gulf Coast region. *Energy Procedia* 2009;1:1603–10.
- [5] EU. Novel carbon capture and utilization. Brussel: 2018. doi:10.2777/824461.
- [6] Noothout P, Wiersma F, Hurtado O, Macdonald D, Kemper J, van Alphen K. CO2 Pipeline Infrastructure – Lessons Learnt 2014. doi:10.1016/j.egypro.2014.11.271.
- [7] Jakobsen J, Roussanaly S, Anantharaman R. A techno-economic case study of CO2 capture, transport and storage chain from a cement plant in Norway. *J Clean Prod* 2017;144:523–39. doi:10.1016/J.JCLEPRO.2016.12.120.
- [8] Hertelé S. Coupled Experimental-Numerical Framework for the Assessment of Strain Capacity of Flawed Girth Welds in Pipelines. PhD dissertation. Ghent University; 2012.
- [9] API Specification 5L, specification for Line Pipe. American Petroleum Institute; 2004.
- [10] Gao H, Yu Z, Zhang Z, Shi H. The Concepts For Pipeline Strain-Based Design. Twent. Int. Offshore Polar Eng. Conf., Beijing, China: International Society of Offshore and Polar Engineers; 2010, p. 7.
- [11] Law M. Review of Strain Based Analysis for Pipelines Review of Strain Based Analysis for Pipelines. Menai, NSW: 2007.
- [12] Offshore standard DNV-OS-F101. DET NORSKE VERITAS AS; 2010.
- [13] Wang YY, Liu M, Song Y, Stephens M, Petersen R, Gordon R. Second generation models for strain-based design. 2011.
- [14] Revie RW. Oil and gas pipelines: Integrity and safety handbook. John Wiley & Sons; 2015.
- [15] EN 12732:2013 Gas infrastructure-Welding steel pipework-Functional requirements. 2014.
- [16] Rules for Inservice Inspection of Nuclear Power Plant Components: ASME Boiler and Pressure vessel Code XI. New York: American Society of Mechanical Engineers; 2015.
- [17] Api Standard 1104. Welding of pipelines and related facilities. API 1104-2013+ADD2014. 21st Ed 2013.
- [18] Henryk Pisarski. Assessment of Flaws in Pipe Girth Welds. Int. Conf. Weld. High Strength Pipeline Steel, Araxá, Brasil: 2011.
- [19] Varma AK, Hazra B, Samad SK, Panda S, Mendhe VA. Girth weld fitness after multiple SMAW repairs. *Pipeline Gas J* 2014.
- [20] British Standard. BS7910:2013+A1:2015: Guide to methods for assessing the acceptability of flaws in metallic structures. London, UK: BSI Stand Publ; 2015.
- [21] DNV GL. DNVGL-RP-F108 Assessment of flaws in pipeline and riser girth welds. DNV GL AS; 2017.
- [22] API 579-1/ ASME FFS-1. Recommended practice for fitness-for-service: API-579-1. 2nd ed. Washington DC, USA: American Petroleum Institute; 2007.
- [23] Irwin GR. Onset of fast crack propagation in high strength steel and aluminum alloys. NAVAL RESEARCH LAB WASHINGTON DC; 1956.
- [24] Irwin GR. Fracture dynamics, Fracturing of Metals. Cleveland: American Society of Metals; 1948.
- [25] Orowan E. Fracture and strength of solids. *Reports Prog Phys* 1949;12:185.
- [26] Irwin GR. Analysis of stresses and strains near the end of a crack traversing a plate. *J*

- Appl Mech 1957.
- [27] Rice JR. A path independent integral and the approximate analysis of strain concentration by notches and cracks, ASME; 1968.
 - [28] Eshelby JD. The continuum theory of lattice defects. Solid state Phys., vol. 3, Elsevier; 1956, p. 79–144.
 - [29] Cherepanov GP. On crack propagation in solids. Int J Solids Struct 1969;5:863–71.
 - [30] Kumar V, German MD, Shih CF. Engineering approach for elastic-plastic fracture analysis. General Electric Co.; 1981.
 - [31] Wang X. Fully plastic J-integral solutions for surface cracked plates under biaxial loading. Eng Fract Mech 2006;73:1581–95.
 - [32] Yagawa G, Kitajima Y, Ueda H. Three-dimensional fully plastic solutions for semi-elliptical surface cracks. Int J Press Vessel Pip 1993;53:457–510.
 - [33] Wells. Application of fracture mechanics at and beyond general yielding. Br Weld J 1963.
 - [34] Shih C. Relationships between the J-integral and the crack opening displacement for stationary and extending cracks. J Mech Phys Solids 1981;29:305–26. doi:10.1016/0022-5096(81)90003-X.
 - [35] Zhu X-K, Zelenak P, McGaughy T. Comparative study of CTOD-resistance curve test methods for SENT specimens. Eng Fract Mech 2017;172:17–38. doi:10.1016/J.ENGFRACMECH.2017.01.007.
 - [36] Burdekin FM. CRACK OPENING DISPLACEMENT: A REVIEW OF PRINCIPLES AND METHODS. Sandberg, London; 1969.
 - [37] Dawes MG. Elastic-plastic fracture toughness based on the COD and J-contour integral concepts. Elastic-plastic Fract., ASTM International; 1979.
 - [38] British Standard. Methods for crack opening displacement (COD) testing- DD19. British Standards Institute.; 1972.
 - [39] British Standard. BS 5762. Methods for Crack Opening Displacement (COD) Testing. BSI Stand Publ 1979.
 - [40] British Standard. BS 7448-2:1997 Fracture mechanics toughness tests. BSI Stand Publ 1997.
 - [41] ISO 12135: 2002 Metallic materials-Unified method of test for the determination of quasistatic fracture toughness. 2002.
 - [42] Australian Standard. AS 2205.7.3: Methods for destructive testing of welds in metal. Fracture mechanics toughness tests. 2003.
 - [43] Chinese Standards Association. Crack Opening Displacement (COD) Testing Method, GB 2358-80. 1980.
 - [44] ASTM E1290: Standard Test Method for Crack-Tip Opening Displacement (CTOD) Fracture Toughness Measurement. West Conshohocken: 2008.
 - [45] ASTM E1820-96, -05. Standard test method for measurement of fracture toughness. West Conshohocken: American Society for Testing and Materials; 1996.
 - [46] Tetsuya Tagawa, Yoichi Kayamori, Mitsuru Ohata. Comparison of CTOD standards: BS 7448-Part 1 and revised ASTM E1290. Eng Fract Mech 2010;77:327–36. doi:10.1016/J.ENGFRACMECH.2009.02.009.
 - [47] Verstraete MA, Denys RM, Van Minnebruggen K, Hertelé S, De Waele W. Determination of CTOD resistance curves in side-grooved Single-Edge Notched Tensile specimens using full field deformation measurements. Eng Fract Mech 2013;110:12–22. doi:10.1016/j.engfracmech.2013.07.015.
 - [48] Moore PL, Pisarski HG. Validation of methods to determine CTOD from SENT specimens. Twenty-second Int. Offshore Polar Eng. Conf., International Society of Offshore and Polar Engineers; 2012.
 - [49] Tang H, Macia M, Minnaar K, Gioielli P, Kibey S, Fairchild D. Development of the SENT test for strain-based design of welded pipelines. Proc. 8th Int. Pipeline Conf. IPC, 2010.
 - [50] Wu S-X, Mai Y-W, Cotterell B. Plastic rotation factors of three-point bend and

- compact tension specimens. *J Test Eval* 1988;16:555–7.
- [51] Kawabata T, Tagawa T, Kayamori Y, Ohata M, Yamashita Y, Kinefuchi M, et al. Applicability of new CTOD calculation formula to various a0/W conditions and B×B configuration. *Eng Fract Mech* 2017. doi:10.1016/j.engfracmech.2017.03.027.
 - [52] Zhih-shen D. Measuring and calculating CTOD and the J-integral with a double clip gauge 1980;63–7.
 - [53] Willoughby AA, Garwood SJ. Single specimen estimates of R-curves using a double compliance technique in bending. *Int J Fract* 1981;17:R11–5.
 - [54] British Standard. BS8571:2014 Method of test for determination of fracture toughness in metallic materials using single edge notched tension. BSI Stand Publ 2014.
 - [55] Schwalbe K-H, Newman Jr JC, Shannon Jr JL. Fracture mechanics testing on specimens with low constraint—standardisation activities within ISO and ASTM. *Eng Fract Mech* 2005;72:557–76.
 - [56] API 1104:1973 Standard for welding pipelines and related facilities. 13th editi. American Petroleum Institute; 1973.
 - [57] Moore P, Pisarski H. CTOD and pipelines: the past, present, and future. *J Pipeline Eng* 2013;12.
 - [58] ASTM International. ASTM 1820 Standard test method for measurement of fracture toughness. 2011. doi:10.1520/E1820-11.2.
 - [59] Zerbst U, Ainsworth R a, Schwalbe K. Basic principles of analytical - aw assessment methods 2001;77:855–67.
 - [60] Rules for Construction of Nuclear Facility Components-ASME Boiler and Pressure vessels code - Section III. New York, US: The American Society of Mechanical Engineers; 2017.
 - [61] Kumar V, German MD, Shih CF. An Engineering Approaches for Elastic-Plastic Fracture Analysis. Rep EPRI/Electric Power Res Inst 1981.
 - [62] Nourpanah N, Taheri F. Ductile crack growth and constraint in pipelines subject to combined loadings. *Eng Fract Mech* 2011;78:2010–28.
 - [63] BS 7448-Fracture mechanics toughness tests: Part 4 Method for determination of fracture resistance curves and initiation values for stable crack extension in metallic materials,". London, UK: British Standards Institute,; 1997.
 - [64] Van Minnebruggen K. Experimental-Numerical Study on the Feasibility of Spirally Welded Pipes in a Strain Based Design Context (PhD thesis). Ghent University; 2016.
 - [65] Edwards BR, Russell JK. Distribution, nature, and origin of Neogene–Quaternary magmatism in the northern Cordilleran volcanic province, Canada. n.d.

Chapter 3

Flaw interaction

3.1. Introduction

Whenever two or more flaws are observed in structures, an evaluation of their interaction is part of the integrity analysis. Under the influence of an applied load, a small (and acceptable) flaw could grow and coalesce with an adjacent flaw. The interaction between flaws in cases of stress corrosion cracking, fatigue or severe plastic loading plays a dominant role in fracture behavior [1–4]. It should be taken into consideration that flaws may occur at different locations, not necessarily in the same plane, and with different shapes (See Figure 3-1). Therefore, a sound identification of flaw interaction comprises many influencing parameters.

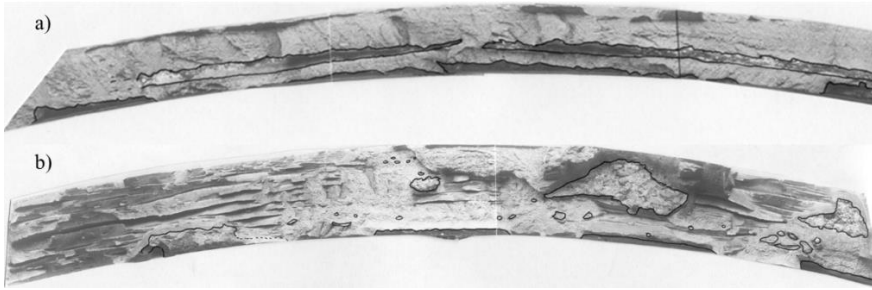


Figure 3-1: Coplanar adjacent flaws in API X65 pipe weldment made by a) Shield Metal Arc Welding (SMAW), b) Gas Metal Arc Welding (GMAW) (from Soete Laboratory’s archive).

Figure 3-2-a schematically shows two identical coplanar cracks in an infinite plate. The stress concentration effects of the cracks are represented by the lines of force. When the cracks are closer to each other, the ligament between the cracks shrinks in size and the area through which the force must be transmitted decreases. Consequently, the mode I stress intensity factor, K_I , will be magnified for each crack as the two cracks approach one another [5]. Contrarily, the interaction effect can also reduce the SIF due to a shielding effect, for example in parallel cracks as shown in Figure 3-2-b.

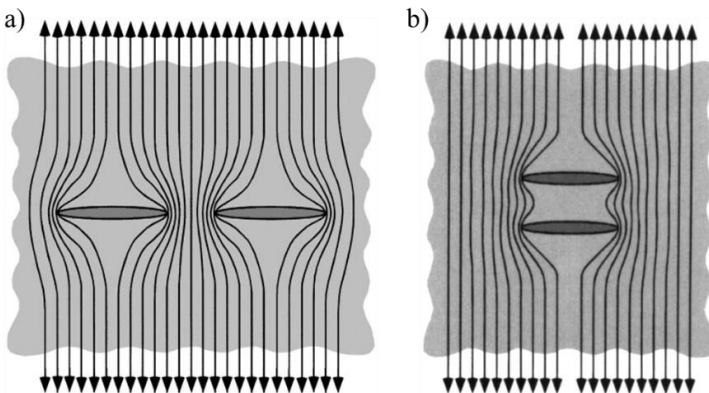


Figure 3-2: Effect of flaw interaction on stress concentration, for a) coplanar cracks, and b) parallel non-coplanar cracks [5].

In computational fracture mechanics and ECA guidelines through-thickness flaws are normally assumed to have a rectangular shape. Irregularly shaped planar flaws are replaced and idealized into a semi-elliptical (surface breaking) flaw or an elliptical (embedded) flaw. The dimensions of the (semi or total) ellipse are determined by the “bounding rectangle”, which is constructed around the flaw. According to the ASME B&PV Code sec. XI [6] and the British standard BS7910 [7], the rectangle should be constructed in such a way that its sides are normal or parallel to the component boundary. For surface breaking flaws, the idealized semi-ellipse minor and major axes end points match with a mid-point and two corners of the bounding rectangle. For an embedded flaw an ellipse is constructed whose major and minor axes end points coincide with mid points of the rectangle (See Figure 3-1). In cases that multiple flaws are located close enough to each other to interact, these flaws may be characterized into one encompassing single flaw.

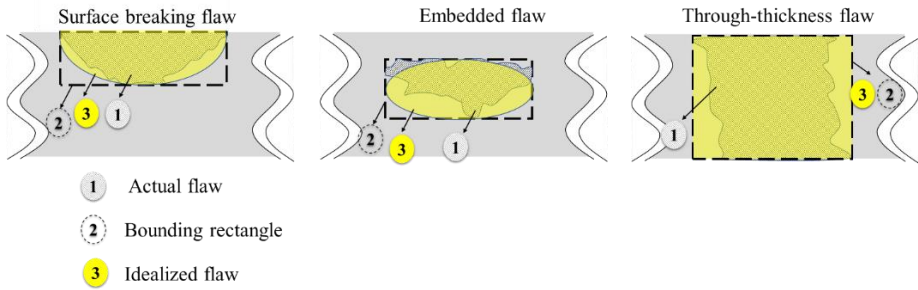


Figure 3-3: Flaw idealization.

The idealization of flaws is vital because of practical rationality, recognizing that most conventional NDT methods are not able to describe the detailed crack front profile. Furthermore, fracture mechanics solutions are only available for a selection of simple flaw shapes [5]. Ongoing improvements in NDT accuracy and advanced FE techniques, should allow a more realistic assessment of flaw severity in the near future. This will be illustrated in chapter 4.

Even though various codes, standards and guidelines are slightly different in addressing adjacent flaws, in general the following steps are considered to assess multiple flaws. When flaws are detected close to the free surface, surface-proximity rules are applied to check whether they should be converted into a surface breaking flaw (in case of embedded flaw) or a through wall flaw (in case of surface breaking flaw or embedded flaw), which are more amenable to analysis. Evaluation of interaction typically consists of a two-step procedure, i.e. a combination of alignment criteria and interaction (or combination) criteria. When flaws are located in different planes (referred to as non-coplanar, non-aligned, offset or parallel flaws), it should first be identified whether flaws are to be analyzed as non-aligned or may be treated as aligned (coplanar) according to the alignment rules. Subsequently, if the flaws are (treated as) aligned, they may be assessed as independent (non-interacting) or combined (interacting) flaws using combination criteria. Provided that interaction criteria are satisfied; multiple flaws may be “re-characterized” into an encompassing single flaw. This procedure is summarized in Figure 3-4.

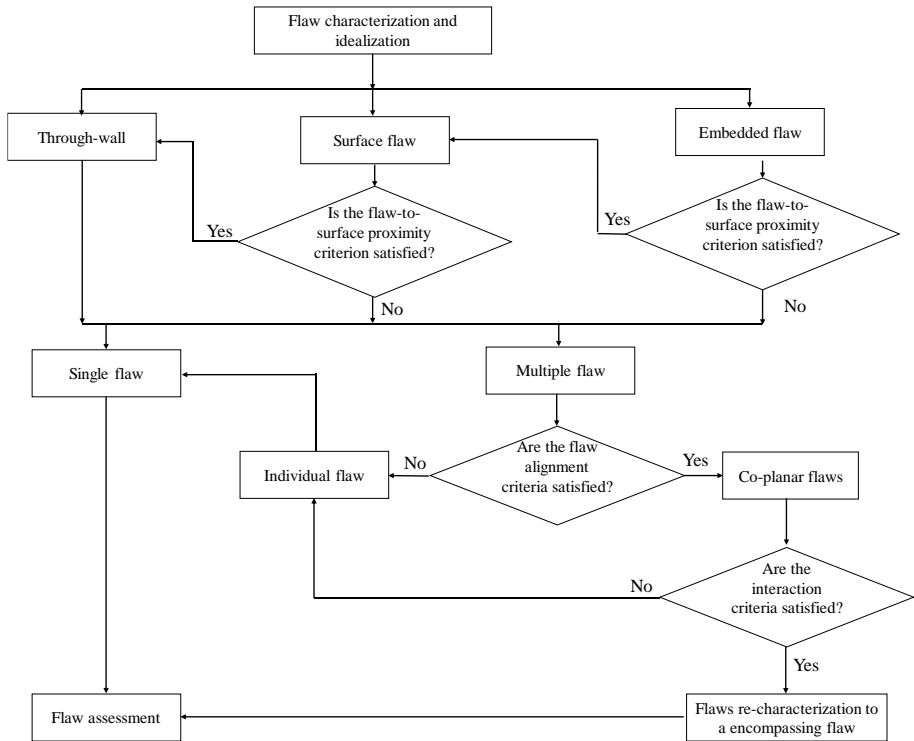


Figure 3-4: Flaw characterization flowchart.

3.2. (Comparison of) interaction rules in ECA guidelines

In this section interaction rules in ASME B&PV Sec XI, API 579/ASME FFS-1, BS7910, DNV-OS-F101, API1104 and CSA-Z662 are reviewed. The very first step in any flaw interaction assessment is the definition of alignment and interaction criteria to define which flaws are to be considered aligned and interacting. The parameters of these criteria can be related to flaw length, flaw depth, spacing between two flaws or a combination of these. According to recent versions of studied ECA norms/standards/guidelines it is not necessary to consider further interaction of a re-characterized flaw with other neighboring flaws. Suppose three neighboring flaws (A, B and C) were detected. If flaw B is interacting with both A and C, an encompassing flaw containing all of them should be considered. If flaw B is only interacting with A, then an encompassing flaw containing flaws A and B is assumed. However, the potential interaction of this (virtual) encompassing flaw with flaw C is not necessary to be evaluated.

This chapter reviews the flaw alignment, interaction and surface proximity rules in the most acknowledged ECA procedures for structural integrity assessments.

3.2.1. Alignment rules for non-coplanar surface flaws

Table 3-1 shows the alignment rules for surface breaking flaws of various international codes/standards; the rules for embedded flaws are similar. An overview of involved dimensions and their symbols is depicted at the top of this table.

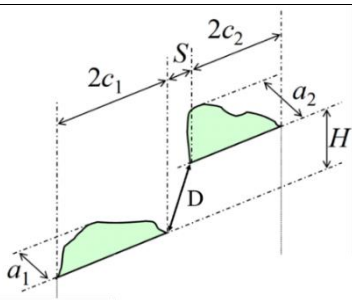
According to ASME B&PV Code sec. XI, flaws first should be projected on planes normal to the principal stresses (σ_1 and σ_2) to determine the most critical orientation for comparison with allowable indication standards. When the separation distance between the planes of the flaws is less than 12.5 mm, these flaws should be considered as coplanar (aligned). BS7910, however, suggests measuring the direct distance between adjacent flaws, project them on a plane normal to the principal stresses to determine their projected lengths and depths, and subsequently to compare these values with the direct distance. In API 1104:2013 [8] and CSA-Z662:2015 [9] the vertical distance H is compared to the sum of the flaw depths ($a_1 + a_2$). API 579:2009 required a comparison of horizontal (S) and vertical (H) distances with the sums of flaw semi lengths and flaw depths respectively. This guideline's rule has been changed in 2016 to comply with ASME and is now referred to as API 579/ASME FFS-1.

ASME B&PV Code section XI and API 579/ASME FFS-1 are the only guidelines where a fixed dimension is bluntly put forward as a criterion for alignment. API579 until its previous version (2009) used a different criterion based on the sum of the flaw lengths, and just in its recent version changed the criterion to comply with ASME section XI. Reviewing the history of changes in ASME section XI during past versions revealed the following. In the very first version published in 1970, the rule required that two flaws to be treated as a single planar flaw if the distance between flaw planes was less than total depth dimension of the larger flaw, the same criterion was applied for distance between the two tips of the coplanar flaws [10]. In 1977, when sec. XI was enormously updated (the first version was just 70 pages), the criterion of alignment changed to the present 12.5 mm (0.5 inch) and remains as it is to date [11]. As described in EPRI-NP-1406 [11], this change has been applied to recognize potential flaw growth behavior in service, which may result in a single planar indication upon enlargement of the individual indications. An earlier report from EPRI (NP-719-SR) stated that for two equal flaws, by applying the previous criterion based on depth, the raise in K_I due to interaction could be slightly higher for non-coplanar flaws than for coplanar flaws.

Another possible reason for this change is the limitations of ultrasonic testing (UT) capabilities in the 1970s, although this has not explicitly been mentioned. As noted by Lacroix [12], due to a similar reason which is explicitly mentioned in EPRI-NP-1406 [11], the interaction criterion of laminar flaws³ is a fixed value as well. If the projected distance between these flaws becomes less than 25.4mm (1 inch) they are considered as interacting by ASME B&PV Code section XI.

³ According to ASME B&PV code sec. XI, laminar flaws are planar indications oriented within 10 degrees of a plane parallel to the surface of the component.

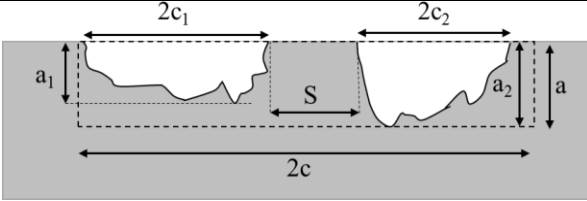
Table 3-1: Alignment rules in various ECA guidelines.

		
Standard/ Code/ Guideline:	Criterion (flaws should be aligned if)	Action (if flaws are aligned)
BS7910:2013+A1:2015 DNV-OS-F101:2012	$D \leq a_1 + a_2$	Flaws should be projected onto the same plane and assessed as coplanar.
API1104:2013 CSA-Z662:2015	$H \leq a_1 + a_2$	
ASME B&PV Sec XI:2017 API 579/ASME FFS-1:2016	$H \leq 12.5 \text{ mm (0.5 inch)}$	

3.2.2. Coplanar surface breaking flaws

Interaction of coplanar surface-breaking flaws is particularly relevant to damage mechanisms such as stress-corrosion cracking, fatigue and various types of weld cracks. ECA standards, codes and guidelines typically provide criteria solely based on flaw dimensions. Table 3-2 indicates large discrepancies between different rules.

Table 3-2: Coplanar flaw interaction criteria in various ECA guidelines.

		
Standard/ Code/ Guideline:	Criteria (interaction occurs if)	Re-characterized dimension (if deemed to interact)
BS7910:2013+A1:2015 DNV-OS-F101:2012	$S \leq 2c_1$ for a_1/c_1 or $a_2/c_2 > 1$ $S \leq \max. \{0.5a_1, 0.5a_2\}$ for $a_1/c_1 < 1$ and $a_2/c_2 < 1$	$a = \max (a_1, a_2)$ $2c = 2c_1 + 2c_2 + S$
API1104:2013 CSA-Z662: 2015	$S \leq 2c_1$ for $c_1 < c_2$ and $a_1 < a_2$	
ASME B&PV sec. XI:2017 API 579/ASME FFS-1:2016	$S \leq \max \{0.5a_1, 0.5a_2\}$	
EPRG Guidelines:2014 (Tier 2)	$2c_1 + 2c_2 \leq L_2$ $L_2 = \frac{tW}{a_{\max}} \left[1 - M \left(1 - \frac{\sum s_i a_{\max}}{tW} \right) \right]$	

Many of the abovementioned guidelines have been prone to changes upon document revisions. Among them, BS7910 and ASME B&PV Code section XI have longer histories and have more wide applications. The British flaw assessment procedure BS 7910 has now been in use for over 20 years and it evolved from the PD6493 which has been first published in 1980 and revised in 1991. In 1999 the British Standard BS7910 was first published and essentially utilized most of the PD6493:1991 procedures with updates to reflect the growing state of knowledge. A minor revision of BS7910 was published in 2005 and then in 2013 the latest version was published which contains considerable modifications compared to previous versions. During the development of the BS7910 and its predecessor, PD6493,

different modifications have been made on the flaw interaction criteria for surface breaking flaws, while the criteria for embedded flaws mostly remained unchanged. Table 3-3 outlines the criteria for surface flaws interaction in different releases of PD6493 and BS7910.

Table 3-3: History of modifications to coplanar flaws interaction criteria in BS7910 and PD6493.

Revisions in which the rules were updated	The updated criteria for surface flaws
PD 6493: 1980- First publication	$S \leq 0.5(2c_1+2c_2)$
PD 6493: 1991	$S \leq 2c_1^*$
BS7910: 1999 - First publication	$S = 0$ (for $a/c < 1$) $S \leq 2c_1^*$ (for $a/c > 1$)
BS7910: 2013	$S \leq 0.5a_2^*$ (for $a/c < 1$) $S \leq 2c_1^*$ (for $a/c > 1$)

* $a_1 < a_2$ and $c_1 < c_2$

The basis for the interaction criterion used in the 1980 version of PD6493 was a 20% increase in the stress intensity factor of the first flaw due to the presence of a second flaw. According to diagrams provided in the document, the second flaw was assumed to be the larger of the two. The interaction criterion was based on linear elastic solutions [13].

To reduce conservatism, the PD6493 adopted the criterion based on the shorter of the two flaw surface lengths in 1991. In BS7910:1999 the criterion was further relaxed by allowing the adjacent flaws to touch prior to performing flaw re-characterization for coplanar surface-breaking flaws with a low aspect ratio ($a/c < 1$). This concept appears to be justified for adjacent cracks growing under fatigue loading. Nevertheless, due to inherent complexity in other failure modes such as ductile failure and cleavage, the BS committee decided to harmonize the flaw interaction rules with those of FITNET and section XI of the ASME B&PV Code by altering the criterion from $S = 0$ to $S = 0.5(\max\{a_1,a_2\})$ in BS7910:2013, i.e. interaction is assumed once the separation distance is less than half of the maximum flaw depth.

Some other highlighted modifications in past decades in this regard are about second order interaction criteria and un-inspectable regions. Second order interaction criteria in the 1980 and 1991 revisions of PD6493 required and interaction assessment of the re-characterized flaw with other neighboring flaws. This requirement is no longer in the BS7910:1999 and later editions. Guidance on un-inspectable regions was given in PD 6493:1980 and 1991 and is no longer stated in BS7910:1999 and later

revisions. The guidance required that the assumption of a flaw size equal to the size of the un-inspectable region should be made [13].

In its 2013 version, BS7910 has additional flaw depth and length characterization restrictions for high strength and low toughness steels. These requirements were added in 2013 based on results by Bezensek et al. [17], which showed the bounding flaw might not provide sufficient conservatism when cleavage fracture is a concern. Based on this set of rules, the maximum depth of the flaw for surface flaws or the larger of the two orthogonal flaw dimensions for embedded flaws should be compared with the simplified calculation of Irwin's plastic zone size. If the maximum flaw depth or the larger of the two orthogonal flaw dimensions is less than Irwin's plastic zone size, then the normal assessment procedure is followed. Otherwise, either the actual flaw remains intact and its SIF is increased by 10%, or flaw length and depth are increased by 20%, or calculated tolerable flaw size should be reduced by 20% in both length and depth.

ASME B&PV Code sec. XI was first published in 1970 to regulate in-service inspections in nuclear power plants. ASME section XI criteria for flaw interaction have been updated a few times. Initially the distance between coplanar surface flaws was compared to two times the maximum flaw depth, and if the distance was equal or less, the flaws were treated as interacting. Later, this criterion was reduced to the maximum flaw depth in 1998. Hasegawa et. al. [14] in 2001 showed that even this released criterion is over-conservative since it puts the threshold on stress intensity factor (SIF) increase at 8% for dissimilar adjacent flaws and around 5% for similar adjacent flaws. They argued that since ASME B&PV Code sec. XI already allowed an 18 to 25% increase in SIF at subsurface to surface flaw proximity rules, a 10 to 15% increase for two similar surface flaws is a more appropriate criterion. Accordingly, in the 2003 version, the ASME criterion was updated to compare the distance between the flaws to half the flaw depth instead of the whole depth. Table 3-4 compares ASME B&PV Code sec. XI criteria for coplanar surface flaws in various editions. Hasegawa et. al. [14] also suggested that in fatigue analysis interaction should not be considered. This made another difference between ASME and BS; whilst ASME XI IWA-3000 states that the combination of multiple planar flaws is not required for fatigue or stress corrosion cracking, BS7910 states that combination is only not required for fatigue assessments. Moreover, ASME B&PV Code sec. XI specifies that the effective dimensions for flaws will be based on the containment rectangles surrounding them and has additional restrictions on their aspect ratios. The flaw depth to length ratio of the containment rectangle should be less than or equal to 0.5, otherwise the flaw is considered unacceptable and there is no need for further investigation. Yet, such flaws can be assessed by BS7910.

Table 3-4- History of modifications to coplanar flaws interaction criteria in ASME B7PV Code section XI.

Revisions in which the rules were updated	The updated criteria for surface flaws
ASME sec. XI:1970- First publication	$S \leq \max (2a_1, 2a_2)$
ASME sec. XI:1998	$S \leq \max (a_1, a_2)$
ASME sec. XI:2003	$S \leq \max (0.5a_1, 0.5a_2)$

API1104 rules for coplanar flaws have been revised in the 2008 addendum. This change is applied in the criterion for the longitudinal spacing between two flaws. In the prior version, two flaws were considered as interacting if the space between them was less than the sum of the half flaw lengths. In the last version the interaction criterion is satisfied if the space between two flaws is less than the shortest flaw length.

All of API579/ASME FFS-1 combination (interaction) and alignment rules have been updated in 2016 to comply with ASME B&PV Code section XI. It should be noted that as per clause 9.3.6.3 a) from API579 2nd edition, if the depth of the feature is unknown then a conservative assumption is that the effective flaw depth is equal to the component thickness ($a = t$). In addition, a crack with an angle (θ) relative to the principal plane for Mode I orientation, the crack should be first projected onto the principal plane and then modified with a correction factor that depends on the angle, $W(\theta)$. Values for $W(\theta)$ range between 1.0 and 1.2. Another specific rule in API579 is for networked and branched cracks; a rectangular box is drawn around the entire area and the length of this box is projected onto the principal plane for Mode I orientation. The depth is the maximum measured depth multiplied by a factor of 1.2. API579/ASME FFS-1 also states that multiple flaws do not have to be combined into an equivalent flaw for evaluation if a stress intensity factor and limit load solution can be obtained for the interacting flaw geometries.

The EPRG Tier 2 “guidelines on the assessment of flaws in transmission pipeline girth welds” [18] are significantly different compared to other ECA guidelines when it comes to assessing flaw interaction. This guideline provides rules for the interaction of coplanar surface breaking flaws and ductile material behavior by the performance requirement of remote yielding or plastic collapse. Failure by plastic collapse is only controlled by the geometrical parameters and the strength properties of the material; increased toughness beyond a toughness threshold does not further increase the allowable flaw size limit. Besides, plastic collapse assessments relate the initial flaw size to the applied stress. In other words, in determining the allowable flaw size for plastic collapse no allowance is normally made for ductile crack growth [19]. The EPRG guidelines for interaction are available for coplanar surface flaws only.

To sum up, it can be concluded that interaction rules which were developed based on LEFM inherently consider brittle failure mode. Therefore, these codes/standards

are essentially based on Stress Intensity Factor (SIF) variation due to interaction, and toughness has the main role in their assessment. On the other hand, the EPRG Tier 2 guidelines assume ductile material behavior so it is applicable only above a certain toughness threshold ($CTOD_{min} \geq 0.10$ mm and $CTOD_{avg} \geq 0.15$ mm or $CVN_{min} \geq 30$ J and $CVN_{avg} \geq 40$ J, based on a minimum of three tests). Hereby, $CTOD$ refers to the fracture toughness of a three-point bend specimen and CVN refers to the (full-size equivalent for sub-sized specimens) impact energy of a Charpy V-notch specimen. It should be noted that since the EPRG interaction criteria have been developed based on experimental results, in addition to toughness requirements it has other limitations for material properties and loading level [18]. To assess the interaction between multiple adjacent flaws based on EPRG Tier 2, the sum of the individual flaw lengths ($\sum C_i$) should be compared with one of two characteristic flaw lengths L_1 (Option A) or L_2 (Option B), the latter being calculated according as follow:

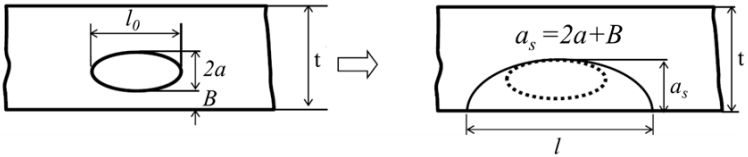
$$L_2 = \frac{tW}{a_{max}} \left[1 - M \left(1 - \frac{\sum s_i a_{max}}{tW} \right) \right] \quad 3-1$$

Where a_{max} is the maximum flaw depth, t is the wall thickness, $\sum s_i$ is the sum of spacing distance between flaws, and W is the width of the specimen. M is a correction factor, which depends on the flaw depth and ensures that L_2 reduces to the length limit of an isolated (single) flaw when the flaws touch and $S=0$ (in the present study M is taken 0.933 which corresponds to $3 \text{ mm} < a_{max} \leq 4 \text{ mm}$).

3.2.3. Coplanar surface and embedded flaws

Embedded flaws are normally less critical than their surface counterparts. However, if an embedded flaw is detected sufficiently close to the component's (free) surface, it should be treated as a surface flaw. Table 3-5 shows the proximity rules for this transformation in various ECA guidelines. Generally, they follow the same logic but have different expressions. The reason for the transformation is the mechanical interaction between the flaw and the free surface of the component that can lead to ligament failure. When the embedded flaw comes close to the free surface, the SIF at the ligament side (closer to the surface) becomes higher than that at the opposite side of the embedded flaw due to stress concentration. Therefore, it is reasonable to expect that initiation of failure of the component will occur at the ligament of the embedded flaw. Hence, below a certain threshold ligament size, the embedded flaw located close to the free surface should be conservatively transformed to a surface flaw.

Table 3-5- Flaw to surface proximity rules in various ECA guidelines.

		
Standard/ Code/ Guideline:	Condition	Flaw length transformed
BS 7910:2013	If ligament failure is predicted (Annex E)	$l = 2a + B + l_0$
ASME sec XI:2017	$B/a < 0.4$	$l = l_0$ if $a/l_0 < 0.5$ $l = 2(2a + B)$ if $a/l_0 \geq 0.5$
API 579/ASME FFS-1:2016	$B/t < 0.2$	$l = 2B + L_0$
API1104:2013	$B/a < 1.0$	$l = l_0$

BS7910 [7] has no specific criterion for the distance to the surface (B); when ligament failure is predicted to occur by local yielding or ductile/brittle mechanism, the subsurface flaw is transformed to a surface flaw. Therefore, the user assessment determines the critical distance B . ASME B&PV Code section XI and API1104 suggest comparing the distance B to the flaw depth; the API 579 criterion is based on a comparison with component thickness. The transformed flaw lengths are also different depending on the guideline; the maximum is ($L = 2a + L_0 + B$) for BS7910. In ASME B&PV Code section XI, the latter equation for the transformed length means that when the flaw aspect ratio is greater than 0.5, the transformed surface flaw is always a semicircular flaw.

When an embedded flaw is detected sufficiently far from the surface, thus avoiding its recategorization into a surface flaw, still its interaction should be assessed with an adjacent surface breaking or other embedded flaw. Table 3-6 compares various criteria for interaction between an embedded and a surface flaw. The difference between BS7910 ($a/c < 1$) and ASME B&PV Code section XI is noteworthy. The former uses the depth of the surface flaw while the latter uses the semi depth of the surface flaw when it comes to interaction with an embedded flaw.

In other words, BS7910 may yield a more conservative assessment in case of interaction between embedded flaws and either a surface flaw or another embedded flaw. These rules in ASME B&PV Code section XI were revised in late 1990’s and early 2000 (as well as those for two surface breaking flaws), considering results of Hasegawa et. al [14] that showed that a criterion based on a surface flaw’s semi depth is more suitable.

Table 3-6- Coplanar surface and embedded flaws interaction rules in various ECA guidelines.

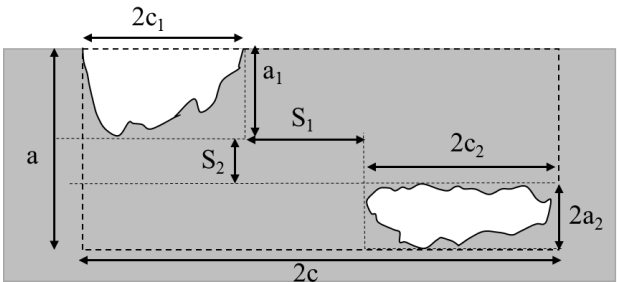
		
Standard / Code / Guideline:	Criteria (interaction occurs if)	Re-characterized dimension (if deemed to interact)
BS7910:2013 DNV-OS-F101:2012	$S_1 \leq \max(a_1, a_2)$ for a_1/c_1 and $a_2/c_2 < 1$ $S_1 \leq 2c_1$ for a_1/c_1 or $a_2/c_2 > 1$ and $S_2 \leq a_1 + a_2$ ($c_1 < c_2$)	$a = a_1 + 2a_2 + S_2$ $2c = 2c_1 + 2c_2 + S_1$
API1104:2013	$S_1 \leq 2c_1$ and $S_2 \leq a_1 + a_2$ ($c_1 < c_2$)	
ASME sec XI:2017 API 579/ASME FFS-1:2016	$S_1 \leq \max(0.5a_1, a_2)$ $S_2 \leq \max(0.5a_1, a_2)$	

Table 3-7 compares the interaction rules for two embedded flaws. Such flaws are the most detected flaws in pipeline welds [20]. This configuration is normally assumed as the least critical interacting flaw pairs. In addition, due to experimental challenges in creating embedded flaws for investigation purposes, very few literatures have been found with respect to this configuration.

Table 3-7-Coplanar embedded flaws interaction rules in various ECA guidelines.

Standard/ Code/ Guideline:	Criteria (interaction occurs if)	Re-characterized dimension (if they are deemed to interact)
BS7910:2013 DNV-OS-F101:2012	$S_1 \leq \max(a_1, a_2)$ for a_1/c_1 and $a_2/c_2 < 1$ $S_1 \leq 2c_1$ for a_1/c_1 or $a_2/c_2 > 1$ and $S_2 \leq a_1 + a_2$ ($c_1 < c_2$)	$2c = 2c_1 + 2c_2 + S_1$ $2a = 2a_1 + 2a_2 + S_2$
API1104:2013	$S_1 < 2c_1$ and $S_2 < a_1 + a_2$ ($c_1 < c_2$)	
ASME sec XI:2017 API 579/ASME FFS-1:2016	$S_1 \leq \max(a_1, a_2)$ $S_2 \leq \max(a_1, a_2)$	

3.3. Highlighted researches on flaw interaction

3.3.1. Non-coplanar adjacent flaws

In recent years various researchers have studied non-coplanar adjacent flaws in different geometries and loading conditions utilizing various approaches. These studies showed that the stress intensity factor changes due to the interaction between the flaws and the magnitude of this change depend on the spacing distance between flaws as well as their sizes and shapes [21–24]. Hasegawa et al. [25] employed finite element analysis to calculate stress intensity factors for through-wall, non-aligned and non-equal flaws. Additionally, they performed brittle fracture experiments at -196°C on structural steel plates ($t = 5.7$ mm) to test similar configurations. They concluded that a 6% increase in stress intensity factor could be considered as a boundary between

aligned and non-aligned flaws, since experiments revealed that above this increase the crack path was influenced by the presence of the second flaw. This confirmed the results of EPRI report No. NP-719-SR [10], which also concluded that the increase in SIF for interacting flaws according to the first criterion of ASME B&PV Code section XI (which was based on flaw length, see 3.2.1) was always less than 6%, regardless of the relative position of the flaws (overlapping or non-overlapping). Hasegawa et al. [25] concluded that when it comes to flaw alignment rules in Linear Elastic Fracture Mechanics (LEFM), the out-of-plane distance is a more important factor than the in-plane distance for coalescence or non-coalescence of flaws [25]. In other words, the occurrence or not of fracture path coalescence is governed by H rather than S . Based on these results, they suggested an alternative criterion for non-coplanar surface breaking flaws, which considers the flaws are aligned if the vertical spacing distance between them becomes less than the minimum of their lengths ($H \leq \min(2c_1, 2c_2)$).

Bezensek and McCulloch [26] also studied J -integral values (using elastic-plastic FEM) for multiple non-aligned through-wall flaws in flat plates based on the abovementioned study by Hasegawa et al. They observed that the largest interaction was for geometries with $S \approx H$ (when the flaws are in 45-degree configuration).

Kamaya [27,28] conducted an elastic-plastic finite element study of a flat plate and a pipe segment with two non-aligned flaws under tensile and bending loads. The results showed that the present alignment rules in ASME B&PV Code section XI in elastic and elastic-plastic conditions correspond to the magnitude of the interaction ratio $K/K_0 = 1.07$ and $(J/J_0)^{0.5} = 1.12$, respectively (K_0 and J_0 represent crack driving forces in a single flaw specimen for elastic and elastic-plastic conditions respectively). Kamaya proposed a new criterion depending on flaw depth for the alignment assessment ($H \leq \max(0.8a_1, 0.8a_2)$).

Lacroix et al. [29] employed the 6% threshold proposed by Hasegawa et al. for studying the interaction of quasi laminar flaws, which are geometrically quite similar to non-coplanar flaws but less detrimental compared to surface breaking flaws. They used 2D and 3D FE simulations to model laminar and quasi laminar flaws resembling those detected in nuclear power plants and suggested an alternative rule (ASME Code Case N-848 Alternative Characterization Rules for Quasi-Laminar Flaw), which is more suitable for realistic flaws.

Although there are only limited references available for the technical background of many of the interaction criteria in ECA guidelines, they have typically been based on (LEFM) for the sake of simplicity and intended towards conservativeness. Nonetheless, the application of these procedures might be questioned when applied to failure modes other than brittle fracture [30]. For instance, in contemporary pipelines failure by brittle fracture can be excluded considering that the toughness of the material (weld metal and HAZ) is sufficiently high to ensure that plastic collapse is the governing failure mode.

Hasegawa et al. [31] in 2009 conducted a remarkable study to validate alignment rules of various ECA guidelines based on their plastic collapse stress. In this study, bending tests were performed on 4-inch (100 mm) diameter stainless steel pipes with 8.6 mm thickness containing two identical circumferential non-aligned and aligned flaws. Fully plastic collapse bending stresses, without internal pressure, were

obtained from the experiments. From the comparison of the experimental and calculated plastic collapse stresses, it could be concluded that some alignment rules give overly conservative and others give un-conservative evaluations. The authors suggested that the alignment rule for plastic collapse assessment based on the proportion of flaw lengths gives a conservative assessment.

Hasegawa et al. [32] in 2010 studied the maximum bending load of 2 and 4 inch ferritic and stainless steel pipes containing two identical non-coplanar flaws with $a/t=0.5-0.8$ in 4-point bending tests. They stated that the reported maximum loads correspond to the plastic collapse loads estimated by limit load solutions. They concluded that for the same circumferential spacing distance S , the maximum load increases with increasing axial distance H for short and deep flaws. However, the maximum load is unaffected by H for long and shallow flaws. This can be due to the fact that when flaw shapes are short and deep, maximum load occurs after the flaws penetrate the outer wall of the pipes (implying significant crack growth). On the contrary, if flaws are long and shallow, maximum load occurs at the point when the flaws penetrate the outer wall of the pipes (See Figure 3-5). The authors also showed that for shallow flaws, the crack initiates at the deepest point of the initial surface flaw and grows in the thickness direction. As the crack does not grow in the circumferential direction, the interaction between two non-aligned flaws at maximum load seems to be low. Therefore, it is suggested that the maximum load for these flaws is not affected by their axial spacing H , even when H is marginal. In another study Hasegawa et al. [33] in 2011 studied two dissimilar non-aligned through wall flaws in a plate subjected to a uniaxial tension test. They have observed that the offset flaws are not sensitive to alignment rules when the two flaw sizes are significantly different. In other words, the collapse load does not show abrupt transition at $H = 12.5$ mm as suggested by ASME B&PV Code section XI.

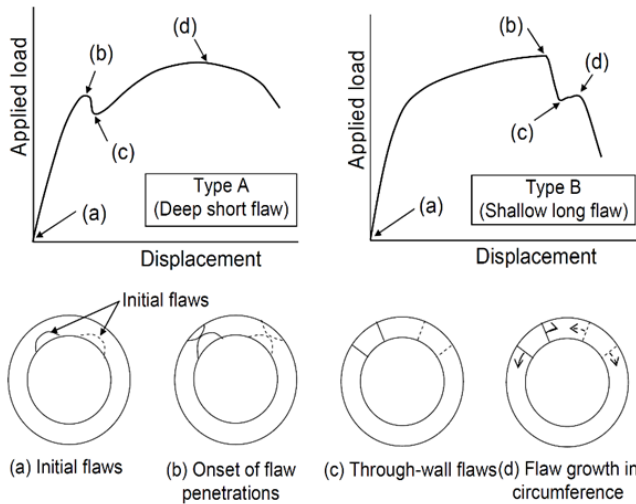


Figure 3-5: Load-displacement curve for a pipe with two non-coplanar flaws, from Hasegawa et al. experiments [32].

Miyazaki et al. [34] in 2011 studied the ductile fracture behavior of two non-aligned surface flaws in stainless steel plates subjected to a uniaxial tensile test. They concluded that for shallow cracks ($a/t=0.4$) the maximum loads were found to be unaffected by H for long and shallow flaws. However, for deep cracks ($a/t=0.8$) the maximum loads were found to increase with increase in H . It can be concluded that the behavior concerning the penetration of flaws at the maximum load in case of shallow flaws, is similar to Hasegawa's observations.

Iwamatsu et al. in 2013 [35] performed fracture tests on a flat plate with two non-aligned through-wall flaws. First, they concluded that whether coalescence occurs or not is insignificant in terms of evaluating the maximum load for plastic collapse, while the distance between flaws affects the maximum load irrespective of flaw growth behavior. They suggested that criteria based on 1.5 times the maximum flaw length or 2 times the average of flaw lengths are appropriate for plastic collapse assessments (for H and/or S). In 2018 Iwamatsu et al. [36] suggested an area ratio criterion. In a nutshell, it is based on comparing the net section of the longer flaw (A_s) with the non-aligned net section (A_m), see Figure 3-6. If the latter is larger than the former ($A_m/A_s > 1$) the notches are not interacting and if $A_m/A_s < 1$ the notches are interacting. As depicted in Figure 3-6, this is in agreement with experimental results, in which the plastic collapse load of a plate with single notch (P_s) has been compared with this of a plate with two non-coplanar notches.

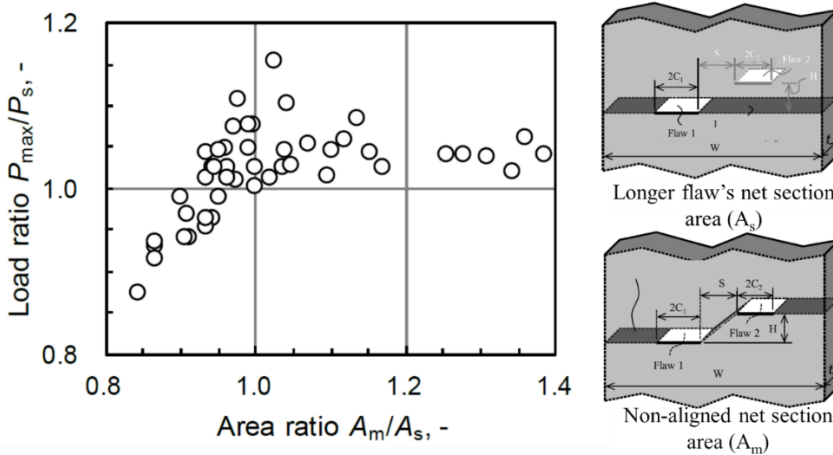


Figure 3-6: Experimental results supporting Iwamatsu's method to assess the limit load of two non-coplanar adjacent notches [36].

These findings make it clear that as far as plastic collapse is concerned, the collapse load is not affected by the vertical distance between flaws (H) in case of shallow flaws. In other words, the load is determined by the cross-section reduction of two (or more) flaws, although it is not intuitively clear on which plane the flaws should be projected. In case of deep flaws, however, the crack driving force is affected by the adjacent flaw and crack growth causes ligament failure. Therefore, before global plastic collapse occurs, the ligament failure reduces the load capacity of the specimen and in this way the collapse load is affected by H in case of deep non-aligned flaws.

As far as crack growth behavior is concerned, the experimental results of Iida and Kawahara [37], also confirmed by Kamaya [3], showed that when two parallel and adjacent surface cracks in a plate grow by fatigue they can curve to join directly at the surface (from a macroscopic viewpoint) or grow past each other and curve to join underneath the surface, or, because of the finite specimen size, grow past each other without joining before specimen failure. The curvature occurs due to interaction not only affecting K_I , but also mode II K_{II} . However, as Bezensek [38] argued, this comparison is not always correct, and that may explain the non-conservatism observed in the experiments by Hasegawa et al. [31]. Under fatigue conditions, plasticity is confined to the crack tip and neighboring flaws behave independently to much closer flaw separations such that the problem is driven largely by the elastic stress field. Conversely, in ductile tearing crack extension occurs in full plasticity and the fracture mechanism is predominantly strain driven.

3.3.2. Coplanar adjacent flaws

Many researchers have put their interest in coplanar surface flaws. Although analytical and theoretical solutions for single cracked specimens have matured in past decades, due to the vast possible combinations generic analytical solutions have not fully developed for multiple adjacent cracks. The analysis of interacting cracks in a linear elastic material has developed the most thanks to the capabilities of computational stress analysis [39]. The most important early work used a ‘body force’ method of analysis based on equivalent Eshelby-type ellipsoidal inclusions [40,41]. Zeng et al. [42] used the line-spring analysis developed by Rice and Levy [43] coupled with the boundary element method to analyse pairs of identical surface cracks.

For such a complex problem, the finite element method has proven to be a very suitable technique, although it requires more severe computational efforts compared to analytical approaches like body force and line-spring methods. Early applications of finite element analysis for flaw interaction are presented by Soboyejo et al. [44], Stonesifer et al. [24] and Yoshimura et al. [45]. In recent years, finite element studies have been used by many researchers to compute the SIF ratio of one of two adjacent cracks to that of a single isolated crack. For instance, works by Sethuraman et al. [46] and Carpinteri et al. [47] showed that the magnitude of the interaction between two adjacent cracks depends strongly on the distance in between them and quickly becomes insignificant as this distance is increased. Coules [39] studied multiple combinations of coplanar semi-elliptical cracks with differing size and aspect ratio. Results show that in most cases, the greatest value of K_I on the crack front is not increased significantly. Interaction mainly affects regions of the crack front which are less severely loaded (low K_I). In addition, the elastic interaction magnitude depends on the distribution of stress that acts on the adjacent cracks. Since flaw interaction criteria used in current integrity assessment procedures are independent of loading mode, there might be a risk of non-conservative interaction classification when through-thickness loading effects are overlooked.

In another remarkable research, Bezensek and Hancock [16] studied coplanar flaws when the failure mode is cleavage (low toughness materials). They concluded that the characterization procedure of BS7910:2005 was marginally non-conservative for conditions when small amounts of plasticity develop in the tip-to-tip ligament. These results have been used to update BS7910 in 2013, and further consideration

have been advised to compare the material's capacity for crack tip plasticity in low toughness, high strength materials (see 0 for more details about these updates).

While all the above cited researches are based on linear elastic modelling of interacting crack pairs and/or experimental observations of fatigue crack growth, very limited literature is available on flaw interaction within the elastic-plastic assumption. De Waele et al. [19] experimentally studied interaction of multiple coplanar flaws in pipeline girth welds under the plastic collapse condition. The results supported the European Pipeline Research Group (EPRG) criteria for assessment of multiple weld flaws, which is supposed to be one of the first published guidelines for flaw interaction assessment considering plastic collapse [18]. Recently, Coules [48] studied flaw interaction in pressurized pipe by FE analysis and failure assessment diagram (FAD) following the R6 procedure [49]. Results show that more severe interaction occurs under elastic-plastic conditions, using a J -integral based interaction factor, compared to linear elasticity. Moreover, based on the FAD approach some non-conservative assessments using BS7910 and R6 have been detected. These observations led to conclude that these criteria do not conservatively predict the initiation of ductile tearing in all realistic cases. Nonetheless, Coules argued that these potential non-conservatisms under elastic-plastic conditions might be compensated by conservatism embedded in other aspects of an assessment, specifically:

- a rising material J-R curve might cause tearing to arrest after a small amount of crack growth;
- constraint loss in the region in between the flaws would inhibit fracture here [17];
- estimates of the limit load used in a FAD analysis might provide some conservatism.

3.4. Strain-based flaw interaction

When it comes to strain-based flaw interaction, the complexity of the problem is significantly increased. In stress-based design, the fracture assessment methodology is consistent with the assumption of small-scale yielding, i.e. crack driving force is well defined and applied for fracture assessment. Given that small scale yielding is assumed, flaw interaction will lead to an increase of crack driving force characterized by the SIF or J -integral. Considering that the spacing distance between adjacent flaws controls the magnitude of interaction, the flaw interaction rules for stress-based design generally define a critical distance for combining the adjacent flaws into a single flaw. In strain-based design, however, plastic deformation and ductile tearing are part of the design scenario. Inherently, two main tensile limit states can be defined, i.e. fracture (onset of ductile tearing instability) and plastic collapse.

The fracture limit state is generally associated with significant stable tearing and localized plastic deformation in crack ligaments conforming to large-scale yielding conditions. Under such large-scale yielding conditions, conventional crack driving force is not well defined and cannot fully capture the interaction of plastic deformation fields around the flaws. A proper criterion for strain-based design should tolerate some safe amounts of crack growth, while keeping eyes on the plastic collapse limit state.

A strain-based flaw interaction procedure was recently presented by Tang et. al [4], as part of ExxonMobil's research on strain-based design and assessment practices. They developed an FE model verified by a series of full-scale bend tests on X60 pipes having a 16-inch outside diameter and containing coplanar surface notches. The tensile strain capacity (TSC) of the pipes was calculated for various combinations of adjacent flaws using finite element analysis and based on the results they suggested an equivalent depth and length calculation. The suggested equivalent length limit goes towards the sum of the lengths of adjacent flaws when the separation distance reaches zero, and it goes towards the largest flaw length when the separation distance tends to infinity (no interaction). With this arrangement, the authors did overcome an inherent limitation of conventional flaw interaction procedures which require the addition of the spacing distance to the re-characterized flaw length. In other words, when the flaws are interacting and the spacing distance increases, the re-characterized flaw length will increase. This is not physically realistic since as flaws become separated with a greater distance, they interact less.

The final equations of Tang et al. [4] for equivalent depth (a_e) and equivalent semi length (c_e) are:

$$a_e = \frac{c_1 \cdot a_1 + c_2 \cdot a_2}{c_1 + c_2} \quad 3-2$$

$$\frac{c_e}{c_1 + c_2} = 1 - \frac{c_1}{c_1 + c_2} \tanh \left[A \left(\frac{s}{c_1 + c_2} \right)^B \right] \quad 3-3$$

Where both A and B are first-order polynomials with the forms:

$$A = \alpha_1 \frac{a_e}{c_1 + c_2} + \alpha_2 \frac{a_e}{t} + \alpha_3 \frac{D}{t} + \alpha_4 \quad 3-4$$

and

$$B = \beta_1 \frac{a_e}{c_1 + c_2} + \beta_2 \frac{a_e}{t} + \beta_3 \frac{D}{t} + \beta_4 \quad 3-5$$

As shown in Table 3-8, there are 8 coefficients in equation 3.3 and 3.4 which are determined by fitting equation 3.2 to FE results.

Table 3-8- Coefficients of flaw interaction rules for equation 3.3 and 3.4 [4].

α_1	α_2	α_3	α_4
-3.118	-4.079	-0.018	2.3176
β_1	β_2	β_3	β_4
-0.602	5.6423	0.000085	-0.768

Although the above described procedure has a unique approach to flaw interaction and is considered as the first strain-based procedure, it has some limitations. First of all, the equation is developed based on results from limited

geometrical parameters (OD=16 inch (406 mm) and 48 inch (1219 mm), $t=0.625$ inch (15.77 mm) and 1 inch (25.44 mm), $2c = 25, 50, 75$ mm and $a = 3, 4, 4.5$ mm). Secondly, although they are presented as closed form solutions, still they are quite complicated. Thirdly, since the results are based on few material properties, the effect of material strain hardening properties and phenomena like Lüders plateau on the results remain unknown. Nonetheless, their results indicated that equivalent flaw depth and length are not affected by weld overmatch, ductile tearing resistance and tensile properties. Also, the effect of misalignment is not considered in these results.

3.5. Conclusion

In this chapter an overview of the latest status of flaw interaction procedures in the most important ECA procedures from different application fields (including pipelines, boilers, pressure vessels and standards of generic nature) have been presented. Although there is a growing consensus among these guidelines, pronounced differences remain between their interaction rules. This chapter reviewed some important updates in ECA procedures during the past 40 years, clearly illustrating that flaw interaction is an active field of research.

A selection of researches with strong impact in this regard have been reviewed. Due to the fact that most flaw interaction procedures were developed based on linear-elastic fracture mechanics, most of the recent researches focus on examining, and possibly updating, these rules for failure modes other than brittle fracture. Particularly, plastic collapse deserves special attention for tougher materials or in the case of strain based design.

References

- [1] Kamaya M, Haruna T. Crack initiation model for sensitized 304 stainless steel in high temperature water. *Corros Sci* 2006;48:2442–56. doi:10.1016/j.corsci.2005.09.015.
- [2] Yan X. Multiple crack fatigue growth modeling by displacement discontinuity method with crack-tip elements. *Appl Math Model* 2006;30:489–508. doi:10.1016/j.apm.2005.05.010.
- [3] Kamaya M. Growth evaluation of multiple interacting surface cracks. Part II: Growth evaluation of parallel cracks. *Eng Fract Mech* 2008;75:1350–66. doi:10.1016/j.engfracmech.2007.07.014.
- [4] Tang H, Fairchild DP, Cheng W, Kan W, Cook M, Macia ML. Development of Surface Flaw Interaction Rules for Strain-Based Pipelines. *Proc. Twenty-fourth Int. Ocean Polar Eng. Conf.*, vol. 3, Busan, South Korea: 2014, p. 476–86.
- [5] Milne I, Ritchie RO (Robert O., Karihaloo BL. *Comprehensive structural integrity*. Elsevier/Pergamon; 2003.
- [6] Rules for Inservice Inspection of Nuclear Power Plant Components: ASME Boiler and Pressure vessel Code XI. New York: American Society of Mechanical Engineers; 2015.
- [7] British Standard. BS7910:2013+A1:2015: Guide to methods for assessing the acceptability of flaws in metallic structures. London, UK: BSI Stand Publ; 2015.
- [8] Api Standard 1104. Welding of pipelines and related facilities. API 1104-2013+ADD2014. 21st Ed 2013.
- [9] Association CS. Oil and Gas Pipeline Systems-CSA Z662-15. CSA Group; 2015.
- [10] Marsdon TU. Flaw Evaluation Procedure: background and Application of ASME Section XI, Appendix A. EPRI NP-719-SR, Electrical Power Research Institute, Palo Alto, CA; 1978.

- [11] Maccary RR. Nondestructive examination acceptance standards: technical basis and development of boiler and pressure vessel code, ASME Section XI, Division 1. Electric Power Research Inst.; 1980.
- [12] Lacroix V. Assessment and improvement of flaw characterization rules in fitness-for-service codes using extended finite element method. 2016.
- [13] Bezensek B, Sharples J, Hadley I, Pisarski H. The History of BS 7910 Flaw Interaction Criteria. ASME 2011 Press. Vessel. Pip. Conf. Vol. 1, ASME; 2011, p. 837–43. doi:10.1115/PVP2011-57857.
- [14] Hasegawa K, Miyazaki K, Kanno S. Interaction criteria for multiple flaws on the basis of stress intensity factors. ASME-PUBLICATIONS-PVP 2001;422:23–30.
- [15] Bezensek B, Hancock JW. The re-characterisation of complex defects Part I: Fatigue and ductile tearing. Eng Fract Mech 2004;71:1001–20. doi:10.1016/S0013-7944(03)00155-3.
- [16] Bezensek B, Hancock JW. The re-characterisation of complex defects: Part II: cleavage. Eng Fract Mech 2004;71:1001–19. doi:10.1016/S0013-7944(03)00156-5.
- [17] Bezensek B, Sharples J, Wilkes M. An engineering approach To characterisation of twin flaws in cleavage. Proc. ASME 2010 Press. Vessel. Pip. Div. PVP2010, ASME; 2010, p. 1–8.
- [18] M Andrews R, M Denys R, Knauf G. The EPRG guidelines on the assessment of defects in transmission pipeline girth welds. J Pipeline Eng Vol 2015;14:620–4.
- [19] De Waele W. The Interaction of Weld Defects under Plastic Collapse. Mater Sci Forum 2005;475–479:2735–8. doi:10.4028/www.scientific.net/MSF.475-479.2735.
- [20] Pepin A, Tkaczyk T, O'Dowd N, K Nikbin. Limit Load Solution and Crack Driving Force Estimation Scheme for. Proc. ASME 2015 Press. Vessel. Pip. Conf., ASME; 2015, p. 1–9.
- [21] Moussa W a., Bell R, Tan CL. The interaction of two parallel non-coplanar identical surface cracks under tension and bending. Int J Press Vessel Pip 1999;76:135–45. doi:10.1016/S0308-0161(98)00125-2.
- [22] Xu W, Wu XR, Wang H. Weight functions and strip yield solution for two equal-length collinear cracks in an infinite sheet. Eng Fract Mech 2011;78:2356–68. doi:10.1016/j.engfracmech.2011.05.007.
- [23] Kamaya M, Totsuka N. Influence of interaction between multiple cracks on stress corrosion crack propagation. Corros Sci 2002;44:2333–52. doi:10.1016/S0010-938X(02)00039-2.
- [24] Stonesifer RB, F.W.Brust, Leis BN. Mixed-mode stress intensity factors for interacting semi-elliptical surface cracks in a plate. Eng Fract Mech 1993;45:357–80. doi:10.1016/0013-7944(93)90021-J.
- [25] Hasegawa K, Saito K, Miyazaki K. Alignment Rule for Non-Aligned Flaws for Fitness-for-Service Evaluations Based on LEFM. J Press Vessel Technol 2009;131:041403. doi:10.1115/1.3152229.
- [26] Bezensek B, McCulloch E. Interaction of Twin Non-Aligned Through-Wall Flaws Under Elastic-Plastic Conditions. Proceedings ASME 2006 Press. Vessel Pip. conference PVP2006, Vancouver: American Society of Mechanical Engineers; 2008, p. 333–40. doi:10.1115/pvp2006-icpvt-11-93373.
- [27] Kamaya M. A flaw proximity rule for interacting surface cracks based on elastic-plastic fracture analysis. Proc. ASME 2009 Press. Vessel. Pip. Div. Conf. PVP2009, Prague, Czech Republic: 2009, p. 1–8.
- [28] Kamaya M. A plastic collapse assessment procedure for multiple cracks under internal pressure. ASME 2011 Press. Vessel. Pip. Div. Conf. PVP2011, Baltimore, MD, USA: 2011, p. 1–7.
- [29] Lacroix V, Dulieu P, Couplet D. Alternative charecterization rules for quasi-laminar flaws. Proc. ASME 2014 Press. Vessel. Pip. Conf., Anaheim: American Society of Mechanical Engineers; 2014, p. 1–12.
- [30] De Waele W, Denys, Rudi, Lefevre A. Development of defect interaction criteria for

- pipeline girth welds subjected to plastic collapse conditions. Proc PVP2006 ASME Press Vessel Pip Div Conf 2006.
- [31] Hasegawa K, Miyazaki K, Saito K, Bezensek B. Evaluation of alignment rules using stainless steel pipes with non-aligned flaws. Proc ASME 2009 Press Vessel Pip Div Conf PVP2009 2009:1–8.
 - [32] Hasegawa K, Miyazaki K, Saito K. Behavior of plastic collapse moments for pipes with two non-aligned flaws. Proc. ASME 2010 Press. Vessel. Pip. Div. PVP2010, Bellevue, WA, USA: 2010, p. 1–7. doi:10.1115/PVP2010-25199.
 - [33] Hasegawa K, Miyazaki K, Saito K. Plastic collapse loads for flat plates with dissimilar non-aligned through-wall cracks 2011:1–5.
 - [34] Miyazaki K. Effect of flaw dimensions on ductile fracture behavior of non-aligned multiple flaws in a plate. Proc. ASME 2011 Press. Vessel. Pip. Div. Conf. PVP2011, Baltimore, MD, USA: 2011.
 - [35] Iwamatsu F, Miyazaki K, Takazawa H, Saito K. Evaluation Procedure of Limit Load for Non-aligned Multiple Flaws. Proc. ASME 2013 Press. Vessel. Pip. Conf. PVP2013, Paris, France: 2013, p. 1–6.
 - [36] Iwamatsu F, Miyazaki K, Saito K. Limit Load Solution of Non-Aligned Multiple Flaws. Proceedings ASME 2018 Press. Vessel Pip. conference PVP2018, Prague: American Society of Mechanical Engineers; 2018, p. 1–8.
 - [37] Iida K, Kawahara M. Propagation and coalescence of fatigue cracks initiated from collinear or parallel adjacent surface flaws. Press Vessel Technol 1980;1:257–63.
 - [38] Bezensek B. Flaw Alignment Criteria Based on Limit Load Solutions for Non-Aligned Through-Wall Flaws 2009:347–53. doi:10.1115/pvp2007-26041.
 - [39] Coules HE. Stress intensity interaction between dissimilar semi-elliptical surface cracks. Int J Press Vessel Pip 2016;146:55–64. doi:10.1016/j.ijpvp.2016.07.011.
 - [40] Nisitani H, Murakami Y. Stress intensity factors of an elliptical crack or a semi-elliptical crack subject to tension. Int J Fract 1974;10:353–68. doi:10.1007/BF00035496.
 - [41] Murakami Y, Nemat-Nasser S. Interacting dissimilar semi-elliptical surface flaws under tension and bending. Eng Fract Mech 1982;16:373–86. doi:10.1016/0013-7944(82)90115-1.
 - [42] Zeng Z-J, Dai S-H, Yang Y-M. Analysis of surface cracks using the line-spring boundary element method and the virtual crack extension technique. Int J Fract 1993;60:157–67. doi:10.1007/BF00012443.
 - [43] Rice JR, Levy N. The Part-Through Surface Crack in an Elastic Plate. J Appl Mech 1972;39:185. doi:10.1115/1.3422609.
 - [44] Soboyejo WO, Knott JF, Walsh MJ, Cropper KR. Fatigue crack propagation of coplanar semi-elliptical cracks in pure bending. Eng Fract Mech 1990;37:323–40. doi:10.1016/0013-7944(90)90044-H.
 - [45] Yoshimura S, Lee J-S, Yagawa G. Automated System for Analyzing Stress Intensity Factors of Three-Dimensional Cracks: Its Application to Analyses of Two Dissimilar Semi-Elliptical Surface Cracks in Plate. J Press Vessel Technol 1997;119:18. doi:10.1115/1.2842261.
 - [46] Sethuraman R, Siva Sankara Reddy G, Thanga Ilango I. Finite element based evaluation of stress intensity factors for interactive semi-elliptic surface cracks. Int J Press Vessel Pip 2003;80:843–59. doi:10.1016/j.ijpvp.2003.10.003.
 - [47] Carpinteri A, Brighenti R, Vantadori S. A numerical analysis on the interaction of twin coplanar flaws. Eng Fract Mech 2004;71:485–99. doi:10.1016/S0013-7944(03)00040-7.
 - [48] Coules HE. On predicting the interaction of crack-like defects in ductile fracture. Int J Press Vessel Pip 2018;162:98–101. doi:10.1016/J.IJPVP.2018.03.006.
 - [49] Assessment of the integrity of structures containing defects- R6. vol. 4. British energy; 2001.

Finite element model development

4.1. Introduction

Systematic flaw interaction studies inherently require an evaluation of numerous cases with different flaw sizes and spacing distances. Such large parametric studies are not practically possible without numerical models that can be automatically generated and post-processed. This chapter elaborates on the development of three finite element (FE) models used in the present study; the first for small scale specimens, the second for medium scale specimens and the third for a full-scale selected application (pipe girth weldment). The first two models were developed in the framework of this PhD project; the third model has been adopted from another work and applied for a flaw interaction study. These models are used to extract crack tip parameters, unstable crack growth onset and plastic collapse load. Before starting the discussion on the technical details of the FE models, the principal assumptions and characteristics of a reliable FE model are briefly reviewed.

4.2. General requirements

The studied problem is highly specific, owing to the combined contribution of both fracture mechanics and plasticity theory. A major challenge is that fine meshes should be generated in a very narrow region between two adjacent cracks. In fracture mechanics problems, basically the goal of the analysis is to solve the stress fields and relevant strains near the tip of a sharp crack or blunt flaw. Since in both cases large gradients are expected near the tip, mesh configuration and density should be defined cautiously. From this perspective, solid hexagonal elements have been used since they perform better for large deformations compared to other three-dimensional continuum element types.

A fundamental assumption to be made relates to the formulation of strain, having two options referred to as “small strain” or “large strain” analysis. A small strain analysis neglects geometric non-linearities in the calculation, by formulating the elements in the original configuration (prior the deformation) throughout the entire simulation. In other words, in a geometrically linear assumption the equations of equilibrium are formulated in the undeformed state and are not updated with the deformation. The main merits are that the analysis speed is significantly increased, and that the calculations converge more easily. The disadvantage is that errors are introduced due to the geometric linearization. For relatively small deformations these errors can be negligible, whilst for larger deformations they can be pronounced. The incorporation of a non-linear geometric effect in a large strain analysis (also referred to as “finite strain analysis”) may adversely affect the simulation convergence. The most significant effects have been observed when non-linear material behavior is assumed. This material behavior, in its simplest form, can be formulated by an incremental plasticity law (based on point wise stress-strain curve definition) or deformation plasticity (reversible non-linear stress-strain behavior based on e.g. Ramberg-Osgood equation). Deformation plasticity is computationally more efficient since the result is not history dependent and is expected to reveal results like incremental plasticity in case of uniaxial tension. However, deformation plasticity has been found to bring more challenges in simulation convergence due to poor treatment of the element distortion near the crack tip. Such problems were less significant in case of materials with incremental plasticity definition. The drawback of incremental plasticity is its effects on J -integral calculation accuracy [1].

For J -integral calculations to be path independent, the existence of a strain energy density is assumed as a potential from which stresses can be uniquely derived. This assumption is valid for deformation plasticity, which is often referred to as Hencky's theory or finite plasticity. The same assumption, however, is not true for incremental plasticity which involves irreversible plastic deformation. In this assumption, not only any local unloading is not included, but also any local re-arranging of stress components, i.e. changing of loading direction in stress space resulting from the yield, is not considered. Actually, all loading paths in stress space are supposed to remain "radial" so that the ratio of principal stresses does not change with time. Since radial stress paths cannot be guaranteed in a non-homogenous stress field, the calculated J -integral becomes path dependent as soon as plasticity occurs, and when the J -integral's counter passes the plastic zone [1].

In small and contained yielding, a path independent integral can be computed outside the plastic zone. However, this can sometimes be impossible in a strain-based assessment, where global plasticity is common and consequently some path dependence will occur. In these situations, J -integral must be understood as a "saturated" value reached in the "far-field" remote from the crack tip. Therefore, any near field integral, which is path dependent, is physically meaningless, since the J -integral value would be an increasing function of distance to the crack tip. In other words, these values represent "energy production" instead of "energy dissipation", and hence violate the second law of thermodynamics. Therefore, the highest calculated J -integral value with increasing domain size is the closest to the real credible far-field J -integral value [1]. The above-mentioned issue is a question of numerical accuracy and it is unavoidable in strain-based assessment since the non-linear geometrical effect must be considered and consequently, to obtain acceptable convergence in high strain regimes, incremental plasticity should be opted.

To sum up, non-linear geometric effects must be incorporated when plastic collapse and high strain regimes are within the concerned scenario. To enhance the convergence in such case, an incremental plasticity definition of plastic material behavior is advised. This implies that numerical calculation of J -integral might be path dependent. To address this issue, either a sufficiently far field saturated value for J -integral should be considered, or an alternative parameter (i.e. crack tip opening displacement, CTOD) should be employed to describe the crack driving force.

The flaw shape and the surrounding mesh configuration are other important matters that need to be selected carefully. In this study, since the problem inherently involves large plastic deformation and tension loading is more pronounced compared to bending, the flaw is assumed as an initially blunt notch (radius $\sim 75\ \mu\text{m}$) with a spider web mesh near the flaw tip (as shown in Figure 4-1). The technical justification can be found in the PhD dissertation of Hertelé [2].

In the following sections, the details of two distinct models developed for flaw interaction studies will be elaborated. Firstly, a small-scale model that includes two through thickness notches, and secondly a medium scale model that includes notches with finite length and depth. The small-scale model is used to develop the basic alternative concepts to investigate flaw interaction in high strain regimes. The medium scale model adopts the concepts developed in the previous model and uses them in a

more relevant geometry. Both models will be verified with a series of tailored experimental tests, which are described in the next chapter (chapter 5).

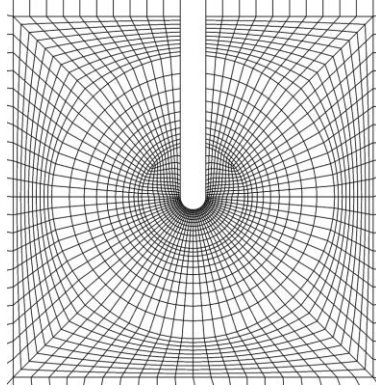


Figure 4-1- Blunt flaw with surrounding spider web mesh.

4.3. Small-scale model

To investigate the strain distribution around interacting notches and their crack driving forces, a finite element model has been developed using ABAQUS® version 6.13 as solver. The approach used is inspired by a Single Edge Notched Tension (SENT) FE model originally developed by Verstraete [3]. The capability to model and post-process multiple adjacent notches is the main contribution achieved in the present project. This has been realized through an object-oriented Python script, which allows to automatically model various geometries while a spider web mesh is generated around the notch tips. The developed geometrical model can be associated with a Double Edge Notched Tension (DENT) specimen; however, the notches are not always positioned symmetrically.

The model strategy consists of two main functions to pre-process the FE model and post-process the simulation results. The former is responsible for creating the global geometry, defining the required partitioning to control the mesh quality, assignment of material properties, defining the boundary conditions and loading and starting the simulation. The post-processing function is dedicated to evaluation of the results and extraction and visualization of certain outputs (eg. stress, displacement) from particular locations (eg. notch tip, notch mouth), and measuring certain parameters like CMOD and CTOD.

The model is made out of eight-node linear brick elements with a reduced integration scheme (C3D8R). The half circle representing a notch tip consists of 40 elements each having a radial dimension equal to $5.8\text{ }\mu\text{m}$ (around 8% of the notch radius). Multiple flaws at various locations can be simulated and in total the models contain between 60,000 and 70,000 elements. A mesh convergence study assured a satisfactory numerical accuracy within acceptable computational time. The model is designed with the aim to have maximum flexibility in positioning the notches. Thereto the mesh around the notch tip and flanks is carefully controlled by means of

partitioning. The remainder of the specimen including the region between the two notches is meshed using the “free mesh” technique.

Symmetry boundary conditions are defined in the thickness direction for the sake of computational effort and time. Ductile tearing is not implemented, and thus the cracks simply blunt out upon loading. In addition, to obtain realistic deformation patterns (including localized necking and other non-linear geometry changes), a finite strain deformation has been used for all simulations [4].

A Python script allows to generate various geometries defined by their length (L), width ($2W$) and thickness (t) and containing two (or more) notches characterized by their depth to half width ratio (a/W) and their relative distance (H), as illustrated in Figure 4-2. The notch tips are initially blunted as a previous study showed that notches with 0.075 mm radius behave similar to infinitely sharp cracks upon the development of considerable plasticity in ductile material [5]. To comply with the clamped boundary conditions of the experiment, the specimen is connected to a rigid body at both ends. One end is kept fixed (displacements and rotations inhibited), and the other is translated under displacement control (rotation being inhibited).

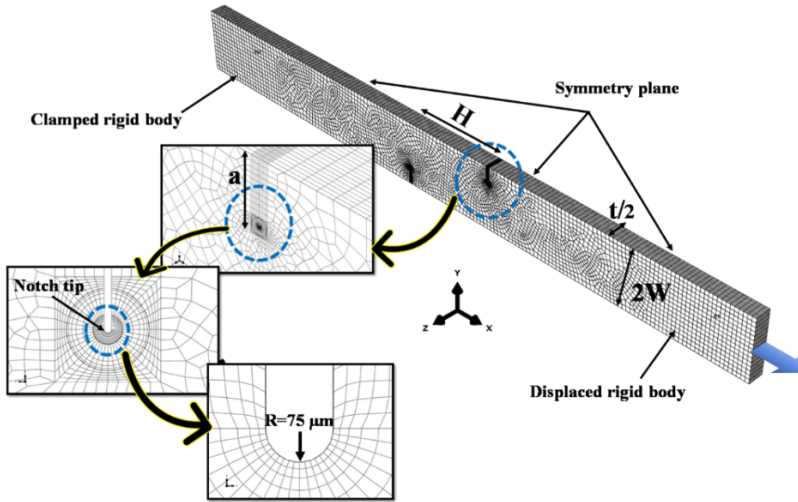


Figure 4-2- Small scale FE model details.

As far as material properties is concerned, the model is capable to use deformation and incremental plasticity definitions, as well as perfectly plastic assumptions.

During post-processing, force is derived from the reaction force in the rigid bodies at the end of the specimen. By dividing this value by the (un-notched) cross section, the gross applied stress is calculated for each increment. Strain is measured in various locations by defining virtual extensometers. J -integral is calculated by ABAQUS’s algorithm in 30 contours around the notch. CMOD is measured by tracking two nodes at the notch mouth, and CTOD is measured based on the 90-

degrees intercept by a user defined algorithm which creates the 90-degrees intercept lines for each increment and then defines their intersection with the notch flanks. The distance between these intersections, subtracted by the initial notch width (0.075 mm), is CTOD.

4.4. Medium scale model

4.3.1. Modelling strategy

The medium scale model is basically developed to answer the requirement for modeling wide plate components, with the possibility to also model curved plates and pipes. Wide plates allow to model notches with finite length and depth, often with semi-elliptical shape, which are representative to real (weld) flaws.

The modelling approaches used are inspired by concepts and procedures initially developed by Hertelé [2]. In order to study the interaction of flaws, the medium scale model has the ability to generate multiple flaws in very close proximity and perform the pre- and post-processing automatically. This is done using a Python code that allows to generate the specimens with various dimensions and flaws.

The structural complexity of building a model with multiple flaws arises from three requirements: being able to locate the flaws at arbitrary positions, generating two (or more) fine meshes in very close proximity, and defining independent mesh refinement strategies for each flaw starting from a coarse mesh remote from the flaws to fine structured spider web meshes around the flaws. The latter is essential to reduce the number of elements for the sake of computational efficiency. Considering that apart from the flaw locations, also their size (depth, length and radius at the tip) and their shape can be different, the model's architecture is developed based on an object-oriented scripting concept. This creates the required modularity to efficiently tackle the abovementioned modelling challenges.

A pragmatic approach aimed to address the above requirements is based on creating each flaw independently inside a box, named "flaw block". Because only the meshes inside these boxes are refined, the required flexibility is achieved. The principle sounds simple, yet it is the backbone strategy of an effective meshing framework for multiple complex shaped defects. Inside each flaw block a flaw is created with the required size and shape, and then the partitioning function generates the required partitions around the flaw to ensure that sufficiently fine meshes can be created around the notch tip (See Figure 4-3). The partitioning function is tailored to facilitate the mesh refinement in such a way that at the borders of the flaw block always regularly shaped meshes with the same size can be created, regardless of the flaw size.

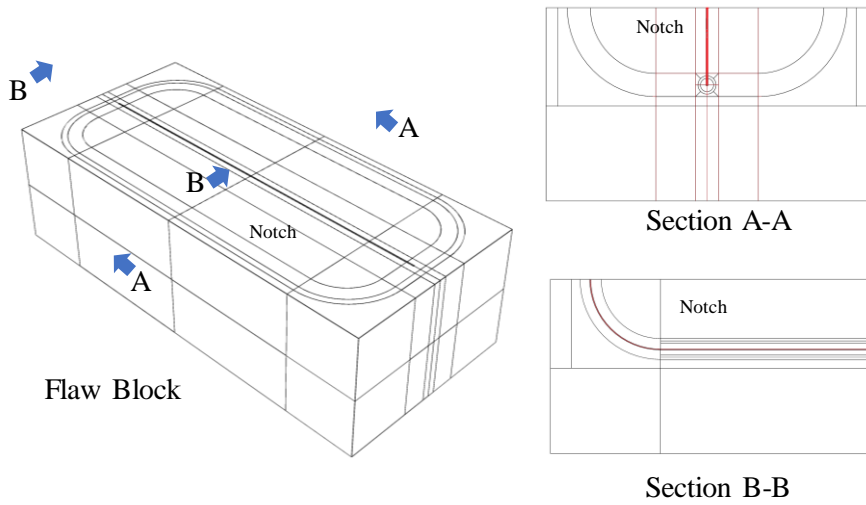


Figure 4-3- Flaw block partitioning scheme.

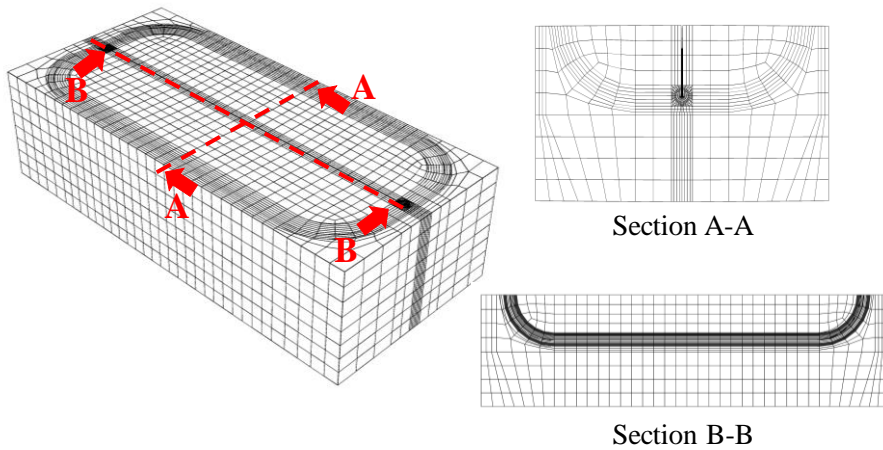


Figure 4-4: Flaw block meshing scheme.

Having created the flaw blocks, they are subsequently placed inside a wide and flat plate specimen based on a defined spacing distance, and then the meshes inside the flaw blocks are generated with a certain order. Finally, the regions outside the flaw blocks are meshed using a free meshing strategy. This approach has proven to be particularly effective for flaws located sufficiently far from each other (i.e. spacing distances larger than the maximum depth of the two flaws). Yet for flaws in close proximity, the area between the two flaw blocks can be too narrow to be meshed with good quality. This challenge is addressed by employing a technique called “nodal

coordinate transformation” which is elaborated in section 4.3.2. In a nutshell, the meshing procedure is subdivided into two stages. In the first stage the flaw blocks are generated and located in a plate with a conveniently large spacing distance and meshed. In the second stage the mesh around the flaw blocks is manipulated such that the notches are translated towards each other to reach the desired spacing distance by applying a transformation of the coordinates of selected nodes.

Using flaw blocks has a distinct advantage for modeling embedded flaws. To put it simple, an embedded flaw can be constructed by placing two flaw blocks face to face. This way, no further effort is required for embedded flaws and very similar functions can be used for these flaws as for their surface breaking counterparts (Figure 4-5). Although it is believed that this approach could serve the purpose well, in the present project an alternative and novel method based on element deletion is employed. This decision was made based on the potential of the element deletion method in modeling irregularly shaped defects for future advanced ECA application. Details about this method can be found in section 4.3.2.

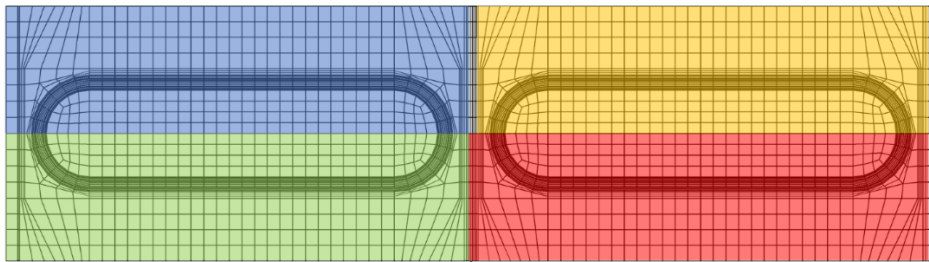


Figure 4-5: Embedded flaws generated by combination of four flaw blocks (cross section view).

Having generated the meshed flaw blocks and positioned them at the desired location, the remainder of the model is constructed around the flaw blocks. As illustrated in Figure 4-6-a, the model contains a main body, which is a wide plate with two notches at the center (see Figure 4-6-b), and two rigid bodies connected to the ends of the main body. One end is kept fixed (no rotations and no displacements) and the other is translated under displacement control (rotation being inhibited) to simulate uniaxial tensile loading.

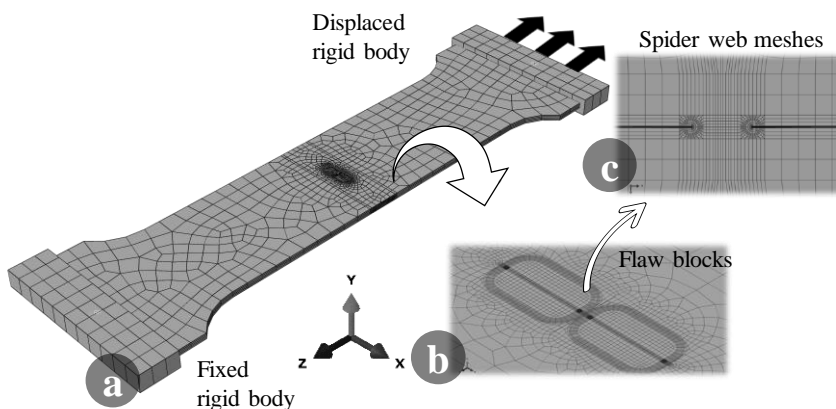


Figure 4-6: Medium scale model (wide plate).

4.3.2. Nodal coordinate transformation functions

Various nodal coordinate transformation functions are employed in the medium scale FE model with the aim to attain the desired geometries. These coordinate transformation functions have an exceptional merit for generating sophisticated geometries. Meshing such geometries is often too cumbersome and even impossible with conventional approaches. Yet, by using the nodal coordinate transformation technique first a simpler geometry, which is easier to be meshed, is generated and meshed, and then the entire or part of the geometry and affiliated meshes are transformed through a succession of nodal coordinate transformations.

Three nodal coordinate transformations have been implemented, each of which modifies a different geometrical feature. In this section a brief overview on these transformation functions and their application are provided.

Semi-elliptical function: Since flaws are commonly assumed to be (semi-)elliptical in fracture mechanics, and that this shape is closer to the shape of notches introduced in experimental testing, the same is desired in FE model. To achieve this shape, first a notch composed of two quarter circles at the ends and with constant depth in between (canoe-shaped) is constructed and meshed. Then a devoted coordinate transformation function is applied to transfer the flaw to a semi-elliptical shape. The transformation is implemented inside the flaw block only. Notches before and after applying this function are shown in Figure 4-7.

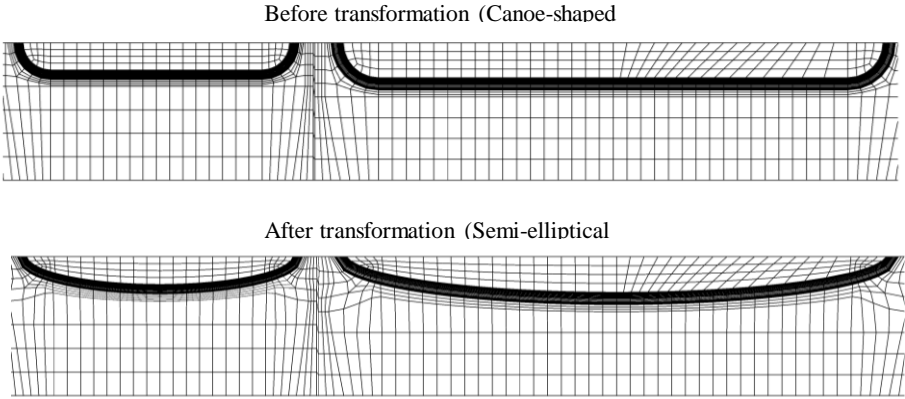


Figure 4-7: Notches before and after applying semi-elliptical nodal transform function (cross-section).

Compression function: An extensive flaw interaction study inherently requires notches at very close distances. However, considering the flaw block partitioning scheme, two adjacent notches cannot be located closer than a certain limit. This limit (D_L) is equal to the sum of the minimum distance from notch tip to flaw block edge (D_1 and D_2) plus a certain minimum distance required between the two blocks to allow a free mesh to be constructed (D_3), as shown in Figure 4-8. When a very close distance between notches is desired, the notches are temporarily modelled with this minimum distance in between them (a_1+a_2). Then a nodal coordinate transform is applied to translate the notches and corresponding meshes closer by compressing the flaw block towards the adjacent notch. As shown in Figure 4-9, the transformation results in a compression of the elements at one side of the flaw block.

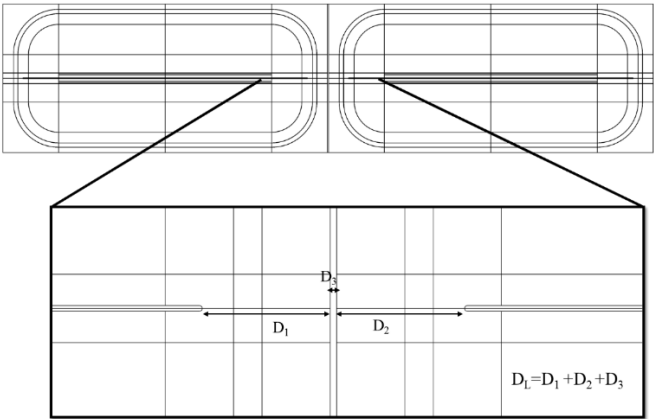


Figure 4-8: Minimum distance required for building the flaw blocks.

The above-mentioned strategy has obvious advantages including simplicity and high flexibility. However, it has an inherent limitation when it comes to very closely

located flaws. The essential partitions constructed in the flaw box for the sake of mesh refinement, cannot be compressed more than a certain limit. In other words, the coordination transformation cannot be applied for further compression of the flaw block when it reaches a certain limit, since the complex partitioning and element shape do not allow such a large shift (the meshes might be distorted due to transformation).

Coordinate transformation by the compression function

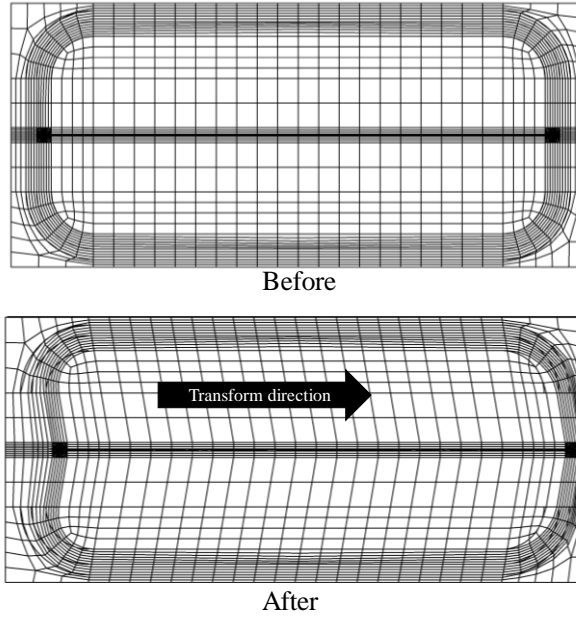


Figure 4-9: Flaw block before and after a compression coordinate transform.

The optimized compression function allows to achieve a minimal spacing distance around 30 percent of the maximum flaw depth. This is less than the critical distance for interaction suggested by several ECA guidelines, i.e. half of the maximum flaw depth ($0.5 \max \{a_1, a_2\}$). Hence, the model is capable of evaluating these guidelines.

Curve function. To allow comparison with large scale experiments, geometries such as a curved wide plate (CWP) or pipe are desired. This can be accomplished by executing the so-called curve function which transforms a flat plate to a curved geometry with certain diameter. The curved character of the pipe is obtained by virtually “rolling” the originally flat plate over a rigid cylindrical mandrel with a diameter D_i (the inner diameter of the pipe) and a longitudinal axis parallel to the z-direction using some basic trigonometry. The width of the flat plate prior to the coordinate transformation, W_{flat} , should be chosen to obtain the eventually desired geometry. In case of a CWP coupon with width W defined at mid-thickness, the following relation can be shown:

$$W_{flat} = D_i \arcsin\left(\frac{W}{D}\right) \quad 4-1$$

For a pipe specimen, W_{flat} should be equal to the circumference of the inner circle of the pipe cross section:

$$W_{flat} = \pi D_i \quad 4-2$$

Figure 4-10 illustrates the geometry of the model before and after application of the curvature transformation. The very same procedure can be used for making a pipe geometry; but it should be noted that this requires both sides of the initially flat plate to be connected by means of tie constraints.

In addition to the above main nodal coordination transformations, only in the element deletion method, other nodal coordinate transformations are also employed mainly with the intention to generate welded pipe joints. These transformations are elaborated in detail in [6].

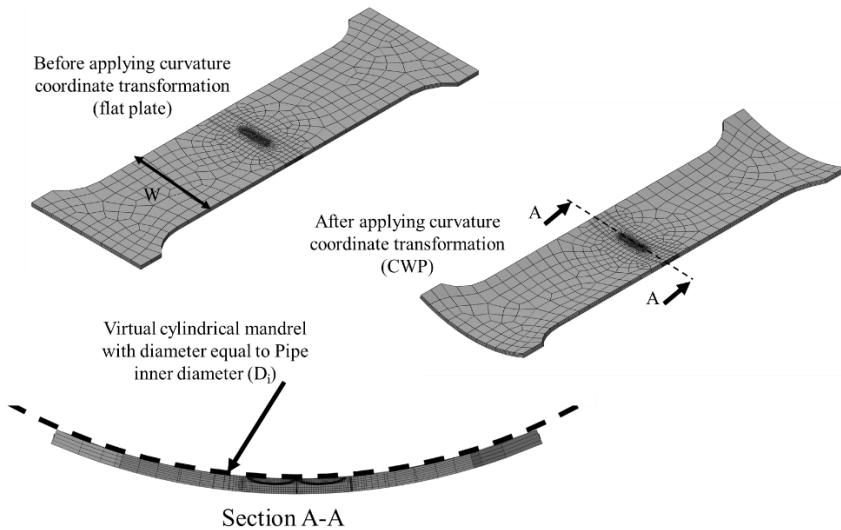


Figure 4-10: The model geometry before and after the curvature coordination transform.

The full procedure employed in the medium-scale model is summarized in the flow chart shown at Figure 4-11. The coordinate transformations are applied in a certain sequence ensuring that the mesh quality can be retained after each transformation. That is an essential requirement since the simulations impose large deformations on the elements which potentially can cause excessive element distortion if mesh quality is low. On the other hand, due to the inherent flexibility required for modelling notches with different sizes and at different locations, a free

mesh strategy is used for regions outside the flaw blocks. Thus, the user has very limited control over element shape and size. This becomes more critical when a nodal coordinate transformation is applied to these elements, for instance to compress the elements to bring the notches closer, which can cause distortion into non-regularly shaped elements.

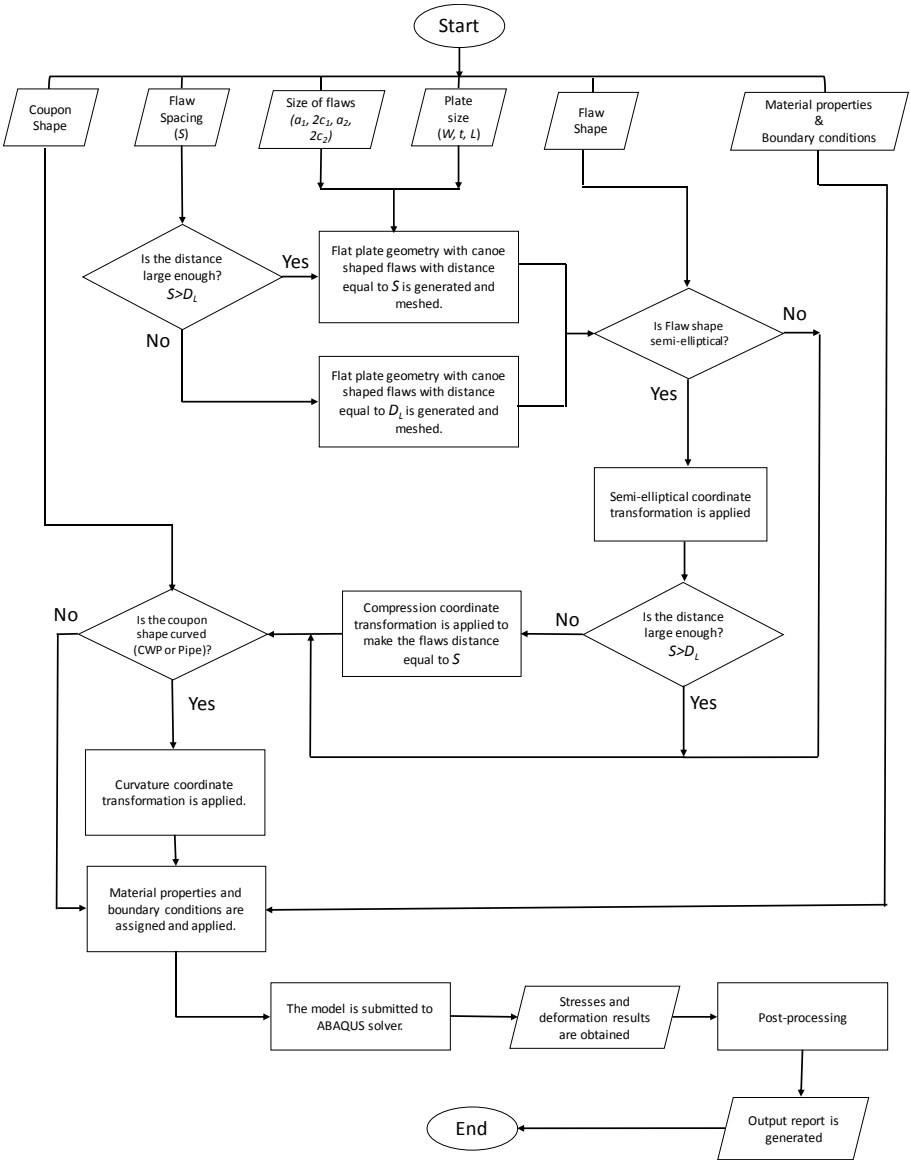


Figure 4-11- FE medium-scale model flowchart.

4.5. Pipe model (element deletion approach)

An alternative method used in this study is to model the flaws based on element deletion. This method can be used to model irregularly shaped planar or volumetric defects and has been developed through a project (No. 201/2018) of the European Pipeline Research Group (EPRG). The modelling approach was developed by Vitor S. R. Adriano, and is briefly summarized here. In chapter 6, the element deletion approach is used to generate a parametric study covering interaction between a surface flaw and an embedded flaw in pipe geometries.

Figure 4-12 schematically shows the working principle of the flaw definition in two dimensions. The “real” flaw is bounded by the green dashed line, a stepwise shaped “virtual” flaw following the green dashed line is obtained. Hereto an element is deleted as soon as one of its nodes (colored red in the figure) is embedded within the “real” flaw. The resulting stepwise “virtual” flaw is larger than its “real” shape; with the difference being determined by the element size. This contributes to conservatism of the approach. The algorithm to delete elements requires a mathematical function representing the flaw boundary (Φ), which is negative for points inside the flaw and positive outside the flaw (and zero along the flaw boundary). Planar defects can be approximated by confining the element deletion process to one single, thin layer of elements. It is straightforward to extend the algorithms above towards the creation of multiple defects (be it volumetric or planar). Each defect is then described by a distinct boundary function and each defect is subsequently created. Example plate models generated by the element deletion process are shown in Figure 4-13 and Figure 4-14.

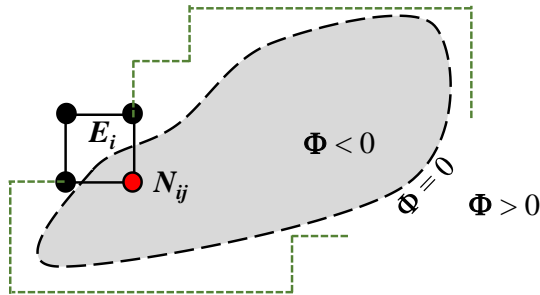


Figure 4-12: Schematic overview of the procedure to determine a flaw based on element deletion.

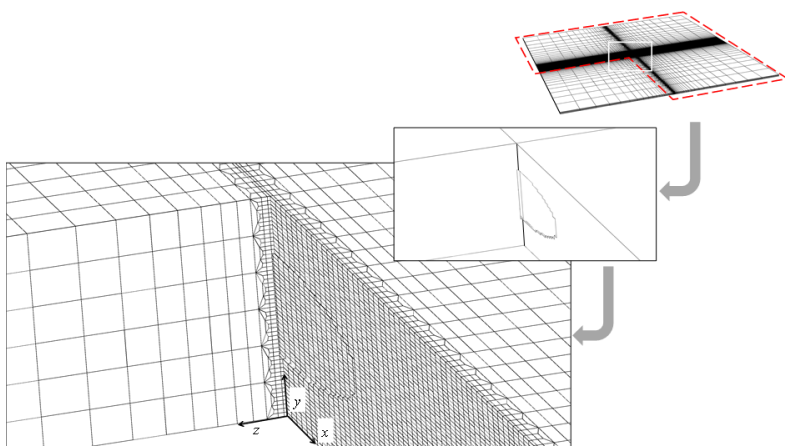


Figure 4-13: Example of sharp embedded elliptical flaw, generated by element deletion.



Figure 4-14: Cross section of a model containing three coplanar defects, defined according to (semi-)ellipses marked by white dotted lines.

The described procedure was applied to generate an example model of a girth weld with irregular fusion line, connecting 30" pipes having 17 mm wall thickness (Figure 4-15). The weld has a high-low misalignment of 2 mm and a weld cap reinforcement of 2 mm. The girth weld contains a surface breaking (semi-elliptical) flaw and an embedded (elliptical) flaw. Both flaws are 3 mm high and 50 mm long and have the thickness of one element. The flaws are coplanar and partially overlapping in the transverse direction. Clearly, the approach to couple flaw generation by element deletion with weld shaping by nodal coordinate transformations offers an unprecedented flexibility for generating defected welds with a high degree of geometrical complexity.

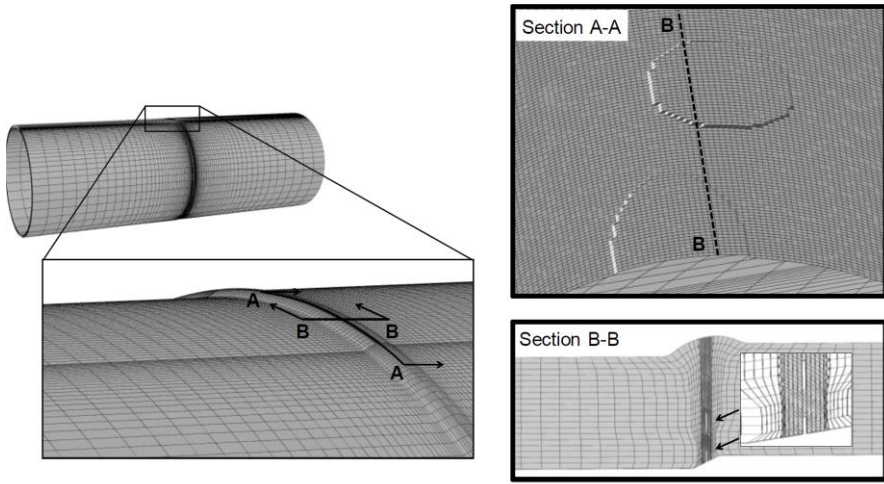


Figure 4-15 : Example model of a misaligned weld with irregular fusion line geometry and cap reinforcement, containing two flaw.

The obvious benefit of element deletion is that user-defined defect shapes of unlimited complexity can be modelled. An obvious drawback is the stepwise nature of the modelled defect, which invalidates the inaccuracy of local stress-strain output of elements that touch the defect tip. As a consequence, conventional fracture mechanics parameters like K and J -integral cannot be derived directly using established methods based on this output. Alternative post-processing procedures were developed to extract crack driving force output, as summarized below (Figure 4-12).

Regarding linear-elastic analyses, in general, the opening of a crack is governed by its surrounding stress field. This stress field, in turn, is governed by K_I in linear-elastic conditions according to the well-known theoretical stress singularity. These relations allow to formulate the following theoretical dependency between COD and K_I (under certain assumptions with are omitted for the sake of brevity):

$$COD = \frac{\kappa + 1}{G} \sqrt{\frac{L}{2\pi}} K_I \quad 4-3$$

with L distance normal to the trajectory of the defect at a point inside the defect which is used to measure COD (in this study $L=0.36$ mm) and G the shear modulus of the material, related to Young's modulus E and Poisson coefficient ν as follows:

$$G = \frac{E}{2(1 + \nu)} \quad 4-4$$

and κ a factor that depends on the out-of-plane boundary conditions:

$$\kappa = \begin{cases} \frac{3-\nu}{1+\nu} & \text{Plane stress} \\ 3-4\nu & \text{Plane strain} \end{cases}$$

The sensitivity of equation 4-5 to out-of-plane boundary conditions is limited. Taking $\nu = 0.3$ for steel, (κ) is 3.08 for plane stress conditions and 2.80 for plane strain conditions. Both factors differ by a mere 10%. From the viewpoint of estimating K_I from COD, it is conservative to assume plane strain conditions, as these yield slightly larger K_I -values than plane stress conditions.

Regarding elastic-plastic analyses, J -integral output cannot be reliably obtained at this point. Instead, CTOD was chosen as an alternative measure for crack driving force in elastic-plastic conditions. The conventional approach to extract CTOD out of a computational fracture mechanics analysis, is by means of Rice's 90-degree intercept method [7]. This method defines CTOD as the displacement between the intersection points of both crack flanks with perpendicular lines that originate from the crack tip in a symmetrical manner. Clearly, this definition is unsuitable for the current modelling approach, as the extraction points for CTOD would be located undesirably close to the stepwise crack tip for small load levels. In the development of their well-known procedures for strain-based defect assessment, ExxonMobil researchers explored alternative (simpler) methods to obtain CTOD, compared to the relatively cumbersome 90-degree intercept method. Their work indicated that the CTOD at the deepest point of a semi-elliptical crack could be well approximated by tracking the displacement of nodes at an initial distance of 0.36 mm to the crack tip (Figure 4-16, adopted from reference [8]).

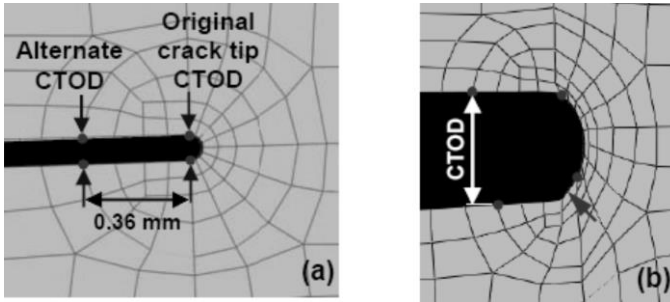


Figure 4-16: Mobil's alternative definition of CTOD [8].

Conceptually, obtaining CTOD from COD is less challenging than obtaining K_I since,

- 1- CTOD is simply considered equal to COD, whereas calculation of K_I is based on a theoretical fracture mechanics analysis (including a list of assumptions);

- 2- the occurrence of crack tip plasticity is expected to fade out the scatter originated by the stepwise nature of the defect tip;
- 3- a value of 0.36 mm for L can be taken as a sound starting point, given the equivalence with ExxonMobil's approach for CTOD calculation based on COD.

The accuracy of K_I and CTOD calculations was evaluated by comparisons with analytical solutions and/or numerical solutions obtained from "conventional" finite element models (having a smooth defect tip surrounded by a spider web mesh). Whereas there is scope for improvement in terms of robustness, the calculations are considered sufficiently accurate for the sake of the selected flaw interaction study discussed further in this work.

4.6. Conclusion

To sum up, this chapter has introduced three finite element (FE) models used to simulate the interaction effect between adjacent notches. Strain-based design conditions inherently involve non-linear plastic deformations, and this imposes some specific challenges to the modelling procedures. These challenges and ways to address them have been briefly reviewed in this chapter.

First, a small-scale model has been developed to investigate the flaw interaction in specimens with relatively low crack tip constraint, with a geometry similar to a single-edge notched tension (SENT) specimen. This model mostly served to develop concepts that would be used later in the medium-scale FE model and compare results with those of an existing (and validated) SENT model. In addition, many post-processing tools like CTOD calculation based on the 90-intercept method were introduced first in this model. As elaborated in chapter 6, the results of this model will be used to develop a novel method to describe flaw interaction based on strain patterns.

Second, the medium-scale model is the main tool of the present study to investigate the interaction between notches. A basic strategy has been adopted to generate the possibility to model various notches size at arbitrary positions within a tension loaded wide plate geometry. The backbone of this strategy is the definition of so-called flaw blocks, in which elements around the notches are created with a complete control on mesh quality. The meshes outside these blocks can be generated by a free mesh method, which increases the user's flexibility in positioning of the notches at arbitrary positions. Thus, notches can be generated with desired length and depth at any arbitrary position, whilst maintaining a fine mesh required for fracture mechanics analysis and high strain regimes around the notch tips. Starting from a model mesh with simplified geometry (which is easier to be meshed), a series of nodal coordinate transformation functions are used to generate the desired geometry of the flaw and spacing distance between the adjacent flaws.

Finally, an alternative approach to generate flaws (based on element deletion) and thus study the flaw interaction problem has been employed in a full scale pipe model. This method can model volumetric flaws as well as blunt surface cracks with arbitrary shape. In the element deletion algorithm, flaws are described by a function representing the flaw boundary, and elements are deleted as soon as this function

reaches a negative value for at least one of their nodes. The resulting stepwise shape of the modelled defects creates challenges with respect to crack driving force calculation, which have been addressed to a sufficient extent for this research. With this model, embedded flaws interaction with surface flaws will be studied.

References

- [1] Brocks W, Scheider I. Numerical Aspects of the Path-Dependence of the J-Integral in Incremental Plasticity. 2001.
- [2] Hertelé S. Coupled Experimental-Numerical Framework for the Assessment of Strain Capacity of Flawed Girth Welds in Pipelines. PhD dissertation. Ghent University; 2012.
- [3] Verstraete M. Experimental-Numerical Evaluation of Ductile Tearing Resistance and Tensile Strain Capacity of Biaxially Loaded Pipelines n.d.
http://www.soetelaboratory.ugent.be/03_research/dissertation/PhDdissertation_MatthiasVerstraete.pdf (accessed October 27, 2015).
- [4] Kim N-H. Introduction to Nonlinear Finite Element Analysis. 1st ed. New York: Springer; 2015. doi:10.1007/978-1-4419-1746-1.
- [5] Verstraete MA, Hertelé S, Denys RM, Van Minnebruggen K, De Waele W. Evaluation and interpretation of ductile crack extension in SENT specimens using unloading compliance technique. Eng Fract Mech 2014;115:190–203. doi:10.1016/j.engfracmech.2013.11.004.
- [6] Hertelé S, De Waele W, Denys R, Verstraete M, Van Wittenberghe J. Parametric finite element model for large scale tension tests on flawed pipeline girth welds. Adv Eng Softw 2012;47:24–34. doi:10.1016/j.advengsoft.2011.12.007.
- [7] Rice JR. Division of Engineering THE APPROXIMATE ANALYSIS OF STRAIN CONCENTRATION BY NOTCHES AND CRACKS Department of Defense Advanced Research Projects Agency Contract SD-86 Material Research Program ARPA SD-86 REPORT E39 May 1967 1967.
- [8] Fairchild DP, Cheng W, Ford SJ, Minnaar K, Biery NE, Kumar A, et al. Recent advances in curved wide plate testing and implications for strain-based design. Int J Offshore Polar Eng 2008;18:161–70.

Experimental procedures and FE model validations

5.1. Introduction

This chapter describes the experimental procedures employed in this study. These procedures are used to measure full-field strains, force, CTOD, CMOD and ductile crack growth. The experimental investigations are aimed to validate the FE models developed in chapter 4 and to provide supplementary results to those of gathered from FE model.

The next section (5.2) will focus on test instrumentation and the main measurement procedure employed in this thesis. Then, validation procedure for each of FE models is described and the specimens used for this purpose are elaborated. This experimental investigation contains 2 types of specimens; first type consists of small scale specimen with a through thickness notch, which by itself consists of Single Edge Notched Tension (SENT) and (a)symmetrical Double Edge Notched Tension (DENT). Second type of specimens is a wide plate contains semi-elliptical notch(es), again this type consists of single notched and double notched specimens. The first type of specimens is used to validate the small-scale model (section 5.3), the single notched specimens from the second type are used to develop a novel experimental procedure for CTOD measurement (section 5.2.4), and together with their double-notched counterparts they are used to validate the medium scale FE model (section **Error! Reference source not found.** and 5.4) . Full scale model (pipe) validation was evaluated within the framework of a parallel project through comparing its results with the medium scale model, and that its accuracy was deemed sufficient for this thesis as well. Finally, section 5.5 concludes the experimental and validation procedures. In the experiments X70 material extracted from spiral welded pipe is used.

5.2. Test instrumentation

5.2.1. (Double) Clip gauge measurements

Two small mounting pieces, are bolted onto the specimen's top surface, facilitating the attachment of the clip gauges (Figure 5-1-a). To that extent, two 3.0 mm deep holes with a diameter of 1.9 mm are drilled at each side of the crack. Generally, these holes are located 4.5 mm apart from the cracked ligament, resulting in an initial clip gauge opening of 3.0 mm. The heights for the attachment of the clip gauges, h_1 and h_2 , equal 2.0 and 8.0 mm respectively. From the change of both clip gauge readings, V_1 and V_2 , the plastic contribution of CTOD can subsequently by using the double clip gauge method employing BS 8571:2014 calculation procedure [1].

Note that the equations in this standard have been defined for SENT, and an assumption is made to apply them for DENT (Figure 5-1-b). The double notched specimen is assumed to be equivalent to two tangent single notched specimens with half the width of the original specimen, and then CTOD is calculated for each notch separately. Hereto, half of the total force is used for calculation of the elastic contribution to CTOD. No assumptions have to be made for the calculation of the plastic CTOD component, since it essentially follows from an experimentally

calibrated plastic hinge calculation (based on the readings obtained from the double clip gauge assembly).

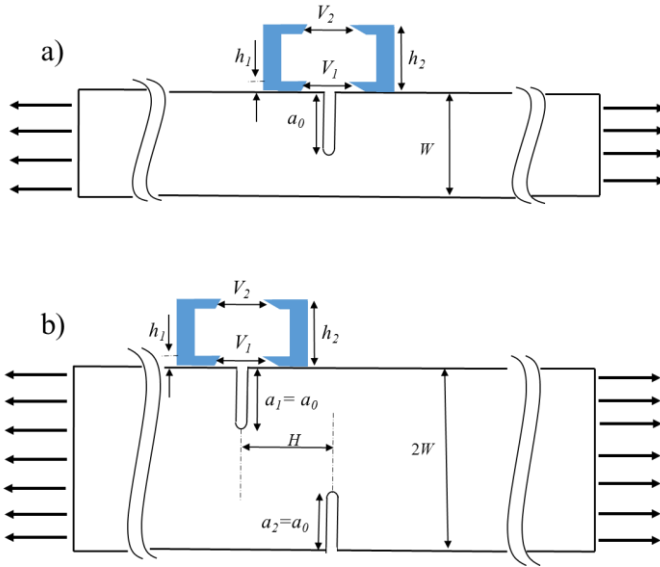


Figure 5-1: Double clip gauge mounting to a) SENT and b) asymmetrical-DENT specimen, for CTOD measurement.

5.2.2. Digital Image Correlation (DIC)

To measure the full field deformation at the surface of the specimen, stereoscopic (3D) digital image correlation (DIC) has been employed. Pictures were captured using a stereoscopic system provided by Limes Messtechnik & Software GmbH, consisting of two synchronized monochromatic 14-bit cameras having a resolution of 2452 by 2054 pixels (5 Megapixels). Three-dimensional surface deformation has been derived from the post-processed images using VIC3D software of Correlated Solutions (version 7.2.4). In addition to the stereoscopic camera system, an additional DSLR camera was employed in some tests to have a wider 2D view of the entire specimen, allowing to measure surface strains remote from the notch, either at the front or at the back of the specimen. Figure 5-1 schematically illustrates the measurement setup with the 3D stereoscopic cameras, 2D camera and mounted speckled specimen. To allow comparison of 2D and 3D images, the whole system was synchronized by a trigger signal generated by the test rig control system at 1 Hz frequency.

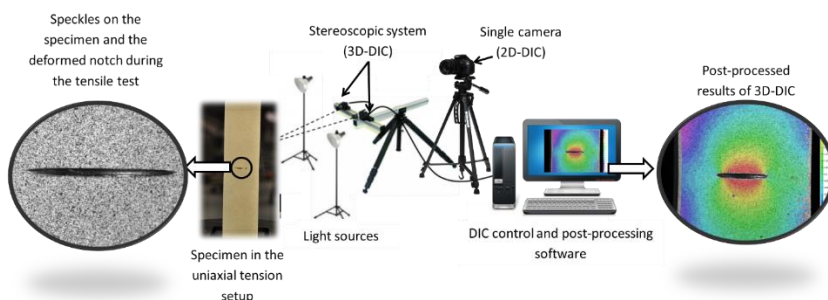


Figure 5-2-Schematic illustration of optical strain measurement setup based on 3D and 2D DIC.

To prepare the specimen for optical measurement, it was first degreased and then a thin layer of white elastic paint was applied to the surface, followed by the application of a random pattern of black speckles. The procedure has been optimized to obtain high contrast speckles with an intended size of 3 by 3 camera. Then the illumination was tuned to provide uniform light density and avoid specular reflection or shadows. Before starting the test, the stereoscopic system was calibrated by analyzing a large set of pictures of a calibration grid pattern in arbitrary positions and angles. Figure 5-3 shows the DIC cameras and the double clip gauge. Alternatively, the CTOD value can also be measured based on the δ_5 definition introduced by GKSS [29], using DIC data to extract the displacements around the notch tip according to this definition. Based on the δ_5 approach, CTOD is equal to the displacement of the two nodes symmetrically placed 2.5 mm apart from the original crack tip. This measurement can be performed either through a clip gauge or by full field optical measurements [2]. The former method requires a special device to make spot contact between the gauge and the specimen, which is not always possible. The latter technique requires less preparation and restrictions and can be performed without contact with the specimen. This can be a practical merit for measuring CTOD compared to the 90-degree intercept approach which is normally measured by the double clip gauge method [3,4]. In the present study CTOD in small scale specimens will be measured by conventional clip gauge as well as δ_5 and results will be compared.

In addition to strain measurement, 3D-DIC has been employed in wide plate specimens for CTOD measurement through a novel method based on crack mouth profilometry. Figure 5-4 shows the DIC setup for a wide plate specimen and a detailed description of measuring CTOD by DIC can be found in section 5.2.4.

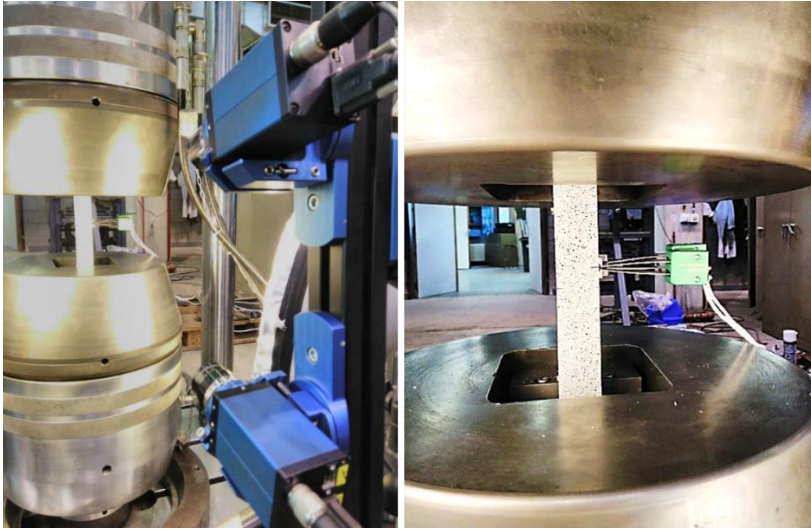


Figure 5-3- Small-scale specimen DIC setup and double clip gauges mounted for CTOD measurement in through thickness notched specimen.

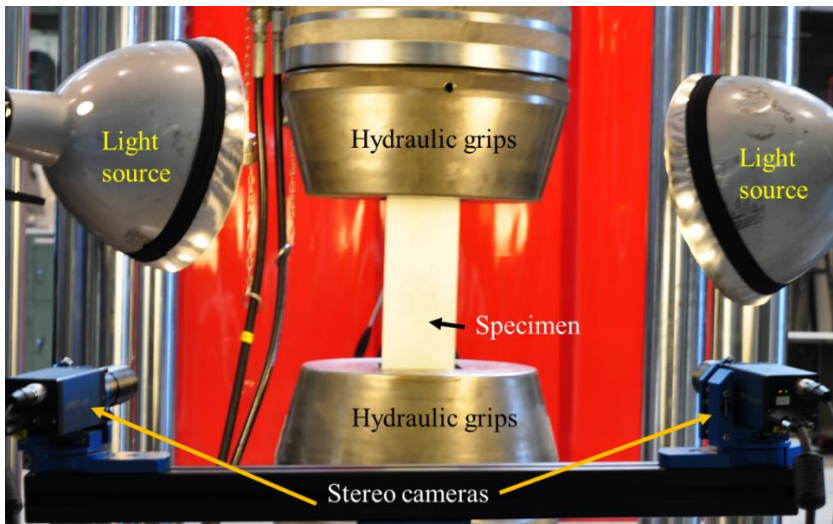


Figure 5-4- DIC setup for medium scale wide plate specimen.

5.2.3. Crack replication procedure (replica casting)

The subsurface nature of CTOD makes its direct measurement very difficult for semi-elliptical notches, if not impossible. In the early days, CTOD was measured with injection and removal of dental implant compound [5]. More recently, casting a replica of the crack and its physical measurement has been employed by some researchers. Østby et al. used it for measuring CTOD, CMOD and/or CTOA in embedded defects [6], through thickness notches in SENT specimens [7,8] and semi-

elliptical cracks in large scale pipes [9]. Tagawa et al. employed catalytically hardening dental impression silicone rubber to make replicas of the active crack tip opening in SENB specimens [10]. Khor et al. casted and sliced silicone replicas of cracks to measure the CTOD at the notch tip (based on the original definition) and compared it with δ_5 values measured by DIC at various loading levels for SENB specimens extracted from austenitic stainless steel [11].

In addition, ductile crack growth measurement techniques like Potential Drop (PD) have been developed for single notched specimens, while very few references are available for finite length notch measurement (surface breaking notches). Therefore, when it comes to measuring the ductile growth of multiple finite length notches, no generic experimental procedure is available in the literature. This is a significant limitation, since in strain-based framework credible information about the crack growth behavior is essential to model the limit state.

Therefore, in the present study the measurement of ductile crack growth and CTOD benchmarks, crack replicas were made for semi-elliptical notches at different load levels (at least five) during the tests. Hereto, the specimen was held at a constant elongation while silicone rubber (Microset RF-101), already mixed with a catalyst, was injected into the notch. After hardening the replica (approximately 5 minutes), the specimen was loaded further, which allowed to remove the cured replica as the notch opening increased. The replica casting procedure was then repeated at the next load level. This procedure is illustrated for a wide plate with single notch in Figure 5-5. After removal, the replicas were sliced at $X = 0$ mm (defined as the central position), ± 2 mm, ± 4 mm and ± 6 mm, as shown in Figure 5-6. Subsequently, CTOD and crack growth were measured on the sectioned planes by optical microscopy.

It was challenging to retrieve the original notch tip in the replicas. A visible profile shift (henceforth referred to as the edge) at the outer side of the replica, as shown in Figure 5-6, was the key to solve this challenge. This shift results from the difference in thickness of the milling blades used and is always located at a constant distance above the initial crack tip. In other words, the initial crack tip is around 0.5 mm below the edge, this is the depth which is cut by fine blade. By measuring this part of the notch accurately at the very first replica casted before ductile tearing initiation, the initial crack tip can be traced in the rest of replicas with ductile tearing.

Having located the initial crack tip, the CTOD is measured based on the 90-degrees intercept definition according to equation 5-1 at both sides of each slice (in YZ plane):

$$\delta_{Rep} = U - 2R_i \quad 5-1$$

Where δ_{Rep} is the CTOD based on 90-degrees intercept definition measured on a silicone replica of the crack, U is the distance between the opposite crack flanks at the replica's cross section (see Figure 5-6), and $2R_i$ is the non-deformed notch width (in this specimen equal to 0.2 or 0.4 mm depending on where the 90-degree lines intersect with the crack flanks, below or above the edge).

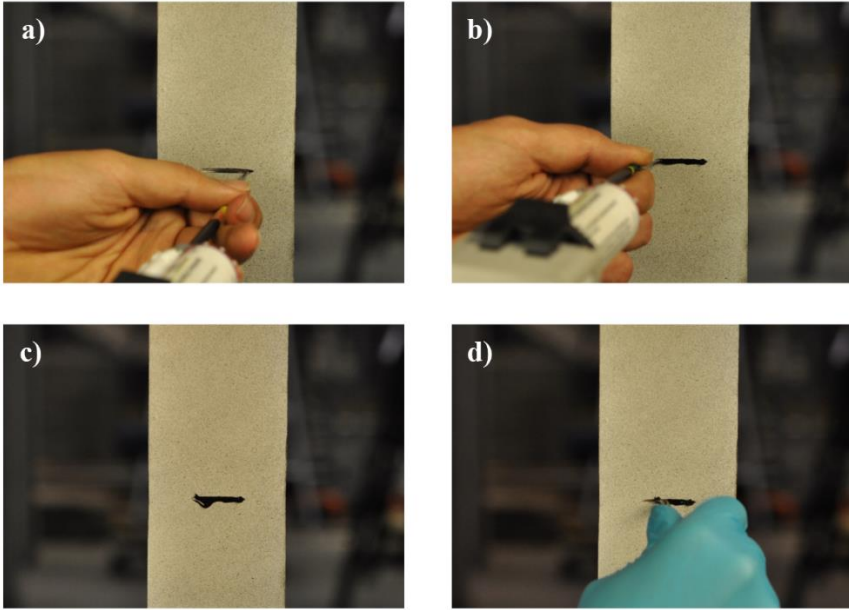


Figure 5-5: Replica casting procedure a) injection start, b) injection end, c) curing time, d) removal of the replica.

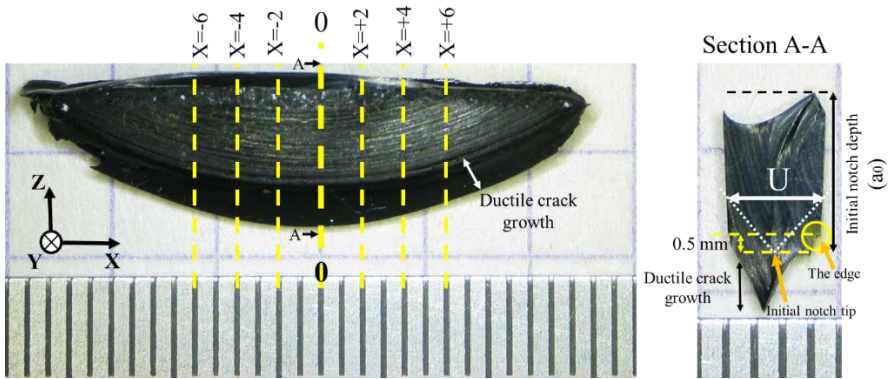


Figure 5-6: Replica cutting plane and an example cross section (dimensions are in mm).

5.2.4. CTOD measurement by profilometry using DIC

During the course of this thesis, it becomes clear that a development is needed to allow measurement of the CTOD in a specimen with multiple notches. Conventional methods to measure CTOD with double clip gauges are not suitable for this study since closely located clip gauges block the optical access to the notches, which is vital for DIC measurements.

CTOD measurement procedures have historically focused on small scale fracture toughness test specimens with through-thickness notches. Realistic defects, however, are rather of finite length and variable depth (e.g. semi-elliptical surface-breaking defects). These types of defects are often introduced in fracture testing of large, component scale specimens. The CTOD development in these defects will be strongly variable along the crack front. Exact knowledge of CTOD over the entire front is useful for detailed calculations, such as crack profile evolution due to ductile tearing or the integrity assessment of multiple interacting defects [12], where the critical location for fracture along the crack front is not known in advance. Since clip gauge based CTOD calculations merely provide information at the location of the gauge, their suitability for such detailed assessments is questionable.

In this work, a novel experimental technique is introduced to measure the CTOD along the crack front of finite length surface breaking notches (resemble to semi-elliptical shape), which are a good representation of commonly introduced notches in wide plate and other large-scale fracture mechanics tests. This method is based on measuring the rotational angle at the crack mouth in a full-field profile measurement, obtained by stereoscopic digital image correlation (DIC). The developments are backed by supporting finite element analysis.

The procedure to calculate CTOD based on DIC is explained as follows. Having extracted the surface deformations in all three directions, assuming a plastic hinge model and by using basic trigonometry, the CTOD (based on 90-degree intercept definition) can be calculated using equation 5-2 (see also Figure 5-7). In case of DIC measurement, the resulting CTOD is referred to as δ_{DIC} and in case of FE simulation it is referred to as δ_θ :

$$\delta = \frac{1}{1 - \tan \theta_2} (CMOD - 2a_x \tan \theta_2) \quad 5-2$$

where delta (δ) is the crack tip opening displacement at the initial notch/crack tip in line with the acknowledged definition. CMOD is the crack mouth opening displacement measured at the specimen surface. θ_2 is the rotation angle measured at the surface plane by DIC, which appears due to rotation of the crack around the plastic hinge. It is assumed that the crack opening angle (θ_1) during the tests remains equal to the rotation angle (θ_2), and a_x is the initial crack depth along the crack front. Crack depth reaches its maximum value at $X = 0$ (the center of the crack) and is referred to as a_0 . Note that the equation assumes symmetrical crack opening. Nonetheless, the

shown in Figure 5-8. The outcome of the measurement of out-of-plane displacement at the line passing through the center of the crack ($X=0$) will be the traditional CTOD, while the other lines allow to calculate the crack opening at other locations along the crack front. The simultaneous measurement of CTOD in locations other than the crack center by conventional techniques (like double clip gauge method) is practically impossible.

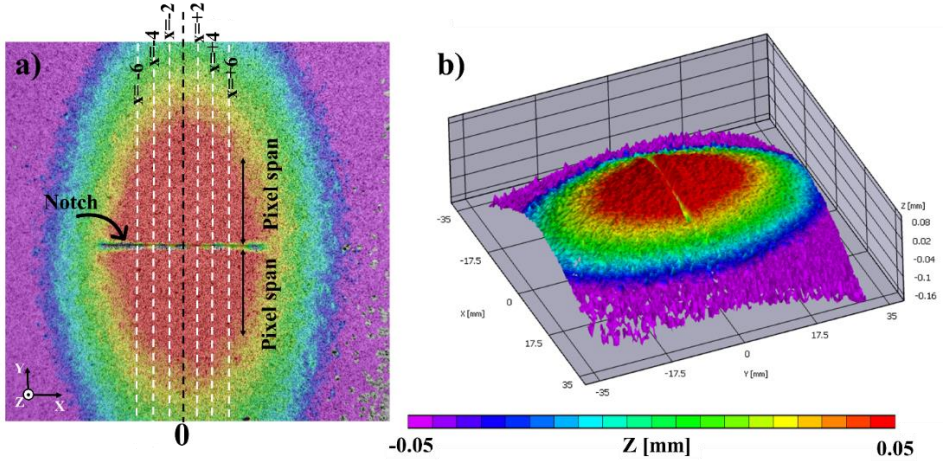


Figure 5-8- 3D-DIC images of out-of-plane displacement (all dimensions are in mm).

The most critical parameter in the present approach is the crack mouth rotation angle, which is gained through a regression analysis. The Ordinary Least Squares (OLS) method is employed to estimate linear regressions of the crack mouth surface profile. Briefly, in this method the sum of the squared distances between each data point and a corresponding point on the regression line is calculated and minimized. However, there are two critical issues involved in the calculation based on the regression model. First, estimations based on the least squares regression are known to be highly sensitive to data outliers. Therefore, to achieve a robust regression analysis, outliers should be eliminated before further analysis. Second, to collect the pixels for generating the regression model, the “pixel span” should be defined and chosen carefully (See Figure 5-8-a). As shown in Figure 5-8-b, deformation in Z direction is significant in the area around the crack shown in red color, and it is reasonable to consider only the pixels inside this area for the regression model. If any pixel from outside this zone is included in the regression model, the accuracy of the model outcome, rotation angle, can be adversely affected.

First, outliers should be identified among the pixels. However, there is no precise definition for an outlier. Further investigation of the DIC output revealed that outliers mostly occur in very close proximity of the notch (Figure 5-9), where due to the presence of the discontinuity digital image correlation becomes less reliable. It is furthermore observed that the zone containing outliers becomes larger with increase in applied force and thus larger deformation in Y axis (tension axis). Maximum deformation occurs at the latest stage of the tensile test, so pixels which act as outlier

in the last picture of the DIC analysis are visually identified and their quantity assumed as the maximum number of outliers permitted. Then, again for the last picture, a backward-stepping algorithm is performed to identify outliers. The procedure is based on the hypothesis that after deleting all outliers, deleting the next pixel will not increase the R^2 value significantly. Subsequently, identified outlier pixels are automatically eliminated in all other pictures by a dedicated MATLAB code. The procedure to eliminate the outliers is a delicate process affecting the accuracy of the proposed measurement technique. Elimination of more pixels as outliers may increase the quality of the regression model fit but as a direct consequence CMOD and CTOD should be measured at relatively remote locations from the crack. Therefore, eliminating more pixels than the above determined maximum number of outliers may lead to an underestimation of both CMOD and CTOD in DIC based measurements.

For the second issue, determining pixel span, the definition of a constant pixel distance is desired to allow easy comparison between the various specimens. The procedure to derive a suitable pixel distance will be explained in the following section.

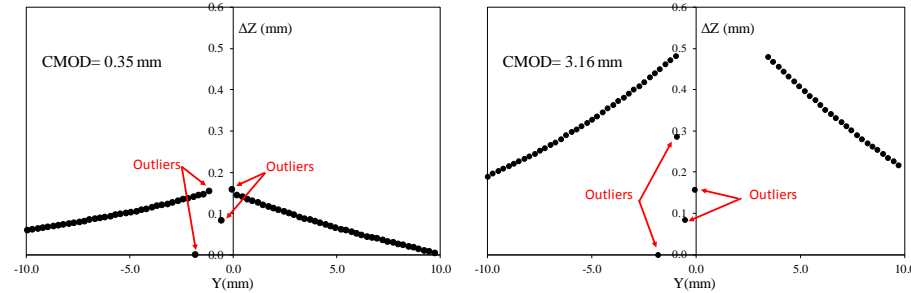


Figure 5-9- Out-of-plane displacement (ΔZ) versus deformed coordinate along Y axis, for two stages of the test with identification of the outliers in the data points.

The finite element model of a medium-scale flat plate containing a semi-elliptical single notch is employed in this section. The aim is to perform a parametric study, as shown Table 5-1, to evaluate the concept of CTOD determination by surface deformations for a wide range of conditions. For each simulation, CTOD has been calculated employing two methods. First using the 90-degree intercept calculation (δ_{90}), and second based on calculation of the surface rotation angle (θ) using the out-of-plane displacement (ΔZ) and the regression model using equation 5-2 (δ_{θ}). This calculation has been repeated assuming different pixel spans at different loading levels and at different points along the crack front. The experimental validation of this model, for the sake of consistency, is provided in section **Error! Reference source not found.**

Having extracted the out-of-plane displacement of a few points near the crack, a line can be generated by linear regression and its slope can be converted to the rotational angle, as described in the previous section. Although such a line can already be generated by two points, a robust approach requires a larger number of data points. To allow a sufficient collection of data points in a consistent manner and to ensure the

ease of application of the method, the regression is conducted in a predefined range of data points, referred to as pixel span.

Table 5-1: Simulation matrix.

Parameter	Values
Crack depth (a)	3, 5 and 7 mm
Crack length (2c)	14 and 28 mm
Thickness of the plate	10, 20 and 30 mm
Yield Strength	480, 530, 600 MPa
Yield to tensile ratio (Y/T)	0.7, 0.8

The optimum value of pixel span is the result of a trade-off, which can be understood from considering the extremes. If only the very first pixels close to the crack are considered, there is a high chance of error in calculation due to the presence of outliers and the relative importance of measurement scatter. However, linear regression based on a very long pixel span will not successfully capture the local profile change near the crack mouth. A case by case defined pixel span would make the measurement procedure cumbersome and undermine the robustness of the technique because the results would become user dependent. Therefore, a fixed pixel span value is desirable. Considering the above, the optimum value for pixel span is the longest possible distance from the crack that allows an accurate regression study to be conducted.

The R^2 value of the linear regression of the surface profile is opted as the criterion to select an accurate regression model and consequently proper pixel span for CTOD measurements using the surface displacement. To generate more output for evaluation, the FE model has been employed in a parametric study comprising various configurations of crack geometries and material properties in order to define a robust pixel span appropriate for a wide range of crack configurations and material properties. Table 5-1 demonstrates the simulation matrix. Power-law strain hardening has been assumed, according to the well-known Ramberg-Osgood equation. This stress-strain model is characterized by its yield strength (0.2% proof stress) and strain hardening exponent (higher values corresponding with less strain hardening).

Figure 5-10 demonstrates R^2 values of surface profile regressions for different pixel span values normalized against crack depth. Figure 5-10 shows that R^2 drops significantly as pixel span increases, which reflects that out-of-plane displacement is linear near the crack but curved at a certain distance. These results show that pixel span values equal to and less than $a_0/2$ have R^2 values larger than 0.99 (the majority even exceeding 0.999) which is assumed to indicate a suitable fit.

Having used R^2 as a measure to select the best fitting regression model (Figure 5-10), a pixel span equal to half of crack depth ($a_0/2$) appears to be a suitable choice. This tentative conclusion is based on two arguments. First, shorter values of pixel span involve fewer data points (particularly for shallow cracks), which reduces the robustness of the regression model. Secondly, increasing pixel span above $a_0/2$ leads to a drop in R^2 value which corresponds to a poorly fitted regression model.

Besides R^2 , the CTOD measurement accuracy should also be verified in the above defined pixel span range. To this end, it is helpful to compare δ_θ from a pixel span equal to $a_0/2$ with δ_{90} measured inside the crack (Figure 5-11). For lower CTOD levels, δ_θ overestimates δ_{90} ; for higher CTOD levels it underestimates δ_{90} . In general, the differences are limited to less than 15%.

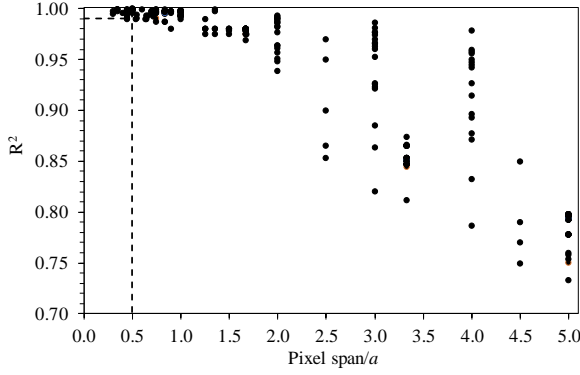


Figure 5-10: R^2 values for different normalized pixel spans.

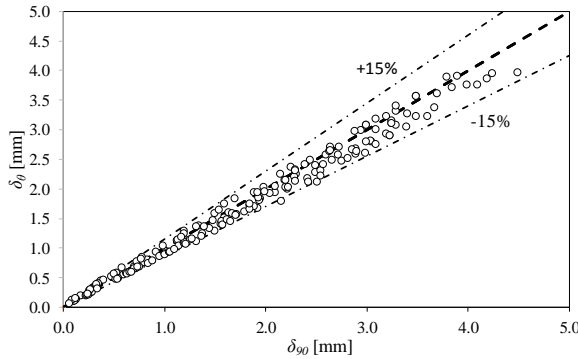


Figure 5-11: δ_θ compared to δ_{90} , taking pixel span= $a_0/2$

As an example, Figure 5-12 shows out-of-plane displacement profiles extracted at the center of the notch for the specimen with $a_0 = 5$ mm, at different deformation levels. The out-of-plane displacement increases with the level of specimen deformation. Note that the profile is not fully symmetric at both sides of the $X=0$ line. The degree of asymmetry is very small (noting the difference in scale of the vertical and horizontal axes). It is assumed that the specimen and/or camera system were mounted with a little angular misalignment. Since the average value of rotational angle at both sides of the notch is used in the CTOD calculation, the effect of asymmetrical deformation is supposed to be cancelled out.

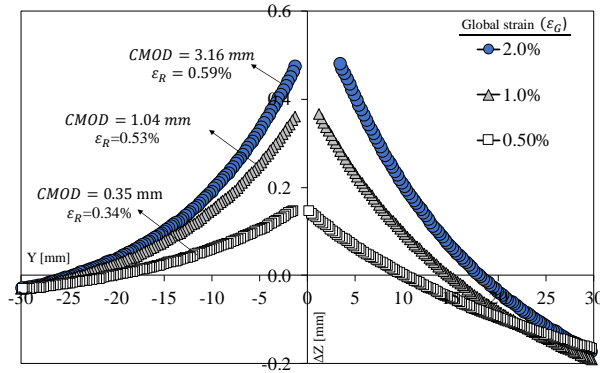


Figure 5-12- Surface profile as out-of-plane displacement ΔZ at various global and remote strain levels versus deformed Y-coordinate for the tensile test on a specimen with initial notch depth 5 mm.

Having determined the pixel span to be $a_0/2$, corresponding δ_{DIC} CTOD values have been accordingly calculated (equation 5-2) and compared with CTOD measurements in replica cross sections (referred to as δ_{Rep}) and FE simulation results (referred to as δ_{90}). Both δ_{DIC} and δ_{Rep} were obtained using the 90-degrees intercept method. Figure 5-13 shows four example replica cross sections at various loading levels for the specimen with $a_0 = 5$ mm. It can be seen that the crack exhibits blunting at the first stage of the test followed by ductile tearing. CTOD and CMOD are similar for most of the test, due to the relatively small rotation of the crack flanks.

Figure 5-14 to Figure 5-16 plot the different CTOD measurements versus CMOD for all three tests. There is a near to perfect agreement between both experimental CTOD results (based on DIC and replica), implying the robustness and accuracy of the DIC based CTOD measurement. Although the FE procedure does not consider ductile crack extension and only simulates the blunting effect, it has a strong agreement with the experimental results until the first observation of ductile tearing. Following, the FE simulated CTOD values slightly underestimate the experimental measurements.

As previously discussed, the DIC measurement can be applied to measure the CTOD at all points along the crack front. Figure 5-17 plots CTOD measurements by DIC and replica along the crack front at three different CMOD levels. Unlike the replica measurements, which could only be carried out in few discrete slices, the DIC measurement was conducted at a larger number of positions to generate a CTOD plot along the crack front. Two observations are made:

- The agreement between replica and DIC based CTOD measurements is highly satisfactory at all common positions.
- The DIC based technique indicates that CTOD drops towards the ends of the notch, which is intuitively logical.

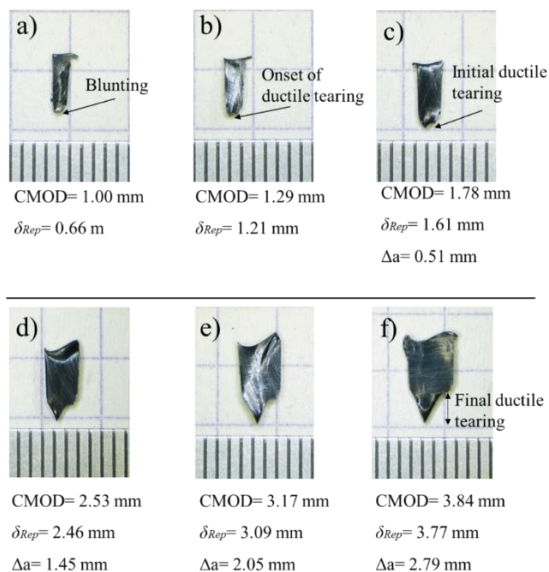


Figure 5-13- Example slices of replicas (extracted at $X = 0$ mm) at different stages of the tensile test for a specimen with initial notch depth equal to 5 mm.

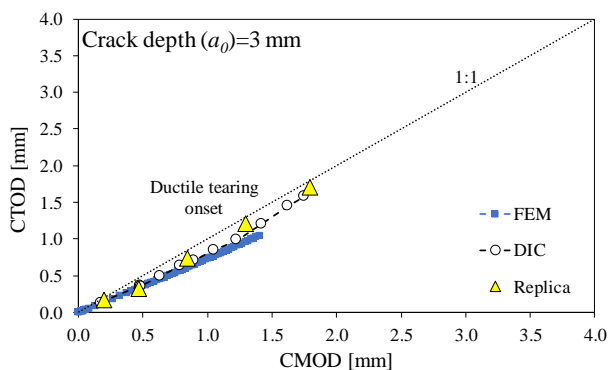


Figure 5-14- CTOD versus CMOD graph comparing DIC, Replica and FE results for 3 mm deep crack.

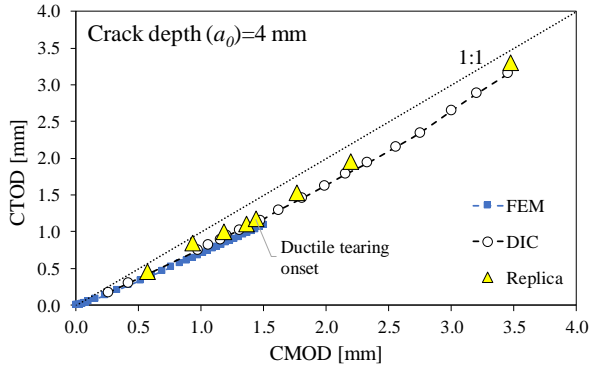


Figure 5-15- CTOD versus CMOD graph comparing DIC, Replica and FE results for 4 mm deep crack.

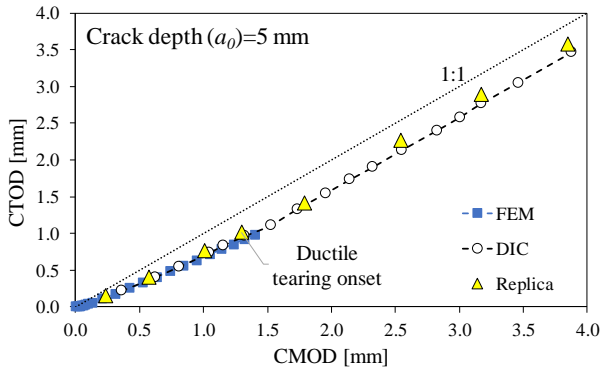


Figure 5-16- CTOD versus CMOD graph comparing DIC, Replica and FE results for 5 mm deep crack.

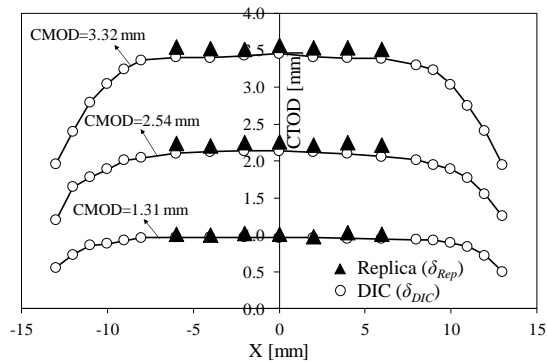


Figure 5-17- CTOD along the crack front at different CMOD levels for the test on a specimen with initial crack depth equal to 5 mm.

Figure 5-11 provides evidence that the proposed technique has a sufficient robustness to measure CTOD over a wide range of crack depths, lengths, plate thicknesses and material properties. It can also be observed that at higher CTOD levels, δ_θ marginally underestimates the CTOD. The FE results shown in Figure 5-18 for the specimen with $a_0 = 5$ mm, illustrate that θ_1 and θ_2 progressively increase as the crack blunts out (ductile tearing is not simulated) and CMOD increases. In the experiment, the onset of tearing significantly alters the angles as well as the CTOD value. Referring to Figure 5-13, starting from a CMOD level around 1.7 mm when the ductile tearing initiates, both θ_1 and θ_2 start to decrease and become almost equal. This observation shows that up to the onset of ductile tearing the CTOD value is dominated by increase in θ_2 corresponding to a rotation around the plastic hinge. However, after the onset of tearing the angle remains almost constant (marginally declines) and considering equation 5-2, the CTOD increases due to tearing. Crack flank rotation no longer has a significant contribution on the CTOD.

The observed good agreement between the angles θ_1 and θ_2 indicates that the assumption of perpendicular crack flanks is valid and explains the good agreement between DIC and replica measured CTOD values already observed in Figure 5-16-Figure 5-14. The decrease of angles after the onset of ductile tearing also explains why in later stages of the test CMOD and CTOD magnitudes become very similar. In addition, the capability of 3D-DIC to accurately measure the rotation angle (θ_2) highlights the possible application of this method for the detection of onset of ductile tearing. The moment that θ_2 starts to decrease marginally or remains constant at increasing load, identifies the onset of ductile tearing.

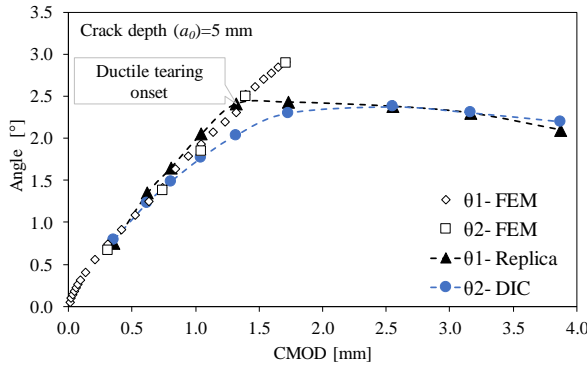


Figure 5-18- Comparing θ_1 and θ_2 from FE and experimental results at different CMOD values.

5.3. Small-scale model validation

5.3.1. Specimens and testing procedure

SENT and (asymmetrically notched) DENT specimens have been extracted from an API-5L X70 pipe, outside diameter was 42 inch (1067 mm) and thickness was 15.9 mm. Through-thickness notches were introduced by fine saw cutting,

producing an initial notch tip radius equal to 0.075 mm (half of the cutting blade's thickness). In total, seven specimens were prepared with two identical through thickness side edge notches (Figure 5-19). Among them, five specimens have two identical non-coplanar notches, each with different out-of-plane distances between the notches. The sixth specimen contained two coplanar identical notches; this is a conventional double edge notched tension specimen (DENT). The last specimen was a single edge notched tension (SENT) specimen which is used as reference (see Table 1). In figure 5-19, H denotes the out-of-plane distance between two notches and for double notched specimens, $2W$ is the specimen width and $T = W$ is the specimen thickness. In the experiments, H/W was varied from 0 to 3 in the following order: 0, 0.7, 1.0, 1.3, 2.0 and 3.0; notch depth a was kept constant at $0.4W$. The same notch depth in terms of a/W was applied in the SENT specimen, its width being W (i.e. half the width of the double notched specimens). Total length and daylight length of the specimen were kept at $20W$ and $14W$, respectively (see Table 7-1).

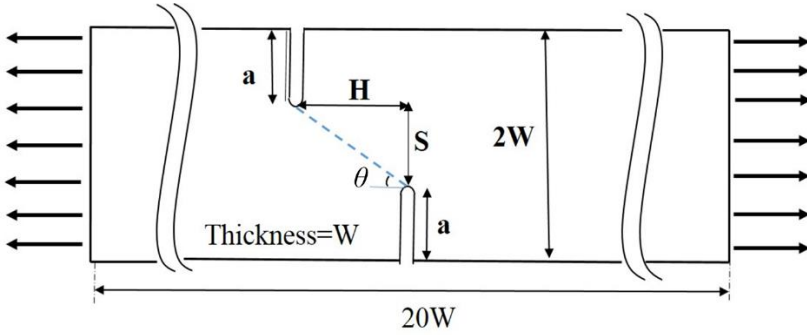


Figure 5-19: Schematic overview of specimen's geometry.

The specimens were clamped by hydraulic grips with restrained rotational degrees of freedom, and then loaded at constant displacement rate mode (0.02 mm/sec). The tests were continued beyond necking and stopped when the force dropped back to 85% of its maximum value. Figure 5-20 shows one of the specimens after the tensile test. The results of DIC measurements are first verified in comparison with clip gauge measurements and then used to verify the FE model and describing the interaction behavior.

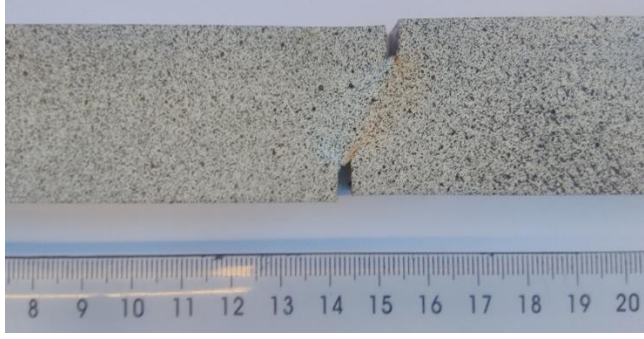


Figure 5-20: Specimen with H/W=0.7 distance between the notches shown after the test.

5.3.2. DIC validation

In order to verify the DIC measurements, crack opening displacement (COD) has been evaluated since this parameter can be directly measured with a clip gauge. The lower clip gauge, as mentioned earlier, is mounted on two knives with 2 mm height above the specimen's top edges, whereas the measurable zone for DIC starts around 1 mm away from the specimen edge. Assuming straight notch flanks (i.e. rigid rotation around a plastic hinge at the crack tip), two lines at both sides of the notch starting at 4 mm below the edge and ending at 1 mm below the edge (the boundary of measurable zone) are assumed. Subsequently, the lines are extrapolated for another 3 mm till the top of the knives (two dashed red lines in Figure 5-21). Then assuming that triangles A and B in Figure 5-21 are equal, U_{+2} (representing COD) can be calculated according to equation 5-3 and this value is compared with clip gauge readings. Using the same principles and basic trigonometry, CMOD could be calculated as well (equation 5-4).

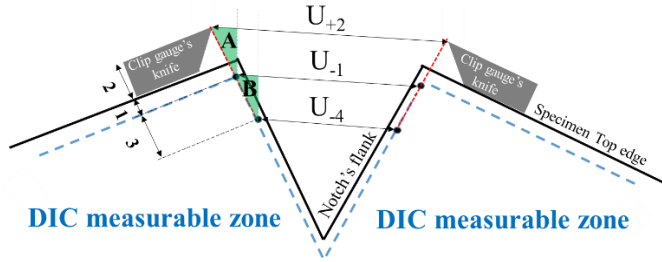


Figure 5-21: DIC measurable zone and clip gauge position for verifying the DIC based COD measurement (units are in millimeter).

$$COD = U_{+2} = 2U_{-1} - U_{-4} \quad 5-3$$

$$CMOD = (4U_{-1} - U_{-4}) / 3 \quad 5-4$$

Figure 5-22 shows the comparison of U_{+2} calculated using DIC measurements and the same value measured directly by the clip gauge for all specimens. In specimens with $H/W=2$ and $H/W=3$ an almost perfect 1:1 agreement over the entire measurement range can be observed. However, In $H/W=0$ a divergence is noted between both methods with increasing value of U_{+2} . The same trend was observed in CMOD by Weeks et al. in a SENT specimen [31]. This slightly diverging error for $H/W=0$ with increasing CMOD can be explained by possible effects of plastic deformation around the notches which affect the obtained displacements through DIC (i.e. U_{-1} and U_{-4}).

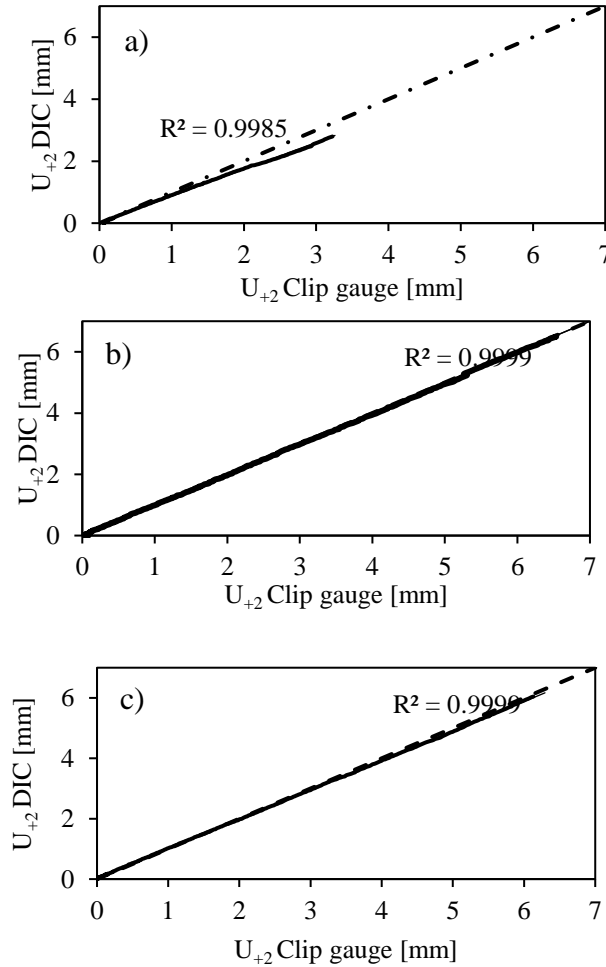


Figure 5-22: DIC validation: plot of clip gauge measured COD vs. COD from DIC: a) $H/W=0$, b) $H/W=2$, c) $H/W=3$

5.3.3. FE model validation

The FE modelling approach needs experimental validation. Constitutive behavior was implemented by a pointwise definition of the experimental stress-strain curve as shown in Figure 5-23 (more details can be found in Table 5-2). An incremental J2 plasticity scheme, which adopts isotropic hardening and the von Mises yield criterion was used. Effects of non-linear geometrical deformation (large strain analysis) were taken into account by activating the ‘nlgeom’ option in ABAQUS.

In this study, the CTOD versus remote stress (load divided by un-notched cross section) response has been opted to verify the model. CTOD and remote stress were chosen because they are unaffected by the compliance of the universal test rig and because both are relevant with respect to a fracture mechanics analysis. Figure 5-24 shows comparisons between numerical and experimental results of CTOD versus remote stress, the latter being normalized against yield strength. The developed model uses a stationary crack approach (i.e. crack growth is not accounted for). Therefore, upon ductile crack initiation, the experimentally determined normalized stress drops after the maximum load point. Since the numerical model is not valid after crack initiation, FEM results are not shown beyond the maximum load point. As apparent from Figure 5-24, in all experiments one flaw eventually opens as reflected in its dominating CTOD. The satisfactory agreement reported in Figure 5-24 for initial yielding (i.e. prior to ductile tearing) is accepted as a first validation of the finite element model.

Table 5-2: Material properties for specimens used in experimental investigations.

Grade	Yield strength (R _{p 0.2})	Ultimate tensile strength (R _m)	Uniform elongation	Y/T
X70	479 MPa	615 MPa	10.32%	0.779

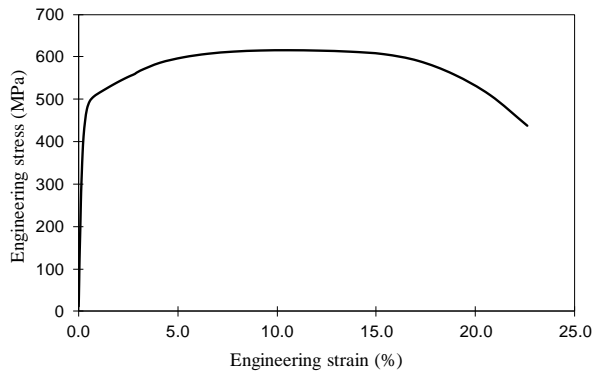


Figure 5-23: Experimentally determined stress-strain curve used in small scale FE model validation.

In addition to force and CMOD, the FE model is verified by comparing strain distributions. This comparison is vital for the following analysis of interaction based on strain and deformation discussed in chapter 7.

In this study, equivalent plastic strain is opted to represent the strain distribution around the two adjacent flaws. The very same definition will be used in chapter 7 for defining so-called “strain concentration bands”. Assuming monotonic loading, points of maximum equivalent plastic strain relate with points of maximum equivalent von Mises stress, as isotropic J_2 plasticity relates both according to the work hardening observed in uniaxial tensile loading. Equivalent plastic strain (ε_{eq}^P) is a monotonically increasing scalar value calculated incrementally as a function of the plastic component of the rate of deformation tensor:

$$\varepsilon_{eq}^P = \int_0^t \dot{\varepsilon}_{eq}^P dt \quad 5-5$$

in which

$$(\dot{\varepsilon}_{eq}^P = \sqrt{\frac{2}{3} \dot{\varepsilon}_{ij}^P \dot{\varepsilon}_{ij}^P}) \quad 5-6$$

Since equivalent plastic strain is a strain tensor invariant, it can be assumed that the coordinate system is oriented along the directions of principal strains (denoted as ε_1^P , ε_2^P and ε_3^P) and then equation 5-5 can be written as follows:

$$\varepsilon_{eq}^P = \sqrt{\frac{2}{3} ((\varepsilon_1^P)^2 + (\varepsilon_2^P)^2 + (\varepsilon_3^P)^2)} \quad 5-7$$

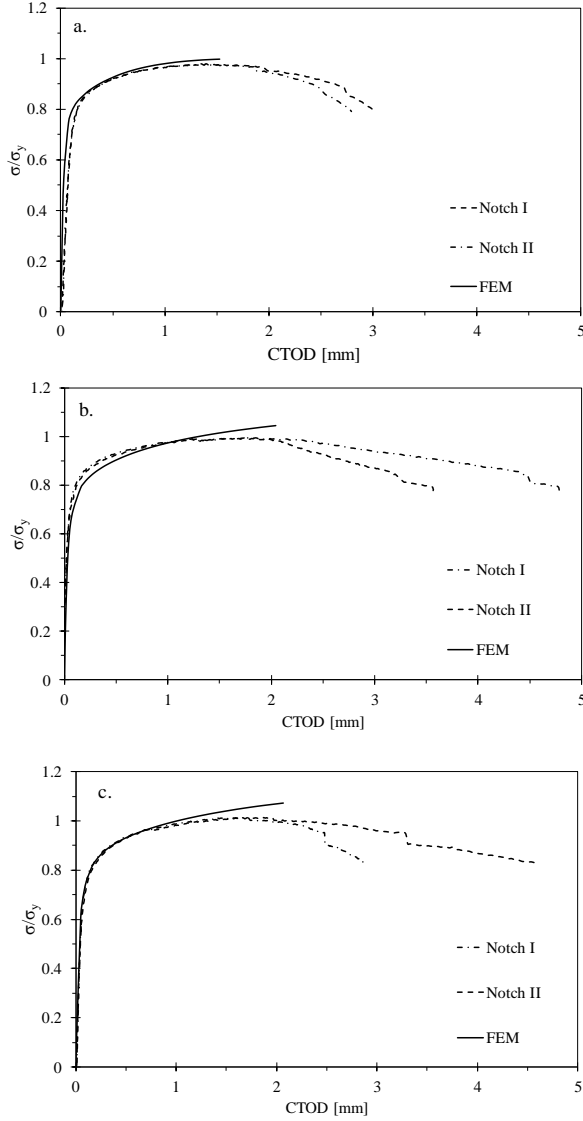


Figure 5-24: CTOD versus normalized remote stress validation graphs: a) H/W=0, b) H/W=2, c) H/W=3.

Strain measurements obtained by DIC do not allow to distinguish between plastic and total strain, therefore in this study equation 5-7 will be used for equivalent total (rather than plastic) strain. Finally, by assuming incompressibility (theoretically valid for plastic strain; assumed here for total strain) and thus substituting ε_3 with $-(\varepsilon_1 + \varepsilon_2)$, equation 5-8 can be obtained for equivalent total strain ε_{eq} . Similar assumptions have been adopted in other notched tension test studies supported by full-field strain analyses [16,17].

$$\varepsilon_{eq} = \sqrt{\frac{4}{3}(\varepsilon_1^2 + \varepsilon_2^2 + \varepsilon_1 \varepsilon_2)}$$

In conclusion, equation 5-8 allows estimating equivalent total strain (from now on referred to as equivalent strain) on the basis of principal surface strains, which can be readily measured by means of DIC.

In Figure 5-25, the Equivalent strain patterns of three specimens are shown at three different stages during the test: at an early stage when the pattern starts to appear, when the maximum force is reached, and at the end of the test when force dropped back to 85% of the maximum load. More in depth comparisons between the experimental and finite element strain patterns are provided in chapter 7.

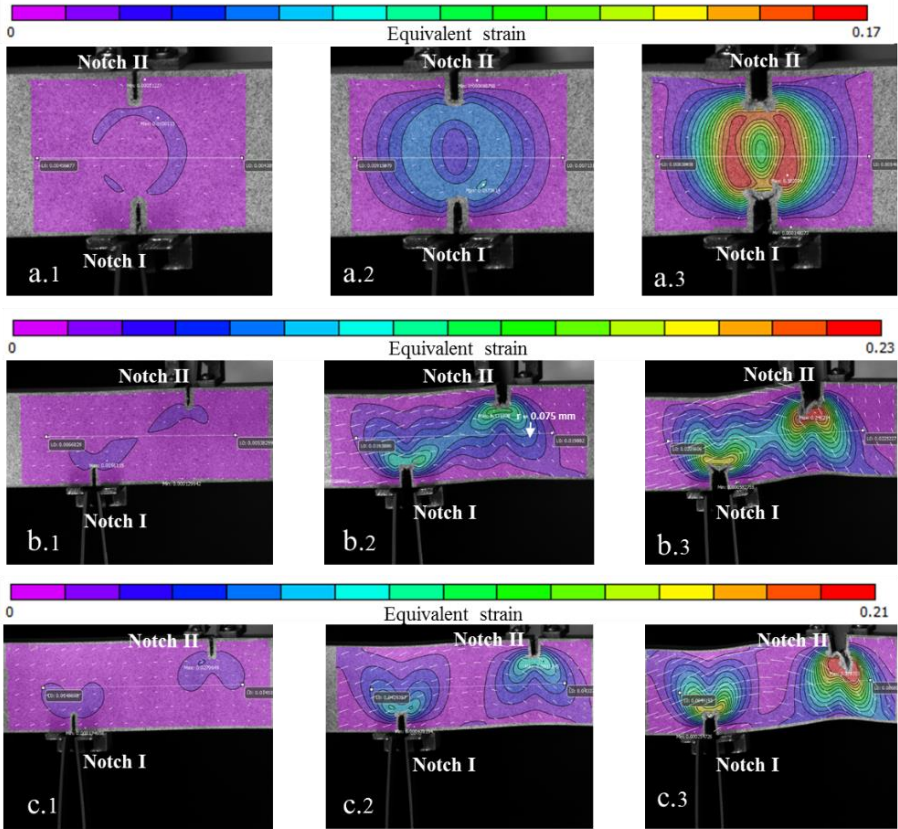


Figure 5-25- Equivalent strain pattern graphs: a) $H/W=0$, b) $H/W=2$, c) $H/W=3$. 1) At the early stages of the test, 2) When maximum force is reached, 3) When the force dropped to 80% of its maximum.

In Figure 5-25, it can be observed that in the specimen with $H/W=0$ (symmetrically notched, conventional DENT specimen) from the onset of loading symmetrical strain patterns were generated around both notches and this continued until the end of loading. As expected, both notches have almost equal surrounding strain patterns. In the specimen with $H/W=2$, the strain patterns clearly tended to interact from the beginning as became visible in non-symmetrical strain pattern development. Crack growth from notch II was observed towards notch I. In the specimen with $H/W=3$ interaction between strain patterns did not occur from the beginning and patterns developed quite independently.

The medium-scale FE model is verified in two stages, first by means of a wide plate containing a single surface breaking notch, and subsequently by a plate containing two notches. The former is essential because analytical solutions are typically only available for single notched specimens. In addition, the single notched wide plate is used for developing a novel method for measuring the CTOD by means of DIC, as described in section 5.5. The double notched specimen serves as validation of the FE simulation approach for flaw interaction studies.

5.4.1. Material and specimens

The experimental investigation is based on three specimens with surface notches of varying initial depth a_0 (3, 4 and 5 mm) and constant length of 28 mm. 10 mm thick and 70 mm wide flat plate coupons were sampled from an X70 grade steel pipe. In all specimens, the initial notches were introduced by fine milling in two stages. A first cut was produced by a 0.4 mm thick milling blade with 80 mm diameter, down to 0.5 mm less than the eventual notch depth ($a_0 - 0.5$ mm). The remaining 0.5 mm was then obtained by a sharp blade with 0.2 mm thickness and 40 mm radius. No fatigue-pre-cracking was performed. The specimens were clamped in a 1000 kN universal test rig by hydraulic grips and then loaded under uniaxial tension in constant displacement rate mode (0.02 mm/sec). The tests were continued beyond necking and stopped when the force dropped back to 85% of its maximum value.

5.4.2. DIC configuration and strain measurement

Figure 5-26 shows an example 2D DIC result (longitudinal strain contours) at the last stage of the test on the specimen with 5 mm deep notch. Three virtual extensometers were defined in the DIC post-processing software to measure the global strain (ε_G), remote strain (ε_R) and local strain (ε_L) separately for each specimen, as indicated in the figure. The positions of the extensometers were adopted from suggestions for strain measurements in similar tests [18]. The main purpose of employing 2D DIC in this study is to measure the strains remote from the crack location, which is not possible by the 3D set up which focused on the crack. However, to compare and mutually validate 2D and 3D DIC systems, ε_L is defined in a position that can be measured by both the 2D and 3D DIC camera setups. Figure 5-27 plots the 2D measured and 3D measured local strains (ε_L) and shows that both agree perfectly during all stages of the test.

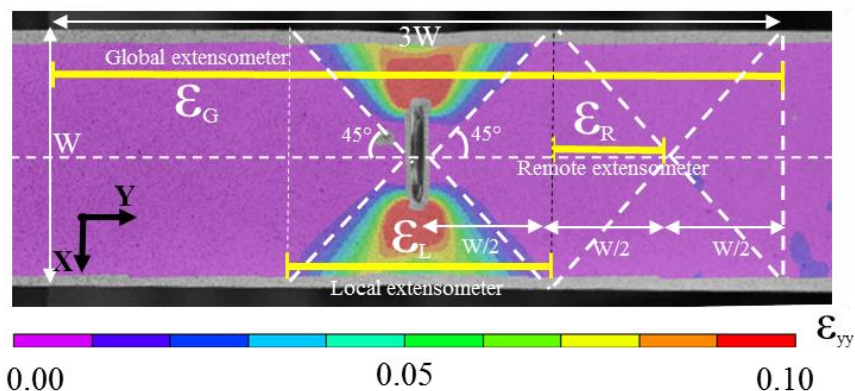


Figure 5-26: 2D-DIC picture illustrating longitudinal strain contours, global (ϵ_G), remote(ϵ_R) and local (ϵ_L) virtual extensometers for the last stage of a tensile test on a specimen with 5 mm deep notch

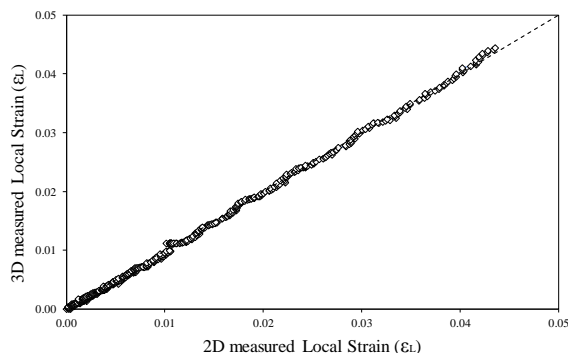


Figure 5-27: Comparison of 2D and 3D measured local strain (ϵ_L) for specimen with $a_0 = 5$ mm.

5.3.4. FE model validation by experimental results

Different outputs of the finite element model have been validated against experimental results for the specimen with $a_0 = 5$ mm. A first validation is provided in Figure 5-28, depicting numerical and experimental force-CMOD plots. The slight decrease in experimental test load at certain intervals corresponds to interruptions for silicone replica casting. The initial agreement is highly satisfactory. Around 1.5 mm CMOD, the numerical and experimental load records start to diverge due to the absence of ductile tearing in the finite element simulation. Figure 5-29 plots a second validation, in terms of force versus remote strain. Again, the agreement is acceptable up to the point where the notched section collapses, at which point the experimental remote strain stabilizes.

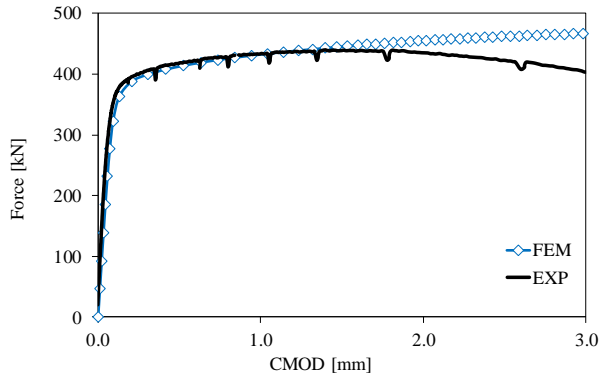


Figure 5-28- Force versus CMOD results of experiment and finite element simulation for a specimen with initial notch depth equal to 5mm.

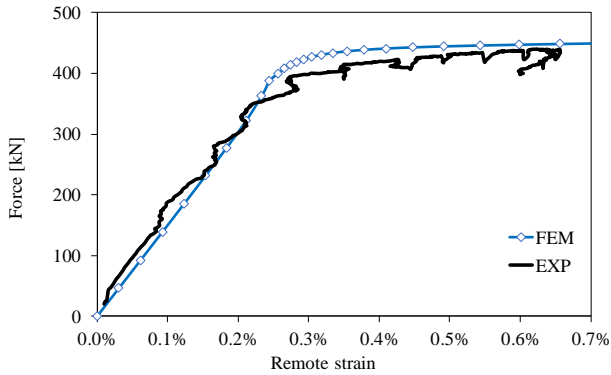


Figure 5-29- Force versus remote strain of experiment and finite element simulation for a specimen with initial notch depth equal to 5mm.

As the final validation, Figure 5-30 shows the notch profiles measured on silicone replicas before the onset of ductile tearing in three specimens with different crack depths and compares them with FE simulation results. The crack profile deformation is reasonably predicted by the FE model and in all three specimens the crack flanks remain highly linear.

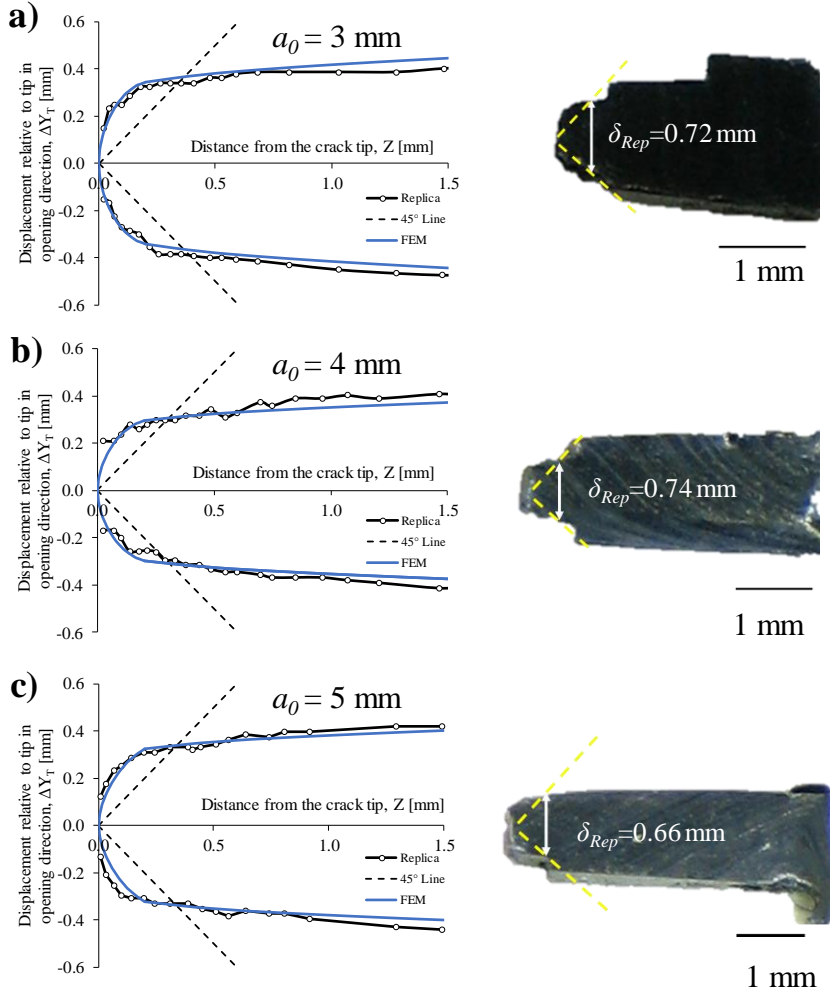


Figure 5-30: Comparisons of crack opening profiles obtained from silicone replicas and FEM analyses at the same level of CTOD for a) $a_0=3$ mm, b) $a_0=4$ mm and c) $a_0=5$ mm.

Recall from section 5.2.4, it is crucial for the accuracy of profilometry CTOD measurement that the crack (notch) flank remains linear even after onset of ductile tearing. Figure 5-31 demonstrates the final measured crack profile on a replica after ductile tearing for the specimen with $a_0=5$ mm. It is evident that the flank retains its linearity and therefore the assumption is considered to hold for the entire trajectory of the tests. Notably, it can be expected that in material with higher strain hardening the crack profile deformation, particularly at the very crack tip, might be non-linear, as reported by Zhu et al. [19]. This can also be observed in the work of Kawabata et al. [20–22] where crack tip deformations of low and high strain hardening materials have been depicted.

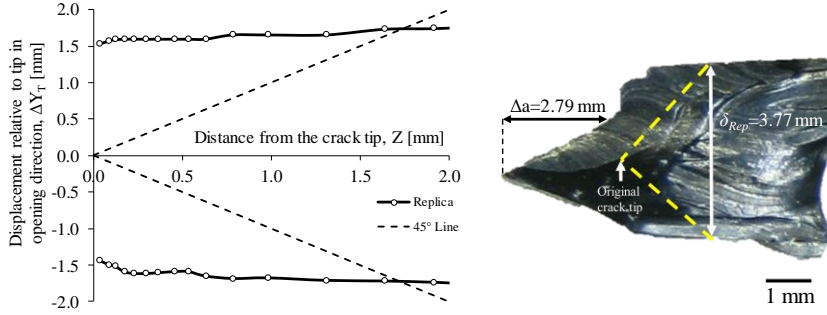


Figure 5-31: Crack opening profile of specimen with $a_0=5$ after final ductile tearing.

5.3.5. Validation with the analytical solution

The FE model results in term of crack driving force have been verified with analytical solutions. The analytical solution of Newman and Raju [23] for calculating the stress intensity factor of a single semi-elliptical surface breaking notch has been opted for this validation study. In ABAQUS basically, K_I is calculated using the J -integral results. For that purpose, a shape factor (f_i) is defined using equation 5-9:

$$f_i = \sqrt{\frac{E'}{\pi a} \frac{J_{el}}{\sigma_m^2}} \quad 5-9$$

(J_{el}) is the elastic J-integral extracted from the very first increment of the FE calculation, a is the maximum notch depth measured at the center of the semi-ellipse. Conveniently, $E' = E/(1 - \nu^2)$ for assumed plane strain conditions and σ_m is remote membrane stress. Poisson's ratio (ν) is assumed to be 0.3. Theoretically, f_i relates with SIF mode I (K_I) according to Equation 5-10:

$$K_I = f_i \sigma_m \sqrt{\pi a} \quad 5-10$$

Figure 5-32 shows the comparison between the dimensionless shape factor calculated by the analytical solution and the same extracted from the FE model. The agreement is close to perfect, yet there are slight differences close to the surface. This is assumed to stem from the fact that contour regions for J calculation are not perfectly perpendicular to the crack front, and probably simply numerical deviations due to mesh discretization. However, since the agreement is acceptable, K_I calculation of the model is assumed to be verified for the next analyses. This also confirms that assumption of blunt notch is valid for K_I calculation.

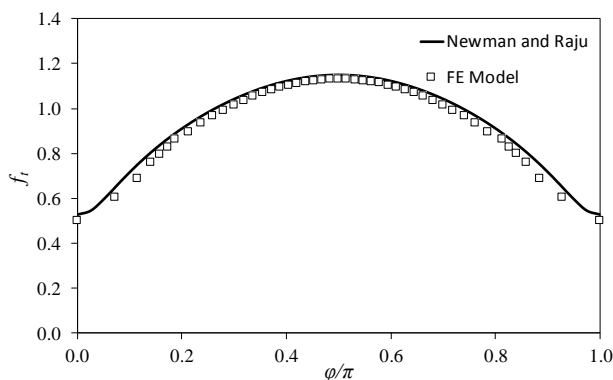


Figure 5-32: Comparison between f_i calculated by FE model and analytical solutions by Newman and Raju [23].

5.4. Medium scale (wide plate) model validation by double notched specimen

In addition to the validation above in presence of a single notch, the medium scale model requires a specific validation for multi-notched specimens. This is essential to provide sufficient certainty about the FE model's applicability for flaw interaction studies. In this validation procedure, X70 spiral welded pipe material has been used to fabricate medium wide plate specimens. The width and thickness of the specimen are 100 mm and 10 mm respectively as shown in the schematic drawing of Figure 5-33. Two notches are introduced in the specimen using the same procedure as described for the single notched wide plate specimen. Table 5-3 shows the length of the notches and (vertical/horizontal) separation distances between them. Specimens are categorized in terms of their notches being coplanar (CP) or non-coplanar (NC) and in terms of their separation distances, either S (horizontal distance) in CP specimens or H (vertical distance) in NC specimens.

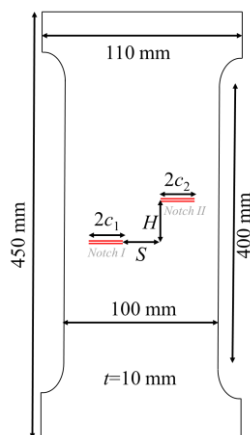


Figure 5-33: Double-notched wide plate specimen schematic.

Table 5-3: Notch related dimensions of the multi-notched MWP specimens.

No.	Specimen Tag	$2c_1$	$2c_2$	H	S
1	CP1	20 mm	20 mm	0 mm	1.5 mm
2	CP4	12 mm	32 mm	0 mm	4 mm
3	CP12	20 mm	20 mm	0 mm	12 mm
4	NC12	20 mm	20 mm	12 mm	12 mm
5	NC24	20 mm	20 mm	24 mm	12 mm
6	NC36	20 mm	20 mm	36 mm	12 mm

Again, a stereo-DIC system has been employed for full-field surface strain measurement, as well as out-of-plane displacement around the notch for the sake of CTOD measurement. A 2D-DIC camera setup was installed at the back side of the specimen to measure the global strain as well as the ligament failure and notch penetration moments. At certain intervals silicone replicas have been taken of both notches to measure their ductile growth and as a benchmark for CTOD measurements.

5.4.1. Non-coplanar notches

Figure 5-34 shows the comparison between FE and experimental results in terms of the evolution of remote stress versus strain. Due to inherent inhomogeneous behavior of the spiral welded pipe, strain at a remote location from the notch cannot be reliably measured, although normally it is preferred over global strain due to its independency from the crack opening. Since the pipe manufacturing process involved, consists of various rolling stages, the pipe material does not show fully homogenous behavior. The effects hereof are most noticeable in strain distribution. Therefore, to avoid the effect of an arbitrary strain distribution on the results, global strain is opted for strain-based comparisons. Further details about spiral welded pipe characteristic in strain-based design can be found in the PhD dissertation of Koen Van Minnebruggen [24]. Figure 5-35 shows the same comparison for the evolution of remote stress versus CMOD highlighting the local behavior of the notches instead of global specimen strain.

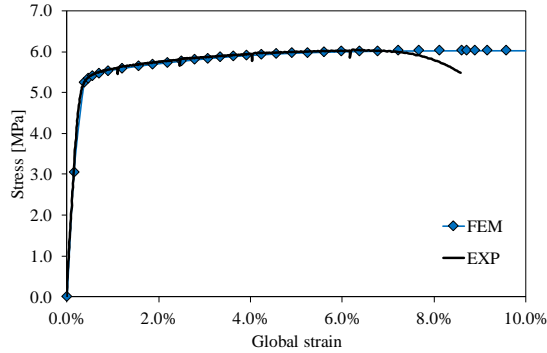


Figure 5-34: Remote stress versus (global) strain curve for NC24 specimen comparing FE and experimental results.

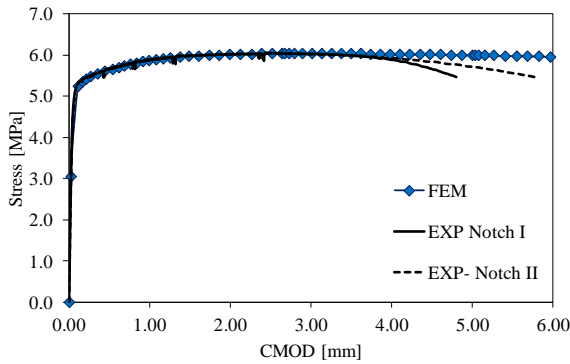


Figure 5-35: Remote stress versus CMOD curve for NC24 specimen comparing FE and experimental results.

While the agreement between the FE and experimental results in terms of stress-strain response as depicted in Figure 5-34 is essential for validation, it is not sufficient for strain-based investigation. It is known that crack opening parameters (e.g. CMOD, CTOD) are very sensitive to applied strain (far more than stress is), particularly in high strain hardening steels like those normally used in contemporary pipelines. Considering the inherent base material variation in pipe steels, although obtaining a perfect agreement between FE and experiment results in terms of the above parameters is very cumbersome, a certain level of agreement is desired. Figure 5-36 illustrates the comparison between FE and experimental results (both notches) in terms of CMOD and global strain. It can be observed that up to a value for global strain around 6%, the agreement is satisfactory. However, after this point, when crack extension started, the FE results deviate from the experimental results. It is worth to mention that between 6-8% global strain, although the CMOD versus strain evolution does not show full agreement, the stress versus strain evolutions (Figure 5-34) remain in agreement. In other words, the validity of FE results in predicting the crack opening, in strain-based design are limited to the onset of ductile tearing, while they can be

used for predicting force until even higher levels of strain. Figure 5-34 also shows that both notches have an almost identical crack opening during the test, which implies that they have very similar depth and length (as intended).

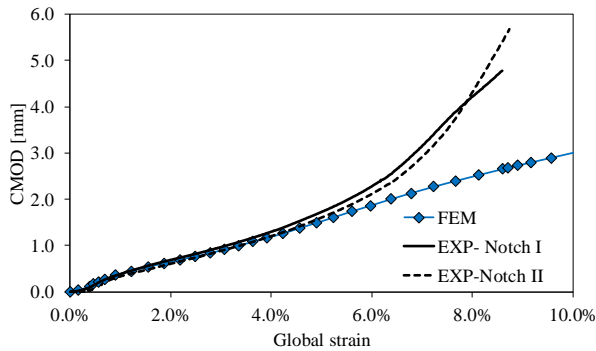


Figure 5-36: CMOD versus global strain curve for specimen NC24 comparing FE and experiment results.

Another comparison is made for FE and experimental results of CTOD versus CMOD. The relation between these two is known to be, from theoretical considerations, linear and its slope depends mainly on material strain hardening and crack depth. Figure 5-37 shows the comparison of FE and experimental results in which a good agreement can be observed. (CTOD has been experimentally measured by the DIC-based profilometry method described in section 5.2.4)

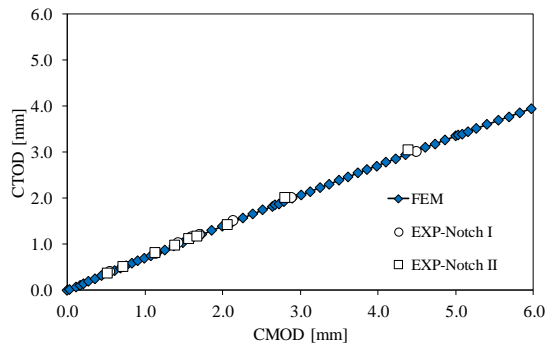


Figure 5-37: CTOD versus CMOD curve for specimen NC24 comparing FE and experiment results.

5.4.2. Coplanar notches

Due to the inherent complexity of flaw interaction, it is reasonable to assume that occurrence of interaction can significantly affect plastic deformation, fracture controlling parameters and stress/strain fields surrounding the flaws. Therefore, to

find out if the FE model is valid in case of severe interaction, a second experimental validation procedure was conducted using the results of the CP1 specimen, which had two coplanar notches positioned very close to each other (1.5 mm). Referring to Chapter 3, this configuration is categorized as interacting according to all of the main ECA guidelines. Similar to the previous part of the validation procedure, first remote stress versus global strain is compared in Figure 5-38, and then remote stress versus CMOD of both notches is compared in Figure 5-39. In both graphs a satisfactory agreement can be observed between FE prediction and experimental results. In Figure 5-40, CMOD versus strain is plotted for botch notches, and as was observed for specimen NC24 here a good agreement between FE and experiment results can be observed before the onset of failure (around global strain equal to 4%). Finally, Figure 5-41 shows that FE prediction of the relation between CTOD and CMOD agrees with experimental results.

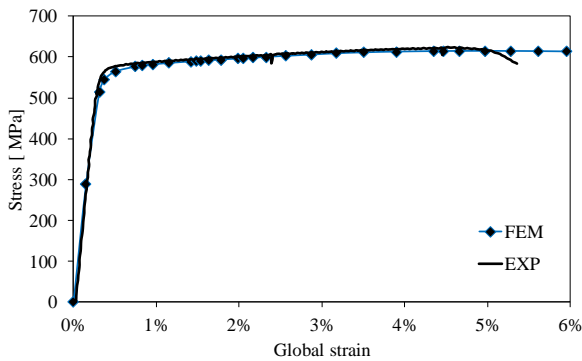


Figure 5-38: Remote stress versus (global) strain curve for specimen CP1 comparing FE and experimental results.

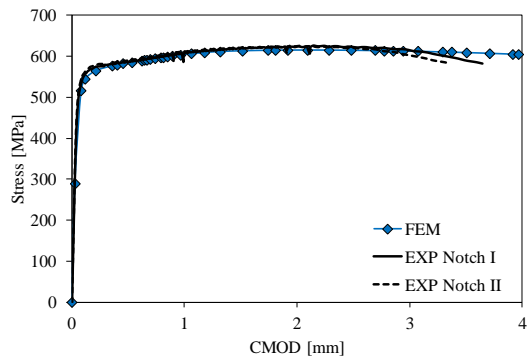


Figure 5-39: Remote stress versus CMOD curve for specimen CP1 comparing FE and experimental results.

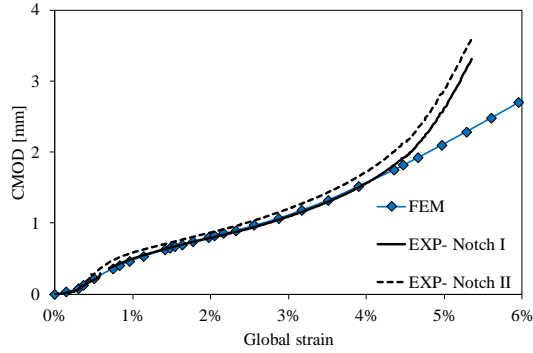


Figure 5-40: CMOD versus global strain curve for specimen CP1 comparing FE and experiment results.

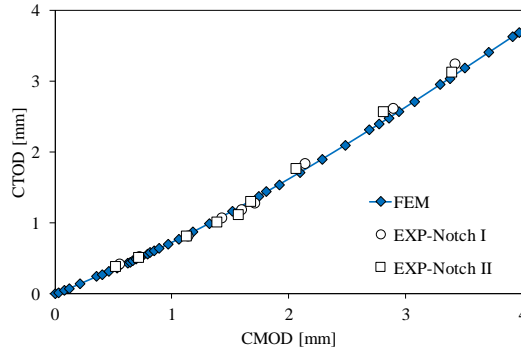


Figure 5-41- CTOD versus CMOD curve for specimen CP1 comparing FE and experimental results.

5.5. Conclusion

To sum up, this chapter reviewed the experimental procedure used in the present study. The experiments were aimed to gain an in depth understanding about the interaction phenomenon, in addition to verifying the FE models. In the course of this study, it turned out that available methods for measuring CTOD are not suitable for case of two closely located surface notches, since clip gauges blocks the optical access to the notches which is required for DIC measurement. To address this challenge, a novel technique for CTOD measurement along the entire crack front of surface notches has been developed based on surface profilometry using stereoscopic DIC. With this technique, and other measurements based on 2D/3D-DIC, clip gauges and crack replicas two finite element models, namely small scale (through thickness notched) and medium scale (wide plate) models are validated by comparing their results with tailored experiments. The models' outcome in terms of force, crack driving force and strain have been compared with the experimental results and good agreements have been achieved up to the onset of ductile tearing.

Since the final purpose of the medium scale model is to simulate flaw interaction, further attention has given to validate the models with two interacting and non-interacting notches. In addition, the medium scale model has been validated in terms of stress intensity factor by an analytical solution from literature. Validation procedures in terms of CTOD response versus strain, which is known as the most sensitive and challenging validation procedure in strain based design, in addition to stress-strain, stress- CMOD, and CMOD-CTOD have shown satisfactory agreements.

References

- [1] British Standard. BS8571:2014 Method of test for determination of fracture toughness in metallic materials using single edge notched tension. BSI Stand Publ 2014.
- [2] Verstraete MA, Denys RM, Van Minnebruggen K, Hertelé S, De Waele W. Determination of CTOD resistance curves in side-grooved Single-Edge Notched Tensile specimens using full field deformation measurements. *Eng Fract Mech* 2013;110:12–22. doi:10.1016/j.engfracmech.2013.07.015.
- [3] Moore PL, Pisarski HG. Validation of methods to determine CTOD from SENT specimens. Twenty-second Int. Offshore Polar Eng. Conf., International Society of Offshore and Polar Engineers; 2012.
- [4] Tang H, Macia M, Minnaar K, Gioielli P, Kibey S, Fairchild D. Development of the SENT test for strain-based design of welded pipelines. *Proc. 8th Int. Pipeline Conf. IPC*, 2010.
- [5] Zhu X-K, Joyce JA. Review of fracture toughness (G, K, J, CTOD, CTOA) testing and standardization. *Eng Fract Mech* 2012;85:1–46. doi:10.1016/j.engfracmech.2012.02.001.
- [6] Østby E, Nyhus B, Thaulow C. Small-scale Testing of the Effect of Embedded Defect Position in the Thickness Direction of an X65 UOE Pipe. *Isope* 2011;8:593–9.
- [7] Østby E, Hauge M, Levold E, Sandvik A, Nyhus B, Thaulow C. Strain capacity of SENT specimens--Influence of weld metal mismatch and ductile tearing resistance. *Proc ISOPE2008, Seventeenth Int Offshore Polar Eng Conf* 2008;8:6–11.
- [8] Østby E, Sandvik A, Levold E, Nyhus B, Thaulow C. The Effects of Weld Metal Mismatch and Crack Position on the Strain Capacity in SENT Specimens in an X65 Material. *Isope* 2009;1:162–8.
- [9] Hellesvik AO. Fracture Control – Offshore Pipelines JIP Results from large scale testing of the effect of biaxial loading on the strain capacity of pipes with defects. *Isope* 2007;3231–7.
- [10] Tagawa T, Kawabata T, Sakimoto T, Kayamori Y, Ohata M, Yamashita Y, et al. Experimental measurements of deformed crack tips in different yield-to-tensile ratio steels. *Eng Fract Mech* 2014;128:157–70. doi:10.1016/j.engfracmech.2014.07.012.
- [11] Khor W, Moore PL, Pisarski HG, Haslett M, Brown CJ. Measurement and prediction of CTOD in austenitic stainless steel. *Fatigue Fract Eng Mater Struct* 2016. doi:10.1111/ffe.12487.
- [12] Samadian K, Hertelé S, De Waele W. A strain-based approach to study interaction between non-coplanar through-thickness edge notches. *J Strain Anal Eng Des* 2018;0309324718778440.
- [13] Verstraete MA, Hertelé S, Denys RM, Van Minnebruggen K, De Waele W. Evaluation and interpretation of ductile crack extension in SENT specimens using unloading compliance technique. *Eng Fract Mech* 2014;115:190–203. doi:10.1016/j.engfracmech.2013.11.004.
- [14] Fairchild DP, Macia ML, Wang X, Kibey S, Krishnan VR, Bardi H, et al. A Multi-Tiered Procedure for Engineering Critical Assessment of Strain-Based Pipelines. *Int Soc Offshore Polar Eng* 2011;8:698–705.
- [15] Van Minnebruggen K, Verstraete M, Denys R, Thibaux P, De Waele W.

- Determination of CTOD resistance curves in SENT specimens with a tilted notch. 2014 10th Int. Pipeline Conf., American Society of Mechanical Engineers; 2014, p. V004T11A015-V004T11A015.
- [16] Fagerholt E, Østby E, Børvik T, Hopperstad OS. Investigation of fracture in small-scale SENT tests of a welded X80 pipeline steel using Digital Image Correlation with node splitting. *Eng Fract Mech* 2012;96:276–93. doi:10.1016/j.engfracmech.2012.08.007.
 - [17] Hertelé S, Gerven F Van, Naib S, Gubeljak N, De Waele W. Experimental and numerical slip line analysis of welded single-edge notched tension specimens. *Struct. Integr. Procedia Procedia Struct. Integr.*, Catania, Italy: 2016, p. 1763–70. doi:10.1016/j.prostr.2016.06.222.
 - [18] Hertelé S, De Waele W, Denys R, Verstraete M. Investigation of strain measurements in (curved) wide plate specimens using digital image correlation and finite element analysis. *J Strain Anal Eng Des* 2012;47:276–88.
 - [19] Zhu X-K, McGaughy T. Testing and application of fracture resistance curves using SENT specimens for low and high strain hardening steels. In: Hertelé S, editor. *Technol. Futur. ageing pipelines conferances*, Ghent: 2018.
 - [20] Kawabata T, Tagawa T, Kayamori Y, Ohata M, Yamashita Y, Kinefuchi M, et al. Applicability of new CTOD calculation formula to various a₀/W conditions and B×B configuration. *Eng Fract Mech* 2017. doi:10.1016/j.engfracmech.2017.03.027.
 - [21] Kawabata T, Tagawa T, Kayamori Y, Ohata M, Yamashita Y, Kinefuchi M, et al. Plastic deformation behavior in SENB specimens with various crack length to width ratios. *Eng Fract Mech* 2017;178:301–17.
 - [22] Kawabata T, Tagawa T, Sakimoto T, Kayamori Y, Ohata M, Yamashita Y, et al. Proposal for a new CTOD calculation formula. *Eng Fract Mech* 2016;159:16–34.
 - [23] Newman JC, Raju IS. Stress-intensity factor equations for cracks in three-dimensional finite bodies subjected to tension and bending loads. 1984.
 - [24] Van Minnebruggen K. Experimental-Numerical Study on the Feasibility of Spirally Welded Pipes in a Strain Based Design Context (PhD thesis). Ghent University; 2016.

Flaw interaction evaluation based on crack driving force

6.1. Introduction

In a fracture mechanics framework, interaction between adjacent flaws is assumed to be significant when the crack driving force (CDF) of one flaw is affected substantially by the presence of the other flaw. This is the most acknowledged approach to investigate multiple flaws and is used in most ECA guidelines because of its simplicity and conservatism. Although CDF-based approaches are normally confined to Linear Elastic Fracture Mechanics (LEFM) assumptions (e.g. K_I), various researchers employed the very same procedure to an Elastic Plastic Fracture Mechanics (EPFM) problem by using J -integral and CTOD [1–4]. This chapter discusses the behavior of multiple flaws and the parameters affecting their interaction, based on a CDF approach. Since strain-based design inherently requires considering the effect of material plasticity, the results are mainly investigated using EPFM, but to be consistent with ECA guidelines, K_I based studies are reported as well.

In this chapter first, the effect of flaw idealization on the interaction is investigated by comparing the severity of interaction of two surface flaw (section 6.2), and the conservativeness of re-characterization of the interacting flaw to encompassing flaw for idealized and non-idealized flaw (section 6.2.6.2.1). Then, the interaction in terms of LEFM and EPFM parameters is investigated for two surface breaking flaws and the results are compared with various ECA interaction rules (section 6.2.2). In section 6.3, results of interaction between one surface and one embedded flaw using the element deletion technique are presented in full scale pipe model with internal pressure effects considerations, and finally 6.4 concludes.

6.2. Interaction of two surface breaking flaws

6.2.1. Effect of flaw shape idealization

In recent years, various researchers studied the interaction between adjacent flaws employing experimental, analytical and numerical techniques. In most studies, multiple flaws are idealized into a (semi-)elliptical flaw. Next, by calculating the stress intensity factor for each flaw, the significance of flaw interaction is described by comparing with the SIF of a similar isolated flaw. To extend these studies to elastic-plastic conditions, J -integral and CTOD have been used to characterize flaw interaction [1,3].

It might be questioned whether interaction criteria lead to accurate results when they are applied to more complex shaped flaws. For instance, a long and shallow notch-like flaw, which has a close to rectangular shape, cannot be represented properly by an idealized (semi-)elliptical flaw (recall the example shown in Figure 3.1). Therefore, applying any rule that has been derived from a fracture mechanics analysis assuming a (semi-)elliptical flaw, might underestimate crack driving force of such a long shallow flaw.

Thus, to conduct a reliable structural integrity assessment for a component with complex shaped flaws, the accuracy and conservatism concerning flaw idealization should be systematically investigated. This has a higher importance in case of multiple adjacent flaws because, in contrast to a single semi-elliptical flaw, the most critical point of the flaw (where SIF or J -integral reaches its maximum) is not necessarily located at the deepest point and can even be close to the surface. This distinction is

prominent because close to the surface, differences between the geometry of the bounding rectangle and this of the (semi-)elliptical flaw are more distinct. Therefore, flaw shape idealization has a higher impact on the assessment of interacting flaws.

As a first study of this chapter, this section investigates the interaction between identical coplanar surface breaking flaw pairs, being characterized by equal major dimensions but a different shape. Two configurations are considered: “canoe-shaped” (quarter-circular ends and constant depth elsewhere) and “semi-elliptical shaped”. Previous research by Kamaya et al. showed that the averaged SIF of different surface breaking flaws with complex front shape is almost the same when their areas are the same [5]. The area of a semi-elliptical flaw is 71% of the bounding rectangle while the canoe-shaped flaw comprises 71-100% % of the rectangle’s area, with the exact value depending on the aspect ratio. Therefore, the canoe-shaped flaw is assumed as a more conservative representation of a complex shaped flaw.

The geometries of the surface breaking flaws considered in the present study are shown in Figure 6-1. This figure also shows the definition of the points on the crack front using the parametric angle φ for semi-elliptical (Figure 6-1-a) and canoe-shaped (Figure 6-1-b) flaws. For each flaw, φ is measured from the intersection point of the crack front with the plate surface (the closest one to the adjacent notch). Thus, φ for a flaw with positive X coordinates is measured anticlockwise-positive and φ is measured clockwise-positive for a flaw located at the negative side of the X axis. This definition allows to describe both semi-elliptical and canoe-shaped flaws in a consistent way. To determine the interaction between the pairs, SIF along the crack front is employed for a linear elastic analysis and J -integral is used for an elastic-plastic analysis. Recall from chapter 5 that SIF is derived from the elastic normalized J -integral (J_{el}) by using f_i given by equation 5.9., which is correlated to K_I by equation 5.10.

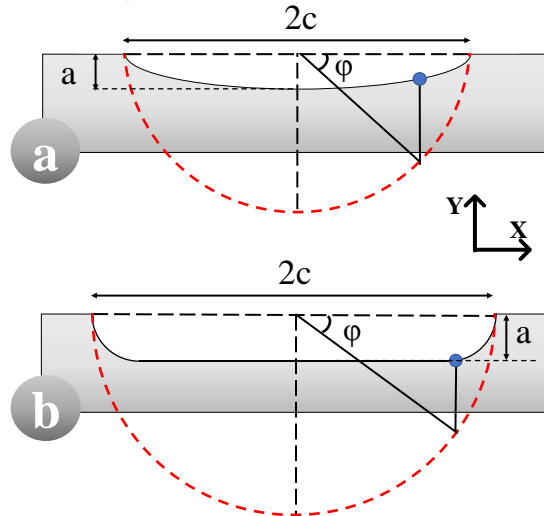


Figure 6-1- Defining points on the crack front using the parametric angle φ for (a) semi-elliptical and (b) canoe-shaped flaw; $\varphi=0$ represents the tip closest to the adjacent flaw.

Considering the above, two interaction factors are defined: γ for elastic analysis based on f_t (equation 6-1) and η for elastic-plastic analysis based on J -integral (equation 6-2):

$$\gamma(\varphi) = \frac{f_t(\varphi)}{f_t^0(\varphi)} \quad 6-1$$

$$\eta(\varphi) = \left(\frac{J(\varphi)}{J^0(\varphi)} \right)^{0.5} \quad 6-2$$

Where $f_t(\varphi)$ and $J(\varphi)$ are mode I normalized stress intensity factor and J -integral value for the flaw pair, respectively. $f_t^0(\varphi)$ and $J^0(\varphi)$ are the same parameters as above, but for a single flaw of the same geometry and under the same loading conditions. Since the (normalized) SIF and J vary as a function of φ , interaction factors are calculated by dividing each value of f_t or J -integral by the corresponding value for the same location (same φ) in the single flaw. Note that, considering equation 5.9 and to make γ and η comparable, square root values of J -integral are used to calculate the elastic-plastic interaction factor.

Two alternative interaction metrics to the factors introduced above also deserve investigation. When it comes to assessing failure, it is reasonable to determine the maximum value of K_I or J along the crack front, and to compare it to the maximum value in case of a single flaw [6]. Therefore, critical interaction factors (γ_{Cr} and η_{Cr}) are defined as follows:

$$\gamma_{Cr} = \frac{\max\{f_t(\varphi)\}}{\max\{f_t^0(\varphi)\}} \quad 6-3$$

$$\eta_{Cr} = \left(\frac{\max\{J(\varphi)\}}{\max\{J^0(\varphi)\}} \right)^{0.5} \quad 6-4$$

For the sake of convenience, notch geometry is described by following dimensionless parameters: $\alpha=a/c$ relates to the aspect ratio of the notch, $\lambda=a/t$ is the normalized notch depth, and S/a is the distance between two notches normalized by notch depth. To study the effect of notch shape on the interaction, both canoe-shaped (Figure 6-2-b) and semi-elliptical notch pairs (Figure 6-2-c) have been modeled. To understand the effect of geometrical parameters on the degree of interaction, various models have been generated automatically employing a devoted Python script. In total 100 pairs of notches were studied along with 20 isolated single notches, in addition to 9 re-characterized notch models of the interacting pairs (in total 129 cases). Table 6-1 summarizes the geometrical parameters.

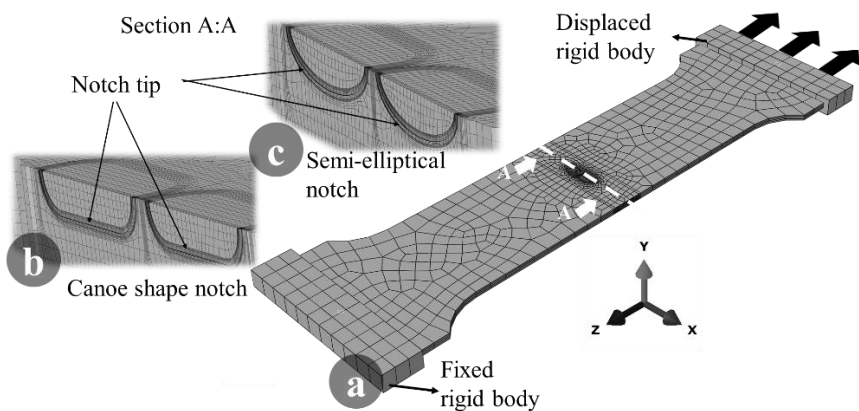


Figure 6-2: (a) Global FE model, (b) canoe-shaped notches, (c) semi-elliptical notches.

Table 6-1: Geometric parameters of FE models to study the effect of shape idealization.

Parameter	Values/ Types	No. of values
Notch shape	Canoe, Semi-elliptical	2
Notch Qty.	1, 2	2
$a=a/c$	0.25,0.375, 0.5	3
$\lambda=a/t$	0.3, 0.4, 0.5	3
S/a	0.5, 1, 1.5, 2, 4	5
n	10, 15	2
	Total notch pair models	100
	Total single notch models	20
	Total re-characterized notch models	9

K_I does not depend on material properties except for Poisson's ratio, which was set to 0.3. For calculating J -integral, an elastic-plastic material with strain hardening exponent n according to the Ramberg-Osgood model in true stress-true strain (σ - ε) terms is considered:

$$\varepsilon = \frac{\sigma}{E} + 0.002\left(\frac{\sigma}{\sigma_y}\right)^n \quad 6-5$$

E , ν (Poisson's ratio), σ_y and n are assumed 200,000 MPa, 0.3, 400 MPa and 10, respectively. In addition, in order to study the effect of strain hardening, a separate study is conducted with two n values, 10 and 15, corresponding to Y/T equal to 0.75 and 0.85, respectively.

Preliminary studies are conducted for sensitivity studies to ensure that the mesh refinements are satisfactory for determination of stress fields. To verify the path independency of the J -integral results, for both canoe-shaped and semi-elliptical geometries, the results of different contours have been compared. The J -integral results are derived from far-field contours, and the calculation procedure is verified with an existing model developed at Soete Laboratory, which by itself had been verified against experimental and analytical results [7,8]. The results are presented for both elastic and elastic-plastic fracture mechanics analyses.

Figure 6-3 shows the elastic interaction factor (γ) for semi-elliptical and canoe-shaped notches. It can be observed that in both cases the SIF is affected significantly at the tip adjacent to the other notch ($\varphi = 0$). When the notches are located very close to each other ($S = 0.5a$, which ASME section XI and BS7910 consider as the interaction onset) the elastic interaction factor increases considerably, and it is slightly higher in case of the canoe-shaped notch. Therefore, it is reasonable to study the effect of interaction at the tip closest to the adjacent notch ($\varphi = 0$). Figure 6-4 plots the elastic interaction factor (γ) of canoe-shaped and semi-elliptical notches for different distances between the notches and various normalized notch depths. Figure 6-4 shows that the canoe-shaped notch has a higher elastic interaction factor compared to its semi-elliptical counterpart. This difference increases when the normalized notch depth is increased and in particular for a lower aspect ratio α . Furthermore, for $\alpha = 0.25$ and very close spacing distances ($S/a=0.5$), the interaction intensities of the canoe-shaped and semi-elliptical notches are almost identical, whereas differences increase for the more distant notches.

Although the tip closest to the adjacent notch has been affected more than any other location along the crack front, it is not necessarily the location with the highest SIF, i.e., the most critical point.

Figure 6-5 plots critical elastic interaction factors (γ_{cr}) for two notch aspect ratios. As shown in Figure 6-5, clearly the influence of interaction on the maximum K_I is less than on K_{II} at the adjacent tip. Additionally, similar to Figure 6-4, the difference between the canoe-shaped and semi-elliptical notch is more distinct for the deeper notches (i.e. higher λ), particularly when the notch has a small aspect ratio. The observed distinctions between the two shapes is prominent, since the canoe-shaped and semi-elliptical notches reach the same interaction intensity at different normalized distances S/a . Thus, canoe-shaped notches experience more significant interaction compared to semi-elliptical notches with equal depth, length and spacing distance.

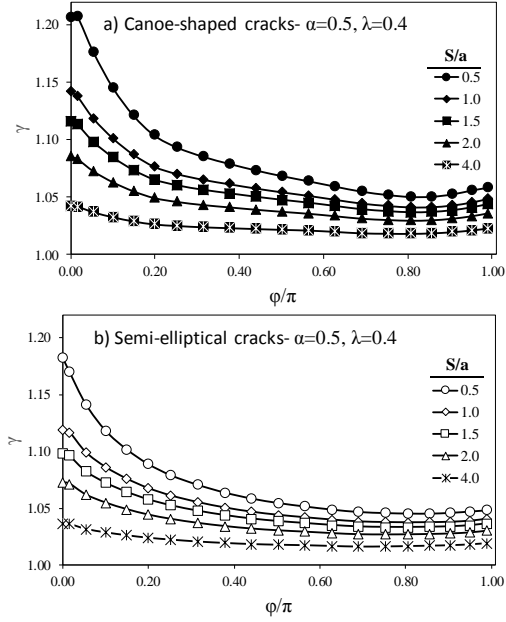


Figure 6-3: Elastic interaction factor for (a) canoe-shaped and (b) semi-elliptical notches.

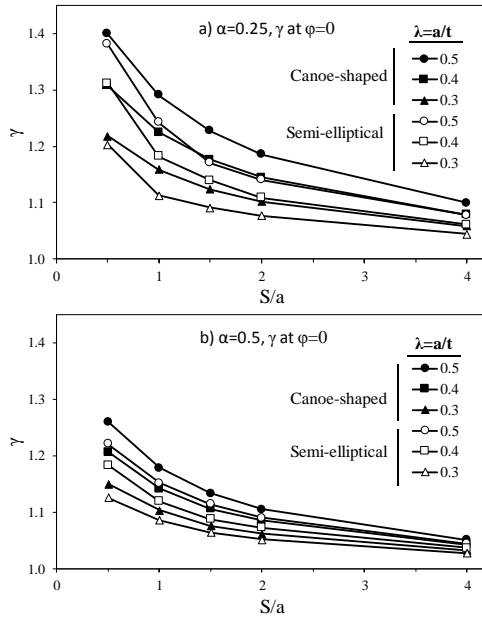


Figure 6-4: Elastic interaction factor at the tip closest to the adjacent notch for (a) $\alpha=0.25$ and (b) $\alpha=0.5$

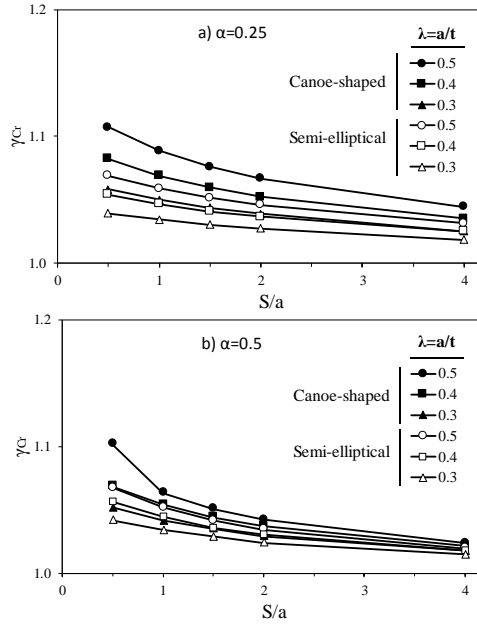


Figure 6-5: Critical elastic interaction factor for (a) $\alpha=0.25$ and (b) $\alpha=0.5$.

Elastic-plastic analyses are carried out using the J -integral. The value of the J -integral depends on the amount of remote stress, contracting to f_t which is dimensionless. Before analyses based on J -integral can be compared two questions should be addressed: first the loading level at which the comparison is to be made; second the point along the crack front where the interaction has the highest intensity. Therefore, for the former the loading level for all the elastic-plastic analyses in this study has been set equal to limit load as per twice elastic slope as described in chapter 2.

Figure 6-6 shows the η value along the crack front for semi-elliptical and canoe-shaped notches at different spacing distances. The magnitude of the elastic-plastic interaction factor (η) is higher than the magnitude of the elastic interaction factor (γ). Like for the elastic interaction factor, the most influenced point due to interaction is the tip closest to the adjacent notch, neglecting the small variation in case of the canoe-shaped notch (Figure 6-6-a). Here, it can be noted that canoe-shaped notch pairs have a relatively higher interaction intensity compared to their semi-elliptical counterparts. Considering very close notch pairs ($S/a = 0.5$), the difference between η for the canoe-shaped and semi-elliptical notches at $\varphi = 0$ is about 4%, quite higher than γ for similar notch pairs located at the same distance (around 1.5%, Figure 6-3). This highlights that not only the intensity of interaction is increased in elastic-plastic analysis, but also the difference between the canoe-shaped and semi-elliptical notch is more pronounced in case of elastic-plastic analysis.

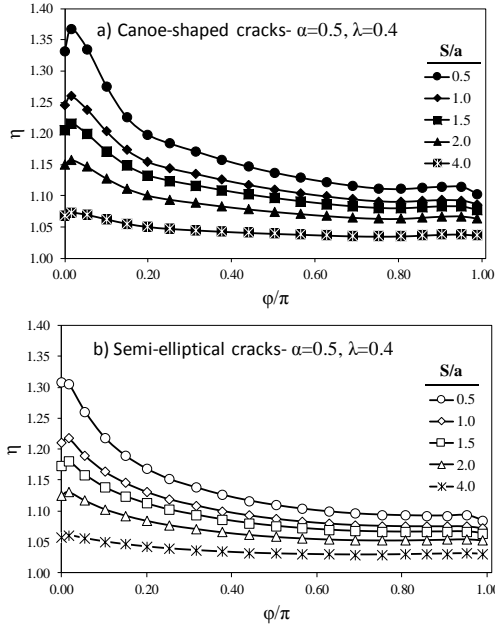


Figure 6-6- Elastic-plastic interaction factor for (a) canoe-shaped and (b) semi-elliptical notches.

Figure 6-7 shows the elastic-plastic interaction factor for different notch aspect ratios α . For lower notch aspect ratios, the inconsistency between canoe-shaped and semi-elliptical notches increases when the aspect ratio decreases. Compared to Figure 6-4, the trend of the graphs is quite similar for γ and η , while the magnitude of the interaction factors and the differences between the two studied shapes are clearly increased in case of elastic-plastic analysis.

The critical elastic-plastic interaction factor (η_{cr}), for two different notch aspect ratios, is shown in Figure 6-8. Like Figure 6-7, for the lower aspect ratios the difference between the two shapes is more evident. Note that in Figure 6-7-a the intensity of interaction is quite similar when the notches are located very close to each other ($S/a = 0.5$). This is where the present criteria in ASME B&PV Code Sec. XI and BS7910 suggest the interaction onset boundary. However, if the critical elastic-plastic interaction factor is considered, the difference between the canoe-shaped and semi-elliptical interaction factors consistently increases as the distance between the notches is decreased.

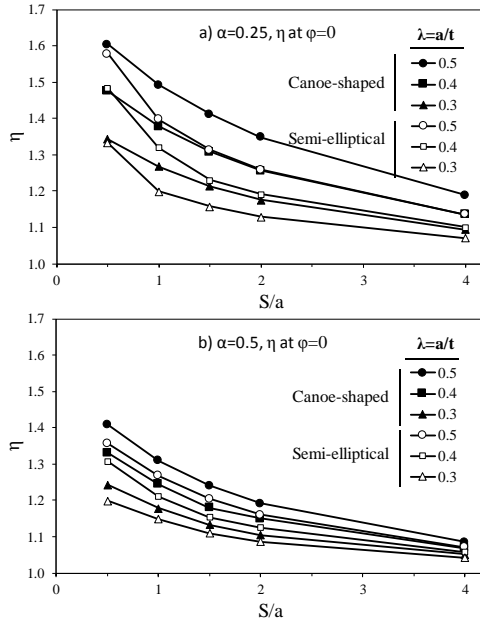


Figure 6-7- Elastic-plastic interaction factor at the tip closest to the adjacent notch: (a) $\alpha=0.25$ and (b) $\alpha=0.5$.

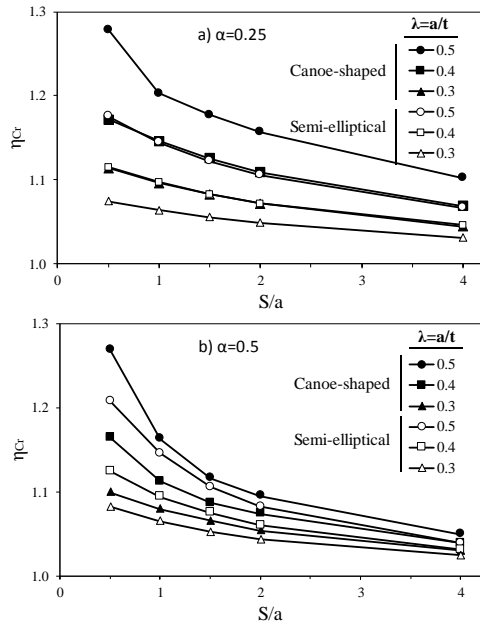


Figure 6-8- Critical elastic-plastic interaction factor: (a) $\alpha=0.25$ and (b) $\alpha=0.5$.

The aspect ratio of the notches also has a significant effect on the inconsistency between the canoe and semi-elliptical flaw shapes. When the notch is deeper, the difference is even more apparent. It can also be concluded that the effect of notch shape is less prominent when shallow notches are introduced. Contrary, for long and deep notches, the difference between the interaction intensity of the two assumed shapes is prominent, when considering elastic-plastic analysis. Additionally, it can be observed that by increasing the notch depths whilst keeping their aspect ratios constant (Figure 6-7 and Figure 6-8), the trend of the interaction graphs is almost similar for both η and η_{Cr} , while their magnitudes are increased. Figure 6-9 shows that the η_{Cr} and γ_{Cr} have an almost linear relationship with constant slope for varying distances between the two flaws. The very same trend can also be observed in Figure 6-10, in which the relation between elastic and elastic-plastic interaction has been plotted for varying notch aspect ratio. It is evident that the geometrical parameters and the distances between the notches do not significantly affect the relation between the elastic and elastic-plastic interaction severity.

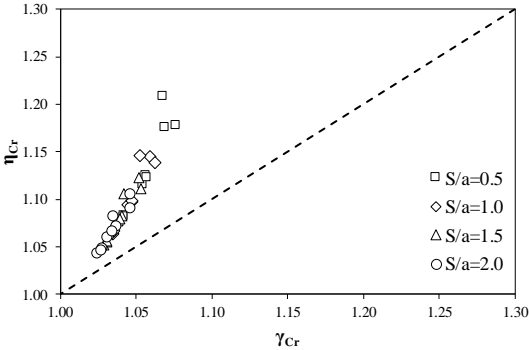


Figure 6-9: Effect of distance on the elastic and elastic-plastic critical interaction factors relation for semi-elliptical flaw.

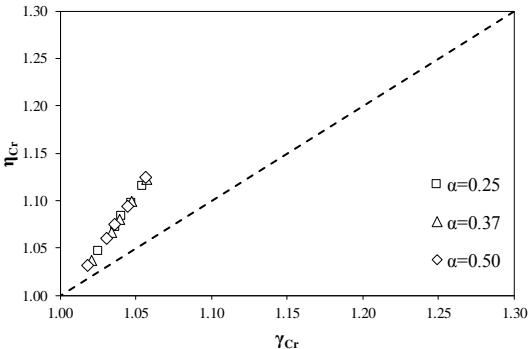


Figure 6-10: Effect of aspect ratio (α) on the elastic and elastic-plastic critical interaction factors relation for semi-elliptical flaw.

The effect of strain hardening on flaw interaction has also been studied. This investigation focuses on η_{Cr} , since γ is unaffected by strain hardening. Four groups of identical notch pairs located at different spacing distance are assumed in this study. First and second groups have an identical strain hardening exponent (n) equal to 10, while the first concerns canoe-shaped notches and the second concerns semi-elliptical ones. As far as the notch shape is concerned, the third and fourth groups are modeled like the first and second group, but their hardening exponents (n) are set to 15. The rest of the material properties are equal to those mentioned earlier. As shown in Figure 6-11, increasing the strain hardening exponent raises the critical elastic-plastic interaction magnitude.

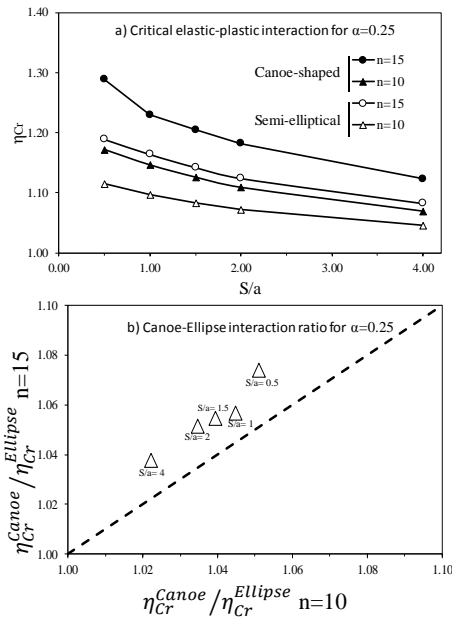


Figure 6-11- Strain hardening effect on elastic-plastic interaction factors.

Figure 6-12 shows that the strain hardening effect on the ratio of the interaction factors of the two shapes is less than 2%, which is not as significant as the effect of geometrical parameters. On the other hand, strain hardening has a pronounced effect on the relation between elastic and elastic-plastic interaction factors as depicted in Figure 6-12. The canoe-shaped and semi-elliptical notches have been studied by different interaction criteria, assuming different fracture mechanics governing parameters (K_I or J -integral), and by changing various geometrical parameters defining the notches.

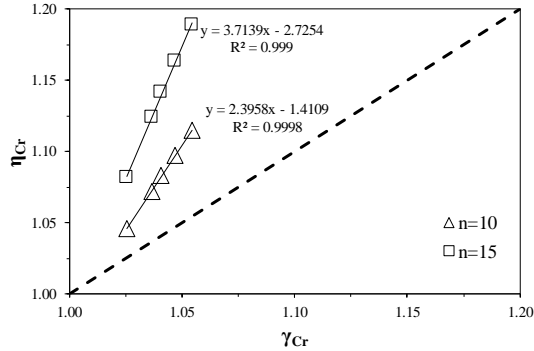


Figure 6-12:Effect of strain hardening on the relation between elastic and elastic-plastic critical interaction factors for semi-elliptical flaws.

The presented results indicate clear differences in the interaction intensity of canoe-shaped and semi-elliptical notch pairs. For example, in case of an elastic analysis, which is the most conventional approach to investigate flaw interaction, the maximum difference between the two shapes in factors γ and γ_{Cr} , can reach to 4%. This can be considered as a significant difference, considering that some literatures suggest 6% increase in SIF as the interaction onset boundary [9]. In other words, such a difference may lead to an underestimation of the severity of the actual flaw interaction, when semi-elliptical idealized flaws are employed in the analysis.

To make a more sound judgment about the significance of the inconsistencies, (critical) interaction factors of canoe-shaped notches are normalized to the values for semi-elliptical shapes, as illustrated in Figure 6-13 (from now on referred to as “inconsistency ratio”). It illustrates to which extent assuming notches to be semi-elliptical can lead to a non-conservative estimation of interaction.

Figure 6-13 compares the (critical) elastic inconsistency ratios for different geometries. From the upper chart in Figure 6-13, it can be seen that there is a marginal correlation between the notch geometry parameters and elastic inconsistency ratio ($\gamma^{Canoe} / \gamma^{Ellipse}$). Contrary to this, the critical elastic inconsistency ratio ($\gamma_{Cr}^{Canoe} / \gamma_{Cr}^{Ellipse}$) has a clear correlation with geometrical parameters. To highlight an example of this correlation, those which are classified as interacting by ASME B&PV code sec. XI and BS7910 are connected by a dashed line. Note that the critical elastic inconsistency ratio is increasing when the distance between the notches is reduced. In other words, in the case of critical elastic interaction, the more significant the interaction becomes, the higher the potential non-conservativeness due to idealization into a semi-elliptical shape.

Figure 6-14 is also quite revealing in several ways. The above graph which plots the elastic-plastic inconsistency ratio ($\eta^{Canoe} / \eta^{Ellipse}$), does not show a significant correlation with geometry of the notch. Contrary to this, the below graph which plots the critical elastic-plastic inconsistency ratio ($\eta_{Cr}^{Canoe} / \eta_{Cr}^{Ellipse}$), illustrates an obvious

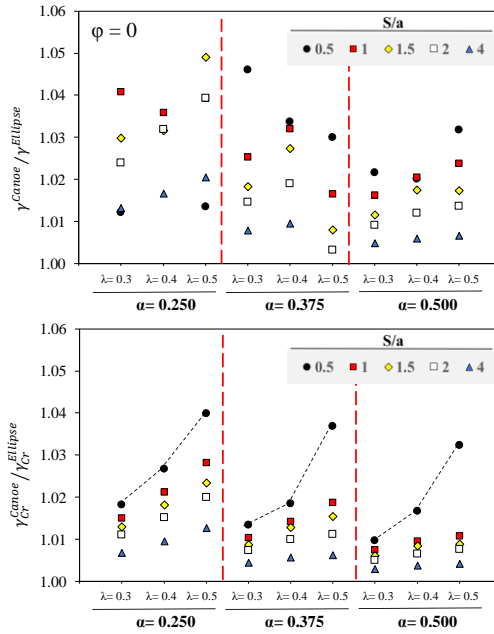


Figure 6-13- Elastic inconsistency ratios for various geometrical parameters.

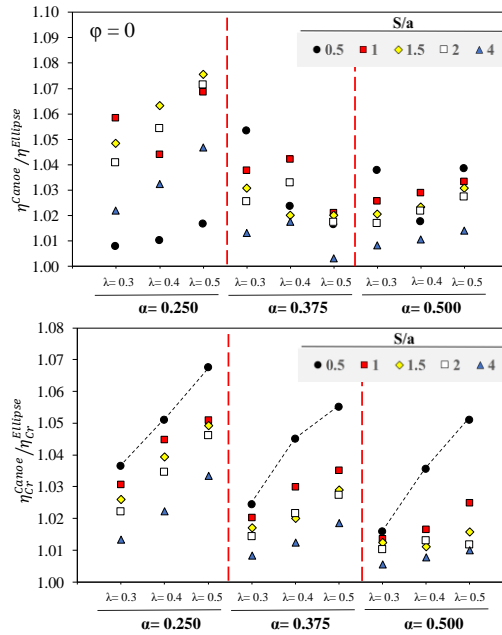


Figure 6-14- Elastic-plastic inconsistency ratios for various geometrical parameters.

correlation with notch shape. To highlight the correlation for very close notches ($S/a = 0.5$), dashed lines connect the points for each a value to each other.

Similar to the observation for the critical elastic inconsistency ratio, here the inconsistency is more significant for very close notches. It is hypothesized that, besides the effect of cross-sectional reduction (which is different for canoe-shaped flaws when compared to semi-elliptical flaws), the local stress distributions of very adjacent notches interact more significantly in the case of canoe-shaped flaws. Whereas the former effect explains the inconsistency in ratios exceeding unity for distant flaws, the latter effect plays a dominant role in escalating the interaction between very close notch pairs.

On the basis of the available numerical results, a linear regression model is suggested only to highlight the significance of each geometrical parameter on the flaw idealization effects to interaction. These equations are not intended to be generic. Since the correlation between the inconsistency ratios can only be observed in the case of critical factors (γ_{Cr} and η_{Cr}), the models described by equation 6-6 (elastic interaction) and equation 6-7 (elastic-plastic) use the ratio of these two factors inside the validity limit of the present study ($0.25 < \alpha < 0.5$, $0.3 < \lambda < 0.5$, $0.5 < S/a < 4$ and $n = 10$):

$$\frac{\gamma_{Cr}^{Canoe}}{\gamma_{Cr}^{Ellipse}} = 0.044 \times \lambda - 0.036 \times \alpha - 0.004 \times (S/a) + 1.019 \quad 6-6$$

$$\frac{\eta_{Cr}^{Canoe}}{\eta_{Cr}^{Ellipse}} = 0.086 \times \lambda - 0.099 \times \alpha - 0.008 \times (S/a) + 1.034 \quad 6-7$$

Figure 6-15 demonstrates that this linear regression model is capable to estimate the inconsistency ratio (between the critical interaction factors), for both elastic and elastic plastic analysis. Clearly, equation 6-6 and 6-7 show that normalized notch depth (λ) and notch aspect ratio (α) are the most important effects. In other words, shallow notches with high aspect ratio are less prone to underestimation due to idealization into semi-elliptical shape, when it comes to interaction assessment.

In addition, the magnitude of the coefficients is clearly higher in case of elastic-plastic interaction, which highlights the fact that the flaw idealization has a more pronounced effect on interaction assessment at higher loads or larger deformations. An increase in strain hardening, in addition to increasing the interaction magnitude, affects the critical elastic-plastic inconsistency ratio. Compared to the geometrical parameters effect, the present study showed that the effect of strain hardening on inconsistency ratio is less pronounced, but it is not negligible.

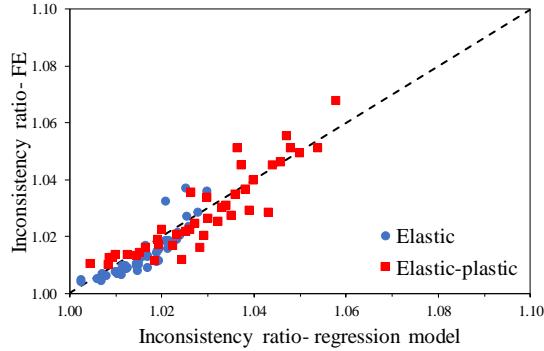


Figure 6-15- Correlation between the regression model and FE results.

Knowing that canoe-shaped flaws have higher interaction than their semi-elliptical counterparts, triggers the question posed at the beginning of this chapter: in case of interaction, does the bounding semi-elliptical flaw conservatively represent canoe-shaped flaws?

To address this question, a new parameter is defined to describe the conservatism involved in re-characterization process. The “global conservatism factor” of the re-characterized bounding flaw (considered semi-elliptical), comparing the maximum crack driving force along the entire crack front ($0 \leq \varphi \leq \pi$) of one of the twin notches (in this section canoe-shaped notch) to that of the bounding notch. This factor should be below unity for a conservative analysis. As this factor is essentially the inverse of the safety factor of the flaw interaction rule, very low values may indicate excessive conservatism.

Figure 6-16 shows the global conservatism factor versus inconsistency ratio, clearly some of the models have conservativeness factor high than unity, which implies that re-characterization of certain canoe-shaped notches into a semi-elliptical bounding notch may be non-conservative. While, clear relation is observed between linear elastic global conservatism factor and inconsistency ratio, global conservatism factor in elastic-plastic material increases with increasing inconsistency ratio.

Figure 6-17 plots the global conservatism factor versus notch aspect ratio (α) and Figure 6-18 plots the same versus notch depth normalized by plate thickness (λ). The results show that global conservatism factor decreases when α is increasing, but it has no obvious correlation with λ . This means, in shallow flaws, it is more likely that due to irregularity in the flaw shape, re-characterization into a semi-elliptical flaw will not be conservative. The fact that this non-conservativeness has been observed both in linear-elastic and elastic-plastic analysis, makes it concerning even for brittle materials.

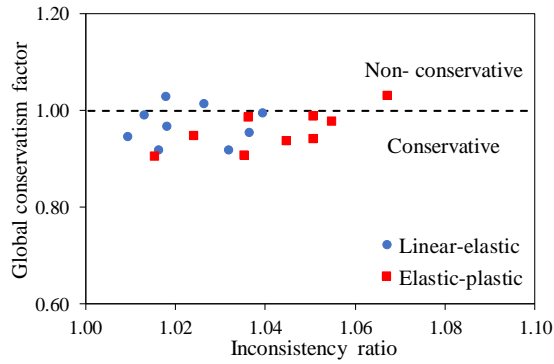


Figure 6-16: Global conservatism ratio versus inconsistency ratio.

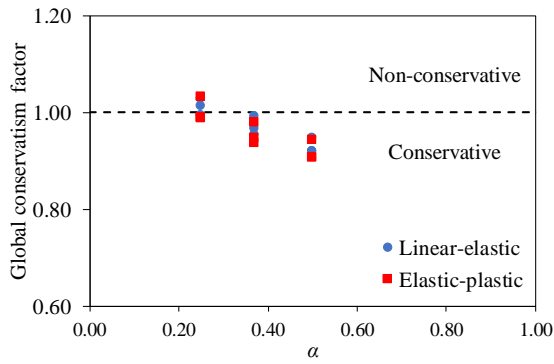


Figure 6-17: Global conservatism ratio versus aspect ratio (α)

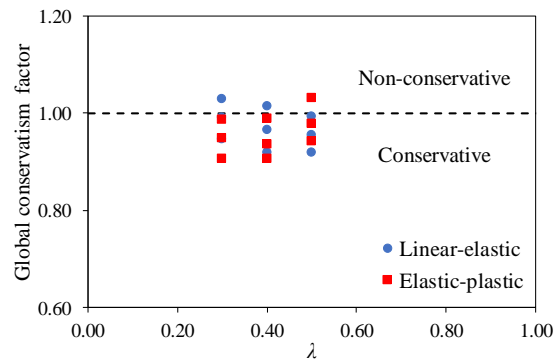


Figure 6-18: Global conservatism versus normalized notch depth (λ)

6.2.2. Elastic-plastic interaction between adjacent surface flaws

This section focuses on scenarios where failure by brittle fracture can be excluded assuming that the toughness of the material (weld metal and HAZ) is sufficiently high to ensure that plastic collapse is the governing failure mode. Interaction criteria for coplanar flaws in various ECA guidelines are summarized in Table 6-2. The observed differences can lead to different assessment of the flaw criticality depending on the choice of ECA procedure.

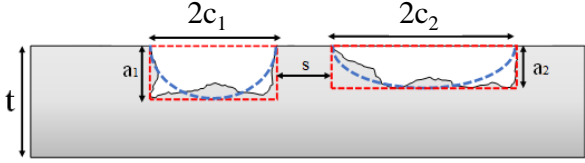
For the shallow notches (having $a/c < 1$) studied in this section, the interaction assessment procedures can be divided into three categories as shown in Table 6-2. Category A consists of guidelines which use notch depth to assess the interaction. Category B contains the only guideline that uses an empirical approach to assess the interaction (EPRG Tier 2). Category C encloses guidelines which consider notch length as the governing parameter for interaction. It is important to state that this is not intended to be a generic categorization of interaction procedures. Indeed, for different flaw geometries and aspect ratios some of the guidelines may use notch depth, length or both to assess the interaction. However, since the present investigation is limited to $a/c < 1$, the proposed categorization allows to highlight the different approaches in interaction assessment for shallow flaws.

In this section, eight different cases are studied. As shown in Table 6-3, the first three cases would lead to interaction according to the criteria of major ECA guidelines in pipeline industry. Both notches are identically long (40 mm) and deep (4 mm) and by changing the spacing distance, the flaw pairs either do meet or do not meet the interaction criteria of a particular ECA guideline. The fourth case is not interacting according to any of the referred ECA guidelines. The fifth case is the same specimen with a single flaw having the same length and depth of the above-mentioned cases and is used as a reference. The last three cases contain re-characterized flaws of the first three cases.

As illustrated in Figure 6-19, the geometrical model is a curved plate with two notches at its center. The curved plate width (arc length) is 300 mm and its thickness is assumed to be 12.7 mm, the rest of assumption are identical to the previous section. The mentioned geometrical assumptions are designed to fit inside all the assessment scopes of the guidelines listed in Table 6-2.

Figure 6-20 plots the normalized SIF of cases 1 to 5 along the crack front. It can be observed that at the tip closest to the adjacent flaw ($\varphi = 0$) the SIF is higher than at the other tip ($\varphi = \pi$). This difference diminishes when the flaws are spaced far enough (case 4), as can be expected. However, although case 4 SIF values at the tips ($\varphi = \pi$ and $\varphi = 0$) are almost equal to the reference case, its SIF value at the deepest point ($\varphi = \pi/2$) is higher. Figure 6-21 plots the elastic interaction factor (ratio to the reference case) for the studied cases. Here, it can be seen that the intensity of interaction is considerably higher at $\varphi = 0$ and there is a significant difference between the intensity of interaction for the various cases.

Table 6-2: Coplanar surface flaws categorization based on different ECA guidelines [4,10–12]



Category	Standard/ Code/ Guideline:	Interaction occurs if:
A	ASME B&PV code sec. XI: 2017 API 579: 2016 BS 7910:2013+A1:2015 (for a_1 / c_1 <u>and</u> $a_2/c_2 \leq 1$)	$S \leq \max (0.5a_1, 0.5a_2)$
B	EPRG Guideline:2014 (Tier 2)	$2c_1 + 2c_2 \leq L_2$ (see equation 3.1)
C	API1104:2013	$S \leq 2c_1$ for $c_1 \leq c_2$ and $a_1 \leq a_2$

Table 6-3:Simulation matrix and categorization based on ECA guidelines.

Size Tag	Spacing Distance (S)	Flaw 1		Flaw 2		Classification as interacting		
		Length (2c ₁)	Depth (a ₁)	Length (2c ₂)	Depth (a ₂)	Cat. A	Cat. B	Cat. C
Case 1	2 mm	40 mm	4 mm	40 mm	4 mm	Y	Y	Y
Case 2	10 mm					N	Y	Y
Case 3	20 mm					N	N	Y
Case 4	30 mm					N	N	N
Case 5	Single Flaw	40 mm	4 mm	-	-	Reference Case		
Case 6	Single Flaw	82 mm	4 mm	-	-	Re-characterized of Case 1		
Case 7	Single Flaw	90 mm	4 mm	-	-	Re-characterized of Case 2		
Case 8	Single Flaw	100 mm	4 mm	-	-	Re-characterized of Case 3		

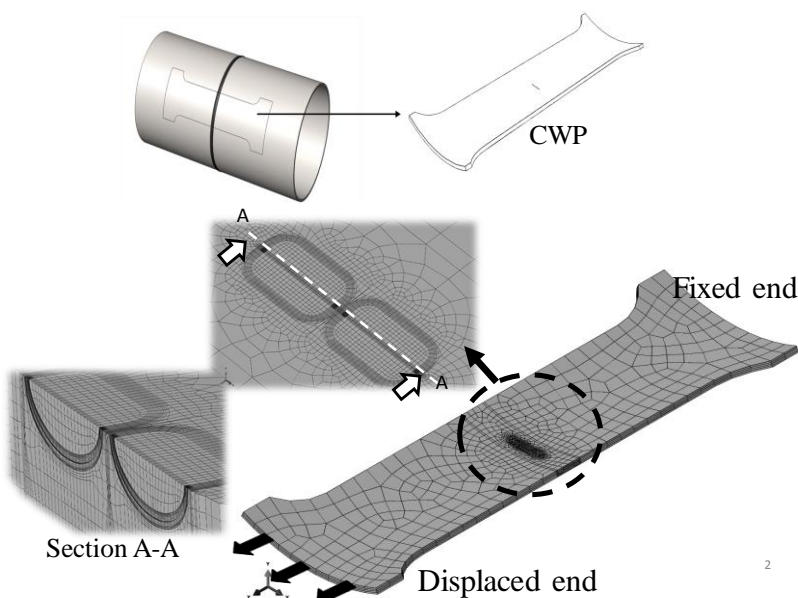


Figure 6-19: Schematic geometry of CWP specimen, FE model, notch block meshing and semi-elliptical notches.

As shown in Figure 6-20, the interaction between very close adjacent flaws starts from the early stages of loading. SIF along the crack front for case 1, which has very close flaws ($s = 2$ mm), can be distinguished easily from the other cases in Figure 6-20. Along the crack front and close to the adjacent flaw ($\varphi < \pi/4$), it has a notably higher SIF. Besides, considering the closest tip to the adjacent flaw in Figure 6-21 ($\varphi = 0$), there is an evident difference between case 1 and other cases. On the other hand, it can be seen in Figure 6-21 that SIF for case 3, having a spacing distance that corresponds to the onset of interaction according to Category C, does not show a pronounced difference compared to case 4, which is assumed as a non-interacting configuration. Clearly in cases 1 and 2, the adjacent flaw considerably affects the SIF.

J -integral values are plotted in Figure 6-22 for the different cases and at different applied strain levels. Since the EPRG Tier 2 scope is limited to strain levels below 0.5%, the results are plotted until this strain value. It can be seen that the difference between the various cases increases when the applied strain is increased. Figure 6-23 shows that, like f_i , J -integral is not evenly distributed along the crack front, and its maximum value has marginally been shifted from the deepest point towards the adjacent notch. This non-even distribution and shift in maximum value are more pronounced for case 1, for which it can be assumed the most severe interaction exists.

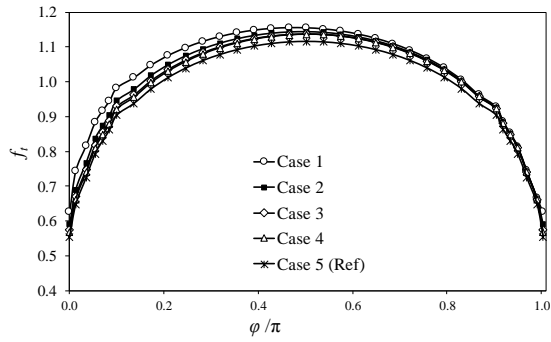


Figure 6-20: Normalized SIF along the crack front.

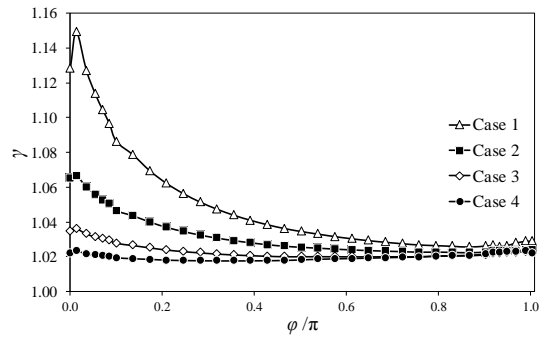


Figure 6-21: Elastic interaction factor ($\gamma = f_I / f_I^0$) along the crack front.

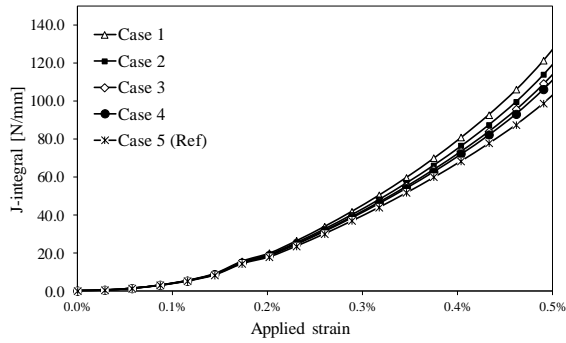


Figure 6-22: J-integral at $\varphi = \pi/2$ versus applied strain for various cases.

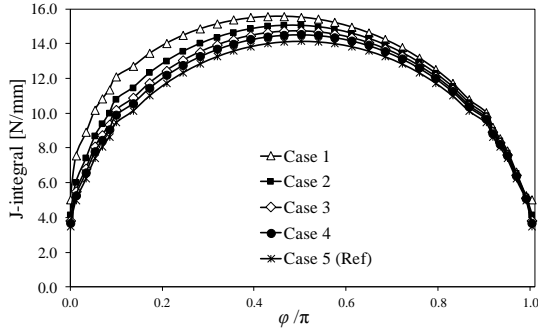


Figure 6-23: J -integral along the crack front for various cases.

Like the elastic analyses, the ratios between the J -integral values are also compared in terms of η_{Cr} , which is the square root of the ratio of the maximum J -integral of one of the adjacent notches to its counterpart of a single notch. As illustrated in Figure 6-24, it is evident that the difference between interacting and non-interacting cases depends on the applied strain. In the other words, elastic-plastic critical interaction intensity, which it is deemed to be the most relevant factor to assess the failure, increases with increasing applied strain.

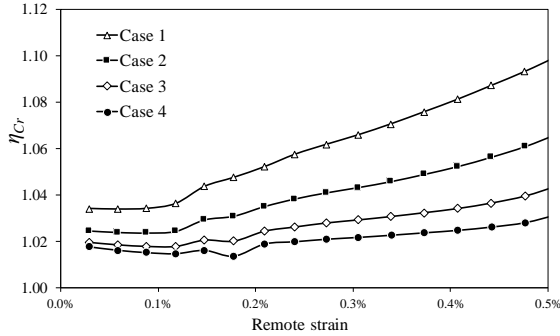


Figure 6-24: Critical elastic-plastic interaction ratio (η_{Cr}) versus applied remote strain.

Having extracted J -integral values along the crack front, their ratio to the reference case is plotted in Figure 6-25. It shows a very similar trend to Figure 6-21, but with much higher magnitude. In other words, the interaction affects the J -integral and SIF in the same way. The most affected points are the same and the highest crack driving forces are observed at the same location, but the severity of the interaction is higher for the elastic-plastic case. For instance, close to $\phi = 0$ the difference between case 1 and 4 was around 10% in Figure 6-21, while it is up to 40% in Figure 6-25.

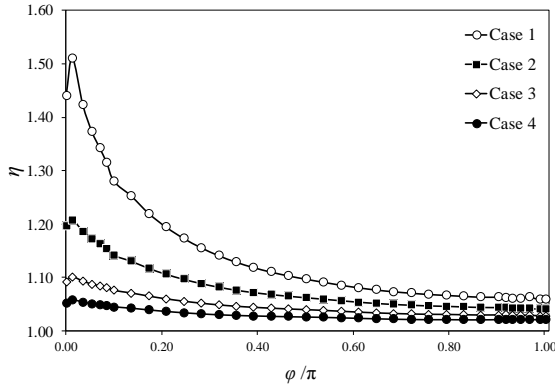


Figure 6-25: Elastic-plastic interaction factor ($\eta = J/J_0$) along the crack front

Figure 6-26 compares the elastic interaction ratio (γ) with the elastic-plastic interaction ratio (η) for various cases. Since η depends on the stress level (contrary to γ), it has been reported at a remote strain level of 0.5% (which is the validity limit of the EPRG Tier 2 guidelines). Ratios are calculated along the crack front (varying ϕ) and their comparison indicates that for cases 1 and 2, where the trend between the two ratios is almost linear and higher interaction is expected, the elastic-plastic ratio is around 3.5 times higher than the elastic ratio. In other words, the interaction between two adjacent notches in these examples is 3.5 times more severe at the onset of yielding (remote strain = 0.5%) compared to the linear elastic interaction.

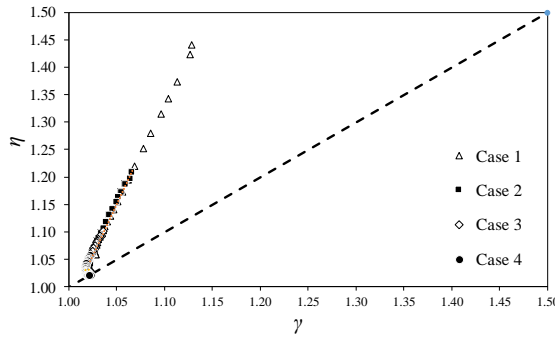


Figure 6-26: Comparing elastic interaction ratio with elastic-plastic interaction ratio at applied strain 0.5%. The ratios are calculated for varying ϕ along the crack front.

The interaction criteria used in assessment procedures are supposed to be conservative, i.e., they should not indicate non-interaction when the adjacent flaws have a significant effect on one another. Considering that these criteria have mostly been developed based on elastic analysis, it might be questioned if they are conservative enough for higher loads, when elastic-plastic interaction is more severe (Figure 6-26). For sufficiently tough materials the difference between elastic and

elastic-plastic interaction factor might be less significant. In these materials the failure is governed by plastic collapse, which may speed up by ductile crack growth.

To find out how to assess flaw interaction in an elastic-plastic framework, Coules [2] used a failure assessment diagram (FAD) based on R6 [10] to demonstrate that particular pairs of adjacent flaws, which are treated by BS7910 as non-interacting, can be unacceptable at higher loads while each of them independently are safe according to FAD. Although this is not a surprising result considering that interaction intensity increases with increasing load (see Figure 6-24), it highlights a shortcoming in flaw interaction assessment based on CDF. This is a significant weak point for present interaction criteria based on CDF because it shows that when load increases, eventually many non-interacting configurations can be interpreted as interacting flaws.

As a counterargument for the above, Coules [2] argued that potential non-conservatism observed in FAD under ductile conditions is offset by conservatism in other aspects of an assessment, specifically:

- A rising J -R material curve might cause tearing to arrest after a small amount of notch growth.
- Constraint loss in the region in-between the flaws would inhibit fracture.
- Estimates of the limit load used in a FAD analysis might provide some conservatism

Even if the above counterargument leads to treating some flaw pairs as non-interacting under elastic-plastic or ductile tearing conditions, despite the high values in their CDF (i.e. J -integral or CTOD), the above results show that such a conclusion indeed needs very careful further analysis. In other words, criteria simply based on geometry of flaws (depth, length and spacing distance), particularly when they are developed based on LFEM, should not be used to judge if flaw pairs are interacting or not. Although more conservative criteria (like API 1104) are less prone to the underestimation of SIF in an elastic-plastic analysis, all of them essentially have the same shortcomings since the interaction severity is assessed independent from the load level. Alternatively, procedures based on case by case analysis, probably supported by FEM, can lead to more conservative assessments.

CTOD can also be used instead of J -integral to evaluate interaction. Its merit is that experimental measurement of CTOD is easier than J -integral, particularly for non-standard specimens, and in case of alternative FE procedures (like element deletion) CTOD-based numerical calculation is more straightforward (see section 4.5). Figure 6-27 compares the interaction ratio, calculated as square root of the ratio of CTOD of one of the adjacent notches to single notch CTOD, with η (based on J -integral) for all four cases at $\varphi = \pi/2$ (deepest point). The good agreement between these two parameters, as expected, shows that the CTOD can also be used to describe

elastic-plastic interaction. Therefore, hereinafter η and η_{Cr} will be used for describing the interaction factor in elastic-plastic material, either using J -integral or CTOD.

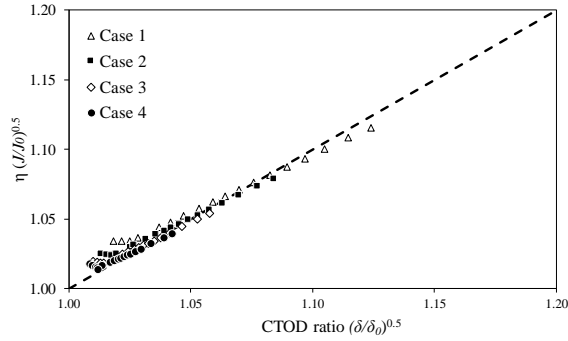


Figure 6-27: Comparison between interaction ratios based on J -integral and CTOD.

In this study, due to its higher practical relevance, the comparison between interaction criteria is based on the global proximity to failure rather than local increases of CDF at a given ϕ . In such case, a flaw interaction factor should relate to the maximum occurring crack driving force along a crack front. The corresponding factors are denoted as γ_{Cr} (when based SIF) or η_{Cr} (when based on CTOD).

From this perspective, Figure 6-28 plots the ratio between the maximum magnitude of SIF of one of multiple flaws to that of the reference case ($\gamma_{cr} = f_{I\max}/f_{I0\max}$) on the left axis in black color, and the ratio between the maximum magnitude of SIF at the re-characterized flaw $f_{IR\max}$ (cases 6-8) to that of one of the adjacent flaws $f_{I\max}$ (cases 1-3) on the right axis in blue ($f_{IR\max}/f_{I\max}$). With the same analogy Figure 6-29 plots CTOD ratios.

Comparing Figure 6-28 and Figure 6-29 shows that the studied ECA guidelines are more conservative in elastic analysis compared to elastic-plastic analysis. It is also evident that guidelines in category A define the onset of interaction at higher interaction intensities and re-characterize the two adjacent flaws into a more realistic virtual flaw. Applying guidelines of category C leads to re-characterizing the flaws with a marginal interaction intensity to a new flaw with considerably higher crack driving force. Indeed, based on the result of this study, procedures in category A follow a more coherent logic in interaction assessment and re-characterization compared to those in categories B and C which can lead to more conservative assessments.

Comparison between interaction criteria of different guidelines indicated that, for shallow flaws (i.e. $a/c < 1$), flaw depth-based interaction criteria define the boundary of interaction onset at a relatively higher interaction intensity, and their re-characterized flaw has the lowest safety factor. Guidelines based on notch length define the interaction onset at a relatively lower interaction intensity, but their re-characterized flaw has a higher safety factor. The empirical guideline provided by EPRG Tier 2 stands between these two extremes, for the cases investigated.

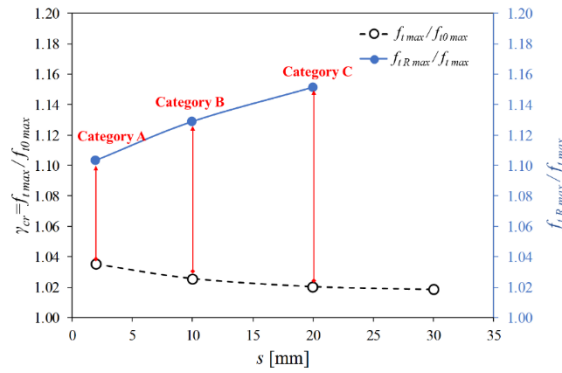


Figure 6-28: Comparison of ratio of maximum SIF values at one of multiple flaws to single flaw (reference) on the left axis and the ratio of SIF value of a re-characterized flaw to one of multiple flaws on the right axis.

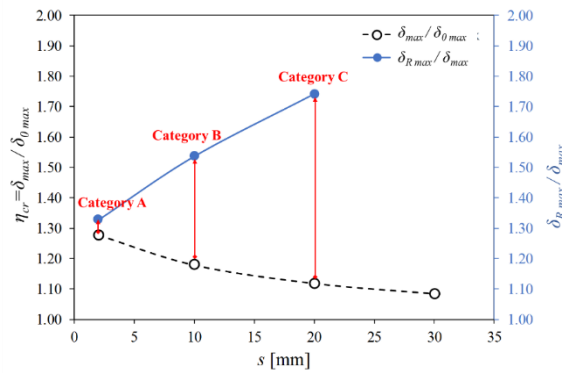


Figure 6-29: Comparison of ratio of maximum CTOD values at one of multiple flaws to single flaw (reference) on the left axis and the ratio of CTOD value of a re-characterized flaw to one of multiple flaws on the right axis.

6.3. Evaluation of the interaction between surface-breaking and embedded flaws using the element deletion method

This section describes the study performed for assessing the interaction between one surface and one embedded flaw using the element deletion technique described earlier in chapter 4. Element deletion provides a unique capability for modelling embedded flaws, when the use of conventional methods is restricted due to challenges in generating meshes in a close proximity. Figure 6-30 shows the definition of the geometrical symbols used for this study.

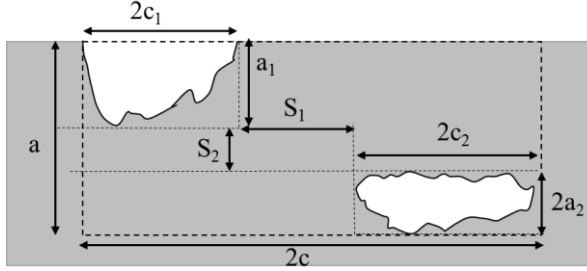


Figure 6-30: Definition of geometrical symbols for the flaw interaction case considered for this study: an embedded flaw adjacent to a coplanar surface breaking flaw. Image adopted from BS7910 [11].

The surface breaking flaw was intended to be the more critical one, allowing to focus the analysis on this flaw (rather than having to analyze both flaws). Hereto, two measures were taken:

First, setting the dimensions of both flaws equal ($a_1 = 2a_2$ and $2c_1 = 2c_2$), as surface breaking flaws are known to be more critical than embedded flaws of the same size; Second, positioning the embedded flaws sufficiently remote from the inner and outer pipe surfaces to avoid their re-categorization into a surface breaking flaw (ligaments exceeding 20% of the flaw depth $2a_2$, according to ASME B&PVC code sec. XI).

Four metrics are defined to evaluate flaw interaction and re-characterization, based on the CDF output along the front of the semi-elliptical flaw ($0 \leq \varphi \leq \pi$). Two cases were considered:

- The purely linear-elastic response, analyzed by means of K_I at the first increment of an elastic-plastic simulation, corresponding with a remote stress level around 85 MPa or 17% of the yield strength;
- The elastic-plastic response analyzed by means of CTOD at the limit load level of the twin flaw configuration.

Similar to the previous analysis methodology, the results are used to investigate flaw interaction and re-characterization rules from two viewpoints, critical interaction factor (γ_{Cr} for linear elastic and η_{Cr} for elastic plastic analysis), and global conservatism factor.

Interaction and conservatism factors have been based on K_I values or the square root of CTOD values. Taking the square root of CTOD is in line with conventional assessments using the failure assessment diagram, where all CTOD or J output is translated into an “equivalent” K_I factor by taking its square root (see Table 6-4).

Table 6-4: Definition of four metrics to evaluate flaw interaction and re-characterization.

in terms of... Evaluation of...	K_I ("linear-elastic")	CTOD (at the limit load) ("elastic-plastic")
"Critical interaction factor", compared to single flaw configuration	$\gamma_{Cr} = \frac{\max_{0 \leq \varphi \leq \pi} (K_I)_{twin}}{\max_{0 \leq \varphi \leq \pi} (K_I)_{single}}$	$\eta_{Cr} = \left(\frac{\max_{0 \leq \varphi \leq \pi} (CTOD)_{twin}}{\max_{0 \leq \varphi \leq \pi} (CTOD)_{single}} \right)^{0.5}$
"Global conservatism factor" of the bounding flaw configuration	$\frac{\max_{0 \leq \varphi \leq \pi} (K_I)_{twin}}{\max_{0 \leq \varphi \leq \pi} (K_I)_{bounding}}$	$\left(\frac{\max_{0 \leq \varphi \leq \pi} (CTOD)_{twin}}{\max_{0 \leq \varphi \leq \pi} (CTOD)_{bounding}} \right)^{0.5}$

6.3.1. Parametric Study

The section below describes the executed parametric study for assessing the interaction between a surface and an embedded flaw. The study was designed to focus on varying flaw sizes and position as summarized in Table 6-5. In total, 36 flaw combinations have been considered in a full-factorial manner, and these are motivated hereunder.

Depths of both the surface breaking (a_1) and embedded ($2a_2$) flaws were considered constant and equal, as 3 mm. This reflects the common observation that a flaw spans over one girth weld bead, which is typically around 3 mm high. A similar consideration was made for the development of the original EPRG Tier 2 and Tier 3 guidelines for acceptability of girth weld flaws [12].

Three values were chosen for the length of both flaws (being equally long, $2c_1 = 2c_2$). 25 and 50 mm correspond with common workmanship criteria related to various types of weld anomalies (e.g., as prescribed by API 1104 [13]). The third value, 119 mm, relates to the EPRG Tier 2 acceptability criterion for girth weld flaws under plastic collapse scenarios (7 times the pipe thickness for a 3 mm deep flaw).

Four levels were chosen for vertical spacing S_2 , normalized against $(a_1 + a_2)$. The levels 0.33 and 1.00 correspond with thresholds for flaw interaction according to respectively ASME B&PV Code Sec. XI:2017 on the one hand, and {BS7910:2013, DNV-OS-F101:2012, API1104:2013, API579:2007} on the other hand. The other two levels, 0.50 and 2.00 were added to reveal clear trends.

It is important to realize that none of the chosen levels would influence the outcome of any of the flaw interaction rules. In other words, if one of the configurations is identified as an interacting flaw pair, the other two will also be. Nonetheless, large differences in actual levels of flaw interaction may occur, and these potential differences are investigated in this study.

To enable calculation of the interaction metrics of Table 6-5 all corresponding single and bounding flaws were also simulated.

Table 6-5: Configurations considered in parametric study.

Parameter	Number of values	Value(s)
$a_1 = 2a_2$	1	3 mm
$2c_1 = 2c_2$	3	25, 50, 119 mm
$S_2/(a_1 + a_2)$	4	0.33, 0.50, 1.00, 2.00
Transverse offset / $2c_1$	3	0.0, 0.5, 1.0
Total	36	

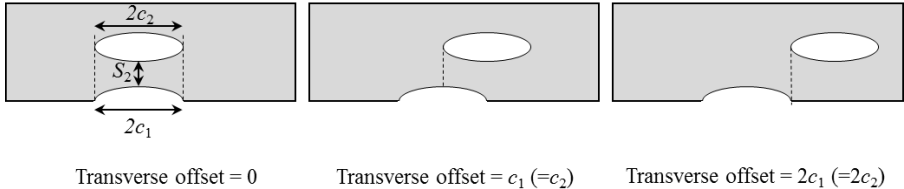


Figure 6-31: Schematic overview of three simulated levels of transverse offset.

Other parameters were kept fixed to the following values; Pipe outer diameter is 762 mm (30”) with 17 mm wall thickness; Pipe material constitutive behavior representing an API 5L X70 line pipe steel having the yield strength ($R_{p0.2}$) equal to 500 MPa, and strain hardening exponent $n = 15$ (according to Ramberg-Osgood’s model), corresponding to a yield-to-tensile ratio of 0.85.

Weld properties were considered equal to pipe properties, resulting in an even-matching weldment. No weld cap reinforcement was applied. These simplifications are generally conservative from the perspective of established girth weld flaw assessment procedures. For instance, the EPRG Tier 2 guidelines for weld flaw assessment [12] state that the minimum yield strength of the weld metal should exceed the minimum longitudinal yield strength of the base pipe by at least five standard deviations (or 100 MPa if no distribution is known), “to ensure that girth welds along the pipeline spread do not undermatch the actual yield strength in the axial direction of either adjacent pipe length.” Nonetheless, it should be kept in mind that more advanced assessments can be performed by assigning different material properties and/or geometrical properties to the girth weldment.

Two load cases were considered for all configurations, purely uniaxial loading in absence of internal pressure and axial loading after application of 156 bar internal pressure, introducing a hoop stress equal to 70% of the yield strength. In total, considering single, twin and bounded (re-characterized) flaws, 142 simulations were performed in this section for the parametric study described above.

6.3.2. General observation

Figure 6-32 summarizes all simulated cases in terms of global conservatism factor and global interaction factor (interacting flaws are re-characterized based on BS7910 rule). Points on the left side of this graph indicate little interaction, and vice versa. Points on the bottom side of this graph indicate a high conservatism associated with re-characterizing the flaw pair into one bounding flaw, and vice versa. Interaction metrics are plotted for linear-elastic (at 85 MPa remote stress) and elastic-plastic analyses (at the limit load).

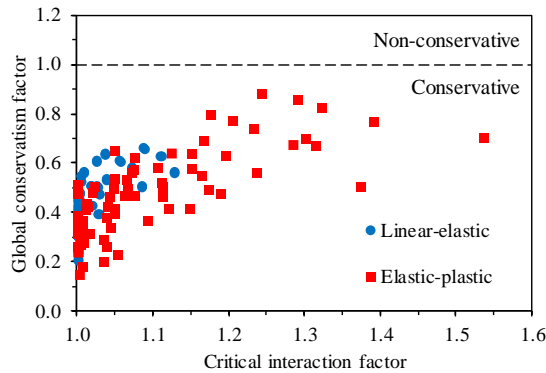


Figure 6-32: Overview of all results in terms of global interaction factor and global conservatism factor.

A large subset of simulated cases shows very moderate flaw interaction levels, as their global interaction factors approach unity. Factors contributing to little flaw interaction are elaborated in subsequent sections. None of the bounding flaws acts non-conservatively with respect to the actual flaw pair. In other words, if flaw interaction is identified, it will be treated in a conservative manner. However, the degree of conservatism may be excessive as a subset of data points is located towards the bottom of the graph.

6.3.3. Effect of through-thickness spacing between flaws on their interaction

Figure 6-33 is a re-plot of Figure 6-32, separated into linear-elastic and elastic-plastic load cases and indicating different levels of through-thickness spacing by means of different markers. The plotted dataset allows to judge the performance of flaw interaction procedures, which are essentially based upon through-thickness spacing for the investigated configurations. Recall that, normalized spacing levels of 0.33, 0.50 and 1.00 would be treated as interacting by BS7910:2013, DNV-OS-F101, API1104 and API579; and, ASME B&PV Code Sec. XI would only indicate a normalized spacing level of 0.33 as interacting and treat all other spacing levels as non-interacting.

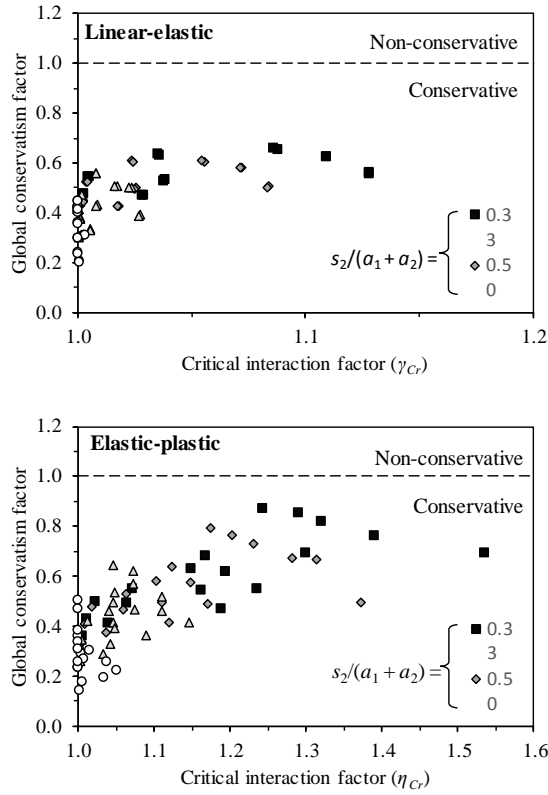


Figure 6-33: Through-thickness defect spacing S_2 has a major effect on flaw interaction and conservatism of the bounding flaw. Top: linear-elastic loading. Bottom: elastic-plastic loading at the limit load

It is clear from Figure 6-33 that through-thickness defect spacing has a major effect on flaw interaction and the conservatism of the bounding flaw, for both linear-elastic and elastic-plastic loading. As spacing increases, interaction factors tend to decrease, and the conservatism of the bounding flaw tends to increase (as the conservatism factor decreases).

6.3.4. Effect of transverse offset between flaws on their interaction

Figure 6-34 is a re-plot of Figure 6-32, separated into linear-elastic and elastic-plastic load cases and indicating different levels of transverse offset between both flaws by means of different markers. The plotted dataset allows to judge the “robustness” of flaw interaction procedures with respect to this offset, which does not affect the outcome of the ECA criteria for the considered cases.

From the figures, it is clear that transverse offset has a significant effect on flaw interaction, and on the conservatism of a re-characterized bounding flaw. Increasing the transverse offset (normalized against $2c_1 = 2c_2$) from 0 to 1 tends to:

- strongly decrease the critical interaction factor, down to a level which can even be considered negligible for linear-elastic loading;
- decrease the global conservatism factor, which implies greater conservatism in translating the flaw pair into its bounding flaw. This effect is most pronounced for elastic-plastic loading.

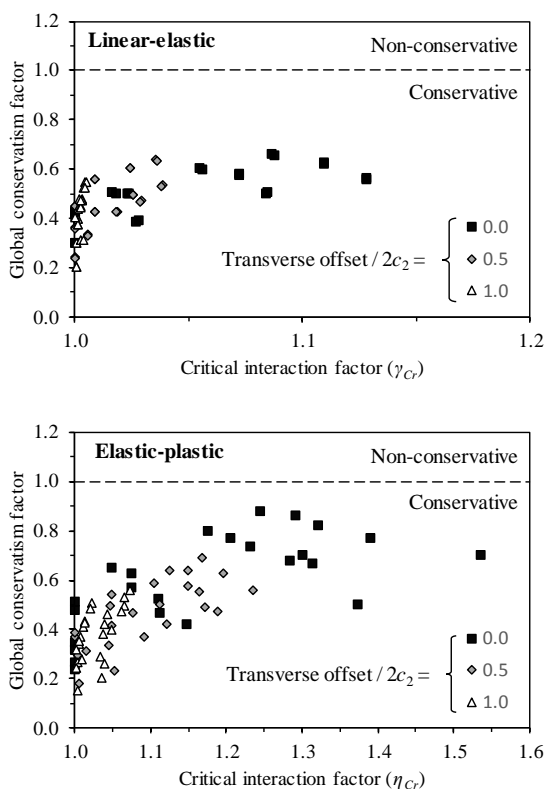


Figure 6-34: The transverse offset between both defects has a major effect on flaw interaction and conservatism of the bounding flaw. Top: linear-elastic loading. Bottom: elastic-plastic loading at the limit load.

6.3.5. Effect of load level on flaw interaction

As already observed in Figure 6-32, the parametric study reveals that interaction effects significantly change as the load level changes from purely linear-elastic into elastic-plastic.

Focusing on critical interaction factors first, obtained values for both load levels are compared in Figure 6-35. Clearly, critical interaction increases as plasticity comes into play. Surprisingly, the figure shows a rather linear trend between linear-elastic and elastic-plastic interaction factors. Linear regression analysis indicates that the global interaction factor at the limit load is on average 3.2 times higher than for linear-elastic loading. This number should not be seen as a constant, since it is expected to be influenced by strain hardening ($n = 15$, in this study) and the elastic-plastic load level (the limit load in this study); nonetheless it highly resembles the trend observed in another similar study plotted in Figure 6-26.

For those cases where a flaw pair would be re-characterized into a single bounding flaw, there is no clear influence of load on the level of conservatism introduced. A comparison of global conservatism factors for linear-elastic loading and at the limit load (Figure 6-36) reveals a point cloud that embraces the 1:1 line (albeit a slightly deviating trend may be suggested for configurations with higher conservatism factors).

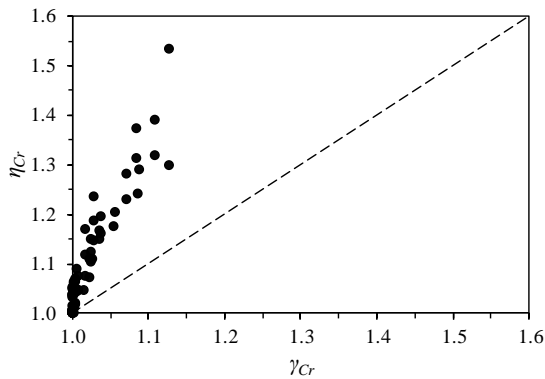


Figure 6-35: Comparison of global interaction factors for linear-elastic loading, and at the limit load level.

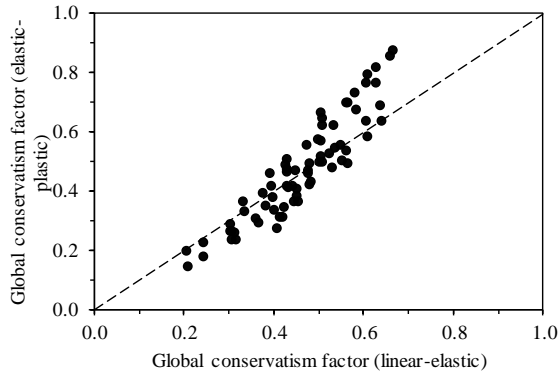


Figure 6-36: Comparison of global conservatism factors for linear-elastic loading, and at the limit load level.

6.3.6. Effect of internal pressure on flaw interaction

Figure 6-37 and Figure 6-38 compare global interaction and conservatism factors respectively, in absence and presence of internal pressure.

For linear-elastic loading, the effect of internal pressure on interaction metrics is clearly negligible, as all open circle data points are essentially located along the 1:1 line. Stronger differences are observed for elastic-plastic loading, but a clear overall agreement is retained between interaction factors in absence and presence of pressure. It can be concluded that, for the simulated coplanar circumferential defect pairs, the biaxial stress state induced by internal pressure did not significantly affect the flaw interaction.

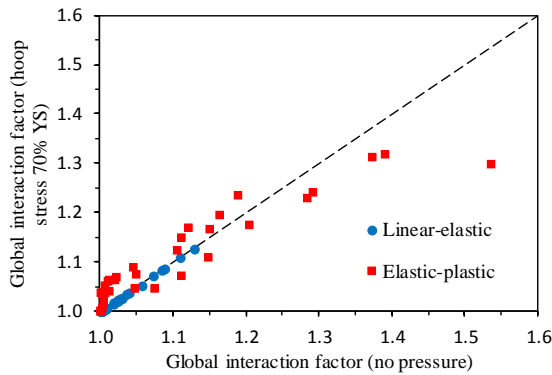


Figure 6-37: Comparison of global interaction factors in absence (horizontal axis) and presence (vertical axis) of internal pressure.

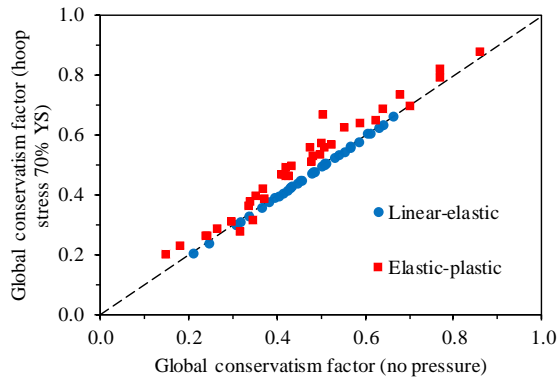


Figure 6-38: Comparison of global conservatism factors in absence (horizontal axis) and presence (vertical axis) of internal pressure.

This observation is positive in the sense that established flaw interaction criteria can be reliably adopted to pressurized pipelines, notwithstanding that the majority (if not all) of them were calibrated on the basis of uniaxial loading. It is also in line with BS7910, which would impose for the pressurized load cases that only the stress component perpendicular to the defect plane (i.e., axial stress) is to be taken into account in the assessment.

6.4. Conclusion

In this chapter, in the first section, the effect of flaw idealization on the interaction of two identical coplanar surface breaking flaws has been studied. Flaws are assumed to be notch-like either as canoe-shaped or semi-elliptical. A canoe-shaped flaw is more representative of actual flaw geometry, but a semi-elliptical flaw is the most conventional idealized shape in fracture mechanics studies. The interaction has been assessed using two criteria: interaction factor at the tip closest to the adjacent notch where it has the highest influence, and critical interaction factor considering the most severe SIF or CDF. In this approach it is assumed that single-parameter LEFM/EPFM is a valid predictor of “failure”, re-entrant region tearing is unacceptable, SIF/CDF can be calculated accurately across whole crack front. The results showed that the inconsistency between the canoe-shaped and semi-elliptical notches starts from the first stage of loading and increases with load. Compared to canoe-shaped notches, employing semi-elliptical notches in an elastic-plastic analysis leads to an underestimation of the interaction significance for the results generated in this study. To quantify the effect of various notch geometries, a regression model is proposed to estimate the ratio between the critical elastic(-plastic) interaction factor of canoe-shaped and semi-elliptical notches. The model’s variables are notch aspect ratio, depth to thickness ratio and spacing distance between the notches. The regression model suggests that notch shape has a more important influence on interaction assessment for deeper notches with lower aspect ratio. Analyses also indicated that strain hardening affects flaw interaction in elastic-plastic conditions. ECA guidelines suggest to re-characterize the interacting flaws into a bounding flaw contains all of them, as a conservative procedure. However, comparing SIF and CDF

of bounding notches with those of the interacting twin notches revealed that re-characterizing the interacting canoe-shaped notches into a single bounding semi-elliptical notch is not always conservative. Therefore, implication of some degree of caution would be required since in reality the flaws are normally irregularly shaped.

Since understanding the interaction behavior at higher load levels is supposed to be critical in strain-based design, the interaction between two surface breaking defects has been studied for both linear elastic and elastic-plastic scenarios. To compare various ECA guidelines, eight different cases have been put forward. These cases represent the onset of interaction based on three main approaches in ECA guidelines which consist of comparing the distance between the flaws against the flaw's depth and length, or rather comprise an empirical criterion. Also, one case was considered which is not classified as interacting according to all criteria. In addition, the re-characterized defects based on each of the three approaches have been studied. The results of FE simulations revealed that interaction intensity increases when the loading level is increased. All the ECA rule assessment are concluded to be conservative for the studied cases. ASME sec XI, BS7910 and API579 rules are more accurate compared to EPRG Tier 2 guideline and API1104, and the latter tends to over-conservatively assess the interaction.

The second section of this chapter has focused on the flaw interaction of coplanar, circumferential surface-breaking and embedded defects in axially loaded pipes. A parametric study was designed, executed and analyzed, making use of the element deletion modelling approach. Varied parameters relate to the size of the defects, their spacing, the axial load level and the potential presence of internal pressure.

The parametric flaw interaction study has revealed that all ECA bounding flaws treat the actual flaw pair in a conservative manner, however, the conservatism introduced by considering the bounding flaw can be substantial. Moreover, results showed that not only elastic-plastic interaction tends to be more severe compared linear-elastic interaction, but also unlike linear elastic interaction, elastic-plastic interaction depends on the strain hardening properties and the exact load level.

In addition, the limitations of standardized “yes-or-no” criteria which are solely based on geometrical characteristics and on linear-elastic fracture mechanics have been highlighted. The level of conservatism of these criteria is strongly dependent on the actual geometry, and the applied load level. These limitations can be eliminated by making use of the developed modelling approach to perform a direct assessment of crack driving force for the actual configuration of interest.

References

- [1] Kamaya M. A Criterion for Combination Rule in Flaw Assessment of Parallel Surface Cracks. *J Press Vessel Technol* 2011;133:061204. doi:10.1115/1.4004563.
- [2] Coules HE. On predicting the interaction of crack-like defects in ductile fracture. *Int J Press Vessel Pip* 2018;162:98–101. doi:10.1016/J.IJPVP.2018.03.006.
- [3] Kotousov a., Chang D. Local plastic collapse conditions for a plate weakened by two closely spaced collinear cracks. *Eng Fract Mech* 2014;127:1–11. doi:10.1016/j.engfracmech.2014.05.009.
- [4] Yi DK, Xiao ZM, Tan SK, Zhang YM. Elastic–plastic fracture behavior of a radial

- matrix crack interacting with a circle inclusion with generalized Irwin corrections. *Acta Mech* 2013;225:91–107. doi:10.1007/s00707-013-0954-7.
- [5] Kamaya M, Totsuka N. Influence of interaction between multiple cracks on stress corrosion crack propagation. *Corros Sci* 2002;44:2333–52. doi:10.1016/S0010-938X(02)00039-2.
 - [6] Coules HE. Stress intensity interaction between dissimilar semi-elliptical surface cracks. *Int J Press Vessel Pip* 2016. doi:10.1016/j.ijpvp.2016.07.011.
 - [7] Hertelé S. Coupled Experimental-Numerical Framework for the Assessment of Strain Capacity of Flawed Girth Welds in Pipelines. PhD dissertation. Ghent University; 2012.
 - [8] Hertelé S, De Waele W, Denys R, Verstraete M, Van Wittenberghe J. Parametric finite element model for large scale tension tests on flawed pipeline girth welds. *Adv Eng Softw* 2012;47:24–34. doi:10.1016/j.advengsoft.2011.12.007.
 - [9] Hasegawa K, Saito K, Miyazaki K. Alignment Rule for Non-Aligned Flaws for Fitness-for-Service Evaluations Based on LEFM. *J Press Vessel Technol* 2009;131:041403. doi:10.1115/1.3152229.
 - [10] Assessment of the integrity of structures containing defects- R6. vol. 4. British energy; 2001.
 - [11] British Standard. BS7910:2013+A1:2015: Guide to methods for assessing the acceptability of flaws in metallic structures. London, UK: BSI Stand Publ; 2015.
 - [12] M Andrews R, M Denys R, Knauf G. The EPRG guidelines on the assessment of defects in transmission pipeline girth welds. *J Pipeline Eng* Vol 2015;14:620–4.
 - [13] Api Standard 1104. Welding of pipelines and related facilities. API 1104-2013+ADD2014. 21st Ed 2013.

Flaw interaction based on alternative criteria

7.1. Introduction

Interaction between flaws affects plastic deformation, fracture controlling parameters and stress/strain fields around the flaws. To determine whether this interaction is significant for fracture initiation, conventional criteria have mainly been developed based on linear elastic fracture mechanics parameters. The feasibility of these procedures might be questioned when applied to failure modes other than fracture. In this chapter alternative approaches, based on strain pattern and plastic collapse load, have been investigated to describe the interaction behavior for failure in presence of plastic deformation and ductile tearing. This chapter focuses on non-coplanar flaws, since similar assessment procedures for their coplanar counterparts have been developed in a relatively more straightforward manner. For instance, limit load assessment for two coplanar flaws is known to be mostly a matter of total cross section reduction; the very same assessment for two non-coplanar flaws is more cumbersome.

Two sections of this chapter are devoted to the results of interaction studies based on strain-based methods in a small-scale model with through thickness notches and a medium-scale model with semi-elliptical notch, respectively. In the next section a specific methodology used to describe the interaction based on strain morphology is introduced, and then used for both small-scale and medium-scale models.

7.2. Evaluation of interaction of two non-coplanar flaws based on Strain Concentration Bands (SCB)

To investigate interaction of non-coplanar flaws, Hasegawa et al. [1] employed finite element analyses to calculate the stress intensity factor for through-wall non-aligned flaws. They also performed brittle fracture experiments at -196°C on structural steel plates to test similar configurations. They concluded that a 6% increase in stress intensity factor could be considered as a boundary between aligned and non-aligned flaws, since this increase influenced the crack path. In this section, a novel approach to evaluate the interaction of two non-coplanar flaws in the high strain regime is proposed inspired by Hasegawa's approach for brittle fracture but using strain patterns instead of crack path. To that end, full-field strain patterns in surface flawed and tension loaded specimens are experimentally and numerically investigated. Specimens with two non-coplanar edge notches have been selected as a research tool considering their similarity to relevant laboratory specimens for low crack tip constraint scenarios, such as the single edge notched tension (SENT) specimen.

To realize a robust analysis of the effect of out-of-plane distance on notch interaction, a large number of geometrical configurations was considered in a full-factorial parametric study in combination with some benchmark experiments (see chapter 5). Concretely, 17 levels of out-of-plane distance were defined in the simulation matrix, H/W ranging between 0 and 4. Besides, three levels of a/W were taken into account for each out-of-plane distance ($a/W = 0.3, 0.4$ and 0.5). To define a reference value for detecting the presence of interaction between notches, three SENT models were also added to the simulation matrix. In total 54 simulations were

performed; Table 7 1 summarizes both experiments and simulations. The principal output of the simulations is CTOD (calculated according to the 90° intercept method) as a function of tensile load. The width of specimens ($2W$), see Figure 5-19, was 30 mm and their thickness (t) was 15 mm.

Table 7-1: Overview of specimen configurations and geometrical details used in experimental and numerical studies (see figure 5-6 for notations).

Type of study	Specimen configuration	Notch depth ratio (a/W)	Out of plane distance between the notches (H/W)
Experiments	Double notched	0.4	0.00, 0.70, 1.00, 1.30, 2.00 and 3.00
	Single notched (SENT)	0.4	-
Finite element simulations	Double notched	0.3, 0.4, 0.5	0.00, 0.30, 0.45, 0.70, 0.85, 1.00, 1.15, 1.30, 1.45, 1.60, 1.85, 2.00, 2.30, 2.60, 3.00, 3.30 and 4.00
	Single notched (SENT)	0.3, 0.4, 0.5	-

7.2.1. Evaluation of defect interaction based on strain trajectory

The approach introduced in this section is based on so-called strain concentration bands (SCB) that connect the points of maximum equivalent strain between notch tips (refer to chapter 5 for equivalent strain definition). This is conceptually similar to slip line theory which predicts trajectories along which critical shear stress of a rigid, perfectly plastic material is achieved. There the resulting local discontinuity in tangential displacement velocity represents an infinitely narrow band of plastic deformation. However, for realistic materials, the assumption of original slip line theory is invalidated by linear elasticity and plastic work hardening, creating strain bands having a finite width rather than lines of discontinuous displacement.

7.2.1.1. Algorithm to determine and characterize strain concentration bands

Strain concentration bands arising from the notch tips have been determined and characterized as summarized below and illustrated in Figure 7-1, using a devoted MATLAB® script. The procedure has been applied to finite element results as well as experimental results. Recalling the discussion of the previous section, experimental results have been analyzed in terms of equivalent total strain, whereas numerical analyses make use of equivalent plastic strain.

- 1) Equivalent strain is extracted within the area of interest (Figure 7-1a), and discretized into a rectangular grid of points (Figure 7-1b). This grid is considered within the coordinate system of the undeformed specimen for the sake of simplicity. Notably, this simplification influences the outcome given the finite and non-linear nature of occurring deformations; strain bands would have a slightly different shape when considered within a moving grid [2]. Output has been analyzed at different occasions during the test, allowing to characterize the evolution of strain concentration as a function of applied crack driving force (CTOD).
- 2) By comparing equivalent strain values at all grid points on a transversal line (i.e., perpendicular to the load direction; vertical in Figure 7-1c), the point of maximum equivalent strain for each line is obtained. Connecting these points for adjacent vertical lines creates a trajectory that follows the band of maximum equivalent strain which from now on is referred to as strain concentration band (SCB).
- 3) For small out-of-plane notch distances, SCBs may connect notch tips. Such bands are divided into two halves at specimen mid width and each single half is referred to as a SCB. This is based on the assumption that the double edge notched specimen acts as two tangent single-edge notched specimens (Figure 7-1c).
- 4) Finally, each SCB shape in X-Y coordinates is mathematically described by means of linear regression analysis, with the aim to determine the angles of the best fitting lines originating from the notch tips with respect to the longitudinal direction (α_1 and α_2 in Figure 7-1d).
- 5) These characteristics are then used to identify the presence or absence of interaction between both notches, as discussed in section 7.2.3.

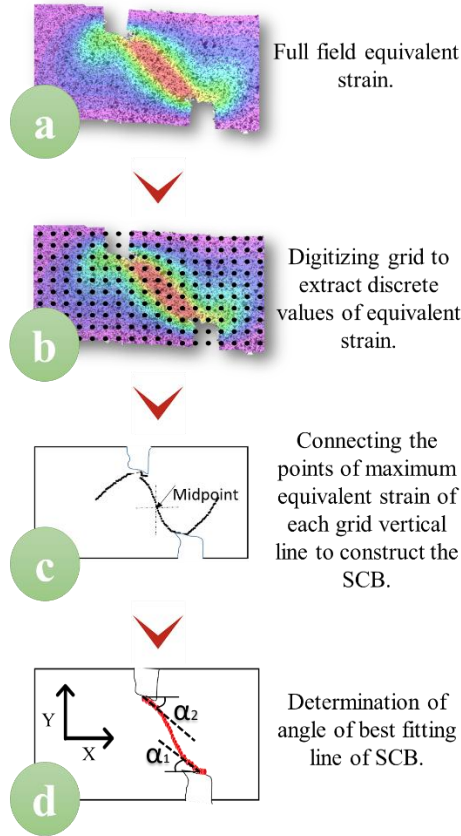


Figure 7-1: Graphical summary of procedure to obtain and characterize strain concentration bands (SCB) connecting notch tips.

7.2.1.2. Twice Elastic Slope (TES) limit load

SCB and CTOD values should be compared for different specimens at equal stages towards failure. The tensile limit state of the specimen can be characterized by its load bearing capacity whereby, given the high toughness of the material tested, failure is a plastic collapse based process. Hence, the proximity to failure is characterized as a percentage of the limit load. In this study, the limit load based on Twice Elastic Slope (TES) suggested by ASME B&PV code section III [3], as explained earlier in chapter 4, is opted as the reference to failure proximity. In the TES method, the material response is characterized by plotting force against displacement. A straight limit load line is then drawn from the origin of the force-displacement curve with a slope equal to twice that of the elastic response (with respect to the vertical load axis). The limit load is then obtained as the intersection between the TES line and the force-displacement curve.

7.2.1.3. Approach to the strain-based evaluation of flaw interaction

The possible interaction between adjacent cracks is investigated considering CTOD (symbolically denoted as δ) as the driving force to failure. Values of CTOD are normalized versus CTOD values (δ_0) for SENT specimens with equal a/W ratio. The deviation of δ/δ_0 from unity is considered as the primary criterion to judge on the degree of defect interaction. Complementary to the analysis of crack driving force, SCBs in the region between the two notches are investigated. The purpose hereto is twofold: to identify whether the shapes of the strain patterns surrounding a notch are influenced by the presence of an adjacent crack, and to evaluate whether changes in strain pattern shape can be associated with changes in δ/δ_0 .

7.2.2. Strain patterns morphology

Figure 7-2 shows the equivalent strain patterns for various test samples at the TES based limit load. It can be seen that, by increasing the out-of-plane distance (H/W) between two notches from 0.00 to 1.30, the strain patterns evolve from a quasi-circular symmetric pattern (fully symmetrical DENT specimen) to a pattern in which one interconnecting band reveals a pronounced strain concentration. There are slight differences in the shape of this band for $H/W = 0.70, 1.00$ and 1.30 . The patterns show more curvature for specimens with a small out-of-plane notch distance such as $H/W = 0.70$ and gradually evolve in a linear pattern for specimens with a larger out-of-plane notch distance ($H/W = 1$), while in the meantime the size of the region with maximum strain concentration increases as H/W increases to 1.30 . By further increasing the notch out-of-plane distance, the strain concentration bands start to separate at $H/W = 2$ and completely disconnect when $H/W = 3$. Figure 7-3 shows examples of numerically predicted strain patterns for two cases. The abovementioned effects can be noted here as well.

Whereas the strain patterns shown in Figure 7-2 reveal valuable qualitative information about the deformation and strain concentration, it is hard to judge on subtle differences in notch interaction, e.g. between $H/W = 0.70$ and $H/W = 1.00$. To obtain a robust quantitative interpretation which allows to differentiate between interacting and non-interacting cases, the methodology introduced in Figure 7-1 is applied to the DIC strain patterns. Figure 7-4 compares trajectories of strain concentration for six experiments with different H/W -values. The lower graphs show the SCB morphology and the upper graphs show the magnitude of equivalent strain along each trajectory. The interpretation of subfigures (b) to (f) somewhat differs from that of subfigure (a) (symmetrical DENT specimen) for which only half of the circular strain concentration band is shown. Figure 7-4 facilitates the translation of qualitative features of strain patterns (Figure 7-2) into quantitative data, as discussed in section 7.2.3.

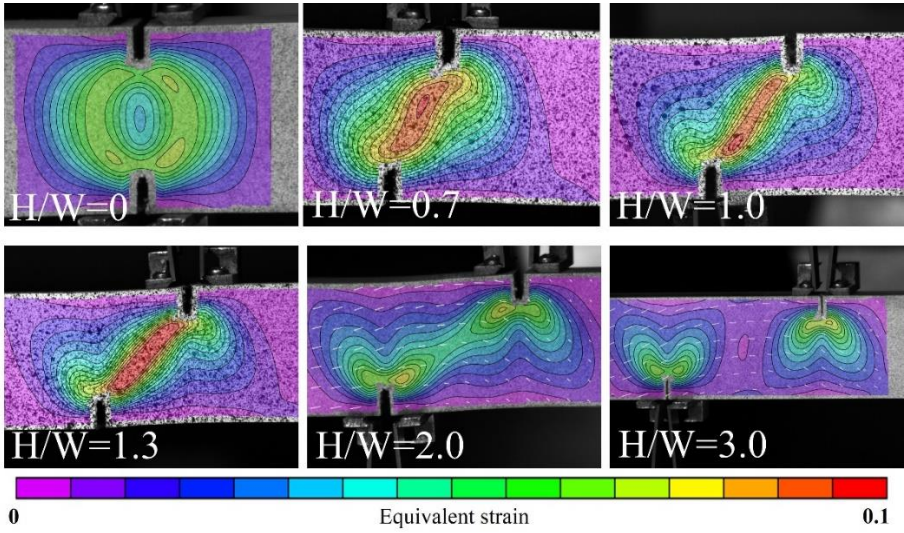


Figure 7-2: Experimental equivalent strain patterns for different specimens (various notch out of plane distances) at the limit load.

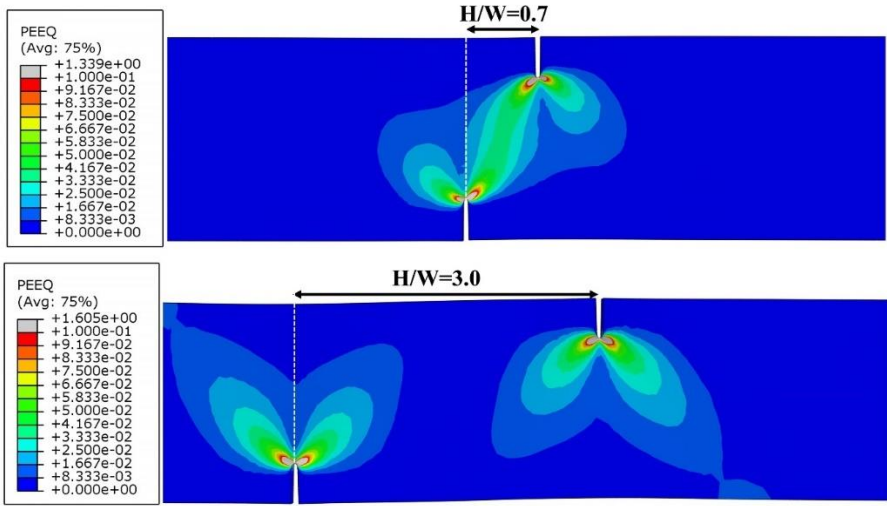


Figure 7-3: Plastic equivalent strain patterns for two specimens with $a/W = 0.4$, having $H/W = 0.70$ (top) and $H/W = 3$ (bottom), at their limit loads.

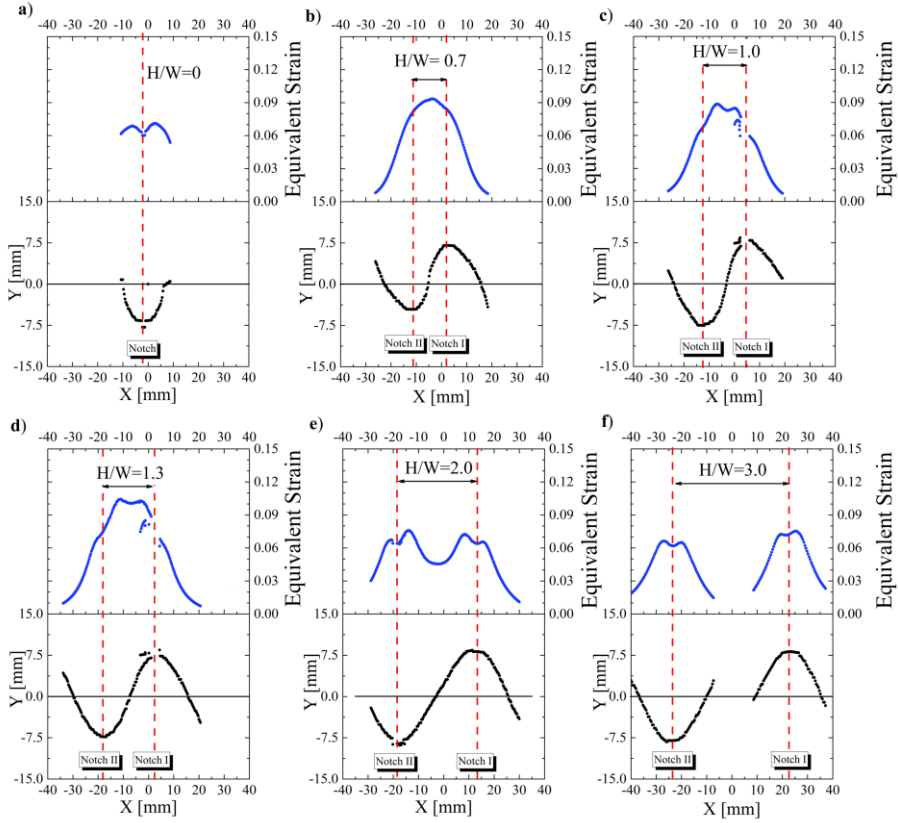


Figure 7-4: SCB trajectories and equivalent strain in DENT specimens.

7.2.3. Analysis of SCB regression line angle

Distinctions between the graphs shown in Figure 7-4 reveal that equivalent strain patterns and magnitudes are considerably affected when the out-of-plane distance between the notches is decreased. This is reflected in the morphology of the SCB, and in the magnitudes of strains adjacent to the notches. As a case study, compare subfigure (b) ($H/W = 0.70$) with subfigure (f) ($H/W = 3.00$). The latter shows that independent notches are associated with straight strain concentration bands (notwithstanding an initially curved shape at the notch tips) and symmetrical strain distributions left and right of the notch tip. On the other hand, subfigure (b) reflects the S-shaped nature of the strain concentration band intersecting the notches, of which the strain level strongly exceeds that of the strain concentrations moving away from the notch pair.

Notwithstanding the added value of Figure 7-4 with respect to judgment on interaction, analyses based on this figure are cumbersome and rely on complete information of strains along a complex trajectory between the notches. Thus, to achieve a more pragmatic judgment on flaw interaction, it is attempted to identify

interaction using a single parameter that describes a relevant morphological change of the SCB. Having extracted the strain concentration bands, lines were fitted by linear regression and characterized by their angle originating from the notch tips as described in Figure 7-1. Figure 7-5 shows the SCB regression angle α (average of α_1 and α_2 as defined in Figure 7-1) versus CTOD during the experiments (up to plastic collapse). The angles appear to be fairly invariable with respect to CTOD, which aids to the pragmatism of using the SCB regression angle as a measure for interaction.

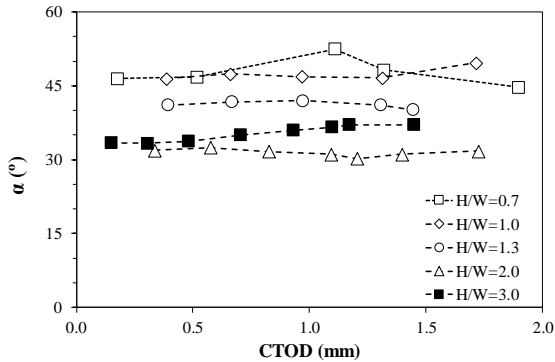


Figure 7-5: Regression angle of strain concentration band versus CTOD.

Notably, the angle for $H/W = 0$ is not shown in Figure 7-5 since in this configuration the vertical grid lines along which strain values are compared show two maxima, thus posing challenges for the algorithm of Figure 7-1 to identify SCB at the early stage of the test. Nonetheless, since in the late stage of the test one of the notches deformed more than the other one, the SCB associated with this notch could easily be identified at the limit load as shown in Figure 7-4. This allows plotting α at the limit load as a function of H/W in Figure 7-6 to Figure 7-8. These angles are then compared with θ , the angle of the line connecting the two notch tips as defined in Figure 5-19. Values for θ are depicted by the dashed red line. Including θ in the analysis is geometrically relevant, as some researchers have suggested using both vertical and horizontal distance between the notches to judge on the interaction between non-aligned flaws [4,5], and these have been adopted by some ECA guidelines [6]. On the right axis of the same figure, the normalized CTOD (δ/δ_0) at different H/W levels is illustrated. All SCB angles and CTOD values have been measured at the limit load. The following graphs are discussed in detail in the next subsection.

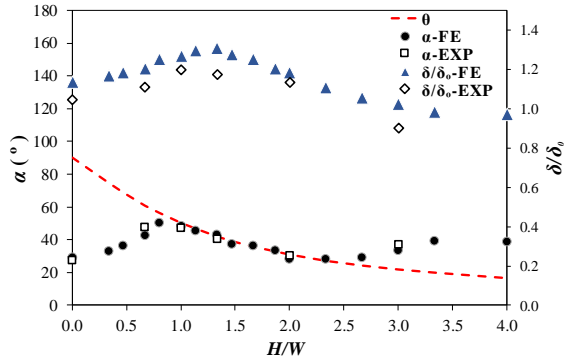


Figure 7-6: SCB regression angle and CTOD at the limit load versus notch spacing for $a/W = 0.4$. Numerical results shown with filled symbols; experimental results shown with open symbols.

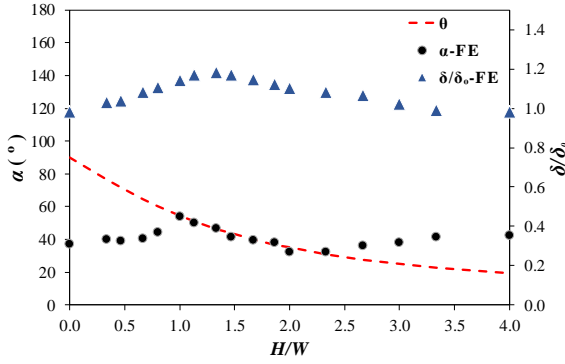


Figure 7-7: SCB regression angle and CTOD at the limit load versus notch spacing for $a/W=0.3$.

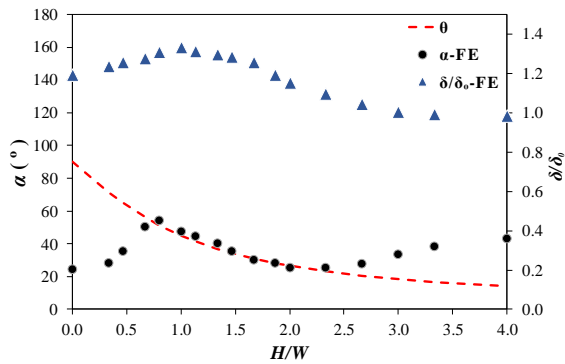


Figure 7-8: SCB regression angle and CTOD versus notch spacing for $a/W=0.5$ at the limit load.

7.2.4. Discussion on application of SCB in flaw interaction analysis

In Figure 7-6 three different trends in angles α versus θ can be observed. From $H/W = 0$ to 1, α is less than φ ; from $H/W = 1$ to 2 the SCB closely follows the straight line connecting both notch tips ($\alpha \approx \varphi$), and finally from $H/W = 2$ to 3, α becomes larger than φ and increases to almost 45 degrees. It can also be noticed that for distant notches δ/δ_0 is almost equal to 1, indicating no interaction in terms of crack driving force. As the out-of-plane distance decreases, δ/δ_0 increases to a peak value around $H/W = 1$. Finally, as H/W further decreases, δ/δ_0 starts to decrease again.

Results from finite element simulations shown in Figure 7-6 to Figure 7-8 reveal that the abovementioned trends between SCB angle and normalized CTOD can be observed for all simulated a/W ratios. Starting from the configuration with most distant notches ($H/W = 4$), the SCB angle α decreases from around 45 degrees to around 30 degrees as H/W drops. Around $H/W = 2.5$ α reaches θ and keeps following θ for lower H/W values. As this transition takes place, δ/δ_0 increasingly exceeds unity. A peak in δ/δ_0 is observed for an H/W level between 1.0 and 1.5 (depending on a/W), indicating maximum notch interaction in terms of crack driving force. Accordingly, a peak in α (reaching up to 60 degrees) is observed around a slightly smaller, but similar H/W level. Going further down the H/W -axis, δ/δ_0 rapidly drops and α deviates significantly from θ . This divergence hypothetically reveals that the effect of flaw interaction gets a new dimension, associated with a fundamental change of SCB morphology. Indeed, the notches in a symmetrical DENT specimen ($H/W = 0$) are connected by two semi-circular SCBs, whereas higher H/W ratios are associated with one (S-shaped or linear) interconnecting SCB. Without further investigation, it is noted that the symmetrical DENT specimen is known to be an example configuration of high crack tip constraint [7], which can be associated with the circular SCB morphology [8]. On the other hand, specimens producing rather straight SCBs (such as SENT specimens but also asymmetrical DENT specimens) are associated with lower crack tip constraint. This discussion implies that besides crack driving force, as a generally accepted parameter to define flaw interaction, crack tip constraint may be considered as well.

When the two SCBs connect, there is considerable deformation between the two notches which can be interpreted as an interaction effect since strain peaks in the SCBs between the notches are higher than those on the outside SCBs (recall Figure 7-2). This is exactly where α is equal or less than θ in Figure 7-6. When the bands between the notches do not connect, α exceeds θ (Figure 7-6) and the symmetrical nature of SCB development around a notch can be interpreted as a non-interacting configuration (e.g. compare Figure 7-4 d and f). This is also reflected in the CTOD analyses of Figure 7-7.

In all abovementioned analyses, flaw interaction was discussed from the viewpoint of H/W . Considering that both vertical and horizontal distances can affect interaction [5], it is worthwhile to investigate interaction from the viewpoint of θ , which combines the influences of H/W and a/W . Figure 7-9 plots observed SCB angles α as a function of θ for all simulated a/W ratios. In addition, the δ/δ_0 -ratio associated with the configuration for which these two angles start to be equal - identified above

as corresponding to notch interaction - are highlighted by dashed vertical lines. Apparently, the point where α equals θ is associated with a CTOD increase due to interaction by almost 10% ($\delta/\delta_0 \approx 1.1$). Depending on a/W , interaction starts at a different angle between the notch tips θ (ranging between 22° and 30° for the simulated cases). This indicates that θ solely is not capable of capturing the combined effects of H/W and a/W on the degree of interaction.

It is finally noted that for notches with higher θ (i.e. shorter distances) the strain patterns are curved, which makes the regression angle less accurate for these cases (see for instance Figure 7-2, $H/W= 0.7$). Figure 7-10 shows the average curvature (= inverse of radius) of SCBs for different θ , highlighting that for higher θ (i.e. smaller H/W) values SCBs have significant curvature compared to highly out-of-plane notches. Hence, the trends in α and in SCB curvature appear to indicate similar events with respect to defect interaction. However, angle analysis is preferred over curvature analysis because accurate calculation of SCB curvature with FE simulations required very fine meshes in the area between the two notches, which made the simulations undesirably expensive.

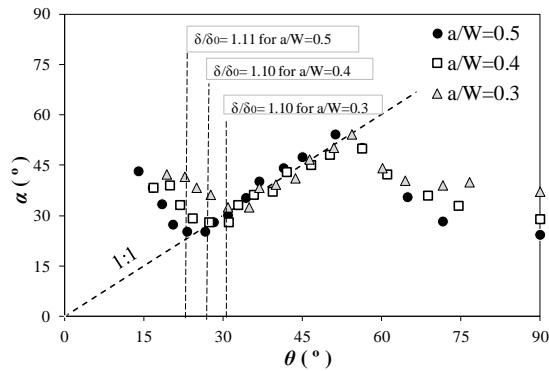


Figure 7-9: α versus θ for various a/W ratios. Dashed vertical lines illustrate CTOD ratios where α and θ become equal.

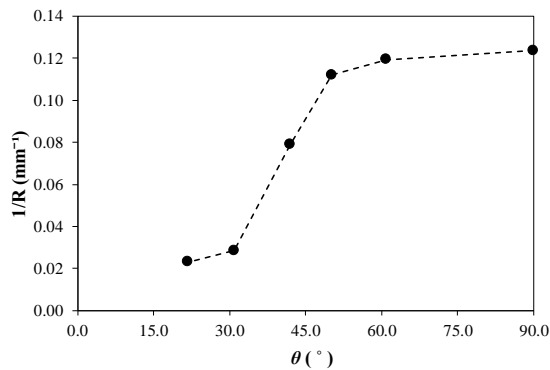


Figure 7-10: Curvature of SCB at TES from the experiments with $a/W=0.4$.

7.3. Interaction of semi-elliptical surface notches

This section elucidates the results of experimental and numerical studies intended to evaluate the feasibility of SCB as an alternative approach to describe flaw interaction. Semi-elliptical surface breaking notches bear closer resemblance to real flaws and are therefore used in these studies. SCB has a clear advantage over conventional methods in evaluating interaction at high strain levels. By observing the SCB trajectory it can be concluded whether ligament failure between adjacent flaws will occur before global plastic collapse or not. In addition, in this section ductile tearing is studied for various configurations to understand the effect of flaw interaction on *R*-curve.

7.3.1. Experimental results for semi-elliptical notches in a wide plate specimen

Experimental studies have been conducted, first to verify numerical simulations and, second to obtain results that are difficult to acquire by numerical studies, like the ductile crack growth. The experimental procedure has been elaborated in chapter 5 and specimen details have been reported in Table 5-1. During all tests, 3D and 2D DIC systems have been simultaneously employed to measure the full field deformation at different scales. In addition, force and displacement have been recorded by the test rig software, which has been synchronized with both DIC systems. Figure 7-11 shows the force-displacement curves for five specimens, three of them (NC12, NC24 and NC36) having two non-coplanar notches with respectively 12, 24 and 36 mm offset distance and 12 mm in-plane distance. The fourth specimen (CP12) has two coplanar notches with the very same 12 mm in-plane distance, and the fifth specimen has two closely located notches with only 1.5 mm distance (see Table 5-1 for more details about the specimens).

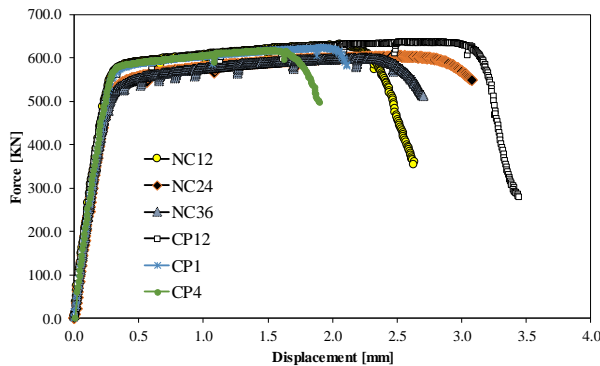


Figure 7-11: Force-displacement curves of three non-coplanar configurations (NC12, 24, 36) compared with three coplanar configurations (CP1, CP4, CP12).

From Figure 7-11 it can be seen that specimens CP1, CP12 and NC12 have different yield loads compared to specimens NC24 and NC36. This is because the circumferential location in the pipe at which specimens had been extracted were

different for these specimens and therefore marginally different yield stress can be expected (around 30 MPa). To acknowledge this difference, CP1, CP12 and NC12 are categorized under Region I, and NC24 and NC36 under Region II. From Figure 7-11 significant conclusions can be made with respect to interaction. First, comparing the maximum loads of CP1, CP12 and NC12, there is no significant difference between them; the same is true for NC24 and NC36. As shown in Table 7-2, the maximum remote stresses, which correspond to plastic collapse, do not show a significant difference with offset distance. This is in accordance with work of Hasegawa [9,10], which showed that for shallow non-coplanar cracks, plastic collapse load is not affected by offset distance. Comparing CP1 and CP12 shows that reducing the distance between two coplanar notches marginally decreases the maximum load. Second, CMOD values at maximum load are almost identical for each specimen. This supports the work of Moon [11] that showed that plastic collapse of tubes with two non-coplanar notches occurs when the COD at both cracks is equal to the COD of a single crack at the failure load. In other words, it may be assumed that when failure happens, CMOD (or COD) is equal to a certain value. This critical value for CMOD can be estimated by analytical or numerical models, or alternatively it can be determined in an experiment comprising one notch. As such, CMOD can be used as an indication to distinguish the failure load for specimens made from the same material with similar (and equal) non-coplanar notches.

Table 7-2: Stress, strain and CMOD at the maximum load.

Material region	Specimen	Maximum stress	Overall strain at maximum load	CMOD at maximum load
I	CP1	624 MPa	3.6%	2.24 mm
I	CP12	637 MPa	6.9%	2.20 mm
I	NC12	634 MPa	4.6%	2.25 mm
II	NC24	604 MPa	6.3%	2.42 mm
II	NC36	602 MPa	6.1%	2.38 mm

As shown in Figure 7-12 and Figure 7-13, CMOD value given that depth and length of the notches are identical. In Figure 7-12 maximum load around CMOD = 2.20 mm (maximum value of the two notches). Beyond maximum load, force starts to drop while crack opening rises significantly. For material region II, the failure can be linked to a CMOD value around 2.40 mm for both specimens.

Another important observation is the evolution of CMOD versus increasing displacement (or applied strain). Figure 7-12 shows that while the evolution of CMOD for CP1 and NC12 is almost equal; the rise of CMOD with applied strain is less for CP12. Figure 7-14 compares the trend of CTOD at the notch center, measured by DIC based profilometry, versus increasing overall strain for specimens CP1, CP12 and NC12. It is evident that CP12 shows less CTOD at equal strains compared to the two others. The difference between CP1 and CP12 can be easily linked to the amount of interaction, but the difference between NC12 and CP12 requires a more in-depth analysis. Based on these tests it can be concluded that CP12 is less critical than NC12 when it comes to CTOD, although both of them are non-interacting according to guidelines like ASME B&PV Code Section XI and BS7910.

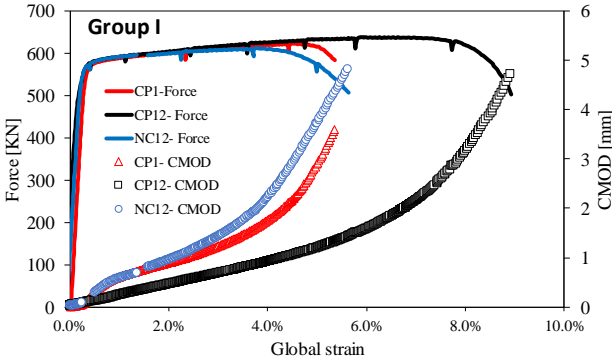


Figure 7-12: Force-global strain and CMOD-global strain curves for group I.

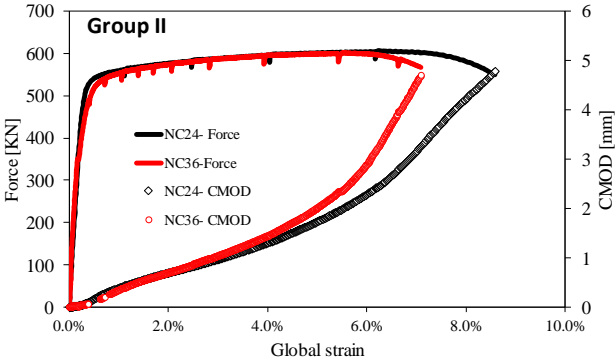


Figure 7-13: Force-global strain and CMOD-global strain curves for group II.

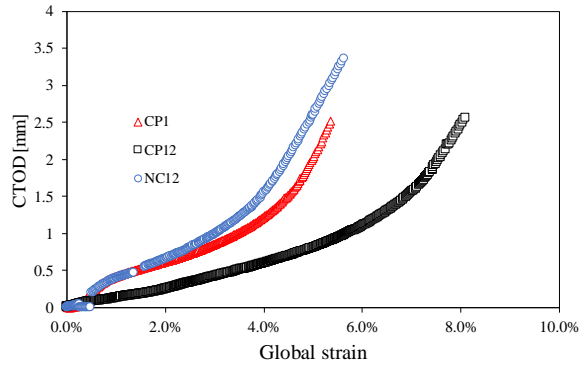


Figure 7-14: CTOD versus overall strain for CP1, CP12 and NC12.

In the present study, specimens CP1, CP4 and CP12 have a coplanar configuration. As depicted in Figure 7-15, both notches in CP1 and CP12 show almost identical evolution in CTOD with increasing strain, as could be expected since their sizes are very close.

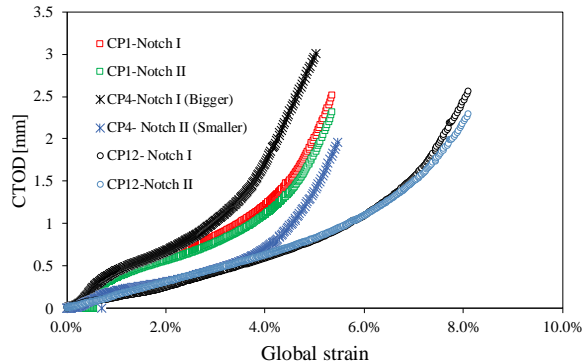


Figure 7-15: CTOD of both notches versus overall strain for CP1, CP4 and CP12

Thanks to two separate DIC systems monitoring the front and back of the specimen during the tensile test, the deformation at both surfaces and the penetration of the notches can be detected. Figure 7-16 shows the equivalent strains at two stages for a specimen with coplanar notches; at the Twice Elastic Slope (TES) load and at maximum load. Specimen deformations at TES are only shown for the front surface, while at maximum load both front and back surface strains are illustrated.

Figure 7-17 illustrates full field deformation results in terms of equivalent strain for three specimens with non-coplanar notches. Again, strain patterns at TES and maximum load are shown separately. Comparing the strain patterns shown in Figure 7-17 at maximum load shows a distinct difference between three different offset distances.

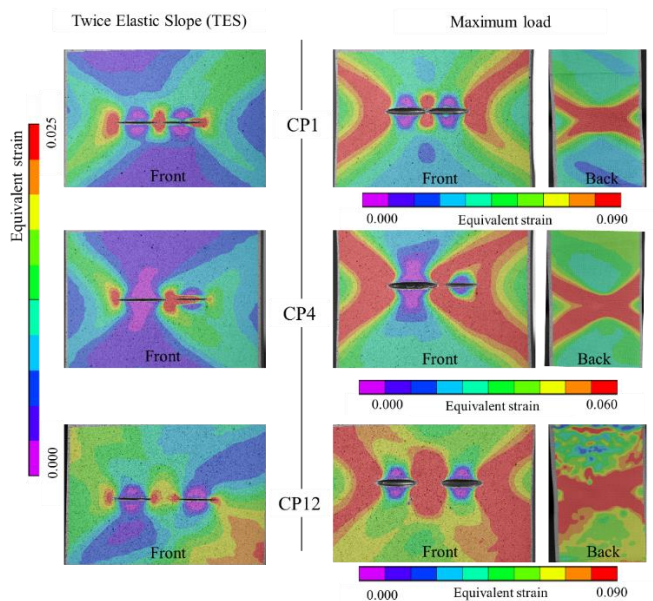


Figure 7-16: Strain distribution for loads corresponding to Twice Elastic Slope (TES) and maximum load for specimens with two coplanar notches.

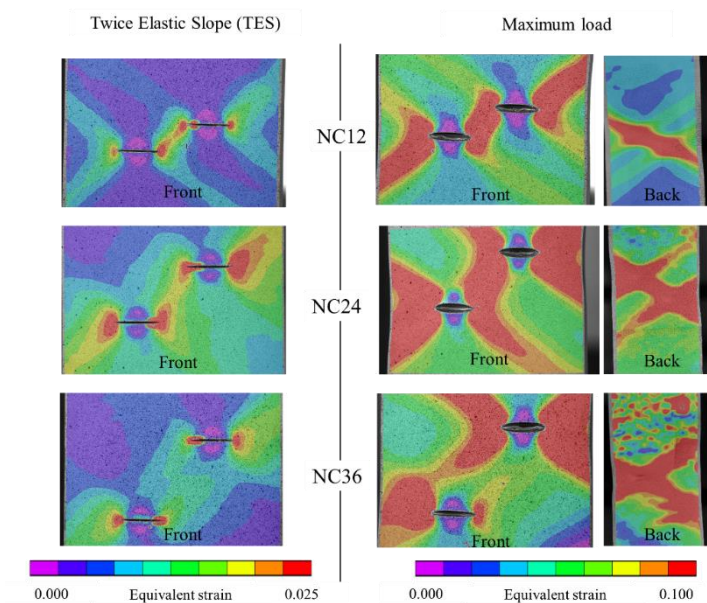


Figure 7-17: Strain distribution at loads corresponding to Twice Elastic Slope (TES) and maximum load for specimens with two non-coplanar notches.

Specimen NC12 at TES (left figure) has the highest deformation on a line passing through both notches with almost 45 degrees orientation to the load direction, this line became a large region in maximum load (right figure). Therefore, it can be concluded that failure on this particular line dictates maximum load. In specimen NC24 at TES not only the line connecting the notches shows a high amount of deformation, regions around the notches also have quite high strains. This became more clear at maximum load and when plastic collapse happened already high amount of deformation has been absorbed by the specimen. Comparing strains in specimens NC12 and NC24 at maximum load also shows that in NC12 apart from the line connecting the two notches, the rest of the specimen only shows limited strains while this is not the case for NC24 and definitely not for NC36. In specimen NC36 the line connecting both notches has not the highest deformation; there are considerably higher strains all over the specimen at maximum load. In other words, placing notches further away than 36 mm may not affect the strain patterns because the second notch is not affected by the failure trajectory.

Unlike the patterns in Figure 7-17, in Figure 7-16 patterns are relatively similar. Failure occurs in the plane containing the notches and the plastic deformation starts from the notch tips and gradually spreads towards the edges in the notched plane. Specimen CP4, however, has a slightly different strain pattern since its notches are not identical. As expected, the largest notch is the dominant one as the smaller notch only shows limited crack opening. In addition, strain patterns in CP4 evolve in such a way that it seems that the smaller notch has a marginal influence on them. This is clear at TES, when the entire smaller notch is contained in the plastic region of the bigger notch.

Although strain patterns for CP1 and CP12 have a similar morphology, a detailed comparison reveals some profound differences. First of all, strains outside the notch planes and the two slip lines in CP1 are less than these in CP12 at maximum load, while their magnitudes in the notch planes and along the slip lines are quite similar. Secondly, the specimen reached to its maximum load before generating a large plastic region between the two notches in CP1, while in CP12 a larger plastic zone has been created between the notches. At the early stages of loading the notches in CP12 deform with lesser interaction compared to CP1. When the load is increased, they start to interact more severely, which is the case at maximum load.

The failure modes observed in all of the above specimens can be described as deformation concentration around the notches, decreasing remote stress (force) in combination with a strongly increasing CMOD (or CTOD). Recall from section 2.2.2, these observations can be linked to “net section collapse” (NSC). When pop-through is happened, it is proceeded by a significant stable ductile crack growth, which can be characterized with a sudden increase of CMOD (or CTOD), the failure may be referred as local (or flaw ligament) collapse. If pop-through is not happened, the failure may be referred to as global collapse, and this indicates that the failure depends more on the material ductility rather to its toughness.

A more quantitative comparison between specimens with various offset distances (H) can be achieved by using the SCB concept, introduced earlier in this chapter. The same methodology used to detect interaction of through thickness notches is evaluated for semi-elliptical surface notches. Figure 7-18 shows the SCB trajectory and its equivalent strain versus the X and Y coordinates at the TES load for three specimens with non-coplanar notches. Comparing graphs A, B and C in Figure 7-18 reveals that in specimen NC12 the maximum strain occurs exactly on the shortest path connecting two notch tips. Unlike NC12, in NC24 maximum strains appear at the far tip of a notch (compared to the other notch), showing that for each notch the deformation pattern is influenced more by its boundary condition than by interaction with the adjacent notch. This behavior is more evident in NC36 (graph C), in which both notches tend to deform more at their far tips, which generates two 45-degree lines from each far tip towards the specimen's edges. In both NC24 and NC36 a 45 degrees line in the middle of the specimen between the two notches can also be observed. In case of NC36 this line seems to be completely separated from the notches, while in NC24 it seems to be connected to the lower notch, but as it can be seen in Figure 7-19, this link almost disappears at higher loads (strains).

Another important conclusion which can be drawn from graphs A, B and C is that the procedure based on SCB angle calculation introduced for through thickness notches in Section 7.2, cannot be directly employed for surface breaking notches. This is because, unlike through thickness notches, SCBs can develop at both sides of a semi-elliptical surface breaking notch, towards the adjacent notch as well as the specimen's edge. For instance, in specimen NC36 no SCB initiated from the tip closest to the adjacent notch; therefore, the SCB's angle or curvature cannot be defined. However, this does not mean that SCB cannot be used for interpreting the interaction between surface breaking notches. There are subtle differences between SCBs for various specimens and this can be used as a tool to clearly distinguish between interacting and non-interacting notches.

Figure 7-18 shows the amount of equivalent strain (at the TES load) on the SCB versus X coordinate in graphs D, E and F and versus Y coordinate in graphs G, H and I. As expected, the amount of strain between the two notches is higher for NC12 (graph D) and becomes less when the offset between the two notches is increased (graphs E and F). Also, since strains at both notches are similar (graphs G, H and I) it can be concluded that the deformation is not affected considerably by marginal differences in notch length and depth. Finally, comparing equivalent strain graphs reveals that in specimens NC24 and NC36 the strains around the tips closest to the adjacent notch are relatively higher than in the region between the two notches. While in NC12, the amount of strain at the tips close to the other notch is quite similar to the strain in the region between the notches.

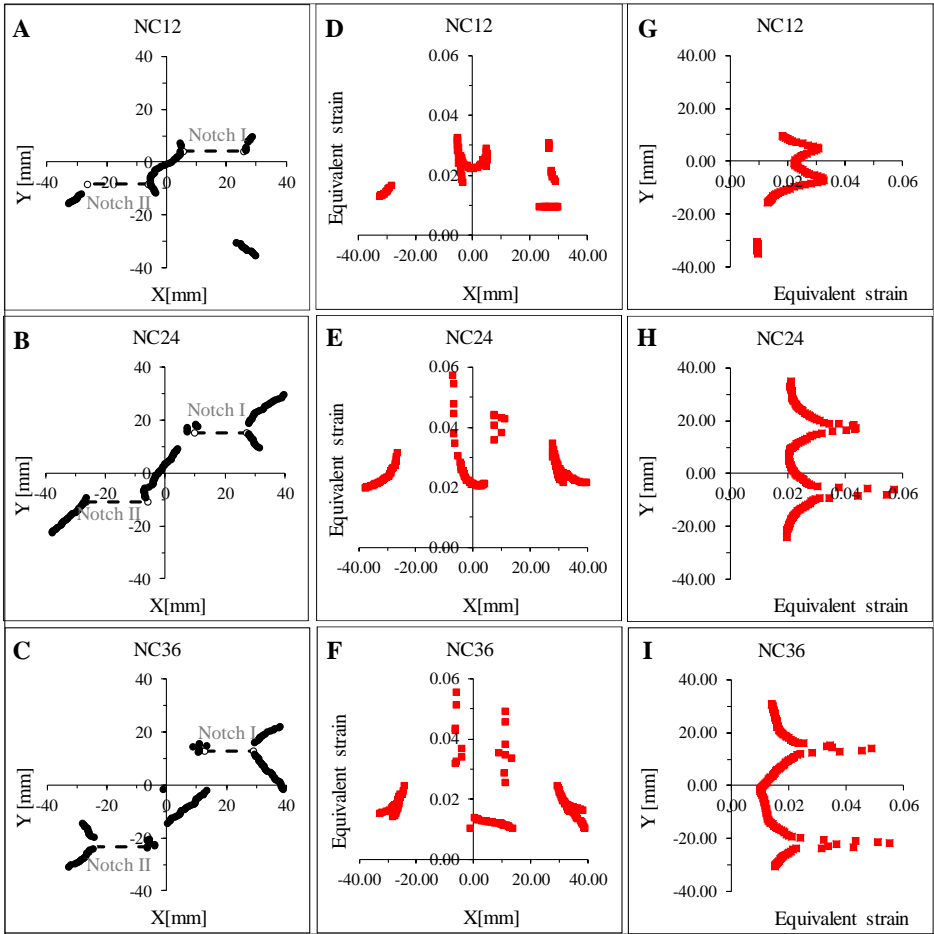


Figure 7-18: SCB trajectory and equivalent strain on SCBs at TES.

Studying the strains in the SCBs on Figure 7-19, shows that the strain between the two notches on graph D for NC12 is higher than in the outer regions, clearly indicating interaction. In specimen NC24 (graph E) there is considerable strain between the notches, but it is less than around the far tips. Graphs G and H show that the amount of strain around both notches is similar for NC12 and NC24, showing that they deform equally during the tensile test. For specimen NC36 this is not the case. As shown in graph I one notch deformed considerably more than the other one and failure is dominated by one notch.

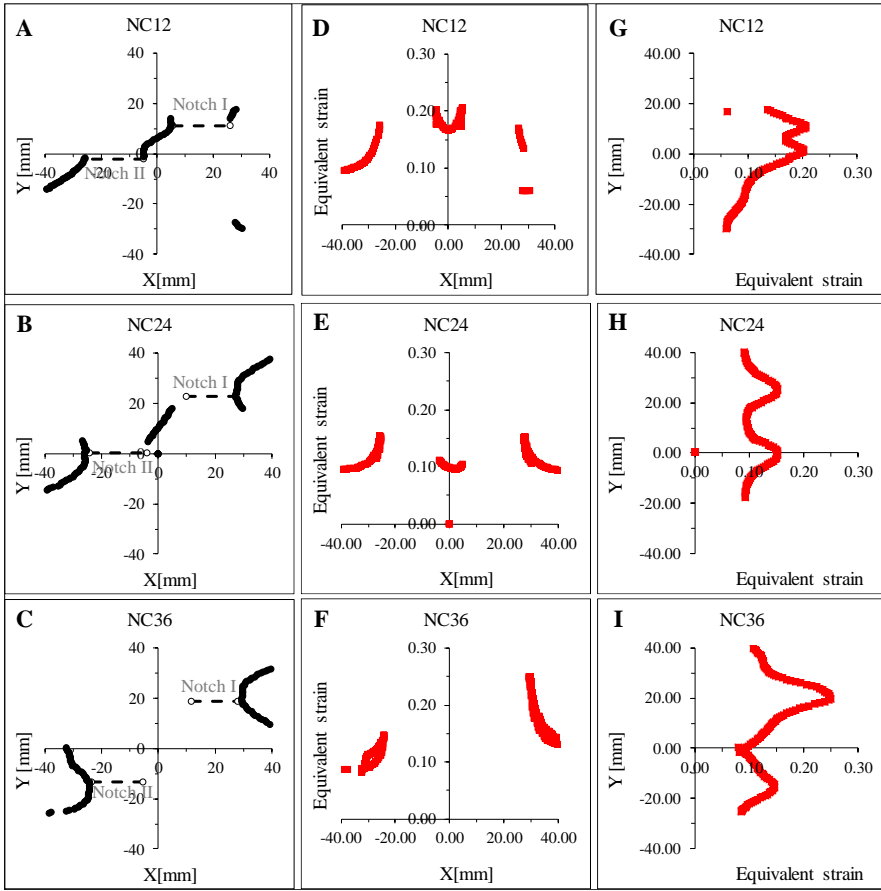


Figure 7-19: SCB trajectories and equivalent strain on SCBs at maximum load.

Considering the results shown in Figure 7-18 and Figure 7-19, it can be concluded that two types of behavior can be observed. On the one hand, notches in specimen NC12 have a clear interaction. Final failure and the trajectory of the deformation leading to plastic collapse is influenced by both notches and the region between the notches experienced strains higher than in any other region of the specimen. On the other hand, in specimen NC36 the notches deform independently. The difference between these two behaviors becomes more clear at maximum load compared to TES, indicating that ductile crack growth, which is more pronounced in later stages of the loading, probably intensifies this difference.

7.3.2. Ductile crack growth evaluation

Last but not least the ductile crack growth is evaluated. Strain-based design procedures normally tolerate a certain amount of stable ductile crack extension; here the question is if crack growth is affected by interaction. The precise answer to this question is not easy and requires investigating many configurations and materials,

which was not possible in the framework of this research. However, crack growth has been evaluated for a few cases in both presence and absence of interaction. The results will provide answers to two main research questions. First, is crack growth resistance in terms of R -curve affected significantly by flaw interaction? And second, does the crack grow towards the adjacent crack, as stress intensity factor may suggest? The second question is raised because fracture mechanics evaluation showed that when interaction takes place, the maximum stress intensity factor occurs in locations other than the deepest point ($\varphi \neq \pi/2$), but it is not clear whether this dictates that the maximum crack growth also happens in locations other than the deepest point.

The answer to the second question also contains the answer to another ambiguity about the growth of a surface breaking flaw: does a surface breaking flaw grow equally in depth and width direction? On the one hand, API 579 [6], in paragraph 9.3.6.6 C-2, suggests that when the plastic strain on the remaining ligament is large and the flaw may grow to the free surface by ductile tearing, the flaw should be assumed to also extend in its length direction by the same amount at each side. Therefore, as a conservative measure, the crack length should be increased by twice the ligament dimension in ECA assessments. On the other hand, Bezensek et al. [12] observed that in case of two interacting cracks, the ductile tearing is initially suppressed at the free surface (far tip) due to the loss of constraint associated with out-of-plane effects. They observed that the amount of crack growth and length extension at the non-interacting tips is negligible. Also, they reported that the maximum crack growth happened at the deepest point of the crack front. If the latter observation is taken into account, it means if there is no crack extension in the length direction, the mapping approach is far more straightforward to apply.

Silicone replica casting has been employed to measure the ductile crack growth during experimental testing. After curing, the replicas were carefully sliced and the crack growth and CTOD have been measured at various locations. Figure 7-20 shows examples of the replicas for some specimens. White triangles indicate the original crack tip and ductile crack growth is shown by Δa . CP1, which has two closely spaced notches, is different from the others due to coalescence of the notches. But, as shown in Figure 7-21 this coalescence was almost negligible until the event of plastic collapse. In other words, the replica slices allow to conclude that ductile growth of one notch is almost independent from the other and that coalescence only happens when the re-entrant section (the region between the two notches) becomes small enough to fail. A similar observation has been made before by Bezensek and Hancock [12]. At the bottom of Figure 7-21, replicas sliced at the notch center are shown. The first replica does not show visible tearing and it can be assumed that it represents the original crack front. Replica 2 is taken at an intermediate stage and replica 3 has been cast around the maximum load. Note that the strange behavior centrally at replica 3 is probably due to replica making (trapped air bubble) and does not represent of the actual crack profile.

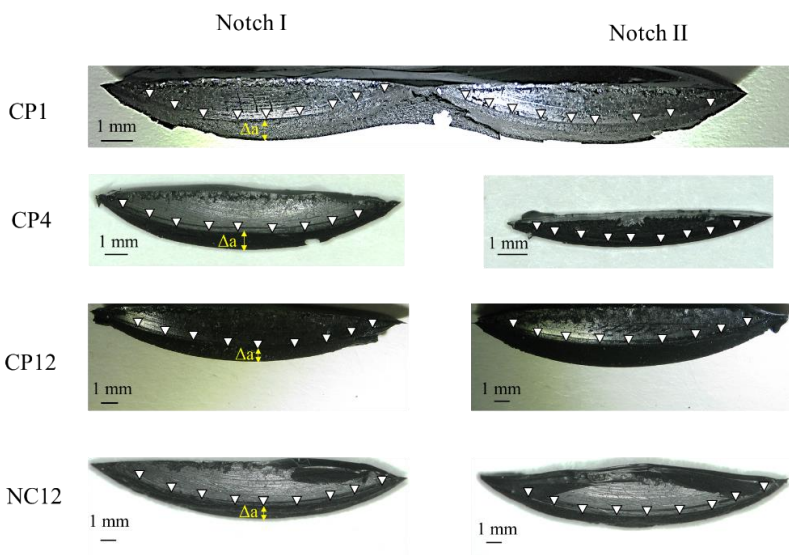


Figure 7-20: Replicas of four specimens (CP1, CP4, CP12 and NC12) at maximum load (white triangles show the original notch tip to highlight the amount of crack growth).

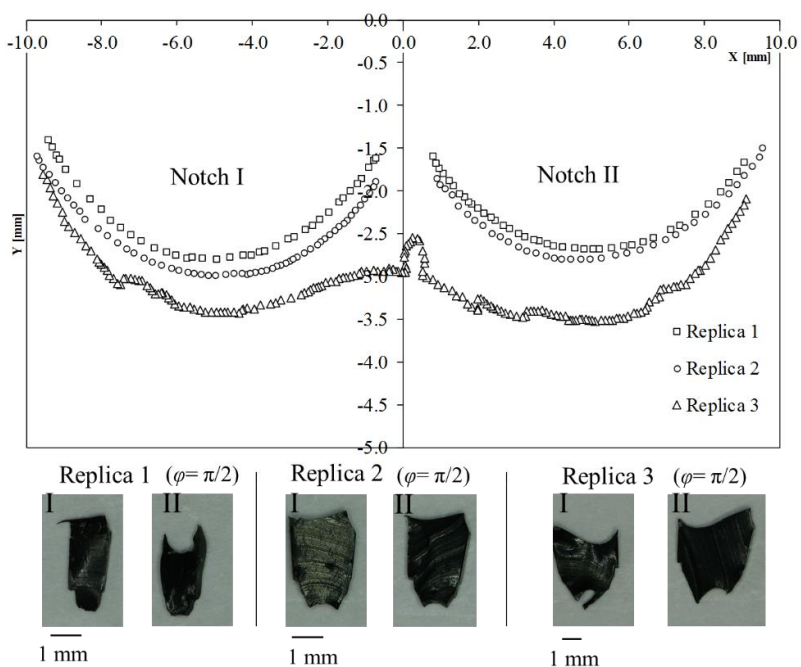


Figure 7-21: Crack front profile during ductile tearing of CP1.

Figure 7-22 shows the slices cut at the center of the notch ($\varphi = \pi/2$) for all specimens before the failure. It can be clearly seen that there is more ductile growth in CP1 compared to CP12, due to the larger distance between the notches. CP4 has two dissimilar notches; while the largest notch shows considerable ductile tearing, the smaller one has almost zero growth. This is corresponding to the observations of strain patterns shown in Figure 7-16. In NC12 and NC24 both notches have a quite similar amount of ductile tearing, while in NC36 only one of the notches grew, which is consistent with the observation of Figure 7-17 indicating that the failure trajectory passed through only one notch. The above observations on replicas of specimens NC12, NC24 and NC36 are also in line with the evolution of SCBs in Figure 7-19, where in graph H and G the strains are equal around both notches whilst in graph I one notch has higher strains.

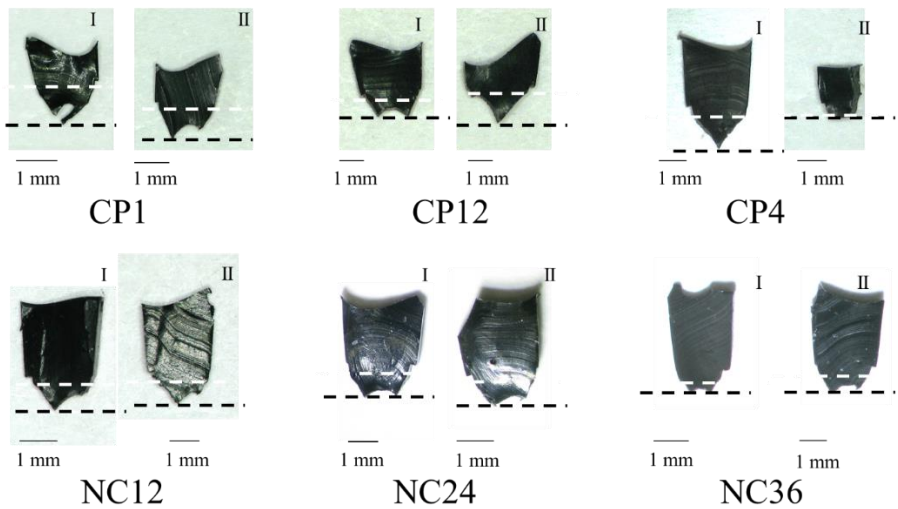


Figure 7-22: Slice of the replicas at $\varphi=\pi/2$ (the deepest point) around the event of failure.

A more quantitative comparison with R -curve is illustrated on Figure 7-23 to. Although measurement of crack growth based on replicas is not very accurate, it allows to reveal the trend of the resistance curve. It can be observed that for all specimens, both notches show a similar trend, whilst one might grow more at the end of the test. The effect of interaction on the R -curve can be seen in Figure 7-24, where the notches with largest crack growth from various specimens are compared.

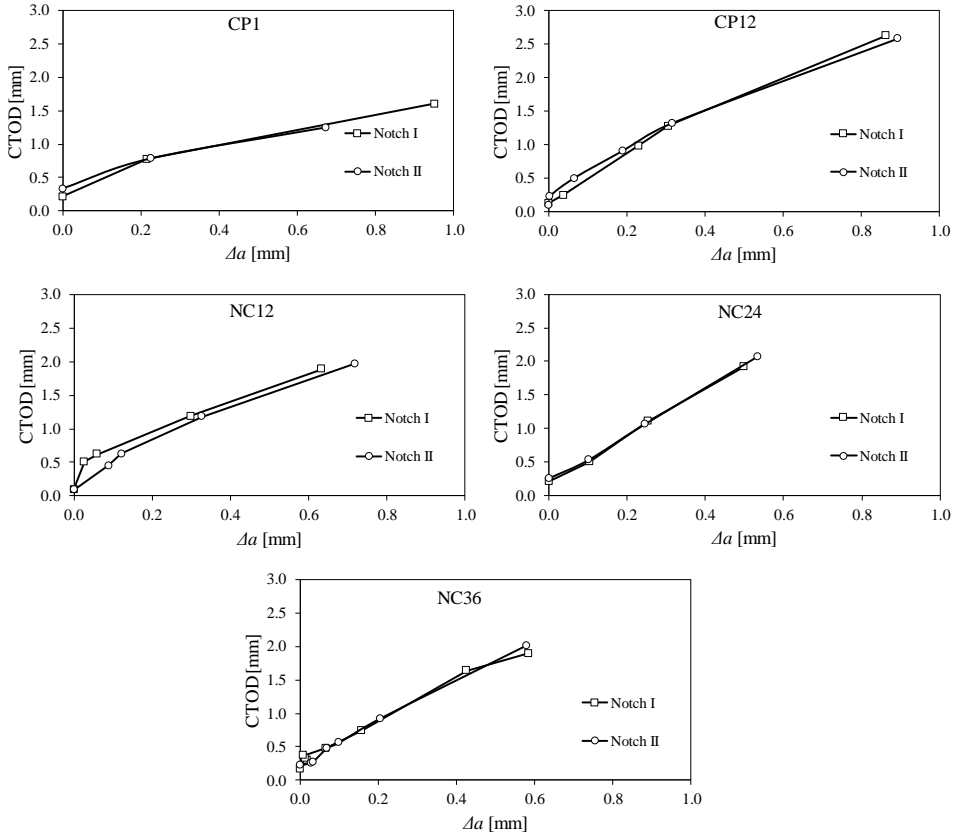


Figure 7-23: CTOD-R curve of CP1, CP12, NC12, NC24 and NC36

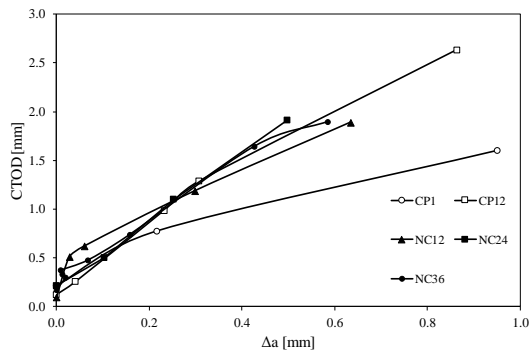


Figure 7-24: Summary of CTOD-R curves from different specimens.

Figure 7-24 shows that R-curves of specimens with identical notches but different spacing can be divided in two categories, in which CP1 clearly differs from

the rest. This is not surprising, since only specimen CP1 has interacting notches according to ASME B&PV code section XI and BS7910. Thus, notches in CP1 show larger crack growth for the same CTOD compared to their counterparts with larger spacing distance. This is an interesting finding because it shows that due to interaction not only SIF is increased, but also ductile crack growth resistance may be influenced (note that the last replica does not necessarily correspond to failure or unstable crack growth).

This result confirms that constraint plays a significant role in flaw interaction when it comes to ductile tearing. As shown in Figure 7-25 for two coplanar cases, both flaws have almost identical *R*-curves at the start of the test. However, beyond 0.2 mm crack growth which corresponds to Replica 2 in Figure 7-21, their *R*-curves become different. This can be linked to the fact that up to this moment the flaws in specimen CP1 did not coalesce; therefore, their *R*-curves are very similar to their counterparts in CP12. However, as can be seen in Figure 7-21, somewhere between Replica 2 and Replica 3 the flaws have coalesced and from this point they behave like a larger single flaw, and exactly from this point their *R*-curve shows more crack growth for the same CTOD. This change in *R*-curve can be linked to an increase of constraint due to the increase in notch length, which has been reported by Verstraete et al. [13] based on tearing resistance analyses of single notched specimens with variable notch length.

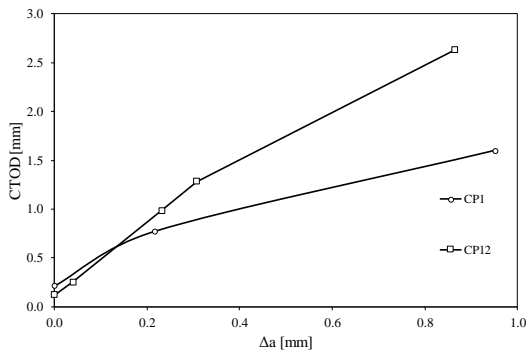


Figure 7-25: R-curve of two coplanar cases (CP1: coalesced, CP12 not coalesced)

Figure 7-26 shows the post mortem fracture faces of specimens CP1, CP4 and NC12. Fracture faces of other specimens are not depicted. Due to the relatively large distance between non-coplanar notches in NC24 and NC36 there was no noteworthy information on their broken surface. The test on specimen CP12 was stopped after pop through of both notches, which made them grow towards each other as well. To avoid confusion, its post mortem fracture surface is not presented. As observed earlier in replicas shown in Figure 7-21, the notches in CP1 have coalesced. The slight difference between the color of the region between both notches and the ductile growth at their crack front (Figure 7-21) shows that the coalescence happened abruptly

after sufficient growth at both notches. In CP4, the growth of the larger notch is visible up to the back surface. Here the region between the two notches has a ductile tear that continues to the small notch. Since this growth at one side of the smaller notch has not been captured in Figure 7-20, it can be concluded that the growth between notches and below the small notch happened only after pop through of the largest notch. In NC12, again pop through happened at the end of the test, again only for one of the notches. Here also crack growth can be noticed between the notches, although the inherent non-coplanar nature of the sample makes it difficult to notice. For the same reason as above, it is concluded that this growth happened only after pop through of one of the notches.

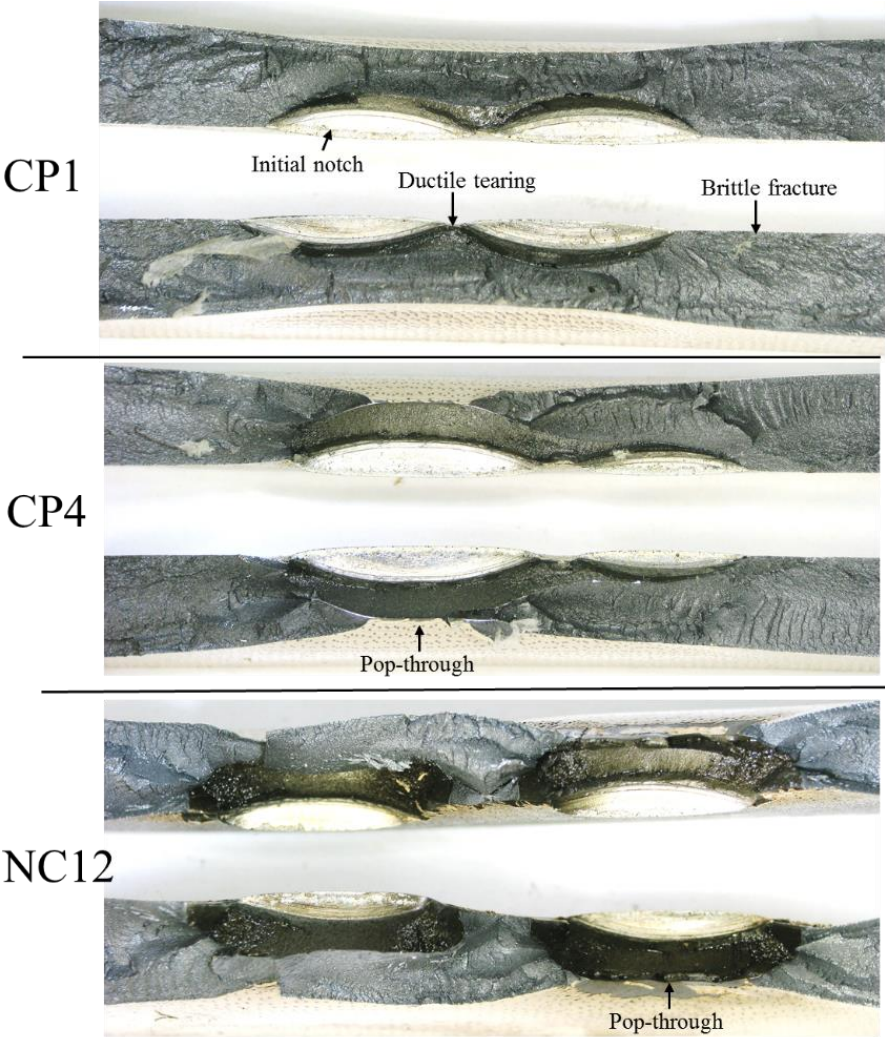


Figure 7-26: Post mortem fracture surfaces of CP1, CP4 and NC12.

7.3.3. Numerical results for semi-elliptical surface notches in a wide plate specimen

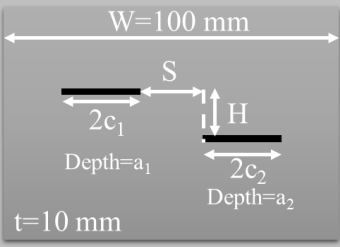
Interaction can be evaluated in two ways. It either means that the presence of one notch affects the behavior of the other (in terms of SIF, ductile crack growth or collapse load), or that before plastic collapse the two flaws coalesce due to ductile crack growth and failure of the re-entrant region. The former, hereinafter referred to as global interaction, is acknowledged by many ECA guidelines as the conceptual definition of interaction. By assuming that its consequence will be the latter phenomenon, hereinafter referred to as local interaction, a conservative assessment can be ensured by substituting both flaws with one larger virtual flaw. It should be noted that limiting the evaluation to local interaction solely is not a conservative approach, because if global interaction is deemed to occur, the larger flaw will not be a conservative representation of both flaws, regardless of the coalescence or ductile growth trajectory. In other words, if a specimen with two non-coplanar flaws fails sooner (i.e. at lower remote stress or strain) compared to the very same specimen with only the largest flaw, then the interaction is there regardless of the local behavior of the flaws.

Moreover, if a specimen with non-coplanar flaws fails at lower (remote) strain compared to a specimen with similar flaws in a coplanar configuration (same depth, length and horizontal distance), a red flag should be raised. This would contradict interaction assessments in ECA guidelines like ASME B&PV Code section XI and BS7910, which assume that flaws in coplanar configurations are always more critical than their non-coplanar counterparts. Actually, more critical non-coplanar flaws compared to coplanar ones is exactly what is observed in section 7.2.1 (e.g. Figure 7-14). Experimental results suggest at least that notches in a 45-degree configuration (horizontal spacing equal to vertical spacing) can be more critical than similar coplanar notches.

The FE study in this chapter is divided into two parts which are hereafter referred to as “pilot study” and “main study”. In the pilot study (limited set of cases), the goal is to find out if the experimental observations presented earlier, in particular the more severe interaction for certain non-coplanar configurations, can be seen in FE results as well. In addition, the pilot study assesses whether flaw size and spacing distance affect the observed severity of interaction in non-coplanar configurations. If the pilot study confirms the experimental observations, the applicability of a two-step alignment and interaction approach for assessing the failure at high strain regimes might be questioned. The goal of the main study is to evaluate whether in wider plates with larger combinations of notch sizes and spacing distances the same conclusion as for the pilot study can be drawn and if non-coplanar configurations with severe interaction exist, which are not defined as interacting by ASME B&PV Code sec. XI and BS7910 criteria.

The first part of the pilot study comprises eight simulations with plate dimensions similar to the experiments described in section 7.2.1, which were also used to validate the FE model (chapter 5). Table 7-3 shows the details of each model. Since the experiments with through thickness notches (section 7.1) suggest that notches located in 45-degree configuration ($H=S$) are the most critical, the pilot study also includes such configurations. All non-coplanar models (P2, P4, P6 and P8) satisfy the alignment criterion of ASME B&PV Code section XI while only P2 and P4 satisfy this of BS7910. Nonetheless only P1 and P2 are categorized as interacting flaws according to these guidelines. Material properties similar to the experimental procedure is used in FE models.

Table 7-3: Details of models used in first part of pilot study (dimensions in mm).



Tag	$a_1=a_2$	$2c_1=2c_2$	S	H
P1	3	20	1.5	0
P2	3	20	1.5	1.5
P3	3	20	6	0
P4	3	20	6	6
P5	3	20	12	0
P6	3	20	12	12
P7	5	24	12	0
P8	5	24	12	12

To allow comparison of different models, their responses based on global strain versus CMOD are plotted in Figure 7-27 and Figure 7-28. To estimate the onset of failure, based on Moon’s suggestion [11], it is assumed that when the CMOD of one of the notches reaches the critical CMOD, failure will occur. The exact value of this critical CMOD is not essential since only a qualitative comparison is intended for the pilot study. If a quantitative comparison is desired, the exact value of critical CMOD will be required. Figure 7-27 shows the global strain versus CMOD for the first six cases with identically sized notches. It can be seen that for the same CMOD value, global strain in non-coplanar configurations (P2, P4 and P6) is slightly less than in coplanar configurations. The difference is not identical for all cases. P5 and P6 have the most prominent distinction, while the difference between P3 and P4 is less evident. As shown in Figure 7-28, however, the opposite behavior can be noticed for longer and deeper notches (P7 and P8). In these two cases, the coplanar configuration has less strain for the same CMOD. Finally, in Figure 7-27, the strain-CMOD curve of P6 is very close to the curves of P1 and P2, which are classified as interacting by ASME

B&PV section XI and BS7910. This indicates that while the coplanar configuration (P5) is not interacting, its non-coplanar counterparts are not only more critical when it comes to strain at failure, but this difference is also significant enough to consider the notches in P6 as interacting (since their response is similar to P1 and P2).

Explaining what is observed in Figure 7-28, however, is not straightforward. It seems that for certain combinations of notch depth, length and spacing distance the non-coplanar notches behave more critical than the same notches in a coplanar configuration. Hypothetically, the trajectory of shear planes which cause the plastic collapse can be influenced by non-coplanar notches leading to earlier collapse. This can be linked to the experimental observations, in which SCBs are altered by the distance between notches. To understand this matter and figure out if the same behavior can be detected in wider plates as well, the main study has been defined. But before that, the second part of the pilot study is performed to validate the approaches used in the main study for assessing plastic collapse and unstable crack growth.

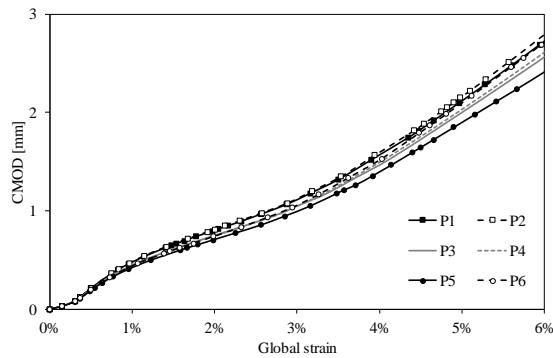


Figure 7-27: Global strain-CMOD curves of P1-P6 from the pilot study.

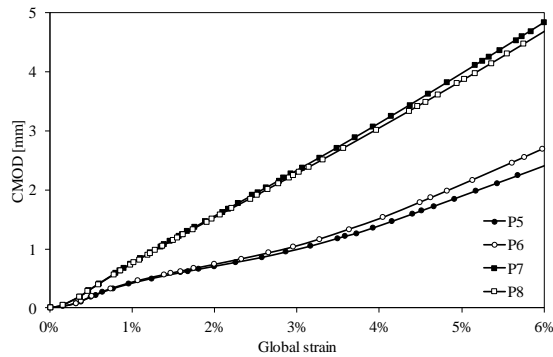


Figure 7-28: Global strain-CMOD curves of P5-P8 from the pilot study.

To evaluate interaction, global strain at failure will be used. Predicting failure in FE models requires some assumptions. Since the material surrounding the notches is identical to the rest of the specimen, one or both notches will be involved in the failure, so failure remote from the notches is not expected. Thus, failure will be in mode of NSC and a combination of plastic collapse and ductile tearing. To determine the critical CMOD at failure, incorporating the effect of ductile tearing, the mapping technique with stationary notches of increasing depth is employed (refer to chapter 2 for more details about the mapping technique). To validate this approach, the second part of the pilot study examines the applicability of the mapping technique for determining the critical CMOD. Hereto, a single notch in a flat plate 100 mm wide and 10 mm thick is modeled. Simulations are repeated with increasing notch depth (0.5 mm increment) and assuming a constant notch length. Comparing simulated CTOD versus Δa at different global strain levels with the CTOD-R curve gained from experiment NC36, the event of pop-through (unstable crack growth) can be identified using the tangency approach. As shown in Figure 7-29, this takes place between 5% and 5.2% global strain, which corresponds to CTOD equal to 1.9 mm. Then, from Figure 7-30, CTOD values can be linked to their corresponding CMOD value, which is 2.3 mm for maximum load (corresponding to the failure). Comparing this CMOD with those observed in the experiments (see Table 7-2), shows a good agreement. Therefore, the procedure of extracting CMOD at failure from the single notch model (using mapping technique) allows to predict the failure for the models with two adjacent notches assuming that failure happens when CMOD reaches its critical value. Note that in this study it is assumed that failure accompanies unstable crack growth. The goal is not to define the exact value of plastic collapse load, but rather to compare and assess different configurations at the critical event of failure, which is the combination of plastic collapse and unstable crack growth. This can be justified considering that flaws are more prone in the welds, where weld metals toughness plays a significant role in determining the failure compared to its ductility.

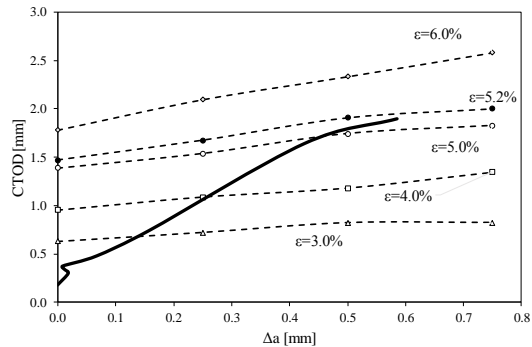


Figure 7-29: Tangency approach to estimate the strain capacity and CTOD at failure.

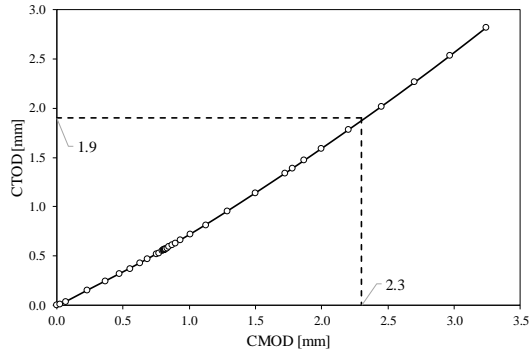


Figure 7-30: CMOD versus CTOD of FE model with single notch ($a=3$ mm, $2c=22$ mm).

The FE simulations of the main study are intended to examine the global interaction between remote non-coplanar flaws. Notch dimensions and spacings are defined in a way that even if they would be categorized as aligned by ECA, they would not satisfy the interaction criteria. This should allow to find certain configurations in which notches are globally interacting but not locally. In other words, given that the pilot study confirmed that certain cases of non-aligned flaws can be more critical than their coplanar counterparts, this study should reveal whether this can undermine the ECA conservativeness of non-coplanar flaw assessment in high strain regimes or not.

The FE results of the main study will be compared with criteria presented in ASME B&PV Code sec. XI and BS7910. In addition, two alternative criteria will be considered to assess the possibility of suggesting a better criterion for non-coplanar flaws. The first alternative is referred to as “area criterion”, based on Iwamatsu et al. [14]. For limit load estimation (or plastic collapse load), it is crucial to understand which cross sections are dominant in the failure trajectory. Unlike the coplanar configuration, it is not clearly known for non-coplanar configurations how the plastic collapse (or limit) load can be calculated since defining the cross section is not straightforward. Among the various suggested methods, Iwamatsu’s approach for assessing the limit load of non-coplanar through thickness notches is attractive due to its simplicity and agreement with experimental results. In a nutshell, it is based on comparing the net section of the longer flaw (A_s) with the non-aligned net section (A_m), see Figure 7-31 (taken from reference [14]). If the latter is larger than the former ($A_m/A_s > 1$) the notches are not interacting and if $A_m/A_s < 1$ the notches are interacting. As depicted in Figure 7-31, this is in agreement with experimental results, in which the plastic collapse load of a plate with single notch (P_s) has been compared with this of a plate with two non-coplanar notches. It should be noted that this approach was originally suggested for through-thickness notches. In this study its applicability for two non-coplanar semi-elliptical notches will be evaluated by FE analysis. This has been inspired by the SCB concept introduced earlier in this chapter (e.g. Figure 7-17). In Table 7-4 configurations for which $A_m < A_s$ are assumed as interacting based on the area criterion. Note that for calculating the area of a notch, its bounding rectangle is

considered. This study aims to examine the application of this criterion for unstable crack growth, this adds a complementary capability to this criterion which has been proved to be successful in plastic collapse assessment.

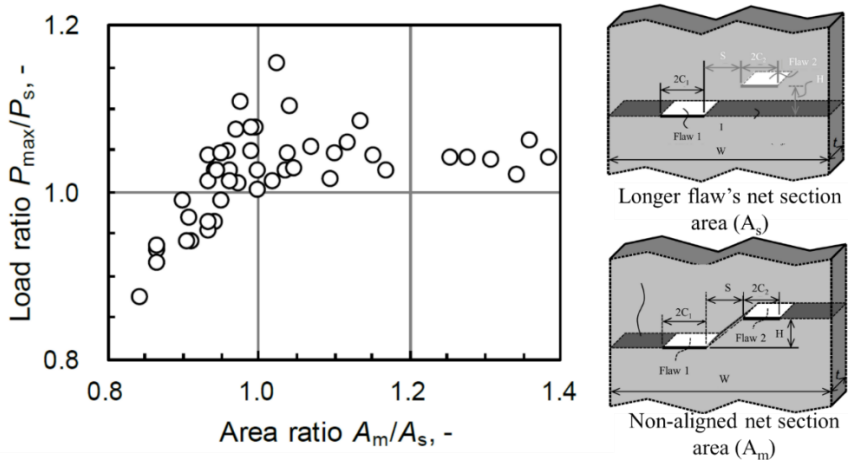


Figure 7-31: Iwamatsu's method to assess the limit load of two non-coplanar adjacent notches [13].

second alternative is called “45 degree”. Recall from chapter 3 that Bezensek and McCulloch [15] reported that the largest interaction, based on FE analysis of SIF, was observed for geometries in which horizontal and vertical spacing distances are equal, i.e. the connecting line between two flaws is at an angle of 45 degrees with respect to the loading direction. They also suggested that, unlike for elastic conditions where the largest interaction is observed for coplanar flaws, the development of plasticity due to a crack shielding effect reduces interaction in coplanar configurations compared to non-coplanar counterparts. This has been confirmed by results presented higher in this chapter for through thickness notches (section 7.2.4). Based on elastic-perfectly plastic simulations, Bezensek and McCulloch [15] reported that the limit load of the ligament is mainly affected by the horizontal distance between flaws (S) rather than the vertical distance (H). Considering a few cases in which notches are under 45° to each other, it will be examined if these are critical when it comes to failure or not.

Table 7-4: FE simulation matrix for the main study.

Group	Specifications	Tag	H [mm]	Interacting	Aligned			45°
				BS7910 ASME XI	ASME XI	BS7910	Area criterion	
A	a ₁ =a ₂ =5 mm 2c ₁ =2c ₂ =36 mm S=2.5 mm	A1	0	YES	Coplanar configuration			
		A2	2.5	YES	YES	YES	YES	YES
		A3	8	YES	YES	YES	YES	NO
		A4	12	YES	YES	NO	NO	NO
		A5	30	NO	NO	NO	NO	NO
		A6	60	NO	NO	NO	NO	NO
B	a ₁ =a ₂ =3.5 mm 2c ₁ =2c ₂ =36 mm S=6 mm	B1	0	NO	Coplanar configuration			
		B2	3	NO	YES	YES	YES	NO
		B3	6	NO	YES	YES	YES	YES
		B4	10	NO	YES	NO	YES	NO
		B5	30	NO	NO	NO	NO	NO
C	a ₁ =a ₂ =7.5 mm 2c ₁ =2c ₂ =48 mm S=10 mm	C1	0	NO	Coplanar configuration			
		C2	10	NO	YES	YES	YES	YES
		C3	15	NO	NO	YES	YES	NO
		C4	25	NO	NO	NO	YES	NO
		C5	40	NO	NO	NO	NO	NO
		C6	60	NO	NO	NO	NO	NO
D	a ₁ =a ₂ =5 mm 2c ₁ =2c ₂ =36 mm S=15 mm	D1	0	NO	Coplanar configuration			
		D2	10	NO	YES	YES	YES	NO
		D3	15	NO	NO	NO	YES	YES
		D4	30	NO	NO	NO	NO	NO
E	a ₁ =7.5 a ₂ =3.5 mm 2c ₁ = 36 mm 2c ₂ =26 mm S=15 mm	E1	0	NO	Coplanar configuration			
		E2	10	NO	YES	YES	YES	NO
		E3	15	NO	NO	NO	NO	YES
		E4	30	NO	NO	NO	NO	NO
F	a ₁ =7.5 a ₂ =5 mm 2c ₁ = 48 mm 2c ₂ =36 mm S=5 mm	F1	0	NO	Coplanar configuration			
		F2	10	NO	YES	YES	YES	NO
		F3	15	NO	NO	NO	NO	NO
		F4	30	NO	NO	NO	NO	NO
G	a ₁ =7.5 a ₂ =5 mm 2c ₁ = 48 mm 2c ₂ =36 mm S=10 mm	G1	0	NO	Coplanar configuration			
		G2	10	NO	YES	YES	YES	YES
		G3	15	NO	NO	NO	YES	NO
		G4	30	NO	NO	NO	NO	NO
H	a ₁ =a ₂ =6 mm 2c ₁ = 48 mm 2c ₂ =36 mm S=15 mm	H1	0	NO	Coplanar configuration			
		H2	10	NO	YES	YES	YES	NO
		H3	15	NO	NO	NO	YES	YES
		H4	30	NO	NO	NO	NO	NO
I	a ₁ =6 a ₂ =6 mm 2c ₁ = 48 mm 2c ₂ =48 mm S=3 mm	I1	0	YES	Coplanar configuration			
		I2	11	YES	YES	YES	YES	NO
		I3	18	NO	NO	NO	YES	NO
		I4	30	NO	NO	NO	NO	NO
J	a ₁ =a ₂ =3.5 mm 2c ₁ =2c ₂ =36 mm S=1.7 mm	J1	0	YES	Coplanar configuration			
		J2	1.7	YES	YES	YES	YES	YES
		J3	3	YES	YES	YES	YES	NO
		J4	6	YES	YES	NO	YES	NO
		J5	10	YES	YES	NO	NO	NO
		J6	20	NO	NO	NO	NO	NO
		J7	40	NO	NO	NO	NO	NO

In Table 7-4 the models are divided into 8 groups; for each the notch size and horizontal spacing (*S*) are kept constant and only vertical spacing (*H*) is varied. For

each group, one coplanar notch configuration is considered in addition to various non-coplanar configurations intended to study one of the criteria mentioned in the table's header. Each group has one or more cases which is/are not categorized as interacting, aligned or critical by any of the abovementioned criteria. In addition to the cases listed in Table 7-4, six models containing only the largest notch of each group with varying depth at 4 levels have been simulated for the mapping approach. The main study contains 93 simulations of wide flat plates with semi-elliptical notches. The plate is 1300 mm long, 15 mm thick and its width is 300 mm to avoid any significant edge effect on the notch behavior (for more details about the model geometry see 6.1). The same material properties as the experiments mentioned in 7.2.1 are assumed for this model. The experimental validation of the medium scale model is described in 5.4.2 and the details of the numerical procedure can be found in chapter 4.

The main study has the ambition to answer to three questions in particular:

1. Can non-coplanar wide plate configurations be more or similarly critical compared to their coplanar counterparts? Note that, being more critical than the coplanar configuration does not necessarily imply that the non-coplanar notches are interacting.
2. Can alignment criteria in ASME B&PV Code sec. XI, BS7910 and alternative criteria detect the cases in which non-coplanar configurations are critical?
3. Can interaction between two non-coplanar notches become sufficiently severe to allow classification as interacting, while their coplanar counterparts are not interacting (according to ECA guidelines)?

To answer the first question, global strain at critical CMOD is calculated for each non-coplanar model and normalized by the strain of the coplanar model at the same CMOD level. By plotting this ratio versus different criteria, the second question is addressed (Figure 7-32 to Figure 7-35). The ratio of global strain for a multiple notched plate to the strain of the model with single notch (the largest in the case of dissimilar notches) at the critical CMOD is calculated to judge the severity of interaction, which answers the third question (Figure 7-36 to Figure 7-39).

In the main study two parameters are used to investigate the effect of interaction at the global strain at failure:

- Normalized global strain (β): this is the ratio of global strain at critical CMOD of non-coplanar notch configuration (ε_c^{NC}) normalized by the strain of the coplanar configuration from the very same group (see Table 7-4) at the same CMOD level (ε_c^{CP}), as shown in equation 7-1:

$$\beta = \frac{\epsilon_c^{NC}}{\epsilon_c^{CP}} \quad 7-1$$

- Strain-based interaction factor (ω): this is the ratio of global strain of multiple notched models (includes both coplanar and non-coplanar configurations) at critical CMOD (ϵ_c) normalized by the global strain of the model with single notch (the largest in the case of dissimilar notches) at the same CMOD level (ϵ_c^{Single}), as shown in equation 7-2:

$$\omega = \frac{\epsilon_c}{\epsilon_c^{Single}} \quad 7-2$$

Figure 7-32 plots normalized global strain versus vertical spacing distance; the vertical dashed line shows the ASME B&PV code section XI criterion (12.5 mm). Ratios below unity (horizontal dashed line) indicate that non-coplanar configurations are more critical than their coplanar counterparts. Figure 7-33 plots the normalized global strain versus the BS7910 criterion that compares vertical spacing distance with the sum of two notch depths.

In addition to the aforementioned ECA guidelines, normalized global strain has been compared with the area criterion. Figure 7-34 depicts normalized global strain versus A_m/A_s , in which A_m is the area of a section containing two notches and A_s is the cross-section area of the model with a single notch (the largest in case of dissimilar notches), as illustrated on Figure 3-6. When A_m/A_s is less than unity, it is assumed that the notches are aligned. These results are plotted at the left side of the vertical dashed line in Figure 7-34. The next criterion which is evaluated, is the angle between the notches calculated as $\arctan(H/S)$. In this figure the vertical dashed line shows the 45° configuration, which corresponds to equal spacing distance in vertical and horizontal direction ($H=S$). Coplanar configurations correspond with an angle of 0° .

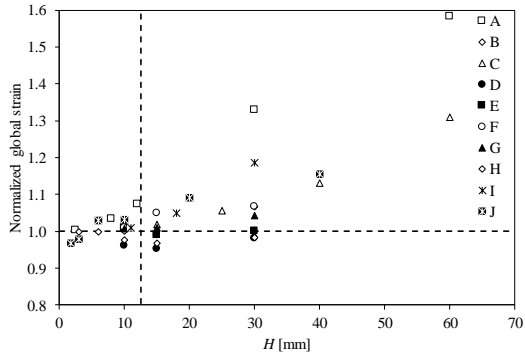


Figure 7-32: Normalized global strain (β) versus vertical spacing distance (H) at critical CMOD.

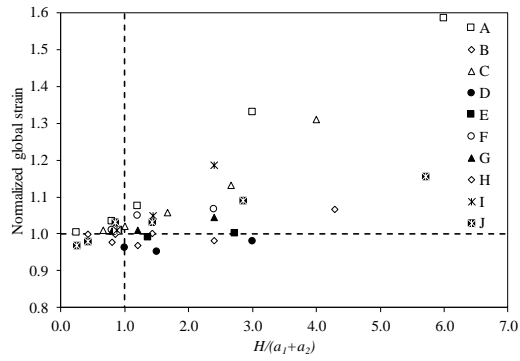


Figure 7-33: Normalized global strain (β) versus BS7910 criterion ($H/(a_1+a_2)$) at critical CMOD.

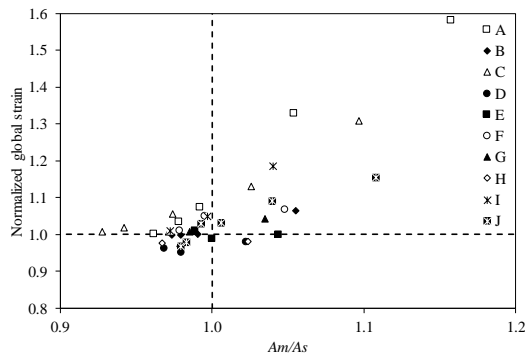


Figure 7-34: Normalized global strain (β) versus area criterion (A_m/A_s) at critical CMOD.

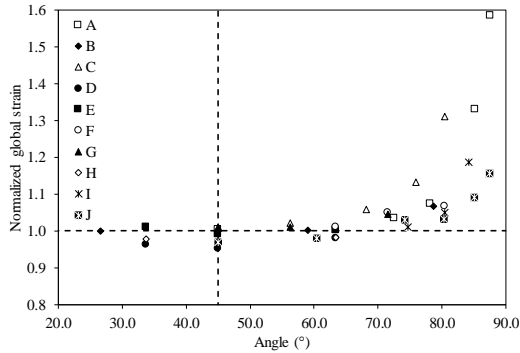


Figure 7-35: Normalized global (β) strain versus angle ($\arctan (H/S)$ at critical CMOD.

Returning to the first question defined above, non-coplanar configurations which became more critical than their coplanar counterparts in the pilot study are clearly less significant in a wider plate. The minimum value of normalized global strain does not reach 0.95, indicating that when plate width is increased this is not as significant as for a narrow plate. Consequently, the concern of critical non-coplanar configurations is more relevant for narrow plates or low diameter tubes.

Regarding the second question, although none of the criteria can perfectly distinguish the cases with normalized global strain less than unity, the area criterion is judged to be the most performant in this respect. As shown in Figure 7-34, almost all cases with normalized global strain close to but less than unity, have been defined as aligned flaws by the area criterion, while many cases are not withheld by ASME B&PV code section XI and BS7910 (Figure 7-32 and Figure 7-33).

As shown in Figure 7-35, although clearly all cases with angle equal or less than 45-degrees have a normalized global strain less than unity, it seems that 65 degrees can be a better boundary; this corresponds with configurations in which vertical spacing distance is two times the horizontal spacing distance ($H=2S$).

Here a distinction should be made between cases in which the non-coplanar configuration is more critical than the coplanar counterparts, and the cases in which non-coplanar flaws may interact. The former has been studied because of its possible role in undermining the ECA two-step alignment-interaction procedures.

Figure 7-36 depicts that strain-based interaction factor versus vertical spacing distance (H); the vertical dashed line shows the ASME B&PV code sec. XI criterion for alignment ($H = 12.5$ mm). Groups A, I and J contain the models which are interacting according to ASME B&PV code section XI and BS7910. The models from these groups which are at the left side of the dashed line are categorized as interacting according to the ASME criterion. Similarly, Figure 7-37 shows the strain-based interaction factor versus BS7910 criterion and those models from group A, I and J

which are at the left of the vertical dashed line are interacting, and those from the other groups are aligned but not interacting according to this guideline. Comparing the assessment results of these two guidelines reveals some discrepancies between them. For instance, A4 and J5 are categorized as interacting by ASME B&PV Code sec. XI but not by BS7910. While strain-based interaction factor of J4 and J5 do not differ significantly, the former is interacting according the BS7910 and the latter is not. Judging a case like I3, which is not interacting according to both guidelines, is also questionable since its strain-based interaction factor is not so different from I2 which is interacting according to both guidelines. Another noteworthy case is J2, which has a lower strain-based interaction factor than its coplanar counterpart.

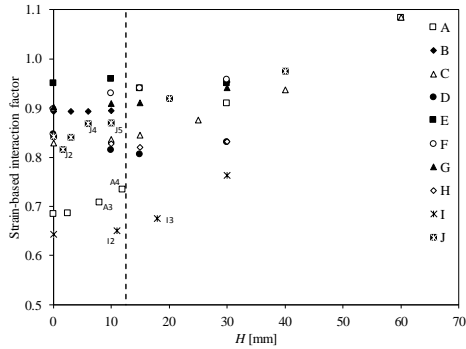


Figure 7-36: Strain-based interaction factor (ω) versus vertical spacing distance (H) at the critical CMOD.

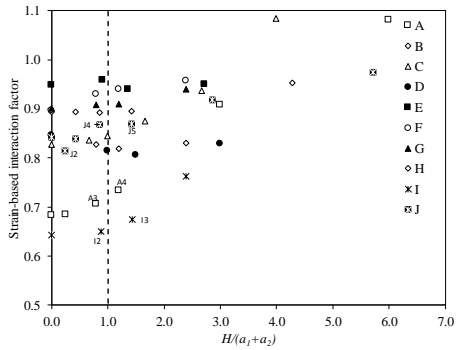


Figure 7-37: Strain-based interaction factor (ω) versus BS7910 criterion ($H/(a_1+a_2)$) at the critical CMOD.

Figure 7-38 shows the strain-based interaction factor versus the area criterion. Notably, A4, I3 and J5 which are supposed to be aligned based on their strain-based interaction factor, but not defined as such by ASME or BS, are categorized as aligned by the area criterion, which can qualify them as interacting as well (based on ASME

and BS interaction criteria for coplanar flaws). The area criterion is inherently a conservative approach since it will detect many non-coplanar flaws as aligned, even in fairly remote vertical and horizontal distances. However, this does not make this criterion an over-conservative approach, because in the second stage of assessment when the aligned flaws are compared with interaction criterion, like those introduced in ASME B&PV code section XI and BS7910, automatically many of them are concluded as not interacting due to their large horizontal spacing distances (S). These are points at the left side of the dashed vertical line with strain ratios around 0.9.

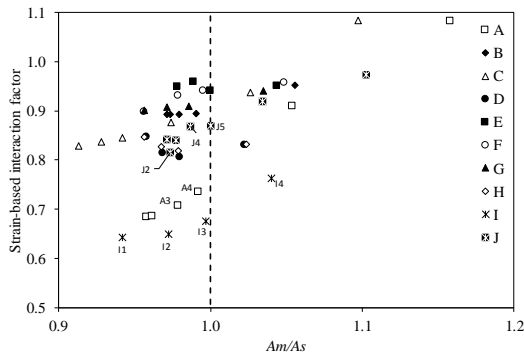


Figure 7-38: Strain-based interaction factor (ω) versus area criterion (A_m/A_s) at the critical CMOD.

Figure 7-39 plots the strain ratios versus the angle between the notches. No correlation can be observed.

It has been observed that some non-coplanar notched models are more critical compared to their coplanar counterparts. To judge on the significance of this observation with respect to flaw interaction (relating to the third question), these cases have been assessed in terms of their strain ratios to the single notched specimen (ω). Hereto, a threshold should be defined to filter out the non-significant cases.

One way to define this threshold is based on the average of strain ratios of interacting configurations according to ECA guidelines. For instance, in Figure 7-38 models from group A and I have the lowest strain ratios and group J has the highest, whilst all of them are interacting according to ASME B&PV Code sec. XI. Based on the average strain ratios of these cases the threshold can be defined around 0.75. Consequently, none of the cases with critical non-coplanar configurations (normalized global strain less than unity) are deemed to be significant, because all have a strain ratio higher than 0.75.

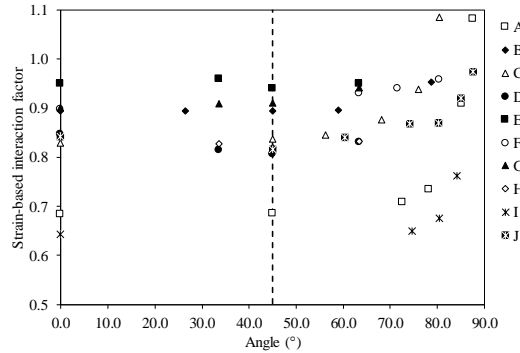


Figure 7-39: Strain-based interaction factor (ω) versus angle (Arctan (H/S)) at critical CMOD.

Another way to define this threshold, which is more conservative, is to take the highest strain ratio of interacting notches which are group J models. The corresponding threshold is approximately 0.85; therefore, more cases are detected as interacting. With this definition, some of the cases from group D and H are deemed to be interacting. Since some of these have already been detected as critical non-coplanar configurations (see Figure 7-34), this may lead to the conclusion that some non-coplanar configurations can be significantly more critical than their coplanar counterparts when it comes to strain-based assessment.

From these two threshold definitions, the former is deemed more robust. Because first of all, the closer the notches are (i.e. group J), the more probable that coalescence will happen due to ductile crack growth. As a result, the strain at critical CMOD will be reduced (i.e. strain capacity will be decreased), and therefore the strain ratio is decreased. In other words, if ductile tearing is considered, strain ratios of group J would decrease more than those from groups D and H, because the interaction of group J models is local and by coalescence and increase in the R -curve their growth would be accelerated which leads to sooner failure (less strain capacity). Therefore, taking the group J strain ratio as the reference is not a good choice since it is very likely that this value reduces if ductile tearing is considered. In addition, the former threshold definition is consistent with Hasegawa et al. [16] observations about non-significant interaction between non-coplanar flaws with depths less than 40% of plate or pipe thickness.

The selection of the former threshold is also confirmed by comparing the SCBs of the FE models. Figure 7-40 shows strain concentration bands at TES for four cases with quite similar vertical spacing distance (H); I2 and J5 are interacting according to the referred ECA guidelines, while H2 and D2 are not. Selection of the latter threshold would suggest that H2 and D2 may interact because their strain ratios are quite close. However, comparing their SCBs (Figure 7-40) clearly shows that the SCBs of H2 and D2 are different from I2 and J5. This proves that the latter threshold is not suitable for

distinguishing interacting and non-interacting cases because it mistakenly suggests that some cases from group H and D are interacting.

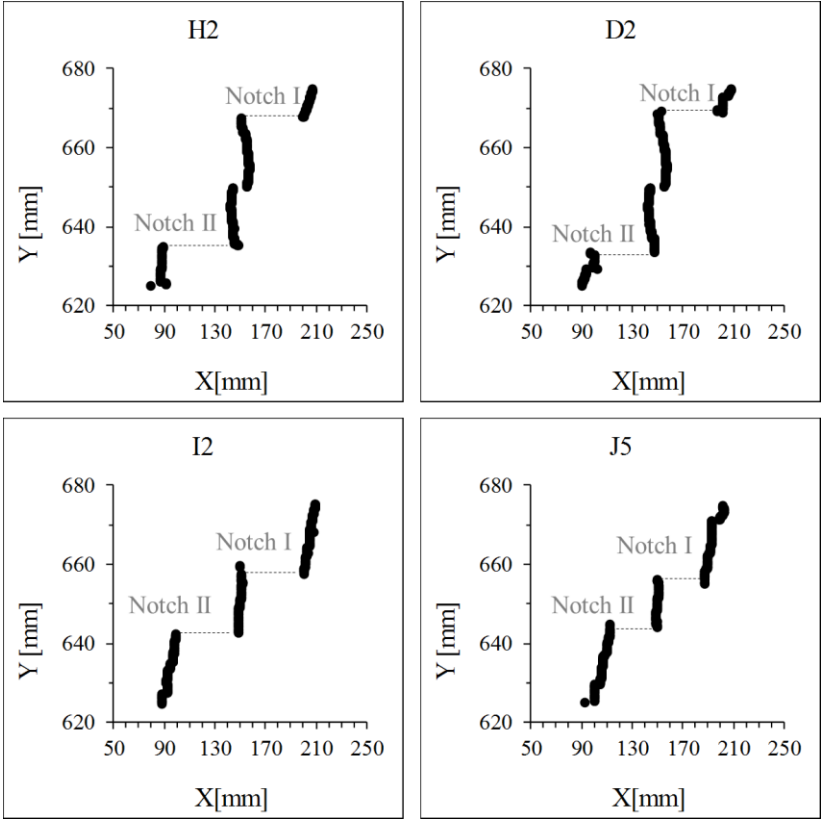


Figure 7-40: SCB at TES for cases H2, D2, I2 and J5.

7.4. Conclusion

In the first section of this chapter, a novel approach based on evaluating strain patterns is introduced with the aim to investigate the interaction between non-coplanar through thickness notches subjected to global plastic deformation. Analysis of the trajectory of strain concentration bands (SCBs) and the magnitude of strains along these bands, allows to clearly distinguish between cases of interacting and non-interacting flaws in asymmetrically double edge notched specimens. CTOD is used as a reference to judge on the (in) existence of flaw interaction.

The most obvious finding from this study is that comparing the angle between the two non-coplanar flaw tips (θ) with the angle of the SCB regression line (α) can characterize flaw interaction. When these angles are equal, the SCBs of the adjacent

cracks are connected to each other and the magnitude of strain in the region between the two cracks increases. The onset of interaction based on this criterion is associated with a CTOD increase of roughly 10 percent due to interaction, and a variable angle φ between the flaw tips. This indicates that θ solely is not capable of capturing the combined effects of out-of-plane distance and flaw depth on the degree of interaction.

In the second section of this chapter, flaw interaction has been studied for semi-elliptical notches in flat plates by experiments and numerical simulations. SCBs have been evaluated for these configurations as well and used to describe the interaction between adjacent notches.

Replicas have been cast in the semi-elliptical notches at several stages during the tensile test to measure crack growth. Results showed that if coalescence does not occur, the *R*-curve is not notably affected by varying vertical or horizontal spacing distance and is similar to that of a single notch. However, if coalescence occurs, one long flaw is obtained and consequently its constraint is raised, which leads to a decreased *R*-curve.

Since the experimental results suggested that certain non-coplanar configurations can be more critical than their coplanar counterparts, FE models of tensioned wide plates have been employed to investigate this matter more comprehensively. Results showed that in wider plates the criticality of non-coplanar configurations is less significant than their coplanar counterparts. This indicates that, the results of experiments with relatively narrow plates, cannot be employed to wide plates, as far as the strain in non-coplanar configurations is concerned.

An alternative criterion based on a suggestion of Iwamatsu et. al, with slight modifications, for flaw alignment is introduced. Based on the FE results, this criterion is proven to be more conservative in assessment based on unstable ductile tearing than ASME B&PV code section XI and BS7910. For strain capacity assessment, in which the failure is combination of plastic collapse and unstable ductile tearing, since the criterion suitability has been proven for the former by Iwamatsu and for the latter in this work, it is concluded that the area criterion can detect the critical non-coplanar configurations better than ASME B&PV and BS7910 criteria. So, if it is combined with the ASME B&PV and BS7910 criteria for co-planar flaws, it can provide more robust predictions of strain based flaw interaction.

References

- [1] Hasegawa K, Saito K, Miyazaki K. Alignment Rule for Non-Aligned Flaws for Fitness-for-Service Evaluations Based on LEFM. J Press Vessel Technol 2009;131:041403. doi:10.1115/1.3152229.
- [2] Van Gerven F, De Waele W, Belato Rosado D, Hertelé S. Characterization of slip lines in single edge notched tension specimens. Sustain Constr Des 2015;6:1–7.
- [3] Rules for Construction of Nuclear Facility Components-ASME Boiler and Pressure vessels code - Section III. New York, US: The American Society of Mechanical

- Engineers; 2017.
- [4] Miyazaki K. Effect of flaw dimensions on ductile fracture behavior of non-aligned multiple flaws in a plate. Proc. ASME 2011 Press. Vessel. Pip. Div. Conf. PVP2011, Baltimore, MD, USA: 2011.
 - [5] Iwamatsu F, Miyazaki K, Takazawa H, Saito K. Evaluation Procedure of Limit Load for Non-aligned Multiple Flaws. Proc. ASME 2013 Press. Vessel. Pip. Conf. PVP2013, Paris, France: 2013, p. 1–6.
 - [6] API 579-1/ ASME FFS-1. Recommended practice for fitness-for-service: API-579-1. 2nd ed. Washington DC, USA: American Petroleum Institute; 2007.
 - [7] Anderson TL. Fracture mechanics: fundamentals and applications. Portland: Taylor & Francis Inc; 2017.
 - [8] Wu S-X, Mai Y-W, Cotterell B. Slip-line field solutions of three-point bend specimens with deep notches. Int J Mech Sci 1987;29:557–64. doi:10.1016/0020-7403(87)90027-0.
 - [9] Hasegawa K, Miyazaki K, Saito K, Bezensek B. Evaluation of alignment rules using stainless steel pipes with non-aligned flaws. Proc ASME 2009 Press Vessel Pip Div Conf PVP2009 2009;1–8.
 - [10] Hasegawa K, Miyazaki K, Saito K. Plastic collapse loads for flat plates with dissimilar non-aligned through-wall cracks 2011:1–5.
 - [11] Moon S-I, Chang Y-S, Kim Y-J, Lee J-H, Song M-H, Choi Y-H. Determination of failure pressure for tubes with two non-aligned axial through-wall cracks. Int J Fract 2007;144:91–101. doi:10.1007/s10704-007-9082-5.
 - [12] Bezensek B, Hancock JW. The re-characterisation of complex defects Part I: Fatigue and ductile tearing. Eng Fract Mech 2004;71:1001–20. doi:10.1016/S0013-7944(03)00155-3.
 - [13] Verstraete MA, De Waele W, Denys RM, Van Minnebruggen K, Hertelé S. Constraint analysis of defects in strength mismatched girth welds of (pressurized) pipe and Curved Wide Plate tensile test specimens. Eng Fract Mech 2014;131:128–41. doi:10.1016/J.ENGFRACMECH.2014.07.018.
 - [14] Iwamatsu F, Miyazaki K, Saito K. Limit Load Solution of Non-Aligned Multiple Flaws. Proceedings ASME 2018 Press. Vessel Pip. conference PVP2018, Prauge: American Society of Mechanical Engineers; 2018, p. 1–8.
 - [15] Bezensek B, McCulloch E. Interaction of Twin Non-Aligned Through-Wall Flaws Under Elastic-Plastic Conditions. Proceedings ASME 2006 Press. Vessel Pip. conference PVP2006, Vancouver: American Society of Mechanical Engineers; 2008, p. 333–40. doi:10.1115/pvp2006-icpvt-11-93373.
 - [16] Hasegawa K, Saito K, Iwamatsu F, Miyazaki K. Prediction of Fully Plastic Collapse Stresses for Pipes With Two Circumferential Flaws. J Press Vessel Technol 2009;131:021209. doi:10.1115/1.3066967.

Conclusions and recommendations for future research

8.1. Background and methodology

Current flaw interaction rules in engineering critical assessment (ECA) procedures are based on linear-elastic fracture mechanics (LEFM) [1], and their application for failure modes different from brittle fracture might be questioned. Research [2,3] has shown that when the applied stress level approaches (or exceeds) yield strength and the design becomes strain-based rather than stress-based, flaw interaction rules in ECA procedures may either under-estimate or over-estimate the severity of interaction. However, only a limited amount of research has been performed related to interaction between adjacent flaws for scenarios wherein the specimen experiences pronounced plastic deformation.

This dissertation has elaborated on the development of numerical and experimental tools to investigate flaw interaction in strain-based design. Due to the inherent characteristic of strain-based scenarios, which allow pronounced plastic deformation, particular attention has been given to elastic-plastic fracture mechanics (EPFM) analysis, plastic collapse as failure mode, strain-hardening effects and the role of ductile crack growth.

The primary objective was to gain insight in the effect of interaction between adjacent flaws on EPFM related crack driving force parameters (J -integral, crack tip opening displacement CTOD), plastic collapse load, deformation behavior (i.e. strain patterns) and tensile strain capacity. Historically, fracture mechanics based solutions were developed for cases of single isolated cracks. Therefore, limited analytical and experimental procedures are available when more than one crack is subject to analysis. The first challenge of this work was to develop numerical and experimental methods that allow to describe the interaction in terms of the abovementioned parameters. Next, the capability of current interaction rules to conservatively assess flaw interaction in high strain regimes has been examined using the abovementioned methods. Finally, alternative procedures and criteria were developed to optimize the accuracy of flaw interaction assessment in strain-based design scenarios.

To gain understanding of the interaction rules, the latest versions of the most acknowledged ECA procedures and the history of their major changes with respect to flaw interaction have been reviewed (chapter 3). In addition, some of the highlighted researches in flaw interaction have been reviewed. Although there is a growing consensus among the ECA procedures on how to treat flaw interaction, pronounced differences remain. Most of the recent and ongoing researches are focused towards examining, and possibly updating, flaw interaction rules for failure modes other than brittle fracture.

To address the abovementioned challenges, an experimental-numerical approach has been conceptualized, implemented and validated. Numerical methods based on finite element (FE) analysis, as described in chapter 4, contain three parametric models: a small-scale notched tensile test model (1st model), a medium scale tension loaded plate model (2nd model) and a full scale tension loaded and potentially pressurized pipe model (3rd model). The small scale tensile test model with through thickness notches has been used to develop fundamental understanding of flaw

interaction in high-strain regimes. It has also been used to develop a novel method to quantify flaw interaction, based on the concept of so-called “Strain Concentration Bands” (SCB). The medium scale plate model contains semi-elliptical surface notches of finite length, which are more representative to flaws detected in real structures. This model has been used to generate the main results of this study in terms of stress intensity factor, crack driving force, deformation behavior and strain capacity. The pipe model adopted a novel approach in modeling the flaws by deleting elements rather than including the flaws in the initial model geometry. This technique has a great advantage in modelling realistic flaws of arbitrary shape and can be potentially linked with non-destructive examination (NDE) output to directly simulate the detected flaws. In this study the element deletion technique has been used due to its particular merit in modelling embedded flaws. In total, this thesis contains 438 finite element simulations.

In this thesis, several experimental investigations have been undertaken to calibrate the material properties of FE models, to validate the methodology and results of these models, and to quantify ductile crack growth which was not implemented in the developed FE model. Digital Image Correlation (DIC) has been used extensively to measure the full-field 3D surface deformation and in-plane strain distributions. These results were used to describe flaw interaction by the SCB method as well as measuring CTOD through a novel experimental method developed in the course of the present work. Silicone replica casting was used to measure the ductile crack growth in adjacent notches and also to measure CTOD to validate the DIC based method. Chapter 5 describes all the experimental techniques, provides FE model validations by experimental and analytical approaches and elaborates the novel method for measuring CTOD by DIC along the crack front.

8.2. Results

Using the methodology described above, many results have been generated that shed new light on the interaction of flaws in strain based conditions. These are subdivided in separate sections below. At the time of submission of this dissertation, the outcomes of this work have been disseminated in 2 peer reviewed journal papers and 4 conference proceedings papers.

8.2.1. Flaw idealization effect on the interaction

Flaw interaction is conventionally defined by the ratio of linear-elastic stress intensity factor (SIF) of the largest flaw (which is expected to control interaction) in a multiple notched specimen to that of the same flaw when it is isolated. A ratio above unity represents an increase in SIF due to the presence of another flaw in a close proximity. Flaw geometry idealization is the first step of flaw characterization. It may affect the outcome of the flaw interaction assessment in the sense that irregularly shaped flaws may have higher SIF compared to their idealized counterparts. This would make them more prone to interact with remotely located flaws. To investigate this effect, in section 6.1, flaws have been modelled as both canoe-shaped and semi-elliptical shapes. A canoe-shaped flaw may be more representative of actual flaw geometry, but a semi-elliptical flaw is the most conventional idealized shape in fracture mechanics studies. Compared to canoe-shaped notches, employing semi-

elliptical notches in an elastic-plastic analysis leads to a potential underestimation of flaw interaction effects by established ECA procedures for the results generated in this study. This difference is less pronounced in linear-elastic analyses. It should be noted that

Linear regression analysis of the obtained results suggests that flaw idealization has a more important influence on interaction for deeper notches having lower aspect ratio. When it comes to re-characterization of the interacting flaws, as per ECA procedures' suggestion, results showed that re-characterizing the interacting canoe-shaped notches into a single encompassing semi-elliptical notch is not always conservative. This non-conservativeness has been observed both in linear-elastic and elastic-plastic analyses and it is more pronounced for notches with low aspect ratio (i.e. long and shallow flaws). It should be noted that the results based on the canoe-shaped notch are insufficient to provide a generic statement about arbitrarily shaped flaw. Although, conventional NDT tools do not provide detailed information on real flaw shape, they are qualified according to FFS codes. As such, sizing of flaw indication is always larger than the actual flaw. This oversizing provides implicit conservatism which is believed dominates any non-conservatism of assumed flaw shape. Therefore, to develop remedial action for the possible shortcomings due to flaw idealization, the study of arbitrary flaw shapes combined with advanced NDT flaw characterization is suggested for future research (See 8.3.3).

8.2.2. Linear-elastic and elastic-plastic interaction of coplanar surface breaking flaws

The severity of interaction at higher load levels is supposed to be the main concern in strain-based design. However, strain hardening and the occurrence of stable ductile tearing prior to unstable fracture may compensate this concern to some extent. With this perspective, the interaction between two surface breaking defects has been studied for both linear-elastic and elastic-plastic scenarios, and the results are compared with various ECA rules. Linear-elastic interaction has been investigated and quantified by means of SIF and elastic-plastic interaction by means of CTOD. The medium-scale FE model has been applied to various configurations, each corresponding to the onset of interaction based on one of three main approaches in ECA guidelines. These approaches consist of either comparing the distance between flaws against the flaw's depth and length, or rather comprise an empirical criterion. In addition, for the interacting flaws their corresponding re-characterized shape has been modelled according to each ECA rule.

Results showed that all ECA guidelines were conservative for both linear-elastic and elastic-plastic studies. However, pronounced differences were observed in their assessment. Assessments based on ASME B&PV Code sec. XI, BS7910 and API579 were concluded to be more accurate compared to API1104. This last one was concluded to over-conservatively re-characterize flaws with marginal interaction into moderately large encompassing flaws. The EPRG Tier 2 guidelines for girth weld defect assessment in transmission pipelines stands between these two types of rules, as regards their conservatism.

8.2.3. Linear-elastic and elastic-plastic interaction of coplanar (circumferential) surface braking flaw and an embedded flaw

A full-scale model of pipe geometry (3rd model) is used in section 6.2 to study the interaction in terms of linear-elastic and elastic-plastic fracture mechanics parameters for a circumferential surface breaking flaw with an adjacent embedded flaw. Flaws have been modelled by making use of an element deletion approach, allowing for their straightforward generation without requiring a cumbersome mesh partitioning strategy.

The evaluation comprised two aspects: the increase in crack driving force for which the rule is activated, and the conservatism introduced by re-characterizing the interacting flaws into its encompassing flaw. The obtained results have confirmed that standardized interaction criteria are conservative for the studied flaw configurations, when assessed in terms of their global conservatism factor. The global conservatism factor has been defined as the ratio of the maximum crack driving force along the entire crack front of one of the notches to that of the encompassing (bounding) notch.

The results showed that “yes-or-no” flaw interaction criteria solely based on defect spacing, provide a highly simplistic view on actual flaw interaction. Primary influence factors such as transverse offset (overlapping co-planar between surface and embedded flaws) and flaw dimensions are not (sufficiently) taken into account. As a result, non-consistencies can be observed between the treatment of different flaw pair configurations. Cases with a moderate increase of crack driving force may be treated as interacting and vice versa.

Moreover, once re-characterized, the bounding flaw of all ECA procedures treats the actual flaw pair in a conservative manner. However, the conservatism introduced by considering the bounding flaw can be substantial. For instance, considering linear-elastic analysis, the conservatism factor of many interacting configurations was in the order of 0.5, implying a safety factor 2 being introduced on the level of mode-I stress intensity factor K_I .

In addition, there are substantial differences in flaw interaction for linear-elastic and elastic-plastic load levels. Although not explicitly covered in this study, it is expected that material strain hardening properties and the exact load level will affect elastic-plastic flaw interaction. These differences are not accounted for in flaw interaction rules that are solely based on geometrical properties.

8.2.4. Effect of interaction on the strain trajectory

Unlike SIF based interaction studies, very limited research is available on the effect of interaction on the development of deformation and eventually on failure due to plastic collapse. This encouraged an in-depth study on the strain morphology when a multi-notched specimen is loaded beyond its yield strength. Due to the inherent complexity of non-coplanar notches the focus has been given to this configuration, while a few coplanar and single notched configurations have been studied as a reference as well.

A novel approach based on evaluating strain patterns between non-coplanar through thickness notches subjected to global plastic deformation has been developed in this work. As elaborated in section 7.1, an in-depth analysis of the trajectory of strain concentration bands (SCBs) and the magnitude of equivalent strain along these bands allows to clearly distinguish between cases of interacting and non-interacting flaws. Significant differences in SCBs were observed as the out-of-plane distance between the notches was changed. Based on these results, interaction is deemed to occur when SCBs at plastic collapse are developed between the two adjacent notches, and second SCBs are connected to each other. In such a case, both notches are simultaneously involved in the plastic collapse mechanism as the trajectory of maximum shear passes through them and the region between them. Otherwise, when SCBs are not connected or not developed between the two notches, interaction is assumed to be negligible.

With the above definition and SCB as a measure, the small-scale double-edge notched tension test and its corresponding FE model have been used to study the interaction in specimens with through-thickness edge notches, as a low-constraint representative of non-coplanar flaws. Based on these results, a clear relation has been observed between the development of SCBs and the interaction between the notches in terms of CTOD. These results gave the first confidence on the approach to distinguish between interacting and non-interacting cases solely based on strain morphology and deformation patterns.

8.2.5. Strain-based flaw interaction criteria

To develop the interaction rules for structures undergoing strain-based designed scenarios, as described in section 7.2, the medium-scale wide plate test and its corresponding FE model with semi-elliptical notches have been employed. Effects of interaction on the plastic collapse, strain pattern, strain-capacity and ductile tearing have been studied for non-coplanar as well coplanar configurations. The innovative concept of SCBs has been evaluated for these configurations as well and used with success to describe the interaction between adjacent notches.

Regarding the effect of interaction on ductile tearing, crack growth measurements based on replica casting showed that this effect depends to the occurrence of coalescence between the two adjacent flaws. In absence of coalescence, the R-curve is not affected by varying vertical or horizontal spacing distance. Comparing the R-curve of notches in various spacing distances showed that ductile tearing of interacting notches before the coalescence is similar to remote notches. Therefore, it is concluded that interaction does not change the R-curve significantly before the coalescence. However, if coalescence occurs the notch length increases and consequently its constraint is raised which leads to a lower crack growth resistance curve. This highlights another facet of challenges involved in flaw re-characterization in ECA procedures; when interacting flaws are re-characterized into larger encompassing flaw the R-curve is decreased. In other words, not only the encompassing flaw has a higher CDF which shifts its ductile tearing onset to the lower load levels, but also encompassing flaw tends to grow more compared to each of the original interacting flaws. Therefore, if the toughness value is based on single notch configuration this may lead to a non-conservative assessment.

Earlier studies [4–6] and experimental results of the present study (section 7.2) suggested that plastic collapse load is not affected by the interaction of non-coplanar shallow flaws. Due to the practical relevance of these types of flaws to pipelines, this study has focused on the tensile strain capacity of non-coplanar shallow flaws ($a/t \leq 0.5$). Results showed that in (curved) wide plates, which is a relevant geometry to pipelines, the effect of non-coplanar flaws on the strain capacity is less severe compared to coplanar flaws, as assumed in ECA procedures. However, the same cannot be concluded for narrow plates. In these geometries non-coplanar flaws may interact more severely than their coplanar counterparts, which requires more attention when it comes to assess their strain capacity since ECA guidelines have not considered this behavior. An area criterion, which is adopted with slight changes from Iwamatsu et al. [7], and a criterion based on the angle between the flaws, are shown to address the non-coplanar flaws interaction better than ASME B&PV code sec. XI and BS7910. The area criterion, as introduced in 7.3.3. (see figure 7-31) considers the non-coplanar flaws as aligned when the net section of the longer flaw (A_s) is bigger than the non-aligned net section (A_m).

In conclusion, the author proposes a draft procedure to evaluate flaw interaction in a strain-based design context. This draft procedure is based on flaw interaction rules from present ECA procedures - from the viewpoint of optimal industry acceptance and user adoption - but a few updates are suggested. Figure 8-1 summarizes this procedure, in which the asterisk (*) indicates the steps which are modified or added in comparison to figure 3-4. First, a safety factor should be considered for flaw idealization when the flaw aspect ratio is less than 0.4 ($a/c < 0.4$). This safety factor can be implemented in terms of increase in area of the idealized (semi-)elliptical flaw, since in chapter 6 it has been observed that canoe-shaped flaws can have 4% more interaction (in terms of interaction factor) compared to their semi-elliptical counterparts. Based hereon it is suggested to increase the area of the idealized flaw by keeping its central point and increasing all axes of the (semi-)ellipse with 2%. This increase with 4% is also in line with observations made by Kamaya et. al [8]. With this safety factor not only the long and shallow flaws ($a/c < 0.4$) are deemed to interact for slightly shorter spacing distances, but also the size of the encompassing flaw is increased as a measure for the non-conservativeness observed in the re-characterization process (see figure 6-16 to 6-18). The most pronounced update is for the evaluation of flaw alignment; for which the area criterion is put forward. Finally, considering the empirical nature of the EPRG criteria being based on a wide range of large-scale experiments, it is also suggested to employ the EPRG Tier 2 criterion (see equation 3.1) to assess the interaction of the coplanar flaws. The latter is a remedial action to compensate the potential non-conservativeness due to the severity of interaction at load levels corresponding to the onset of global plastic deformation. It is important to note that the validity of this draft procedure for strain-based conditions has been demonstrated (for a range of defect and material parameters) by means of finite element analyses and analysis of SCB's.

The outcome of the suggested procedure, either as a single flaw or a re-characterized flaw, can be used for a multi-level assessment carried out by well-acknowledged ECA procedures like ASME B&PV code sec. XI or BS7910. With respect to a higher level assessment based on finite element analysis, the deformation-based procedure based on an evaluation of SCB's is suggested for strain-based

conditions. Although this SCB procedure requires more development, the author is of the opinion that it can be used to classify adjacent flaws as interacting or not based on an analysis of stress concentration bands.

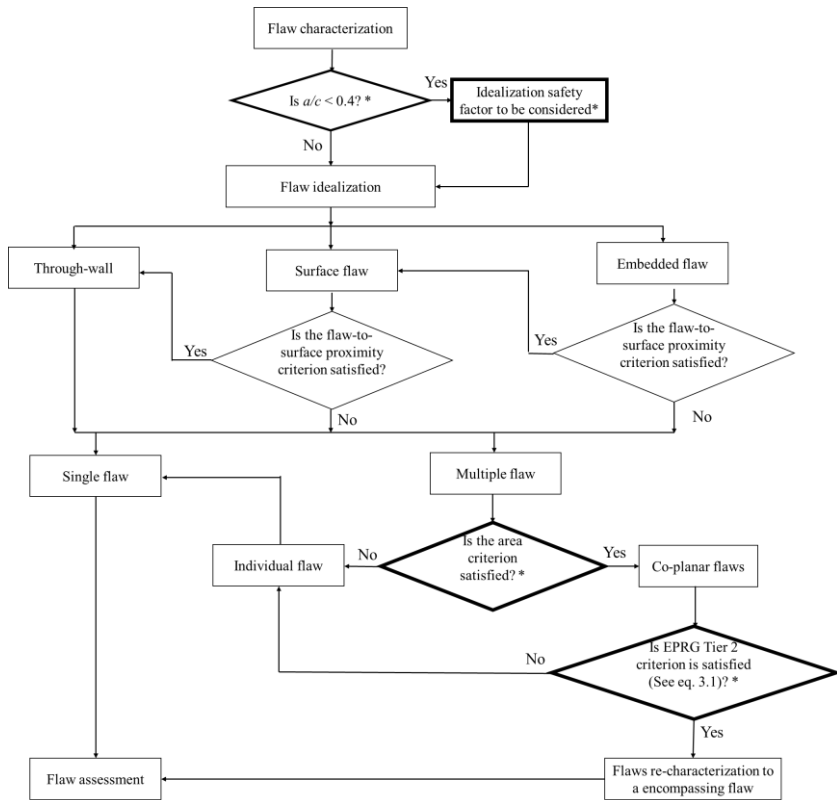


Figure 8-41: Strain-based flaw interaction flowchart, * represents the steps which are added or modified due to the result of this thesis.

8.3. Outlook for future research

8.3.1. Extensions in FE simulations

Additional studies are required for the validation of the suggested criterion in a strain-based design context. A particular point of attention is related to the effect of material toughness and strain hardening. Strain hardening has been proven to affect flaw interaction in an elastic-plastic analysis, so further attention should be directed to the influence of post yielding behavior on the interaction. In addition, the majority of flaws in pipelines are detected in the welds. However, except EPRG tier 2, all ECA procedures neglect the difference between weld and base material for the development of flaw interaction rules. The weld properties are normally different from base metal properties and they are known to be heterogeneous with respect to strength and toughness, which can affect the crack growth path and alter the coalescence between adjacent flaws. Previous experimental investigations in Laboratory Soete highlighted

the effects of these parameters on the interaction when the failure mode is plastic collapse. However, still there is a need for a more comprehensive experimental-numerical study for a broader range of parameters including toughness, strain hardening, weld strength mismatch and flaw location.

Further extension of developed models to consider the ductile tearing is another point of interest. FE simulation of multiple cracks incorporating ductile tearing based on continuum damage mechanics is herefore suggested. This investigation can be broadened to include (weld) material heterogeneity, weld over-matching effect and flaws located in different regions of a weldment (e.g. in the weld metal versus in the heat affected zone).

8.3.2. Effect of stress triaxiality (constraint)

It is known that the apparent fracture toughness and resistance curve (R-curve) of a material is strongly geometry dependent [9–11]. This is a reflection of the effect of stress triaxiality (constraint) ahead of the crack tip, which affects toughness and tearing resistance. Stress triaxiality by itself can be affected by many geometrical parameters including the nearby presence of another flaw. By taking into account these effects, a new dimension would be added to flaw interaction (which would not only be reflected in crack driving force, but also in material resistance). In analytical fracture mechanics, also there is a gap for this subject since very limited efforts have been made to describe the interaction between the adjacent cracks in terms of two parameter fracture mechanics (i.e. J - Q theory).

8.3.3. Interaction of arbitrarily shaped flaws and coupled NDT-FE

The results of this study showed that flaw idealization can impose non-conservativeness in flaw interaction assessments. Most of the researches, and subsequently ECA procedures, have been based on the well-acknowledged assumption that detected flaws can conservatively be represented by a (semi-) elliptical idealized flaw. Although, even for an isolated flaw this may not be always the case, the presence of the interaction can undermine this assumption. This discrepancy opens a new research question; the increase of SIF and CDF due to interaction is varied along the crack front, naturally it is more in regions close to the adjacent flaw ($\varphi \sim 0$). However, the maximum SIF or CDF in (semi-)elliptical idealized flaw happens in its deepest point ($\varphi = \pi/2$). Therefore, in an idealized flaw normally where the interaction affects more is different with where SIF reaches to its maximum. For non-idealized flaw, however, this is not always the case, since the deepest point can be very close to the adjacent flaw. Thus, it might be questioned if interaction rules which were developed based on idealized flaws can safely be applied to assess realistic non-idealized flaws.

Therefore, further investigations are required to quantify to which extent using flaws with non-idealized shapes can affect the outcome of an interaction assessment. The element deletion technique, which is introduced in the course of this work, is potentially advantageous over conventional methods in this respect, as it is able to generate arbitrarily shaped flaws in FE models.

In addition, novel NDT technologies facilitate advanced flaw shape characterization, to the extent that flaw idealization procedures and fracture mechanics calculations in traditional ECA codes/standards may become vintage procedures in the near future. Thanks to present-day cloud computation capabilities, a process can be imagined in which detected flaws are imported directly to FE models and their acceptance or rejection is determined based on their accurate size, actual loads and material properties

8.3.4. Developing experimental techniques for measuring crack extension in specimens with multiple notches

Further attention should be directed to the development of experimental techniques tailored for measuring ductile crack extension in specimens with multiple flaws. Available methods such as AC or DC potential drop and unloading compliance are only suitable for single flaw configurations. Silicone replica casting has been employed for this purpose. However, a more accurate and less cumbersome technique is still desired. For instance, mechanical-electrical finite element simulations can be used as complementary tool to interpret and develop the potential drop technique for multiple cracks growth measurement.

References

- [1] Marsdon TU. Flaw Evaluation Procedure: background and Application of ASME Section XI, Appendix A. EPRI NP-719-SR, Electrical Power Research Institute, Palo Alto, CA; 1978.
- [2] Coules HE. Stress intensity interaction between dissimilar semi-elliptical surface cracks. *Int J Press Vessel Pip* 2016;146:55–64. doi:10.1016/j.ijpvp.2016.07.011.
- [3] Tang H, Fairchild DP, Cheng W, Kan W, Cook M, Macia ML. Development of Surface Flaw Interaction Rules for Strain-Based Pipelines. *Proc. Twenty-fourth Int. Ocean Polar Eng. Conf.*, vol. 3, Busan, South Korea: 2014, p. 476–86.
- [4] Hasegawa K, Miyazaki K, Saito K. Behavior of plastic collapse moments for pipes with two non-aligned flaws. *Proc. ASME 2010 Press. Vessel. Pip. Div. PVP2010*, Bellevue, WA, USA: 2010, p. 1–7. doi:10.1115/PVP2010-25199.
- [5] Hasegawa K, Miyazaki K, Saito K. Plastic collapse loads for flat plates with dissimilar non-aligned through-wall cracks 2011:1–5.
- [6] Miyazaki K. Effect of flaw dimensions on ductile fracture behavior of non-aligned multiple flaws in a plate. *Proc. ASME 2011 Press. Vessel. Pip. Div. Conf. PVP2011*, Baltimore, MD, USA: 2011.
- [7] Iwamatsu F, Miyazaki K, Saito K. Limit Load Solution of Non-Aligned Multiple Flaws. *Proceedings ASME 2018 Press. Vessel Pip. conference PVP2018*, Prauge: American Society of Mechanical Engineers; 2018, p. 1–8.
- [8] Kamaya M, Totsuka N. Influence of interaction between multiple cracks on stress corrosion crack propagation. *Corros Sci* 2002;44:2333–52.
- [9] Brocks W, Schmitt W. Quantitative assessment of the role of crack tip constraint on ductile tearing. *Constraint Eff. Fract.*, ASTM International; 1993.
- [10] Hancock JW, Reuter WG, Parks DM. Constraint and toughness parameterized by T. *Constraint Eff. Fract.*, ASTM International; 1993.
- [11] Garwood SJ. Effect of specimen geometry on crack growth resistance. *Fract. Mech. Proc. Elev. Natl. Symp. Fract. Mech. Part I*, ASTM International; 1979.

Publications

A1- Peer reviewed journal publications included in Science Citation Index

First author: 2 publications

- 1- Samadian K, Hertelé S, De Waele W. Measurement of CTOD along a surface crack by means of digital image correlation. *ENGINEERING FRACTURE MECHANICS*. Elsevier BV; 2019;205:470–85.
- 2- Samadian K, Hertelé S, De Waele W. A strain-based approach to study interaction between non-coplanar through-thickness edge notches. *JOURNAL OF STRAIN ANALYSIS FOR ENGINEERING DESIGN* . SAGE Publications; 2018;53(8):687–98.

P1/C1/A2- Publications in journals not included in Science Citation Index and conference proceedings

First-author: 5 publications

Co-authored: 3 publications

- 1- Samadian K, Hertelé S, De Waele W. Elastic-plastic defect interaction in (a)symmetrical double edge notched tension specimens. *AIMS MATERIALS SCIENCE*. AIMS Press ; 2017;4(2):277–91.
- 2- Samadian K, Hertelé S, De Waele W. A novel flaw alignment approach based on the analysis of bands of maximum strain using full-field deformation measurements. *PROCEDIA STRUCTURAL INTEGRITY*. Elsevier BV; 2017. p. 1245–52.
- 3- Samadian K, Hertelé S, De Waele W. Elastic-plastic interaction between adjacent pipeline girth weld defects. In: Hertelé S, editor. *Proceedings of the Technology for Future and Ageing Pipelines Conference*. Gent, Belgium: Universiteit Gent, Tirsotsoo Technical; 2018.

- 4- Samadian K, Hertelé S, De Waele W. Using 3D Digital Image Correlation (3D-DIC) to measure CTOD in a semi-elliptical surface crack. MDPI AG; 2018.
- 5- Samadian K, Hertelé S, De Waele W. Effects of flaw shape (idealization) on the interaction of coplanar surface flaws. PROCEEDINGS OF THE ASME PRESSURE VESSELS AND PIPING CONFERENCE, 2018, VOL 5. American Society of Mechanical Engineer (ASME); 2019.
- 6- Höhler S, Mondry A, Kalwa C, Samadian K, Van Minnebruggen K, De Waele W, et al. Experimental investigation of strain capacity of pipelines with heterogeneous strength properties. 3R INTERNATIONAL. Vulkan Verlag; 2018;(Special 01):56–72.
- 7- Hertelé S, Van Minnebruggen K, Samadian K, De Waele W, Roovers P. Load bearing capacity of corroded girth welds in vintage pipelines below the ductile-to-brittle transition temperature. In: Hertelé S, editor. Proceedings of the Technology for Future and Ageing Pipelines Conference. Gent, Belgium: Universiteit Gent, Tiratsoo Technical; 2018.
- 8- Hertelé S, De Waele W, Van Minnebruggen K, Samadian K, Höhler S, Mondry A, et al. Influence of material heterogeneity on the strain capacity of pipelines : part 1 : curved and medium wide plate testing. In: Hertelé S, editor. Proceedings of the Technology for Future and Ageing Pipelines Conference. Gent, Belgium: Universiteit Gent, Tiratsoo Technical; 2018.